GFZ

Helmholtz-Zentrum
POTSDAM

HELMHOLTZ-ZENTRUM POTSDAM
DEUTSCHES
GEOFORSCHUNGSZENTRUM

Achim Helm

Ground-based GPS altimetry with the L1 OpenGPS receiver using carrier phase-delay observations of reflected GPS signals

Scientific Technical Report STR08/10

www.gfz-potsdam.de

HELMHOLTZ
GEMEINSCHAFT

Impressum

Helmholtz-Zentrum Potsdam
Deutsches GeoForschungsZentrum

Telegrafenberg
D-14473 Potsdam

e-mail: postmaster@gfz-potsdam.de
www: http://www.gfz-potsdam.de

Gedruckt in Potsdam
Oktober 2008

doi: 10.2312/GFZ.b103-08104
urn: urn:nbn:de:kobv:b103-08104
http://www.gfz-potsdam.de/bib/pub/str0810/0810.pdf

Die vorliegende Arbeit ist in der Schriftenreihe
Scientific Technical Report (STR) des GFZ erschienen

ISSN 1610-0956

Ground-based GPS altimetry with the L1 OpenGPS receiver using carrier phase-delay observations of reflected GPS signals

vorgelegt von Dipl.-Geophys. Achim Helm

Von der Fakultät VI - Planen Bauen Umwelt
der Technischen Universität Berlin
zur Erlangung des akademischen Grades
Doktor der Naturwissenschaften (Dr. rer. nat.)
genehmigte Dissertation

Berlin 2008
D83

Promotionsausschuss:

Vorsitz: Prof. Thomas Kolbe
Gutachter: Prof. Markus Rothacher
Gutachter: Prof. Christoph Reigber

Tag der wissenschaftlichen Aussprache: 19.9.2008

Scientific Technical Report STR 08/10

DOI: 10.2312/GFZ.b103-08104

pour mes mafs, für Anne und Arno und für Alexander und Katja

Nur wer nicht sucht, ist vor Irrtum sicher.

(Albert Einstein)

DOI: 10.2312/GFZ.b103-08104

Abstract

Water, ice and snow covered areas show a high reflectivity for Global Navigation Satellite System (GNSS) signals in the L-band frequency range. A part of the incident signal radiates back from the reflecting surface. The back radiated signal is available at many locations of the Earth for free. Although the signal power is weak this signal source can be used for altimetric purposes.

This study presents methods and field experiments for ground-based GPS altimetry. Although Coarse/Acquisition Code (C/A-code) based methods are introduced, the main part of this work addresses the use of carrier phase-delay observations of the reflected GPS signal and focuses on specular reflection. Model calculations of the reflection coefficients based on the Fresnel equations show that a sufficient fraction of the reflected signal can be recorded by a Right Hand Circular Polarization (RHCP) antenna. Thus, only one unmodified omni-directional RHCP GPS patch antenna is successfully used in the experiments. The antenna was tilted by 45° from zenith direction to allow signal reception from the GPS satellites and the surface reflector simultaneously. The experiments are performed with the OpenGPS receiver which was developed at the GFZ Potsdam for altimetric purposes. The 12-channel single-frequency L1 receiver was modified to allow open-loop tracking. Operating in open-loop mode 2 correlator channels – declared as master and slave channel, respectively – are tuned to the same GPS satellite by setting the appropriate Pseudo Random Noise (PRN) value. The correlation between the received and the generated replica signal is realized in hardware by directly controlling the Zarlink GP2021 correlator chip of the OpenGPS receiver. While the master channel continues to track the direct signal, the slave carrier and code Phase Lock Loops (PLLs) are opened and their loop feed-back is obtained from the master PLL. The carrier loop operates with zero carrier phase offset with respect to the master channel; in the code loop feed-back, however, the estimated delay of the observed reflection event is inserted. The OpenGPS receiver operates in two open-loop modes. In mono-reflection mode all 12 correlator channels are tuned to the same GPS satellite which allows to register the waveform of the reflected signal. In multi-reflection mode the receiver allows tracking of up to 8 direct GPS signals for navigation purposes and open-loop tracking of up to 4 independent reflected GPS signals simultaneously for altimetric purposes. During a predicted reflection event in-phase and quad-phase correlation sums of the slave channel are integrated over 20 ms taking into account the navigation bit boundaries and stored together with code and carrier phases to hard disk at a rate of 50 Hz.

In the first experiment – conducted in July 2003 in the Bavarian Alps in Germany – the OpenGPS receiver was positioned at the Fahrenberg location at 11.32°E, 47.61°N about 1026 m above the water level of lake Kochelsee and 824 m above lake Walchensee. When the correlator-generated model signal of the slave channel is phase-locked to the direct signal and has the expected delay in time, variations in the amplitude of the received signal can be observed. These fluctuations are caused by the interference between the coherently reflected signal and the model signal. From these amplitude variations the height of both lake surfaces can be determined. Several relative height profiles – continuous over lengths of up to 1700 m and an observation duration of more than 15 min – could be acquired from both lake surfaces. Height changes could be observed with an accuracy on the centimeter-level, with amplitudes of about 5 cm at Walchensee and about 10 cm at Kochelsee. Reflections have been measured mainly at elevation angles between 9.5° and 25° and distances between 1.8 km and 6 km from the receiver. The influence of the troposphere and the slope of the lake surface caused by the local gravity field are discussed. The second experiment – conducted on 11 June, 2004 on the roof of Hotel Mercure, Potsdam, at 52.39°N, 13.06°E – shows that at low receiver elevations the reflected signal arrives at the antenna with a comparably small delay after the direct signal. A method was developed to separate the reflected signal from the direct signal. The third experiment was conducted on September 20–24, 2004, during daytime at the chalk cliff coast on Rügen Island, Germany, at the shore of the Baltic Sea. The receiver was positioned at the Königsstuhl cliff top at 54.57°N, 13.66°E at a height of about 118 m above sea level. During all days of the experiment height measurements based on carrier phase-delays with some centimeter-accuracy could be made up to distances of 20 km from the coast. Continuous observation of more

than 20 min duration could be achieved. The roughness of the observed Baltic Sea surface was greater than the carrier wavelength λ_{L1}. Sufficiently strong coherent signals could be acquired at elevation angles below 15°. Here the sea surface appears smooth enough according to the Rayleigh criterion to derive height observations based on carrier phases. At elevation angles below 4° height fluctuations of several decimeter can be observed, caused by the influence of the local troposphere not represented in the applied troposphere correction model based on European Centre for Medium-Range Weather Forecasts (ECMWF) data. During the Inylshik 2005 expedition – conducted by GFZ Potsdam and Central Asian Institut of Applied Geosciences (CAIAG), Bishkek, during July 22 and August 13, 2005 – the fourth GPS experiment was conducted at the border of the Merzbacher Lake at 42.196°N, 79.847°E and a height of 3271 m above sea level in a height of 43 m above the glacier lake in order to monitor changes of the lake level. Although the lake surface was fully covered with ice floes and icebergs, the OpenGPS receiver collected several height profiles every day and monitored the temporal change of the lakes water level during 15 days, between July 27 and August 10, 2005. The replenishment of the lake could be fixed from the OpenGPS measurements to a rise rate of 4 cm/h, until the dam broke and the estimated water level decreased with an estimated value of 29 cm/h. Single measurements state a water level drop of 13.75 m between July 31 and August 3. The Standard Deviation (STD) of the derived height profiles - used as an estimate of the surface roughness - significantly increases and the power of the reflected signal decreases by a factor of 10.

This study approves the feasibility of ground-based GPS altimetry with the OpenGPS receiver and with only one low-gain and wide field-of-view RHCP antenna using L1 carrier phase-delay observations of reflected GPS signals. The work shows the potential of GPS reflectometry for remote water level monitoring from a safe position in cases where in-situ measurements are not possible, are dangerous or sensors may get destroyed by the highly dynamic sea or glacier environment. The remote measurements are not bound to one observation point but cover a hole area only limited by the freely available signals of the actual GNSS satellite constellation. Most observations are performed at low elevations. Thus, one of the major error sources is the influence of the local troposphere. A tropospheric correction model could be implemented but the measurements show that this model has to be further refined in order to correct observations at very low elevations.

Zusammenfassung

Wasser, eis- und schneebedeckte Flächen weisen eine hohe Reflektivität gegenüber Global Navigation Satellite System (GNSS) Signalen auf, die Frequenzen im Bereich des L-Bandes haben. Ein Teil des einfallenden Signals wird von der reflektierenden Oberfläche wieder abgestrahlt. Dieses zurückgestrahlte Signal ist an vielen Orten der Erde frei verfügbar. Obwohl die Signalstärke schwach ist, kann diese Signalquelle für altimetrische Zwecke genutzt werden.

Die vorliegende Arbeit präsentiert Methoden und Feldexperimente für bodengestützte GPS Altimetrie. Obwohl Coarse/Acquisition Code (C/A-code) basierte Methoden eingeführt werden, beschreibt der Hauptteil der Arbeit die Verwendung von Trägerfrequenz basierten Phasenbeobachtungen des reflektierten GPS Signals und konzentriert sich dabei auf spiegelnde Reflektion. Modellrechnungen der Reflektionskoeffizienten, die auf den Fresnel Gleichungen basieren, zeigen, daß ein ausreichender Teil des reflektierten Signals von einer rechtszirkular polarisierten (RHCP) Antenne aufgezeichnet werden kann. Deshalb konnten die Experimente mit nur einer nicht modifizierten, omnidirektionalen RHCP GPS Patch Antenne durchgeführt werden. Die Antenne wurde bezogen auf die Zenitrichtung um 45° gekippt, um parallel sowohl das Signal zu empfangen, welches direkt vom GPS Satelliten kommt als auch das Signal, welches von der reflektierenden Oberfläche zurückgeworfen wird. Die Experimente wurden mit dem OpenGPS Empfänger durchgeführt, der am GFZ-Potsdam für altimetrische Zwecke entwickelt wurde. Der 12-Kanal L1 Einfrequenzempfänger wurde modifiziert, sodaß open-loop Tracking durchgeführt werden kann. Im open-loop Modus werden 2 Korrelatorkanäle auf den selben GPS Satelliten festgelegt, indem die entsprechende Pseudo Random Noise (PRN) Nummer gesetzt wird. Ein Korrelatorkanal wird als Master, der andere als Slave Kanal definiert. Die Korrelation zwischen dem empfangenen und dem generierten Replika Signal ist in Hardware realisiert, indem der Zarlink GP2021 Korrelator Chip direkt vom OpenGPS Empfänger angesteuert wird. Während der Master Kanal das direkte Signal verfolgt, werden die Träger und Code Phase Lock Loop (PLL) Schleifen des Slave Kanals geöffnet und die Rückkopplungssignale der PLL Schleifen des Master Kanals eingespeist. Die Trägerschleife arbeitet in Bezug auf den Master Kanal mit Null Trägerphasen Versatz, in die Code Schleife wird aber die geschätzte zeitliche Verzögerung des reflektierten Signals zusätzlich eingefügt. Der OpenGPS Empfänger arbeitet in zwei open-loop Modi. Im mono reflection Mode sind alle 12 Korrelator Kanäle auf den selben Satelliten abgestimmt und es kann die Wellenform des reflektierten Signals aufgezeichnet werden. Im multi reflection Modus kann der Empfänger für Navigationszwecke bis zu 8 direkte GPS Signale verfolgen und mit open-loop Techniken gleichzeitig bis zu 4 unabhängige reflektierte GPS Signale für altimetrische Messungen registrieren. Während eines vorhergesagten Reflektionsereignisses werden die Korrelationssummen der In-phase und der Quad-phase Komponente des Slave Kanals über 20 ms integriert, wobei die Bitwechsel der Navigationsnachricht berücksichtigt werden. Anschließend werden die Daten mit einer Datenrate von 50 Hz zusammen mit den Code- und Trägerphasen auf Festplatte geschrieben.

Im ersten Experiment, welches im Juli 2003 in den bayerischen Alpen in Deutschland durchgeführt wurde, befand sich der OpenGPS Empfänger auf dem Fahrenberg bei 11.32°O, 47.61°N, etwa 1026 m oberhalb des Wasserspiegels des Kochelsees und 824 m oberhalb des Walchensees. Sobald das Modellsignal, welches vom Slave Korrelator erzeugt wird, phasensynchron zum direkten Signal ist und die erwartete Zeitverzögerung besitzt, können Amplitudenvariationen im empfangenen Signal beobachtet werden. Diese Fluktuationen werden durch Interferenzen hervorgerufen, die zwischen dem kohärent reflektierten Signal und dem Modellsignal stattfinden. Auf Basis dieser Amplitudenvariationen konnten die Höhen beider Seeoberflächen bestimmt werden. Mehrere kontinuierliche relative Höhenprofile, mit einer Länge von bis zu 1700 m und einer Beobachtungsdauer von mehr als 15 min, konnten von beiden Seeoberflächen gewonnen werden. Höhenänderungen konnten mit Zentimetergenauigkeit beobachtet werden, mit Amplituden von etwa 5 cm am Walchensee und etwa 10 cm am Kochelsee. Reflektionen konnten hauptsächlich unter Elevationen im Bereich von 9.5° und 25° mit Entfernungen zwischen 1.8 km und 6 km zum Empfänger hin beobachtet werden.

DOI: 10.2312/GFZ.b103-08104

Der Einfluss der Troposphäre und die Neigung der Seeoberfläche, die durch das lokale Schwerefeld hervorgerufen wird, werden diskutiert. Im zweiten Experiment, welches am 11 Juni 2004 auf dem Dach des Mercure Hotels in Potsdam bei 52.39°N, 13.06°O ausgeführt wurde, konnte nachgewiesen werden, daß bei geringen Beobachtungshöhen das reflektierte Signal mit einer verhältnismäßig kleinen Zeitverzögerung nach dem direkten Signal bei der Antenne ankommt. Eine Methode wurde entwickelt, um das reflektierte Signal vom direkten Signal zu trennen. Das dritte Experiment wurde tagsüber in der Zeit vom 20-24 September 2004 auf den Kreidefelsen von Rügen direkt an der Ostseeküste durchgeführt. Der Empfänger befand sich auf dem Königsstuhl bei 54.57°N, 13.66°O in einer Höhe von 118 m oberhalb des Meeresspiegels. An allen Tagen des Experiments konnten Höhenmessungen, welche auf Trägerphasenmessungen basieren, im Genauigkeitsbereich weniger Zentimeter gewonnen werden. Es konnten kontinuierliche Beobachtungen von mehr als 20 min Länge gemacht werden und die Messungen reichten bis zu einer Entfernung von 20 km von der Küste. Die Rauigkeit der beobachteten Ostseeoberfläche war größer als die Trägerwellenlänge λ_{L1}. Ausreichend starke kohärente Signale konnten bei Beobachtungswinkeln unterhalb von 15° registriert werden. Bei diesen Beobachtungswinkeln erscheint die Wasseroberfläche entsprechend des Rayleigh Kriteriums glatt genug, um mit Hilfe von Trägerphasenmessungen Höhenbeobachtungen zu gewinnen. Bei Beobachtungswinkeln unterhalb von 4° können Höhenschwankungen im Bereich mehrerer Dezimeter beobachtet werden, welche durch die lokale Troposphäre hervorgerufen werden, die nicht durch das verwendete troposphärische Korrekturmodell ausgeglichen werden. Das verwendete Korrekturmodell basiert auf European Centre for Medium-Range Weather Forecasts (ECMWF) Daten. Während der Inylshik 2005 Expedition, welche vom 22 Juli bis zum 13 August 2005 vom GFZ-Potsdam und dem Zentralasiatischen Institut für angewandte Geowissenschaften (CAIAG), Bishkek durchgeführt wurde, fand das vierte GPS Experiment statt. Das Experiment wurde am Ufer des Merzbacher Sees bei 42.196°N, 79.847°O in einer Höhe von 3271 m über N.N. in einer Höhe von 43 m oberhalb des Gletschersees durchgeführt, um die Höhenänderungen des Wasserspiegels zu überwachen. Obwohl die Seeoberfläche völlig mit Eisschollen und Eisbergen bedeckt war, konnte der OpenGPS Empfänger jeden Tag mehrere Höhenprofile registrieren und die zeitlichen Änderungen des Seewasserspiegels während der 15-tägigen Beobachtungsperiode vom 27 Juli bis 10 August 2005 überwachen. Der Auffüllungsprozeß konnte mit Hilfe der OpenGPS Messungen mit einer Steigrate von 4 cm/h bestimmt werden bis zu dem Zeitpunkt, wo der Eisdamm gebrochen ist und der geschätzte Seewasserspiegel mit einer geschätzten Sinkrate von 29 cm/h gefallen ist. Einzelbeobachtungen bestätigen zwischen dem 31. Juli und 3. August ein Absinken des Wasserspiegels um 13,75 m. Die Standardabweichung (STD) der abgeleiteten Höhenprofile, welche als Abschätzung der Oberflächenrauigkeit genutzt wird, erhöhte sich signifikant. Gleichzeitig nahm die Energie des reflektierten Signals um den Faktor 10 ab.

Die vorliegende Arbeit konnte zeigen, daß bodengestützte GPS Altimetrie mit Hilfe des OpenGPS Empfängers und nur einer schwach verstärkenden RHCP Antenne mit großem Empfangsbereich möglich ist, wenn man L1 Trägerphasenbeobachtungen von reflektierten GPS Signalen verwendet. Die Arbeit zeigt das Potential von GPS Reflektometrie für die Fernüberwachung von Wasserständen. Wenn auf Grund der hochdynamischen Umweltbedingungen, die im Bereich von Ozeanküsten und Gletschern herrschen, in-situ Messungen nicht möglich, oder gefährlich sind oder die Sensoren zerstört werden können, können mit Hilfe der GPS Reflektometrie Messungen von einem sicheren Beobachtungsstandort aus durchgeführt werden. Die Fernüberwachung ist nicht begrenzt auf einen einzigen örtlich gebundenen Beobachtungspunkt, sondern deckt einen ganzen Bereich ab, der nur begrenzt wird durch die frei zur Verfügung stehenden Signale der aktuellen GNSS Satellitenkonstellation. Die meisten Beobachtungen fanden bei niedrigen Elevationswinkeln statt. Dadurch stellt die lokale Troposphäre eine der größten Fehlerquellen dar. Es konnte ein Korrekturmodell für die Troposphäre entwicket werden. Die Messungen zeigen aber, daß dieses Modell weiterentwickelt werden muß, um auch unter sehr niedrigen Elevationswinkeln die Beobachtungen korrigieren zu können.

Acknowledgments

This work could not have been started without the open source projects OpenSource GPS and Real-Time Application Interface (RTAI)-Linux. I thank Clifford Kelley and the developers of RTAI-Linux for their great work and making it freely available. Helpful discussions with Estel Cardellach, Roman Galas, Philipp Hartl, Oliver Montenbruck and Robert Treuhaft are gratefully acknowledged. I thank Christian Selke, Wolfgang Burghardt, Alexander Lachmann and Marcel Ludwig for their help, technical and logistic support with the OpenGPS hardware and preparing the experiments. I thank all my colleges at GFZ for all their help and support they gave me in the last years, especially thanks to Anita Brudnjak, Carsten Falck, Katrin Gundrum, Stefan Heise, Grzegorz Michalak, Peter Offermann, Roland Schmidt, Peter Steigenberger, Ralf Stosius, Jens Wickert and Kirstin Winkler. I thank Sylvia Magnussen for her great support in computer administration. I thank Torsten Schmidt for preparing tropospheric data and the ECMWF which provided meteorological analysis fields. I thank Mr. Kremer of the Walchensee Powerplant for lake level observation data at Walchensee and Kochelsee. I thank Markus Nitschke for the help and discussion during work and the Fahrenberg measurement campaigns. I thank Ulf Steiner, Christian Zepf and Rainer Käding of the Königsstuhl Nationalpark-Zentrum for their support and for the possibility to use the wonderful and unique measurement site at Königsstuhl. I thank Bärbel Weiding and Dieter Schrader of the Bundesamt für Seeschifffahrt und Hydrographie (BSH) for their help and access to the Sassnitz and Arkona tide gauge data. Thanks also to Lothar Lindenhan of Potsdam Institut für Klimaforschung (PIC) and Thomas Bleek for the support given during the Wasserturm measurements on the Telegrafenberg. I thank Karin Möst of Bayrisches Landesvermessungsamt (BLVA) for topographic data at the Fahrenberg location. Gratefully acknowledged is the cooperation of the members of the CAIAG institute in Bishkek during the Inylshik2005 expedition, especially thanks to Wasili Michajljow, Bolot Moldobekov, Eugen Bargen and Aidjan Ainbekova. I thank Stefan Novak, Marc Roussel, Christoph Mayer, Astrid Lambrecht, Wilfried Hagg, Alexander Petlenko and Felix Ng for all support, discussion and data during the Inylshik 2005 experiments. I thank all members of the spereology fond for all heartful help in field during the Inylshik 2005 expedition, especially thanks to my mountain guide and friend Vasili Popov who performed the Trimble GPS calibration measurements. I thank Hans-Ulrich Wetzel for all support and discussion preparing the remote sensing data of the area of the Inylshik glaciers and conducting the Inylshik 2005 expedition.

I want to thank Christoph Reigber for making it possible to work on this thrilling topic for the last years and for all his support and fruitful discussions throughout the whole project. I thank Markus Rothacher for all his granted support and discussion especially in the final stage of this work.

Finally I would like to thank Georg Beyerle for his great work on the OpenGPS receiver hard- and software enhancements, his many ideas and fruitful discussions without which this work would not exist.

Contents

DOI: 10.2312/GFZ.b103-08104

DOI: 10.2312/GFZ.b103-08104

1 Introduction

1.1 Motivation

To help solving important issues of climate change and sea level change and to understand the complex system Earth, climate models demand for global ocean height data sets with increasing resolution in space and time. Today's existing satellite-based conventional Radar Altimeters (RAs) on ENVIronmental SATellite (ENVISAT) and Joint French/US altimeter mission (Jason-1) already deliver global ocean height and sea state data sets with incredibly high accuracy. Although the accuracy of Global Navigation Satellite System (GNSS) space-based altimetric measurements is actually far worse compared to conventional radar altimeters, GNSS space-based altimetric measurements can potentially densify ocean data in spatial and temporal resolution. While conventional, active radar altimeter observations are limited to nadir observations, i.e., to the satellite ground track, a passive GNSS altimetry receiver on board a single Space Vehicle (SV) can observe up to a dozen reflections at once within a radius of several 100 km distance around the satellite's foot point (Fig. 1.1).

The passive, bistatic GNSS method uses reflected signals from external sources, namely from SVs transmitting GNSS signals. Thus, an energy consuming transmitter is not required and the amount of instrumentation on board a SV can greatly be reduced. Yunck [2003] proposes a small constellation of orbiters carrying GNSS reflection receivers which can cover the Earth globe in a few hours. The constellation can collect enough data to average the height error to a few centimeters with a spatial resolution of a few hundred kilometers allowing for the first time the detection and continuous observation of eddy-scale circulation [Le Traon et al., 2002, Le Traon and Morrow, 2001].

On 26 December 2004, the entire world was shocked to hear of the sub-oceanic earthquake off the coast of Sumatra and the subsequent tsunamis which devastated shoreline communities from Indonesia to Thailand and from Sri Lanka to Somalia. A warning system based on GNSS space-based altimetric measurements is discussed in Soulat et al. [2005]. Martin-Neira et al. [2005] propose a constellation of ten satellites with an orbital inclination of 45° that could cover the most populated central part of the Earth (from 45°S to 45°N in latitude) with a revisit time of less than an hour. A 30–60 cm, 100 km wavelength tidal wave or tsunami in this region would be observable since the typical vertical achievable resolution is 5–10 cm with a spatial resolution of 20–50 km.

In coastal zones satellite radar altimetry data get coarse and decrease in quality because the radar footprint gets contaminated by the land area [Fu and Cazenave, 2001, Helm et al., 2002]. Additionally, the used global tide models loose accuracy in these shallow regions [Shum et al., 1997]. Ground-based GNSS reflectometry receivers can densify and potentially monitor ocean heights in coastal areas. Unlike a conventional tide gauge or a deployed GPS equipped buoy [Harigae et al., 2005, Schöne et al., 2003, Cardellach et al., 2000] such a receiver can collect the data from a remote position, covering a larger observation area and is protected against rough surf or storm damage which allows undisturbed long term measurements. As a spin-off, the tide gauge data can directly be related to a global reference ellipsoid as defined in World Geodetic System 1984 (WGS-84), enhancing the inter-comparability of global tide gauge data. GNSS reflectometry receivers are a cheap technology and could be deployed as dense station network along the coast. Thus, a network of GNSS tide gauge receivers can potentially contribute directly to studies of absolute or relative sea level changes which help to understand the processes involved in global climate changes. Additionally, GNSS tide gauge receivers can densify tide gauge observations of Indian Ocean tsunamis [Merrifield et al., 2005]. Furthermore, GNSS ground-based tide gauge receivers can regularly deliver valuable water level information in difficult to access areas like high mountain lake areas.

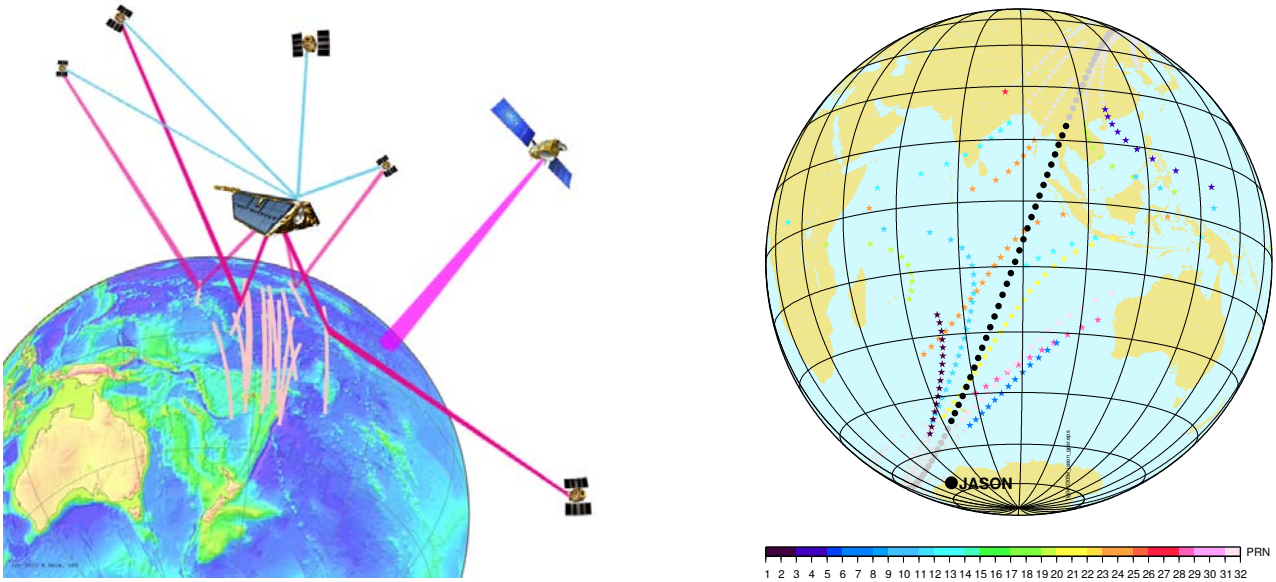

Fig. 1.1: *Active RA observations like on Jason-1 are limited to nadir observations, i.e., to the SV ground track. An additional passive GNSS altimetry receiver on board of the SV can observe several reflections at once around the SV foot point. Left: Model data calculated from TLE and ephemeris data for a imaginary omni-directional GPS antenna on board Jason-1 between 02:15 GPST and 02:40 GPST on December 26, 2004, at the time of the Indian Ocean tsunami event.*

1.2 Overview of Current Research Activites

Since the early times in the history navigation was an important issue of human life. Using hand-held devices like a magnetic compass or sailing with the aid of star maps opened the door to new vistas for mankind. Nowadays GNSS, like GLObal'naya NAvigatsionnaya Sputnikova Sistema (GLONASS) and Global Positioning System (GPS) are available, which were mainly established at first to satisfy the requirements for the military forces to accurately determine their position, velocity, and time in a global reference system, anywhere on or near the Earth on a continuous basis [Wooden, 1985]. Due to the fact that the U.S. Congress, with guidance of the U.S. President, directed the Department of Defense (DoD) (the initiator of GPS) to promote its civil use, GPS became more and more a versatile tool in civil life, too.

In December 1993 GPS achieved its initial operational capability. Since then the GPS system not only delivers successfully positional and timing information to the civil user for applications such as navigation, mapping or precision farming. Today numerous scientific applications of GPS measure seismic tectonic motions, Earth orientation and polar motion, gravimetry, neutral atmospheric temperature and water profiles, ionospheric electron density profiles and global monitoring [Beutler et al., 1996]. Space-borne GPS geodetic receivers deliver sub-decimeter orbit accuracy [Kang et al., 1997], such as on low Earth orbiting satellites like CHAMP and GRACE, making it possible to recover the static and time-variable Earth gravity/geoid within millimeter range [Förste et al., 2008, Reigber et al., 2005, 2006] and derive vital information about the global water balance [Schmidt et al., 2008]. GPS radio occultation measurements emerge as a new powerful technique for atmospheric and ionospheric research, climate change studies and meteorological weather forecasting [Pavelyev et al., 1996, Kursinski et al., 1997, Wickert et al., 2001, Jakowski et al., 2002].

It was in 1993 when the remote sensing of the sea surface with reflected GPS signals has its starting point. Martín-Neira [1993] proposed the concept of the PAssive Reflectometry and Interferometry System (PARIS) which uses the existing GPS signals for mesoscale ocean altimetry. Further discussions about the potential use of GPS signals as ocean altimetry observables can be found in Wu et al. [1997]. During tests of a GPS-based vehicle tracking system Auber et al. [1994] reported multipath errors especially when the aircraft flew at low altitudes above the sea. Reflections from the sea-surface were nearly as strong as the incident signals and caused the GPS receiver to lock to the reflected signals yielding false positioning information. Thus, they measured the first documented

DOI: 10.2312/GFZ.b103-08104

GPS reflections. Since then many theoretical and experimental studies have been carried out with different receiver designs, at different observation heights and platforms.

The research activities within the field of GPS reflectometry split up mainly into two, not independent streams: altimetry and scatterometry. While the altimetry stream tries to achieve highly accurate height measurements comparable to accuracies of RA, the scatterometry stream develops methods for recovering sea state conditions, wind speed and wind direction [Picardi et al., 1998, Zavorotny and Voronovich, 2000, Soulat et al., 2004]. Additionally, effort is put into the recovery of soil moisture [Masters et al., 2000, 2004, Torres, 2004, Larson et al., 2007].

Airborne campaigns have been conducted (e.g. Garrison et al. [1998], Garrison and Katzberg [2000], Rius et al. [2002]) and recently reached a 5-cm height precision [Lowe et al., 2002b]. The MEBEX balloon experiment [Cardellach et al., 2003] was conducted in August 1999 in the Earth's stratosphere. The experiment confirms the feasibility of GPS reflectometry from a height of about 37 km. [Lowe et al., 2002a] observes a first Earth-reflected GPS signal from space by analyzing SIR-C data collected on board of the space shuttle during the Shuttle Radar Laboratory-2 mission in October 1994. Beyerle and Hocke [2001] found evidence of Earth-reflected GPS signals in GPS/MET and CHAllenging Minisatellite Payload (CHAMP) occultation data [Beyerle et al., 2002, Cardellach et al., 2004]. While the CHAMP and Satelite de Aplicaciones Cientificas - C (SAC-C) satellites are equipped already with Earth/nadir-looking GPS antennas, work is in progress in order to establish satellite-based GPS altimetry [Hajj and Zuffada, 2003]. In 2004 Gleason et al. [2005] could record waveforms of ocean-reflected GPS signals that have been detected using the experiment on board the United Kingdom's Disaster Monitoring Constellation satellite (UK-DMC).

The experimental demonstration of ground-based sea surface altimetry using reflected GPS signals followed in 1997 with the BRIDGE experiment. Only the C/A-code was used for correlation leading to an altimetric accuracy of about 3 m [Martín-Neira et al., 2001]. In 1998 Anderson [2000] placed GPS antennas about 10 m above the water surface and could determine the water level and tides with interferometric observations of GPS signals with an accuracy of about 12 cm. During the Crater Lake Experiment in October 1999 Treuhaft et al. [2001] could reach a 2-cm accuracy by using GPS L1 carrier phase data. In the pond experiment Martín-Neira et al. [2002] reached 1-cm accuracy. On a calm water surface inside a harbour phase altimetry became possible with the Oceanpal instrument and reached an accuracy of about 3.1 cm [Ruffini et al., 2006].

In order to use the former error source "multipath" as measurement quantity, different approaches have already been realized in GPS receiver design. A standard GPS receiver, either for navigation or geodetic purposes, normally does not grant access to the necessary information within the GPS signal. Access to the raw GPS signal is required to recover the altimetric information. One approach (e.g. Garrison et al. [1998], Garrison and Katzberg [2000]) is to record this data stream with high-rate data recorders. In a second step – in real-time or during post-processing – the data stream is analyzed and processed with software, giving the receiver type also the name "software radio". Fundamentals of GPS software receivers are described in Tsui [2000]. PC-based GPS civilian L1 software receivers or so-called GPS radios have been developed by Akos et al. [2001], Kelley et al. [2002], Beyerle [2003], Ledvina et al. [2003], Pany et al. [2004], MacGougan et al. [2005] and have been extended to dual-frequency civilian GPS software receivers [Ledvina et al., 2004]. In order to obtain adequate gain from reflected GPS signals research has been done with multi-element digital beam-steered antenna arrays and High-gain Advanced GPS Receivers (HAGRs) [Gold et al., 2005].

1.3 Contributions of this Study

GPS receiver technology is a key issue of GPS reflectometry. GPS software radios offer, naturally, the highest flexibility but require powerful hardware in order to record and process the large data sets. This study uses an OpenGPS receiver. The OpenGPS receiver realizes part of the processing in hardware. This significantly lowers the necessary data rate to be recorded and the required processing power. The OpenGPS receiver is based on the Zarlink GPS chip set with good documentation available [ZARLINK, 2001, 2002a]. Much work on the receiver has already been done in the past by Kelley et al. [2002] who transformed a standard standalone GPS receiver board (`http://home.earthlink.net/~cwkelley/how_to_hack_a_superstar.htm`) into a GPS navigational receiver which can be completely controlled by software. Due to the granted access

DOI: 10.2312/GFZ.b103-08104

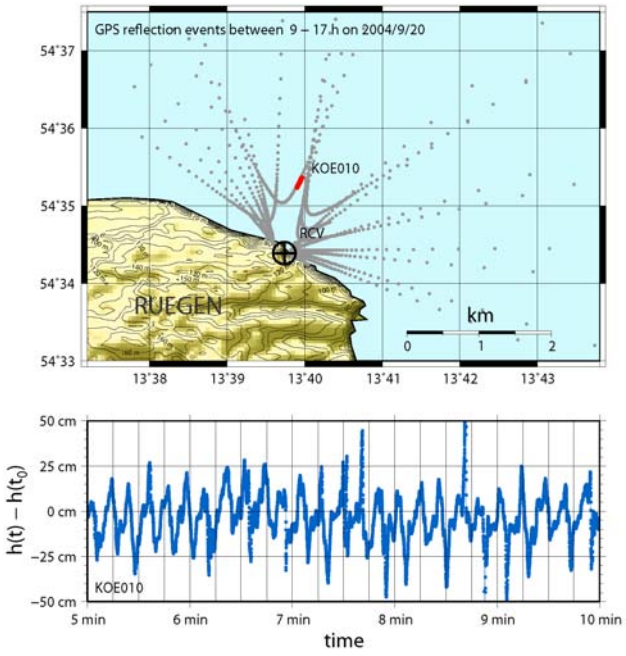

Fig. 1.2: *In comparison to a conventional tide gauge a ground-based GPS reflectometry receiver can collect ocean height data from a remote position, covering a larger observation area and is protected against rough surf or storm damage which allows undisturbed long term measurements.*

to the GPS chip set, it is now possible to directly control the GPS correlator chip. Beyerle (personal communication, 2003, 2004) extended the functionality of the open source software receiver for altimetric purposes.

This study tackles the question if carrier phase observations of reflected GPS L1 signals can be successfully used to obtain altimetric information with cm-precision. Focus is put on coherent specular reflections from water surfaces. The study verifies the proof-of-concept of ground-based GPS altimetry with the L1 OpenGPS receiver and a single RHCP antenna, using carrier phase-delay observations and open-loop tracking of reflected GPS signals. The necessary methods are developed and discussed to archive a working ground-based GPS reflectometry receiver which remotely monitors the height of the reflecting surface above a reference frame.

This first introductory part gives the motivation and an overview of recent research activities. The second part includes the necessary background on topics of the GPS system and signal structure relevant to GPS altimetry. It illustrates the method of correlation and tracking to detect the weak GPS signals. The third part describes the methods involved in GPS altimetry using reflected GPS signals. A simple model is introduced and refined, which describes the path difference between the direct signal ray and the reflected signal ray. Methods are developed and discussed how to derive the absolute and relative altimetric height and its accuracy from the measured receiver quantities. The fourth part describes the OpenGPS receiver hard- and software, its functional concept and how open-loop tracking is performed. The post-processing software and necessary processing and filtering steps are described. The fifth part documents and discusses experiments and their results at test and possible target locations for a ground-based GPS receiver monitoring water levels. The Fahrenberg experiment describes the situation at high observation elevations. Due to the geometry direct and reflected path delays are clearly separated from each other. Processing of the data and known error sources are described. The Mercure hotel experiment describes the situation at much lower elevations. Direct and reflected path delays are very close to each other. Thus, the reflected signal and the direct signal overlap in code space and, secondly, classical multipath interference in the tracking of the direct signal can appear. A changed processing chain has to be chosen in order to recover the reflected signal. During the Königsstuhl experiment the baltic sea surface is monitored over a period of five days from a fixed location at low elevation at the coast. In comparison to the previous experiments with smooth reflecting surfaces this experiment describes the conditions with a rough reflecting surface. The Merzbacher lake experiment documents the first real-world application of the method during the Inylshik 2005 expedition during which the Merzbacher lake was monitored for a dam failure event. The last part sums up the results of this study and gives an outlook into the future of the discussed altimetric methods.

DOI: 10.2312/GFZ.b103-08104

2 Background

2.1 GPS Reflectometry

GPS reflectometry belongs to the class of bistatic radar systems which can be used as a tool for Earth remote sensing [Pavelyev et al., 1996, Martín-Neira, 1993]. Transmitter and receiver reside at different locations. The receiver passively uses emitted signals of sources of opportunity. A GPS reflectometry receiver can potentially use all reflected signals from GPS transmitter satellites which can be received beside the direct line-of-sight signals at the receiver position. As the GPS signals are transmitted continuously, the receiver can continuously receive the data, allowing continuous measurements of the reflecting surface.

The transmitted GPS signal interacts with the reflecting surface and a part of the signal is reflected and can be registered at the receiver. In comparison to the directly received signal the reflected signal arrives at the receiver with a certain delay. From the associated path difference and the knowledge of transmitter and receiver positions the altimetric height of the specular reflection point can be calculated from the geometric relations. Observations of this kind belong to the field of GPS altimetry and are subject of this study.

As the surface roughness scatters the energy pattern of the signal, significant wave height and wind speed can be derived from the temporal development – the waveform – of the received reflected signal. Observations of this kind belong to the field of GPS scatterometry.

One of the relevant new aspects introduced by the bistatic character of GPS reflectometry is the dependence of its capabilities on the measurement geometry. Different measurement geometries occur due to different positions of the transmitting GPS satellites at the same time. Thus, the receiver can acquire reflector height and surface roughness information, i.e., sea state from different reflection point locations simultaneously. Potentially, the sea state information can be recovered from different observation angles leading to information about the wind direction.

The following sections introduce the relevant topics of the GPS system and the reflection process.

2.2 GPS System

The U.S. GPS is a one-way ranging system and is fully operational since 17 July 1995. The GPS system provides accurate, continuous, worldwide, three-dimensional position and velocity information to users with appropriate receiving equipment. GPS also allows for an accurate timing in Universal Time Coordinated (UTC). The GPS system consists of the space segment, the control segment and the user segment.

The space segment consists of a nominal constellation of 24 satellites arranged in 6 equally placed Earth-centered orbital planes with 4 satellites per plane. The satellites have a revolution/orbit period of 12 hours sidereal time and a semi major axis of about 26560 km, thus having an altitude of about 20160 km above the Earth's surface. One mean sidereal day is equal to 23 h, 56 min and 4.009054 s of one mean solar day. The satellite orbits are inclined with respect to the equator by 55°. This satellite orbital constellation provides to a user anywhere in the world simultaneous access (*multiple access*) to four or more satellites at any time, a necessity to solve for the position of the user. The control segment consists of a worldwide ground control network which monitors the health and status of each satellite, i.e., range measurements are made to each of the satellites. these measurements are used to produce precise orbital parameters and timing information which is uploaded to each satellite at the four ground uplink facilities on a S-band link. The user segment consists of receivers and processors receiving and processing the GPS navigation signals which allow users to calculate geocentric position coordinates, velocity and time.

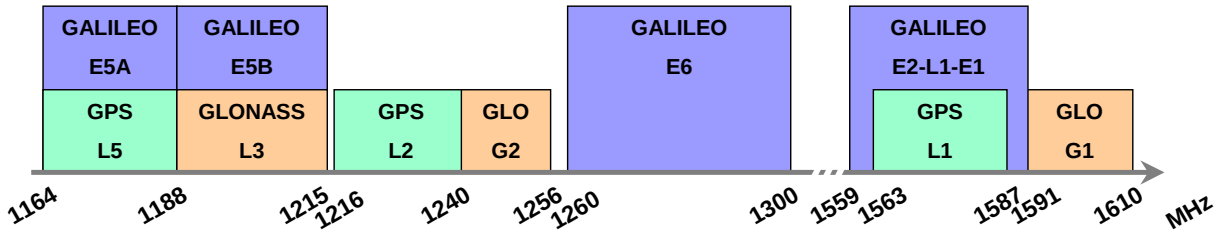

Fig. 2.1: *Frequency bands for GPS, Glonass and GALILEO dovetail together to provide the spectrum of GNSS services (after [GALILEO, 2003]).*

Each GPS satellite continuously transmits radio signals at 2 frequencies. The frequencies are situated in the L-band at 1575.42 MHz (L1) and 1227.6 MHz (L2). All satellites transmit on the same two carrier frequencies. Their signals do not interfere significantly with each other because each satellite modulates its navigation signal with a unique PRN code assigned to each satellite. Thus, the satellite signals can be separated and detected by a technique called Code Division Multiple Access (CDMA). The radio signal is transmitted with an antenna with RHCP.

In order to keep very precise time each satellite carries two rubidium and two cesium atomic clocks that drift off slowly enough that they only need to be calibrated about once each day. GPS Time (GPST) is measured in weeks and seconds from 24:00:00, January 5, 1980 and is steered to within one microsecond of UTC. GPST is ahead of UTC by 14 seconds since January 1, 2006 (13 leap seconds since January 1, 1999) because, in contrast to UTC, no leap seconds are inserted in GPST.

Positioning services are split up into the restricted Precise Positioning Service (PPS) and the open Standard Positioning Service (SPS). PPS has a predictable accuracy of 22 m horizontally and 27.7 m vertically. Time accuracy is 200 nanoseconds. SPS can be degraded intentionally by Selective Availability (SA), a satellite-dependent time-varying clock dithering. With SA activated, SPS has a predictable accuracy of 100 m horizontally and 156 m vertically [Kaplan, 1996]. SA is switched off since May 1, 2000, and the accuracy of SPS improved to $<$13 m horizontally and $<$22 m vertically [GPS SPS, 2001].

Nowadays the GPS system undergoes a process of modernization to meet new military and civil user requirements. New GPS signals will be transmitted with the next launches of Block IIR-M and IIF GPS satellites. On September 26, 2005, a Boeing Delta 2 rocket successfully launched from Cape Canaveral the latest $75 million satellite into orbit, dubbed GPS IIR-M1 (PRN17/SVN53) and built by Lockheed Martin, rising the current number of active GPS satellites to 28. This SV is the first of the modernized GPS satellites that will not only broadcast the navigation signals as previous spacecraft but also provide two new military signals and a second civil signal (see the following section 2.3).

A good description of the GPS system can be found in Kaplan [1996]. Fundamentals can also be found in Wells [1987] and in german language in Mansfeld [2004]. A more detailed description of the GPS system can be found in Parkinson and Spilker [1996].

2.3 GPS Signal

Every GPS satellite transmits two microwave carrier signals in the L-band (see Fig. 2.1) with RHCP. L1 (1575.42 MHz) carries the navigation message and the SPS code signals. L2 (1227.60 MHz) is used to measure the ionospheric delay by PPS equipped receivers. Three binary codes are superimposed on the GPS carrier frequencies L1 and/or L2, shifting the carrier phase:

C/A-code: Each satellite transmits a unique CDMA code. The C/A-code CDMA signal is a PRN sequence of 1023 bit transitions which is Bi-Phase Shift Key (BPSK) transmitted at a rate of 1.023 MHz. Thus, the sequence repeats once a millisecond. As no information is carried by the transmitted code the unit pulse of the code is called chip instead of bit. Taking into account the speed of light the length of one chip can be calculated to be about 300 m. The C/A-code sequences are based on the Gold codes [Gold, 1967]. The sequences have been chosen in a way that correlation between each PRN is minimized.

DOI: 10.2312/GFZ.b103-08104

Precise Code (P-code): The code consists of a very long (seven days) 10.23 MHz PRN code. With Anti-Spoofing (AS) the GPS system can deny access to the P-code to all but authorized users. In case AS is turned on, the Encrypting Code (W-code) is used to encrypt the P-code into the Encrypted Precise Code (Y-code). Deciphering requires a classified module for each receiver. The P-code can only be used by authorized users with cryptographic keys. The ionospheric delay can be measured without decrypting the P-code (geodetic receivers). Methods have been developed for quasi-codeless techniques (e.g. Ashjaee [1993]).

Navigation Message: The message is a 50-Hz binary signal with data bits of 20 ms length which are synchronous with the C/A-code epochs. The GPS Navigation Message consists of time-tagged data bits marking the sending time. A data bit frame consists of 1500 bits divided into five 300-bit sub-frames sent every 30 sec (6 sec for each sub-frame). An entire set consist of 25 frames (125 sub-frames) and is transmitted over a 12.5-min period. The message contains information about the GPS satellite orbits, clock corrections, and other system parameters.

The GPS system undergoes a process of modernization to meet new military and civil user requirements. With modernized satellites of type Block IIR (designated as IIR-M) a new civil signal L2C/L2CS is included on L2. The code can be of moderate length (L2C: 10230 chips, 20 msec) or long (L2CS: 767250 chips, 1.5 sec) and has a power of about 2.3 dB less compared to L1 C/A-code. Additionally, a new military code (M-code) is modulated on both carriers L1 and L2. The next generation Block IIF SVs will additionally transmit a completely new civil signal L5 (1176.45 MHz). L5 is modulated with two ranging codes in phase quadrature, the in-phase code (denoted as I5-code) and the quadraphase code (denoted as Q5-code). The PRN L5-codes are independent for each SV ID number, but time synchronized ranging codes of 1 msec in length (10230 chips) and a high chipping rate of 10.23 Mbps like the P-code. Additionally, system data is added modulo-2 to the I5-code only [ICD-GPS-705, 2002]. The signal power of L5 will be about 5.6 dB higher than that of the L1 C/A-code [Fontana et al., 2001]. The future generation Block III satellites will have steerable and focusable antennas which will offer the possibility to transmit the M-code signal with additional 20 dB gain into distinct target areas. The first Block IIR-M SV was successfully launched in September 2005 [NAVSTAR, 2005] and the first Block IIF satellite is scheduled to be launched in 2008.

In this study the discussion is confined to the L1 frequency. The unmodulated carrier can be described by $C_{L1}(t) = A_{L1}\cos(f_{L1}t)$, with A_{L1} and f_{L1} describing amplitude and frequency of the L1 carrier. The state sequences of the P-code, the C/A-code, the W-code, and the navigation message can be denoted by $P(t)$, $C/A(t)$, $W(t)$ and $D(t)$ respectively. The W-code is used to encrypt the P-code to the Y-code when AS is turned on [Hofmann-Wellenhof et al., 2001]. The GPS signal S_{L1} transmitted on L1 can be described by the equation

$$S_{L1}(t) = A_{L1}\,P(t)\,W(t)\,D(t)\cos(f_{L1}t) + A_{L1}\,C/A(t)\,D(t)\,\sin(f_{L1}t). \tag{2.1}$$

The official description of the GPS signal is given in GPS SPS [2001] and the GPS Interface Control Document (ICD) ICD-GPS-200 [2003]. Details can also be found in Parkinson and Spilker [1996].

2.4 GPS Antennas

The GPS receiver receives the GPS satellite signals via a GPS antenna. The GPS signal level at the antenna is about -160 dBW for L1 [Kaplan, 1996]. In standard configuration the antenna has Right Hand Circular Polarization (RHCP) and provides near-hemispheric coverage. Left Hand Circular Polarization (LHCP) antennas are not sensitive to GPS RHCP signals but sensitive to GPS signals, which have switched the polarization orientation from RHCP to LHCP, as in the case when GPS signals are reflected at layers with high conductivity contrast (e.g. air/water, air/ice interface).

Since the directly received GPS satellite signals are RHCP, a conical helix antenna is suitable. Antenna designs vary from helical coils to thin micro strip (i.e., patch) antennas which are used in this study. There are three basic types of GPS antennas, a passive Fixed Radiation Pattern Antenna (FRPA), a FRPA with an integrated preamplifier, and a Controlled Radiation Pattern Antenna (CRPA). An integrated amplifier is required to keep signal loss low between the antenna and the GPS receiver in the case of long cable connections. An array of several coupled antennas of the CRPA type can

DOI: 10.2312/GFZ.b103-08104

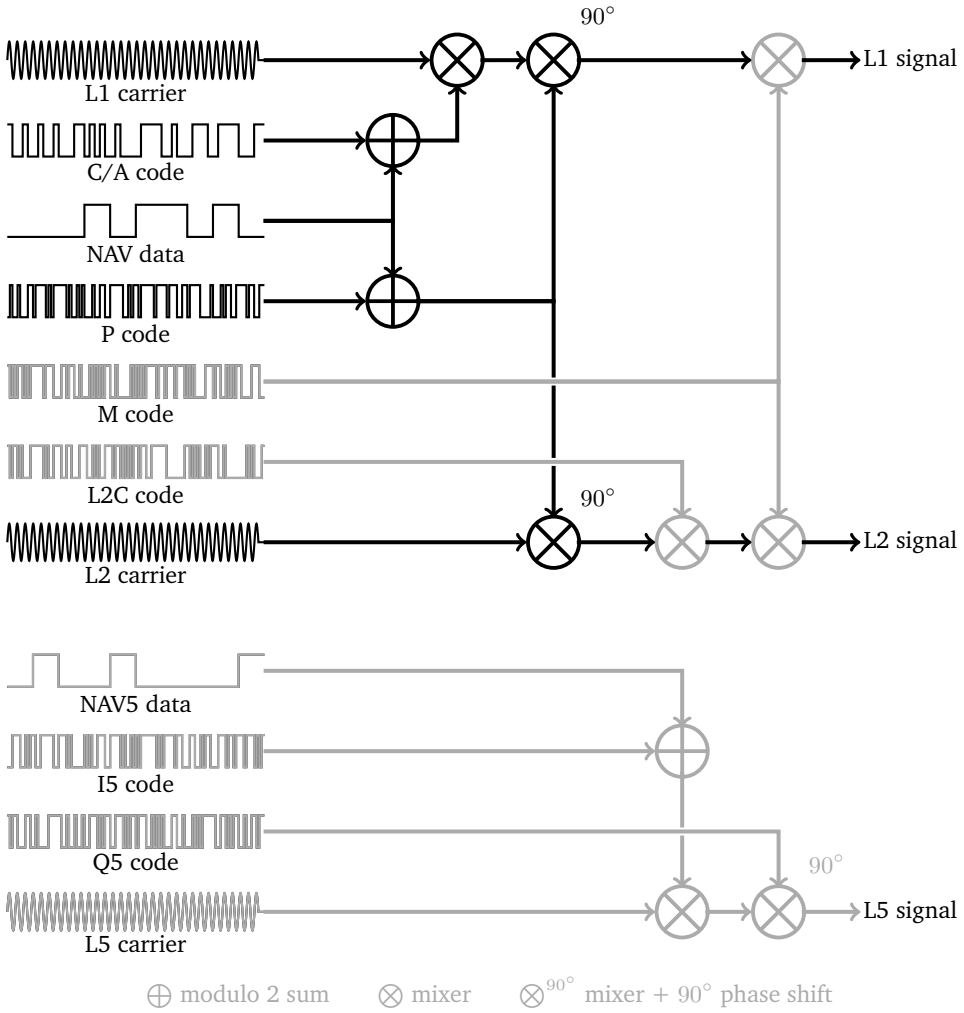

Fig. 2.2: *Every GPS satellite transmits two microwave carrier signals L1 and L2 with binary C/A and P range code and navigation data superimposed (black). Modernized satellites of type Block IIR introduce a new civil ranging code L2C/L2CS on L2 and a military ranging code M (gray). The follow-on satellites of type Block IIF will additionally transmit a new carrier L5 with range codes I5, Q5 and navigation data superimposed (gray).*

be used to reduce the effects of Radio Frequency (RF) interference which could jam the receivers's operation. Such a multi-element array can be used to adaptively steer nulls in the presence of interfering jamming signals, when used in conjunction with interference cancellation hardware. The antenna (and the receiver) must have a bandwidth of at least 2.046 MHz when tracking the C/A-code on L1 or 20.46 Mhz when tracking the P-code on both L1 and L2 [Kaplan, 1996].

An important parameter of a GPS antenna is the gain. Gain is defined with respect to an isotropic radiator for circular polarisation, expressed as dBic, and the sector of the sphere surrounding the antenna over which the gain can be maintained, expressed as the angle from the antenna bore sight. The bore sight is the central axis of the antenna which is usually the direction of maximum gain. In order to receive the signals from GPS SVs, which may be at any angle in the upper hemisphere in case of ground-based observations, the gain must not drop below -5 dBic.

2.5 GPS Receiver

A standard GPS receiver consists of various components. First, an antenna receives the L-band GPS signals. In the following component, called RF front-end, the GPS signal is filtered, down converted to the Intermediate Frequency (IF) and digitized. The IF is obtained by mixing the incoming signal with a pure sinusoidal signal generated by a local oscillator. The frequency of this intermediate or beat frequency is the difference between the original (Doppler-shifted) received carrier frequency

DOI: 10.2312/GFZ.b103-08104

and the local oscillator frequency.

The next component, the correlator component, separates the binary bit stream coming from the RF front-end into different channels. A modern receiver has 12 or much more channels. In general, each channel is allocated to a single GPS satellite. For each satellite the correlator mixes the Doppler-shifted IF signal to base-band and correlates it with an internally generated copy (replica) of the satellites' PRN code.

The correlation of two signals $x(t)$ and $y(t)$ can be described with the following integral operation

$$r_{xy}(\tau) = \int_{-\infty}^{+\infty} x(t)y(t+\tau)dt. \tag{2.2}$$

The correlation function $r_{xy}(\tau)$ describes the matching of both signals in dependence of the displacement time τ (e.g. von Grünigen [2002]). The process of correlation is CPU-intensive and requires a lot of computing power. Thus, the functions of the correlator are normally integrated into a dedicated hardware chip.

The final component fulfills higher order tasks. Software routines search and keep track of each single GPS satellite signal by controlling the appropriate carrier phase and code phase values in the correlator component. Routines extract the navigation message from each GPS satellite signal. The pseudo-range of each received satellite signal is measured by searching for the maximum correlation between the received C/A-code and the delayed internally generated replica of the code. The pseudo-range is defined as the speed of light c times the time difference Δt between the internal clocks of transmitter and receiver. The pseudo-range is not corrected for errors and still includes errors, e.g., the transmitter's and receiver's clock error, atmospheric and ionospheric delay. When the receiver has collected pseudo-range measurements, delta range measurements, and navigation data from four (or more) satellites, it calculates the navigation solution. In principle the pseudo-range equation can be expressed by

$$R = c\,\Delta t = \sqrt{(X-P_X)^2+(Y-P_Y)^2+(Z-P_Z)^2} + c\,C_{clock} - c\,C_{sat}, \tag{2.3}$$

with R expressing the pseudo-range between receiver and transmitter. The four unknown variables (receiver position coordinates P_X, P_Y, P_Z and receiver clock offset C_{clock}) can be calculated by solving a minimum of four simultaneous pseudo-range equations. Equation 2.3 is a simplified versions of the equations actually used by GPS receivers. A receiver also extracts correctional data from the navigation messages, e.g., corrections for the satellite clock offset C_{sat}, relativistic effects, and ionospheric signal propagation delays. The corrections are applied to the pseudo-range data.

A GPS software receiver or GPS radio differs from a standard hardware-based GPS receiver. Except the digitizing and recording of the raw GPS signal all functions of the receiver like correlation, tracking and position calculation, are realized in software running on a general-purpose microprocessor. Recently, efforts are made to migrate the correlator functionality onto Field Programmable Gate Array (FPGA) based processor platforms [Maliniak, 2003] which combine the performance of a dedicated hardware chip (Applications Specific Integrated Circuit (ASIC)) with the flexibility of a software-based solution [MacGougan et al., 2005, Tsui, 2000].

2.6 GPS Signal Acquisition

At startup the GPS receiver is in acquisition state and searches for GPS signals within the received input signal. While during a cold startup the receiver has to start the search without any information, during warm startup the search is assisted by auxiliary information, i.e., visible satellites at the receiver position. In acquisition state the receiver performs for each possible PRN a search process which varies the delay of the specific C/A-code of the PRN and which varies the carrier frequency in the range of possible Doppler values. The Doppler effect is caused by the motion of the GPS satellite as well as the motion of the GPS receiver. Thus, the Doppler effect depends on the relative motion and velocity between GPS satellite and GPS receiver. In case of a stationary receiver like in this study the expected frequency change is very slow. The maximum radial velocity of about 0.9 km/s appears when the satellite crosses the horizon. Assuming a transmitted frequency of about

DOI: 10.2312/GFZ.b103-08104

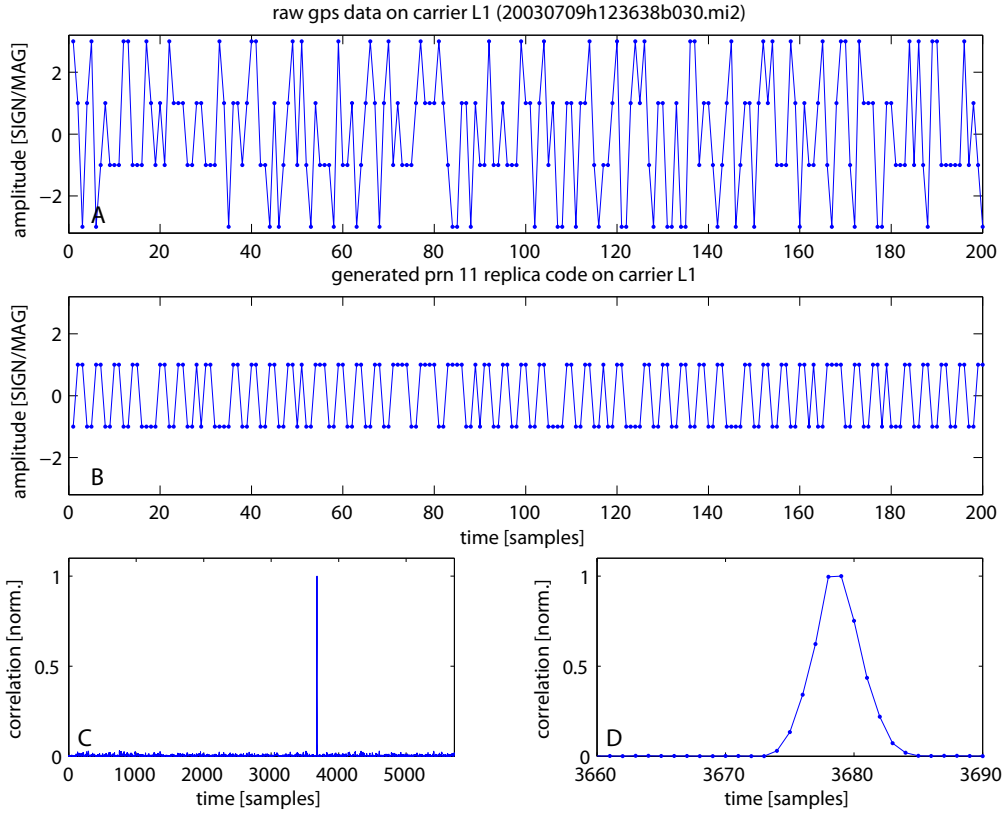

Fig. 2.3: *Panel A: 200 samples of a raw GPS 2-bit data stream recorded on July 9, 2003 at the Fahrenberg location. Panel B: first 200 samples of the generated replica code for PRN 11. Panel C and D show the correlation between the replica code for PRN 11 and the recorded GPS 2-bit data stream. Correlation length of 5714 samples ≡ length of one complete C/A-code cycle. Correlation power scaled to maximum occurring correlation power.*

1.5 GHz, the maximum Doppler frequency shift is 4500 Hz [Hofmann-Wellenhof et al., 2001]. The receiver generates a replica C/A-code of the PRN to be searched for. The correlation sum between replica code and data stream is calculated for each possible signal delay and Doppler frequency. If the correlation sum is above a certain threshold the receiver has acquired the signal of the specified PRN.

2.7 Example of GPS Signal Correlation and Aquisition

In the following the signal correlation and acquisition process is illustrated by means of a dataset recorded by the COMNAV receiver [Jülg, T., 2002] on July 9, 2003 at the Fahrenberg location. In this experiment the data was recorded with a RHCP and LHCP antenna in parallel. The COMNAV receiver is an L1-frequency receiver which allows to store up to 220 ms long continuous data segments of the received GPS signal to hard disc. The COMNAV receiver is based on the GP2015 GPS receiver RF front end chip [ZARLINK, 2002a]. In the following example the replica/Gold code generation and C/A-code correlation is realized in software. The aquisition process is realized by circular correlation [Tsui, 2000]. Fig. 2.3 illustrates the 1-dimensional correlation search process in the code domain. Panel A shows an extract of 200 samples of the raw down-converted GPS 2-bit data stream recorded by the COMNAV receiver with a RHCP GPS antenna. Panel B shows the first 200 samples of the generated replica code for PRN 11 with a delay set to 3678 samples and the Doppler set to 400 Hz. Panel C shows the resulting correlation sums for all possible 5714 delays. At a sampling frequency of 5.714 MHz 5714 samples correspond to the correlation length of one complete C/A-code cycle with a duration of 1 ms. Zooming into the area of the correlation peak (Fig. 2.3, panel D) reveals the typical structure of the correlation triangle.

Fig. 2.4, left, illustrates the 2-dimensional correlation search process in the code- and Doppler-domain for PRN 7 during GPS signal acquisition. The correlation of the recorded data stream with a

DOI: 10.2312/GFZ.b103-08104

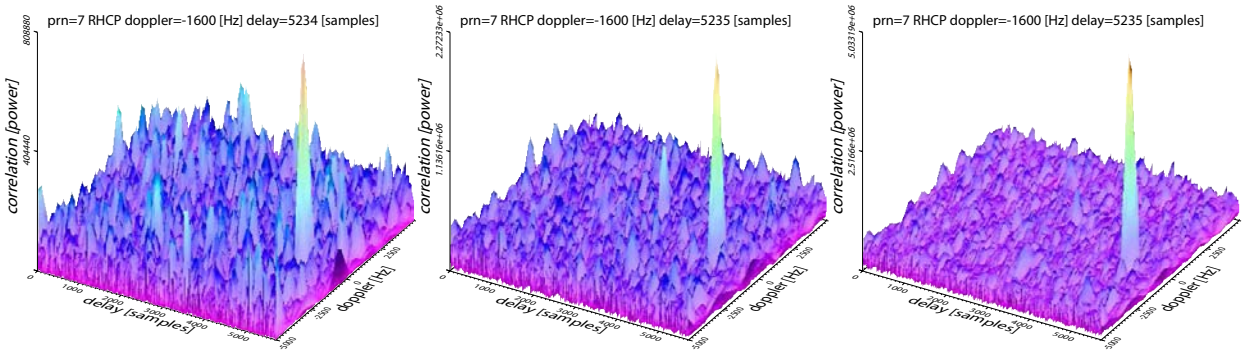

Fig. 2.4: *Example of the correlation search process for PRN 7 during GPS signal acquisition with different correlation sum lengths (from left to right: 1, 4 and 8 times a complete C/A-code cycle). Correlation power scaled to maximum occurring correlation power.*

replica model is calculated for different delays and Doppler values. The delays range from 0 to 5714 samples and the Doppler values vary from -5000 Hz to 5000 Hz.

Stacking the correlation sum can significantly increase the Signal-to-Noise Ratio (SNR). During stacking the correlation sum of consecutive data blocks of 1 ms length are consecutively added. Hence, uncorrelated noise is suppressed and correlated signal amplified. For a successful stacking the data blocks must be synchronized. In Fig. 2.4 from left to right the correlation sum is stacked 1, 4 and 8 times a complete C/A-code cycle which is equivalent to 5714, 22856 and 45712 samples or 1, 4 and 8 millisecond stacking time. Although the signal of PRN 7 can be clearly detected after 1 ms, the SNR can be significantly increased by the stacking process as the uncorrelated noise is suppressed.

The following illustrates the two-dimensional correlation search in the code- and Doppler-domain during GPS signal acquisition. Fig. 2.5, top, from left to right, shows the correlation search process for PRN 7, 8 and 11, always applied to the same raw GPS 2-bit data stream recorded from the RHCP antenna. While the signals of PRN 7 and 11 can be clearly acquired, the signal of PRN 8 cannot be detected in the data. From ephemeris data the positions of all GPS satellites can be calculated. The calculations show that PRN 8 cannot be received, because the transmitting GPS satellite was not visible at that time at the receiver location.

The same correlation search process during acquisition mode of standard GPS receivers can be extended to a dataset recorded in parallel by the COMNAV receiver at the same location with an LHCP antenna. Fig. 2.5, bottom, from left to right, shows the results of the correlation search process for PRNs 7, 8 and 11 within the raw GPS 2-bit data stream which was recorded with an LHCP antenna. A correlation peak for PRN 8 is not expected in the data as the GPS satellite was not visible at the time of data recording. While a correlation peak of the visible satellite PRN 7 cannot be identified in the data stream, a correlation peak of PRN 11 can be clearly detected. In comparison to the correlation data of PRN 11 of the RHCP antenna the correlation sum of the peak drops from $1 \cdot 10^8$ to $1 \cdot 10^6$. Comparing the code and Doppler values of the correlation peak to both PRN 11 data sets, the code values of the correlation peak significantly differ between the correlation results of the RHCP and the LHCP data stream. The correlation peak of the LHCP data shows a delay of 15 samples with respect to the correlation peak detected in the RHCP data. Thus, besides the direct signal of PRN 11 a delayed reflected signal of PRN 11 could be detected in the dataset recorded by the LHCP antenna.

Additionally, this example proves the fact that Left Hand Circular Polarization (LHCP) antennas are not sensitive to GPS RHCP signals but sensitive to GPS signals which have switched the polarization orientation from RHCP to LHCP as in the case of reflected GPS signals.

2.8 GPS Signal Tracking

Once the GPS receiver has acquired and confirmed a GPS signal, the receiver has to follow and keep track of the input signal because carrier and C/A-code frequencies vary over time due to the

DOI: 10.2312/GFZ.b103-08104

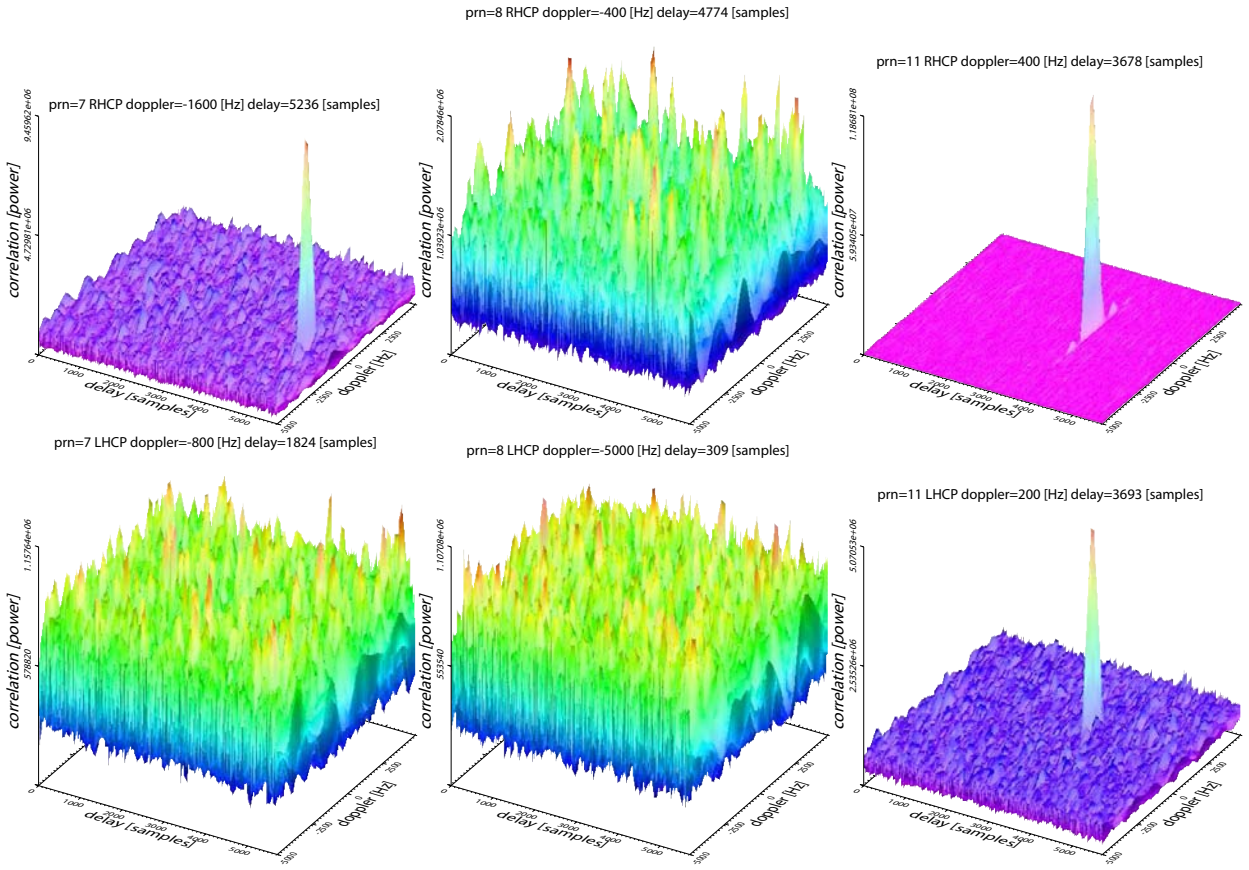

Fig. 2.5: *Two-dimensional correlation search process for PRN 7, 8 and 11 within the raw GPS 2-bit data stream which was recorded with the RHCP (top, from left to right) and with the LHCP (bottom, from left to right) antenna. Correlation power scaled to maximum occurring correlation power.*

Doppler effect and the changing geometry. During acquisition the frequency of the signal is only determined in a coarse resolution and can still be several 100 Hz off the true value. Thus, in a first step the receiver attempts to pull the frequency in close enough that the carrier can be firmly tracked afterwards. The tracking task can be realized by a PLL [Tsui, 2000]. The input to a conventional PLL is usually a Continuous Wave (CW) signal. However, the GPS signal is a bi-phase coded signal. Thus, the signal containing the C/A-code information and the carrier, must be separated and it requires two PLLs – the code and the carrier loop – to track the GPS signal. The C/A-code is applied to the down-converted and digitized input signal. The C/A-code with the correct phase is multiplied onto the incoming GPS signal. The result of the mixing process is a CW signal with the C/A-code stripped off. Now only the phase transitions caused by the navigation message are left. The CW signal is applied to the input of the carrier loop. The carrier PLL adjusts the frequency of a local oscillator to match the frequency of the input CW signal. The output of the carrier loop is a CW signal with a frequency which is tuned to the actual carrier frequency of the received GPS signal. This tuned CW signal is mixed with the received GPS signal in order to strip off the carrier signal. Now a signal is left which contains only the C/A-code and the navigation message. This signal is applied to the input of the code loop.

A conventional C/A-code loop generates not only one but three outputs: an early, a prompt and a late replica code. The early and late replica phases are, according to their name, apart by 1/2 C/A-code chip with respect to the prompt phase. Fig. 2.6, panels A-D, illustrate how the early, prompt, and late correlation sums E, P and L change as the phases of the replica code signals are advanced with respect to the incoming GPS signal. Only one chip of the continuous PRN code signal is shown and noise is neglected. Fig. 2.6, panel E, shows the normalized early minus late correlation sum discriminator error output signal (E-L)/(E+L) which corresponds to the four replica code offsets -1/2, -1/4, 0, and 1/4 plotted in Fig. 2.6: The replica code is shifted by a delay of 1/2 chip (Panel A) and 1/4 chip (Panel B) to an earlier time. Panel C shows the replica code aligned with the incoming

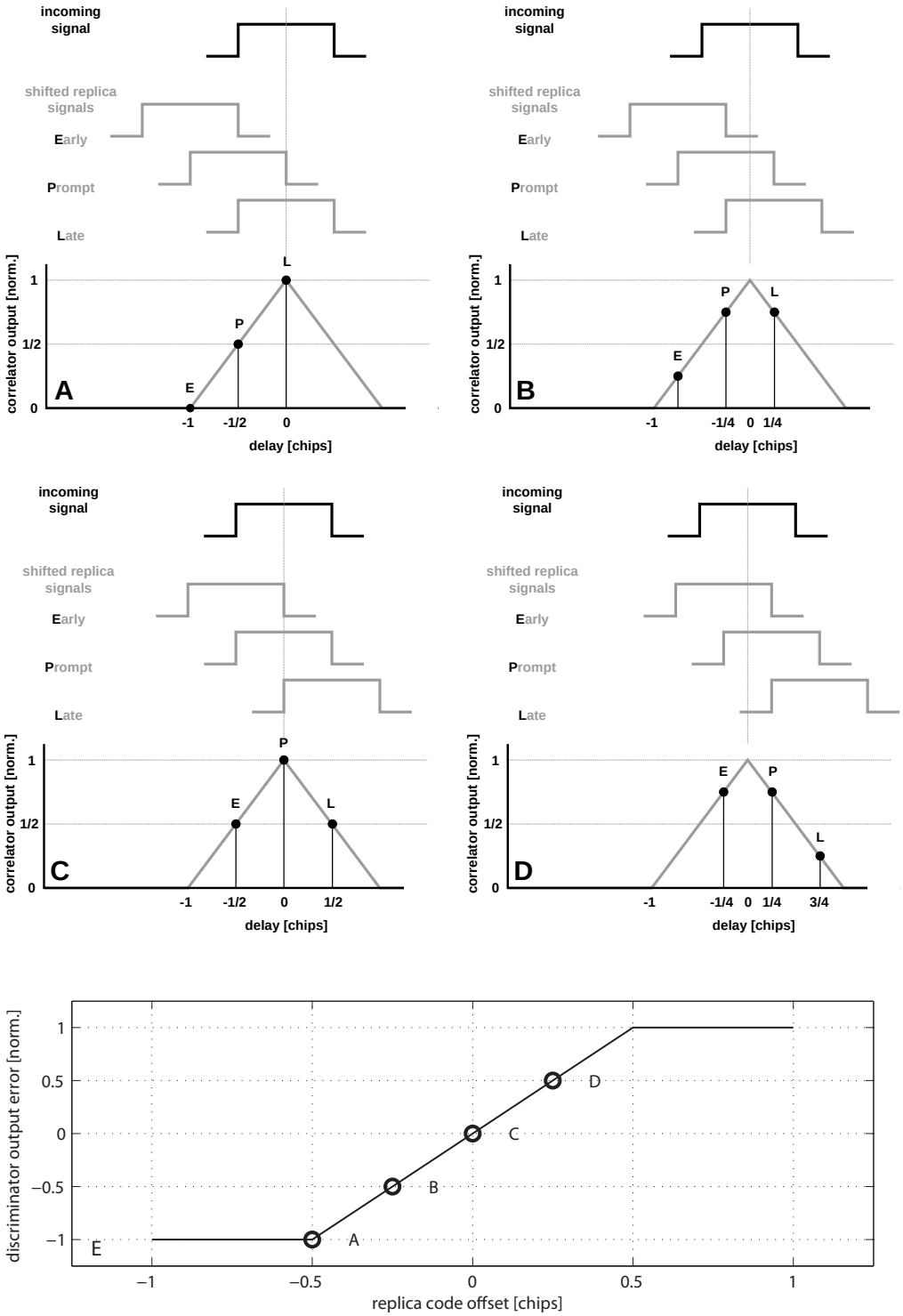

Fig. 2.6: *Four replica code offsets -1/2, -1/4, 0, and 1/4 are shown in panel A, B, C and D. Panel E shows the continuous normalized discriminator output error (gray line) versus replica code offset in an interval of -1 and 1 chips. The discriminator output error at the different replica offsets, shown in panel A, B, C, and D, are marked by black circles A, B, C, and D, respectively (after Kaplan [1996]).*

signal. The replica code is 1/4 chip late (panel D). The code discriminator senses the amount of error in the replica code and the direction from the difference in the amplitude of the early and late correlation sums [Kaplan, 1996]. This error is filtered and then applied to theNumerically Controlled Oszillator (NCO) of the C/A-code loop where the output frequency is tuned as necessary to correct the replica code generator phase with respect to the incoming GPS signal C/A-code phase.

DOI: 10.2312/GFZ.b103-08104

2.9 GPS Signal Errors

The standard GPS measurement is influenced by errors from different sources [Parkinson and Spilker, 1996] which are described in the following paragraphs.

Ephemeris errors: In case the GPS navigation message does not transmit or contain the correct satellite location, ephemeris errors are the consequence.

Clock errors: Fundamental to GPS is the one-way ranging that ultimately depends on satellite clock predictability. The knowledge of the user clock bias and drift is required which represent the phase and frequency errors in the atomic frequency standard of the satellite or the crystal oscillator in the receiver.

Atmospheric effects: The measured GPS signals pass through the Earth's atmosphere where ionosphere and troposphere influence the signal propagation delay. The velocity of signal propagation within the atmosphere deviates from vacuum light velocity. The refractivity of ionosphere and troposphere influence the signal propagation delay causing atmospheric effects. As both influence the signal in different ways due to their specific refractive properties, the two corresponding corrections are handled separately.

Ionospheric effects: The ionosphere is the upper part of the Earth's atmosphere located in the region between about 70 km and 1000 km above the Earth's surface. The ionosphere contains free electrons. Thus, GPS signals do not travel at the vacuum speed of light as they transit this region. The modulation on the signal is delayed depending on the number of free electrons encountered and the carrier frequency f of the signal. The phase of the carrier is advanced by the same amount. These effects can be described [Parkinson and Spilker, 1996] to first order by the ionospheric refractive index n_{iono} with

$$n_{iono} = 1 - \alpha \frac{N}{f^2} \tag{2.4}$$

with $\alpha = 40.3 m^3 s^{-2}$. N denotes the density of free electrons, in electrons per cubic meter. The effect of ionospheric refraction is inversely proportional to the squared frequency and causes a time delay $\Delta\tau_{iono}$ in code measurements leading to a overestimated (longer) range:

$$\Delta\tau_{iono} = \frac{1}{c}\int_T^R (n_{iono} - 1)\, dl = \frac{1}{c} \cdot \frac{\alpha}{f^2}\int_T^R N\, dl. \tag{2.5}$$

The quantity $\int N\, dl$ is the Total Electron Content (TEC), in electrons per square meter, integrated along the signal path between transmitter T and receiver R, c is the speed of light. In carrier phase measurements the effect causes a phase advance leading to an underestimated (shorter) range. The influence of the ionosphere can be modeled using the transmitted (navigation message) Klobuchar coefficients and the effect can be reduced by 50 - 75 %. With a dual-frequency receiver the effect can be eliminated apart from higher order terms almost totally, but with an associated amplification of the noise. For single-frequency spaceborne receivers a general discussion of ionospheric errors can be found in Montenbruck and Gill [2002].

Tropospheric effects: The troposphere is the lower part of the Earth's atmosphere. The thickness of the troposphere is not everywhere the same. It extends to a height of less than 9 km over the poles and it exceeds a height of 16 km over the equator. When GPS signals travel through the troposphere, variations in temperature, pressure and humidity all contribute to variations in the speed of light causing tropospheric errors. Attenuation and delay are caused by the local state of the troposphere. Additionally, these effects vary with elevation angle because lower elevation angles produce a longer path length through the troposphere. Compared with the ionospheric effect, the tropospheric effect is about an order of magnitude less. In zenith direction the troposphere typically causes a delay of about 8 ns causing an excess path of about 2.3 m. The delay increases towards lower elevations as the signals have to travel an increasing path length within the troposphere. The primary effect of tropospheric refraction is caused by the lower speed of light in the lower atmosphere. The effect is a function of local temperature, pressure and humidity. Usually the models are separated into dry effects (temperature and pressure) and wet effects (humidity) and the dry N_{dry} and the wet component N_{wet} of the refractivity are integrated along the signal path between transmitter T and receiver R. Dry (hydrostatic) effects account for typically 90–95 % of the tropospheric refraction and

DOI: 10.2312/GFZ.b103-08104

Error Source	SPS mode (C/A-code)	PPS mode (P-code)
Satellite instability (clocks)	3.0 m	3.0 m
Satellite orbit	1.0 m	1.0 m
Ephemeris prediction and monitoring	5.1 m	5.1 m
Ionosphere	8.0 m	1.2 m
Troposphere	2.5 m	1.5 m
Receiver	1.5 m	1.5 m
Multipath	2.5 m	1.2 m

Tab. 2.1: *Error budget for pseudo range measurements during SPS (using only L1 frequency) and PPS (using L1 and L2 frequency) mode after Mansfeld [2004], Kaplan [1996].*

can be modeled with good accuracy. Wet effects can account for up to about 0.4 m extended path length. Humidity is highly variable and a function of signal path. Thus, humidity is difficult to handle and model. Variations due to humidity can change at low elevation angles for substantially different azimuths. Analyses based on ray-tracing and predicted weather models, e.g. generated by ECMWF, can reduce the problem.

$$\Delta\tau_{tropo} = 10^{-6}\frac{1}{c}\int_T^R N_{dry}dl + 10^{-6}\frac{1}{c}\int_T^R N_{wet}dl \tag{2.6}$$

The excess path delay caused by the troposphere can be modeled at sea level with a simplified model as a function of elevation angle ϵ [Parkinson and Spilker, 1996, Tsui, 2000] as follows:

$$\Delta\tau_{tropo}(\epsilon) = \frac{2.47}{\sin(\epsilon) + 0.0121} \tag{2.7}$$

An exponential profile can be employed to give the following simplified model [Parkinson and Spilker, 1996] which states the excess path delay as function of elevation angle ϵ and height h of the receiver:

$$\Delta\tau_{tropo}(\epsilon, h) = \frac{2.47}{\sin(\epsilon) + 0.0121}e^{-0.133h} \tag{2.8}$$

so that the zenith delay decreases at $h = 7$ km altitude to $e^{-0.133h} = 0.393$ of the sea level value. Common models calculate the delay from local measured or modeled meteorological data, e.g., by the standard model of Sasstamoinen [1972].

Multipath errors: Multipath occurs when an RF signal arrives at the receiving antenna from more than one propagation route (multiple propagation paths). In case a signal arrives at the receiver's antenna via more than one path, the differences in path lengths cause the signals to interfere at the antenna [Teunissen and Kleusberg, 1998]. The environment surrounding the antenna can, therefore, temporarily affect the measured values of pseudo-range and carrier phase. When the GPS signal is emitted from the satellite antenna, the RF signal propagates away from the antenna in many directions. Because the RF signal is emitted in many directions simultaneously and is traveling along different paths, these signals encounter various and differing natural and man-made objects along the various propagation routes. Whenever a change in medium is encountered, the signal is either absorbed, attenuated, refracted, or reflected. Refraction and reflection cause the signals to change direction of propagation. This change in path directions often results in a convergence of the direct path signal with one or more of the reflected signals. When the receiving antenna is the point of convergence for these multipath signals, the consequences of signal polarity shifting and reversal at the receiving antenna vary from minor to significant. As well, refracted and reflected signals generally sustain some degree of signal amplitude attenuation. It is generally understood that, in multipath conditions, both the direct and reflected signals are present at the antenna and the multipath signals are lower in amplitude than the direct signal. However, in some situations, the direct signal may be obstructed or greatly attenuated to a level well below that of the received multipath signal.

Relativistic effects: Time is a relevant factor in GPS navigation and must be accurate to 20–30 nsec with 1 nsec $= 10^{-9}$ sec to ensure the necessary accuracy. Therefore the fast movement of the GPS satellites themselves – nearly 12000 km/h – must be considered. According to the theory of relativity,

time runs slower during very fast movements. For satellites moving with a speed of 3874 m/s, clocks run slower when viewed from Earth. This relativistic time dilation leads to an inaccuracy of time of approximately 7.2 msec/day with 1 msec = 10^{-6} sec. Additionally, time moves the slower the stronger the field of gravitation is. For an observer on the Earth surface the clock on board of a satellite is running faster because the satellite in 20000 km height is exposed to a much weaker field of gravitation compared to the observer. This second effect is six times stronger compared to the time dilation effect explained above. Altogether, the clocks of the satellites seem to run faster. The shift of time to the observer on Earth would be about 38 msec/day and would make up for an total error of approximately 10 km per day. In order that the errors do not have to be corrected constantly, the clocks of the satellites are set to 10.229999995453 Mhz instead of 10.23 Mhz but the clocks are operated as if they have 10.23 MHz [Hofmann-Wellenhof et al., 2001]. By this trick the relativistic effects are compensated once and for all. There is another relativistic effect which is not considered for normal position determinations by GPS. It is called Sagnac-Effect and is caused by the movement of the observer on the Earth surface who moves with a velocity of up to 500 m/s at the equator due to the rotation of the globe. The influence of this effect is very small and complicate to calculate as it depends on the directions of the movement. Therefore it is only considered in special cases.

Receiver errors: The receiver tracking loops also introduce measurement errors. Thermal noise jitter and the effects of dynamic stress error are dominant sources of pseudo range measurement error, caused by the tracking loops. Secondary error sources include code hardware, software resolution and oscillator stability. Typical modern receiver 1σ values for the noise and resolution error are on the order of 1.5 m for C/A-code and 20 cm for P-code. Receiver noise and resolution errors affect carrier phase measurements, too. PLL measurement errors are in the order of 1.2 mm and 1.6 mm (1σ) when tracking the C/A-code and P-code, respectively. Extensive treatment of Delay Lock Loop (DLL), Frequency Lock Loop (FLL) and PLL can be found in Kaplan [1996].

2.10 Specular and Diffuse Reflection

Specular reflection and diffuse reflection are simple model approximations describing the reflection process. In reality, surfaces exhibit a continuum of modes of reflection between these two. Following Beckmann and Spizzichino [1963], Ruffini et al. [1999], reflected radiation can be considered as a sum of two components, the specular and the diffuse component. Specular reflection happens when incident electromagnetic waves interact with a smooth, conducting, and mirror-like surface. Specular reflection obeys the laws of classical ray optics, thus has directional character. Phase coherence is retained, specular back radiation occurs only within a limited area which is defined by the Fresnel ellipse (see definition 3.7 on page 31) and amplitude fluctuations are low. The diffuse component is the result of a scattering process happening when electromagnetic waves interact with a rough surface. The diffuse component of the return signal has little directivity and a much larger area than the Fresnel ellipse of the reflecting surface is involved in the process. Phase coherence is lost and Rayleigh-distributed amplitude variations are much higher compared to those of specular reflection. The characteristics rough and smooth have to be defined in relation to the wavelength of the electromagnetic waves according to the Rayleigh criterion (see Eq. 2.11).

Bistatic reflected GPS signals can be classified as specular and diffuse type. Specular bistatic GPS signals are characterized by an optimal, mirror-like reflecting surface and provide powerful reflections. Only a small surface area is involved in the reflection process. The strength of the specular return depends on the roughness of the reflecting area. Diffuse bistatic return signals are generated by scattering processes originating from a much larger surface area. Thus, diffuse signal returns can potentially provide information over a much larger region compared to specular returns. However, diffuse return signals are much weaker compared to specular return signals and, therefore, require much more efforts in receiver and antenna technology.

2.11 Interference and Coherence Length

Interference can be observed when electromagnetic waves are coherent. Coherence is a property that measures the ability of electromagnetic waves to interfere with each other. Two coherent waves

DOI: 10.2312/GFZ.b103-08104

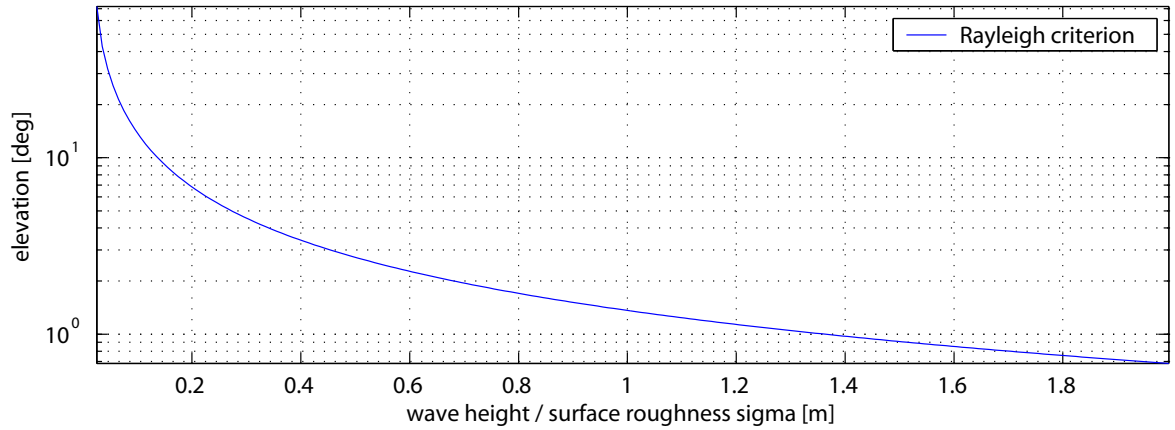

Fig. 2.7: *Maximum elevation angle under which coherent scattering can be observed depending on the surface roughness.*

of frequency f and $f + \Delta f$ can be combined to produce a visible interference pattern. The pattern consists of an unmoving distribution of constructive and destructive interference, depending on the relative phase difference of the signals at their meeting point. Two signals are coherent in case the time-dependent amplitude behaviour of both signals is equal and both signals are in phase or have a constant phase offset to each other [Gerthsen, 1997]. Signals that are incoherent, when combined, do not produce such a visible interference pattern. A signal can also be coherent with itself, a property known as temporal coherence. If a signal is combined with a delayed copy of itself, the duration of the delay over which it produces visible interference is known as the coherence time of the signal, Δt_c. From this, a corresponding coherence length Δx_c can be calculated with

$$\Delta x_c = c \Delta t_c. \tag{2.9}$$

The temporal coherence of a signal is related to the spectral bandwidth of the source. A truly monochromatic signal would have an infinite coherence time and length. The coherence time of the source is inversely proportional to its bandwidth Δf:

$$\Delta t_c = \frac{1}{\Delta f}. \tag{2.10}$$

The Rayleigh criterion predicts that coherent scattering can only be observed up to a certain elevation angle ϵ which depends on the observed wavelength λ and the surface roughness σ:

$$\epsilon \equiv \arcsin \frac{\lambda}{8\sigma}. \tag{2.11}$$

Fig. 2.7 illustrates the maximum elevation angle under which coherent scattering can be observed depending on the surface roughness. The surface roughness can be expressed by the wave height. In case, e.g., we observe wave heights of 0.2 m we can expect coherent scattering up to about 7° elevation for the GPS L1 frequency.

2.12 Fresnel Equations

The Fresnel equations fully describe the behavior of reflected and transmitted radar signals in case of non-conductive, i.e., perfect dielectric media. In case of conductive media the reflection coefficient becomes a complex function, not only depending on relative permitivity, but additionally depending on conductivity and frequency. For an in-depth study of Fresnel diffraction theory see Jackson [1998]. The derivation of the Fresnel equations for non-conductive and conductive media is fully described in Ward and Hohmann [1988] and Lehmann [1996], respectively. The reflection coefficients for perpendicular and parallel polarized electric fields in case of non-conductive ($r_\perp$ and $r_\parallel$)) and conductive media ($\tilde{r}_\perp$ and $\tilde{r}_\parallel$)) are described in appendix B starting on page 147, respectively.

DOI: 10.2312/GFZ.b103-08104

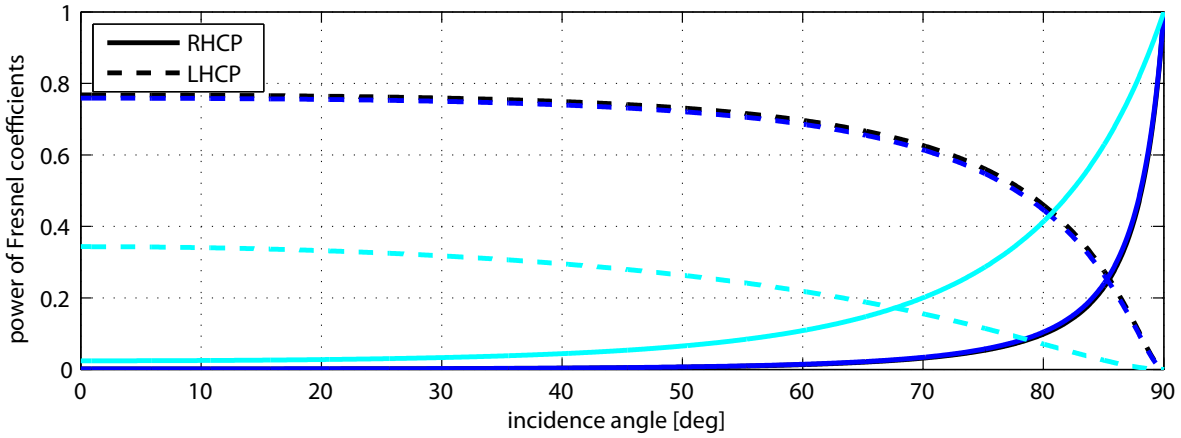

Fig. 2.8: *Reflection coefficients calculated for RHCP and LHCP GPS L1 signals at an air/saltwater (blue), an air/sweet water (black) and air/ice interface (turquoise).*

The reflection coefficients for circular polarized signals as in the case of GPS can be described as a linear combination of the perpendicular and parallel polarized electric fields [Cardellach Galí, 2001] with

$$\tilde{r}_{RHCP} = \frac{1}{2}(\tilde{r}_{\perp} + \tilde{r}_{\parallel}) \text{ and } \tilde{r}_{LHCP} = \frac{1}{2}(\tilde{r}_{\perp} - \tilde{r}_{\parallel}). \tag{2.12}$$

Fig. 2.8 illustrates the relation between the reflection coefficients for circular polarized RHCP (solid lines) and LHCP (dashed lines) GPS L1 signals and incident angle at an air/sweet water (black curves), an air/saltwater (blue curves) and an air/ice (cyan curves) interface. For sweet water $\epsilon_r = 80$ and $\sigma = 0.5\ mS/m$ are used at GPS frequencies [Ulaby et al., 1982]. Zavorotny [1999] states typical values $\epsilon_r = 73$ and $\sigma = 5\ mS/m$ for sea water for an incident field of wavelength $\lambda = 0.19$ m. For pure ice Ulaby et al. [1982] proposes $\epsilon_r = 3.15$ which is independent of temperature and frequency in the microwave region. But conductivity strongly depends on ice density, salinity, temperature and geometrical configuration of the air and brine pockets in the ice volume. Here a conductivity of $\sigma = 0.07\ mS/m$ is assumed [Moore and Fujita, 1993]. In case of a sweet- or saltwater reflector – here we disregard any surface roughness – more than 70% of the GPS signal is expected to be reflected up to incidence angles of 60°. The polarization of the GPS signal changes from RHCP to LHCP. At higher incidence angles the LHCP fraction of the signal decreases more and more. At about 85° incidence angle the reflected signal is composed of equal fractions of RHCP and LHCP GPS signals. At higher incidence angles, i.e., at low elevation angles, the fraction of the RHCP signal rapidly increases. The power level rapidly increases at low grazing angles and can reach the full power of the direct signal. Thus, total reflection can be observed. Compared to a water reflector, an ice reflector is expected to reflect a weaker signal. The reflected signal power varies between 35% and 20% of the direct signal up to incidence angles of 60°. The polarization of the GPS signal changes from RHCP to LHCP. At an incidence angle of about 70° the RHCP fraction of the reflected signal is higher than the LHCP fraction. The power level of the reflected signal rapidly increases at low grazing angles and can reach the full power of the direct signal.

DOI: 10.2312/GFZ.b103-08104

3 GPS Altimetry Methods

3.1 Overview

The target quantity of GPS altimetry is the height of the reflecting surface above a reference surface. In a first step a model of the excess path of the reflected GPS signal is developed under the assumption of ray optics and a flat Earth. This study assumes specular reflection. The model comprises the known positions of receiver and transmitter which can be determined from measurements or predictions. The model is improved in a second step by incorporating the Earth bending by assuming a spherical Earth. The location of the specular reflection point is calculated using an iterative scheme.

Three different methods are used to determine the height of the reflecting surface:

- GPS C/A-code altimetry,
- GPS L1 interferometric frequency altimetry,
- GPS L1 interferometric carrier phase-delay altimetry.

The reflected signal has to travel a longer path compared to the direct signal. Thus, the reflected GPS signal arrives at the receiver antenna with a time delay with respect to the direct GPS signal. The time delay can be directly determined by measuring the time difference between the arrival of the direct and the reflected signal in C/A-code space. The excess path between direct and reflected GPS signal is calculated and with the known positions of receiver and transmitter the altimetric height of the reflecting surface can be derived. GPS C/A-code altimetry is described in Section 3.7. The height accuracy of GPS C/A-code altimetry is limited to several meters due to the wavelength of the C/A-code.

Higher accuracy can be expected utilizing GPS L1 carrier phase-delay observations. The position of transmitter and receiver slightly changes with time. Hence, the reflected signals excess path slightly changes with time, as well. In case the reflected and the direct signal are coherent, both signals interfere at the antenna of the receiver. Periodic changes of the correlation power can be observed.

The interferometric frequency of the periodic changes can be estimated. With the observed interferometric frequency, the known changing geometry of the satellite orbit, and the receiver and spec-

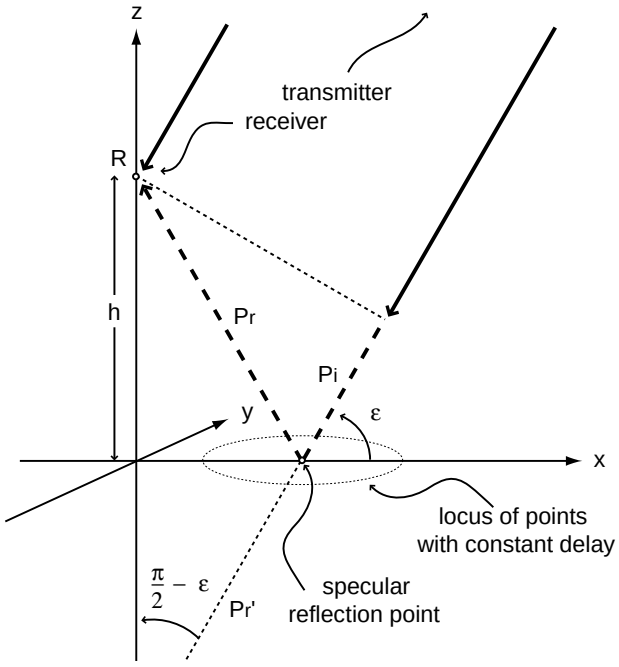

Fig. 3.1: *Geometry of the excess path δ traversed by the reflected GPS signal assuming ray optics and a flat Earth.*

DOI: 10.2312/GFZ.b103-08104

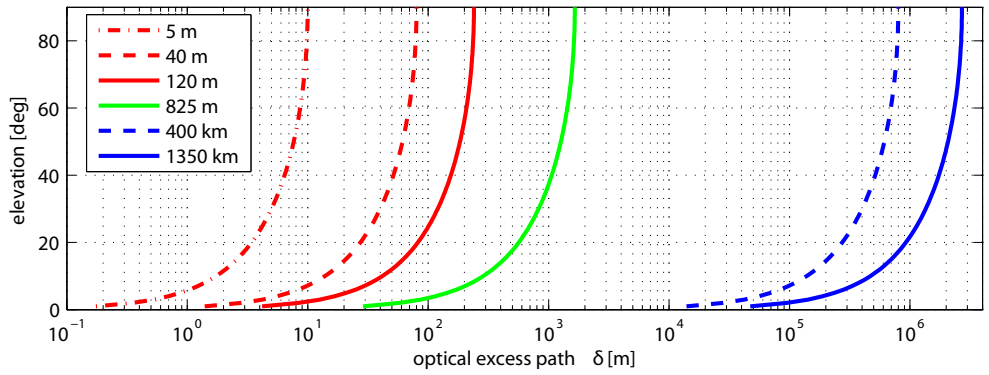

Fig. 3.2: *Excess path δ between direct and reflected GPS signal assuming a flat Earth geometry, calculated for various ground- and space-based receiver heights*

ular reflection point the altimetric height of the reflecting surface above a reference surface can be derived. GPS L1 interferometric frequency altimetry is described in Section 3.11. The height accuracy of GPS L1 interferometric frequency altimetry is limited to meter-level accuracy due to the achievable resolution of the frequency estimate.

The change of the excess path length can be determined from the measured fluctuating correlation data by using L1 carrier phase-delay observations. With the known geometry of the receiver and transmitter, relative height changes of the reflecting surface can be derived at the specular reflection point with some centimeters accuracy. Assuming a horizontal reflector or a reflector with a known general height trend, an altimetric height can be derived by detrending the relative height observations. This is done by accurately tuning the estimated start height. GPS L1 interferometric carrier phase-delay altimetry is described in Section 3.12. In case the surface is not changing during the observation, GPS L1 interferometric carrier phase-delay altimetry can reach decimeter accuracy.

In most ground-based experiments the delay of the reflected signal is much smaller than a C/A-code chip length. Hence, the correlation energy of the direct signal superposes the correlation energy of the reflected signal. A simple retrieval method suppresses the energy of the direct signal from the desired reflected energy pattern.

Accuracy is not only limited by the observation geometry itself. Deflections of the horizontal reflector or estimated general trend cause height offsets and have to be carefully corrected. The influence of the ionosphere can be neglected at ground-based interferometric observations as direct and reflected signal paths approximately travel through the same area of the ionosphere. But troposphere by contrast heavily influences the height measurement as direct and reflected signal paths travel through different tropospheric regions. Tropospheric influence has to be carefully corrected for.

3.2 Reflection Geometry

Straightforward geometric considerations show that the path traveled by the reflected ray is longer compared to the path of the direct ray by the excess path $P_i + P_r$ (see Fig. 3.1). Thus, the reflected signal arrives at the receiver with a time delay $\Delta t = \frac{\delta}{c}$. The excess path δ can be expressed by

$$\delta = P_i + P_r. \tag{3.1}$$

Assuming a flat Earth and with

$$P_r = P'_r \text{ and} \tag{3.2}$$

$$P_i + P'_r = 2h\cos(\frac{\pi}{2} - \epsilon) \tag{3.3}$$

δ can be expressed as function of receiver height h above the reflection point and elevation angle ϵ at the reflection point as

$$\delta = 2\,h\,\sin\epsilon. \tag{3.4}$$

Fig. 3.2 illustrates according to Eq. 3.4, the estimated excess path δ of a reflected GPS signal for different receiver heights above a reflecting surface.

DOI: 10.2312/GFZ.b103-08104

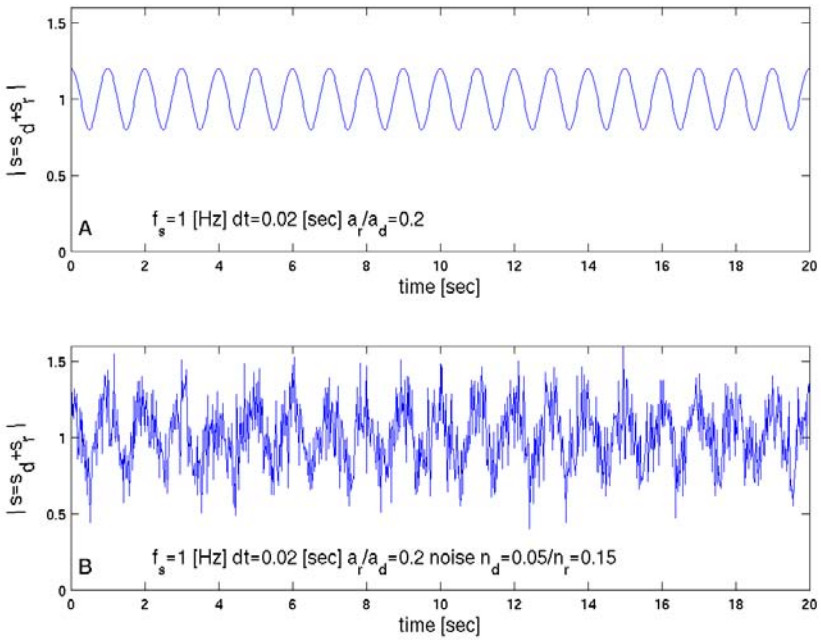

Fig. 3.3: *Panel A shows the resulting signal from two superposed coherent model sinusoidal signals of 1575.42 MHz (L1) frequency with a frequency shift between both signals of 1.0 Hz (Panel A). Panel B shows the signal from the same two model sinusoidal signals added with normally distributed noise.*

3.3 Doppler Shift

The geometry of receiver and transmitter is, in general, not static. Because the GPS satellites as well as the receiver are moving, the excess path δ will vary with time.

The time variation of δ can be expressed by

$$\frac{d\delta}{dt} = \lambda_{L1}\,\Delta f. \tag{3.5}$$

Differentiating Eq. 3.4 with respect to time, then with Eq. 3.5 the Doppler shift Δf of a reflected signal [Parkinson and Spilker, 1996] can be expressed as

$$\Delta f = \frac{2\dot{h}\sin\epsilon \;+\; 2h\dot{\epsilon}\cos\epsilon}{\lambda}, \tag{3.6}$$

this holds for the assumption of a flat Earth and a geometry as shown in Fig. 3.1.

3.4 Bistatic Altimetry Footprint Shape

When the GPS signal is scattered off the reflecting surface, the smallest expected delay corresponds to the scattered signal coming from the specular reflection point. In addition to the time delay, the scattered signal is also Doppler-shifted by an amount determined mainly by the angle between the direction of the scattered signal and the velocity of the receiver [Hajj and Zuffada, 2003]. The signal reflection footprint on the reflecting surface is defined by the intersection of equi-range and equi-Doppler contours in what is called the glistening zone which is centered at the specular reflection point.

The geometric locus d of all points from which secondary radiation arrives at the receiver with a constant phase difference with respect to the direct radiation is defined by the first Fresnel ellipse as

$$d = \sqrt{x^2 + y^2 + h^2} \;-\; x\,\cos\epsilon \;-\; h\,\sin\epsilon. \tag{3.7}$$

Eq. 3.7 assumes that the height of the receiver h is much smaller than the height of the transmitting GPS satellite h_T. Additionally, Eq. 3.7 assumes that the relation $\frac{x}{h_T}\sin(2\epsilon) \;\ll\; 1$ is true [Caparrini

DOI: 10.2312/GFZ.b103-08104

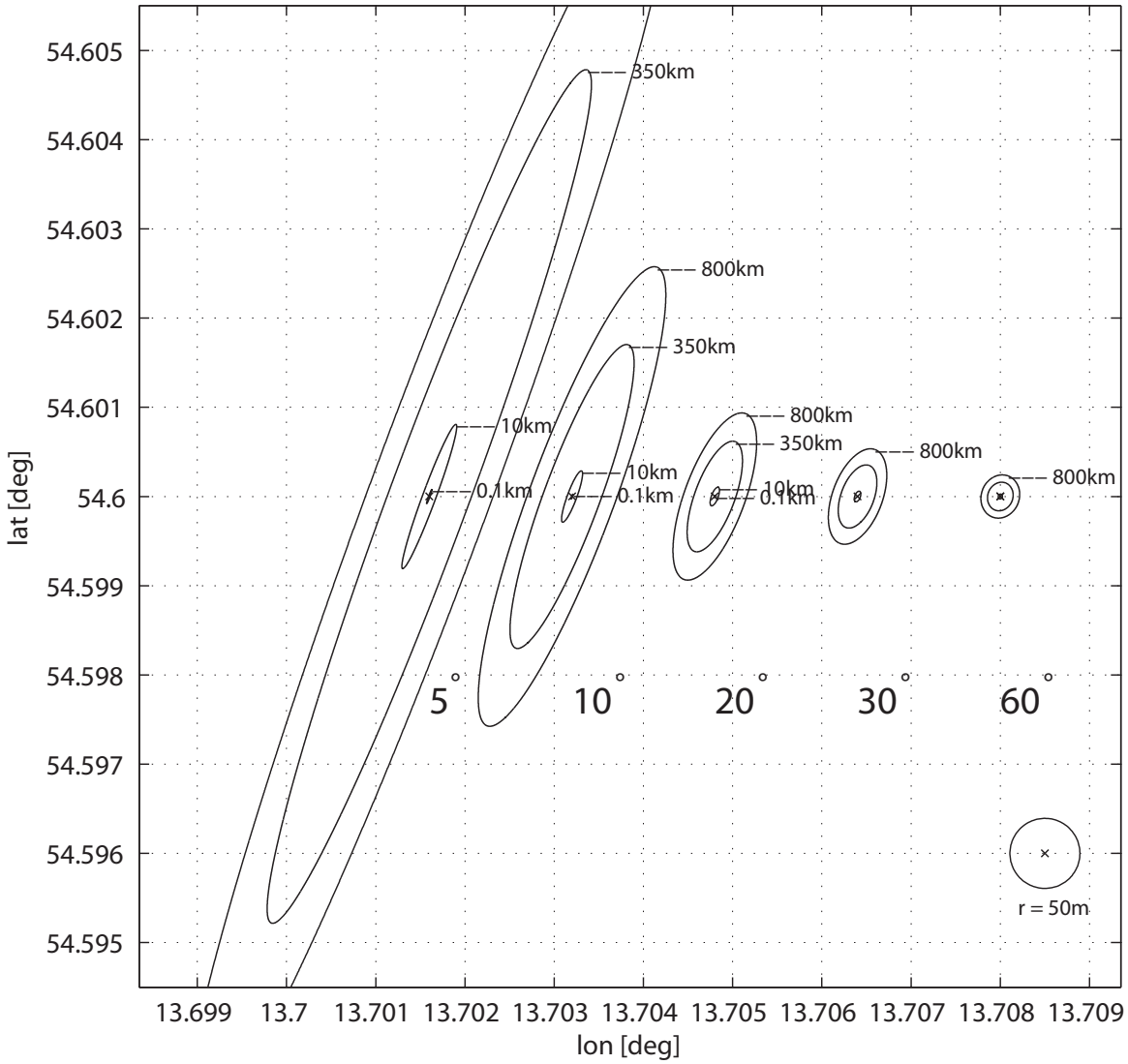

Fig. 3.4: *Estimated footprint shape of the reflected signal at various receiver altitudes and observation angles based on Eq. 3.7 and Eq. 3.8.*

and Martin-Neira, 1998]. Corresponding to one chip length and using Eq. 3.7 the semi-major and semi-minor axes a and b of the Fresnel ellipse, respectively, are given by

$$a = \frac{\sqrt{2\,d\,h\,\sin\epsilon}}{\sin^2\epsilon} \quad \text{and} \quad b = \frac{\sqrt{2\,d\,h\,\sin\epsilon}}{\sin\epsilon}. \tag{3.8}$$

Fig. 3.4 illustrates the estimated shape of the footprint of the specular reflected signal at various ground-based, air-borne, and space-borne receiver altitudes and different observation angles, respectively. The area covered by the footprint increases with increasing altitude of the receiver. Toward lower observation angles the circular footprint transforms more and more into a stretched ellipsoid. At grazing angles the area of the footprint increases significantly by a factor of 100. Fig. 5.29 on page 88 shows the shape of the footprint at the Fahrenberg location calculated from Eq. 3.8. Results from footprint size estimations during the Mercure hotel experiment are shown in Fig. 5.41 on page 96.

DOI: 10.2312/GFZ.b103-08104

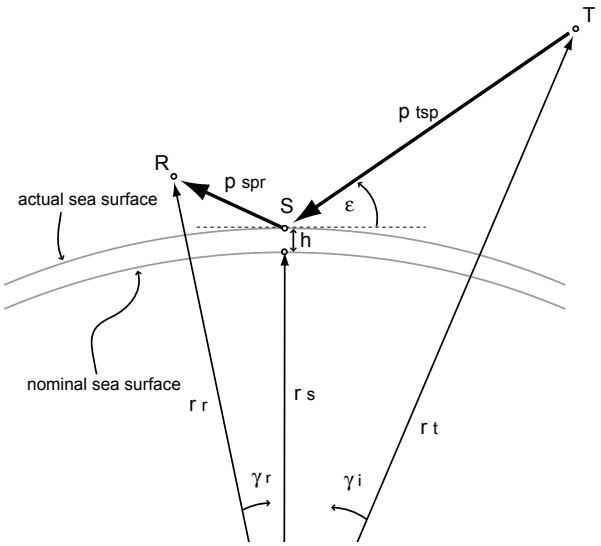

Fig. 3.5: *Altimetric height h determination from reflected transmitter-receiver range measurement. r_s, r_r, and r_t describe the geocentric distance of the reflection point S, the receiver R, and the transmitter T, respectively.*

3.5 Relationship between Height Error and Excess Path Delay Error

Information content of a measurement can be defined in terms of how sensitive the (GPS) height determination is to measurement error. A low error sensitivity implies a higher information content [Wu et al., 1997]. The path length $p = p_{tsp} + p_{spr}$ (see Fig. 3.5) of the reflected GPS signal can be expressed as the sum of

$$p_{tsp} = \sqrt{r_t^2 + (r_s + h)^2 - 2r_t(r_s + h)\cos\gamma_i} \tag{3.9}$$

$$p_{spr} = \sqrt{r_r^2 + (r_s + h)^2 - 2r_r(r_s + h)\cos\gamma_r} \tag{3.10}$$

The partial derivative of the path length with respect to the height h leads to

$$\frac{\sigma_p}{\sigma_h} \equiv \frac{\partial p}{\partial h}|_{h=0} = \frac{r_s - r_t\cos\gamma_i}{p_{tsp}} + \frac{r_s - r_r\cos\gamma_r}{p_{spr}} \tag{3.11}$$

$$= -\cos(\frac{\pi}{2} - \epsilon) - \cos(\frac{\pi}{2} - \epsilon) \tag{3.12}$$

$$= -2\sin\epsilon \tag{3.13}$$

For a spherical Earth the altimetric height error σ_h can now be expressed as a function of the path length σ_p and the elevation angle ϵ at the reflection point as

$$\sigma_h = \frac{\sigma_p}{2\sin\epsilon} \tag{3.14}$$

Fig. 3.6 illustrates that the altimetric height error caused by errors in path length determination is much higher at lower elevations than at high elevation angles. At an elevation of 5° an error of 10 cm occuring during path length determination causes a 50 cm altimetric error. An in-depth discussion concerning GNSS reflectometry range precision can be found in Germain and Ruffini [2006].

3.6 Specular Reflection Point Calculation

In this section the location of the point of specular reflection is calculated from the known receiver and transmitter positions following the formulas given in Martín-Neira [1993]. The geometry used is shown in Fig. 3.8, with a spherical Earth of radius r_E. The Earth sphere is best-fitted to the Earth ellipsoid by a Gaussian osculating sphere. The radius r_E is expressed as function of the latitude of the receiver Φ_{rcv}

$$r_E = \sqrt{MN} \tag{3.15}$$

DOI: 10.2312/GFZ.b103-08104

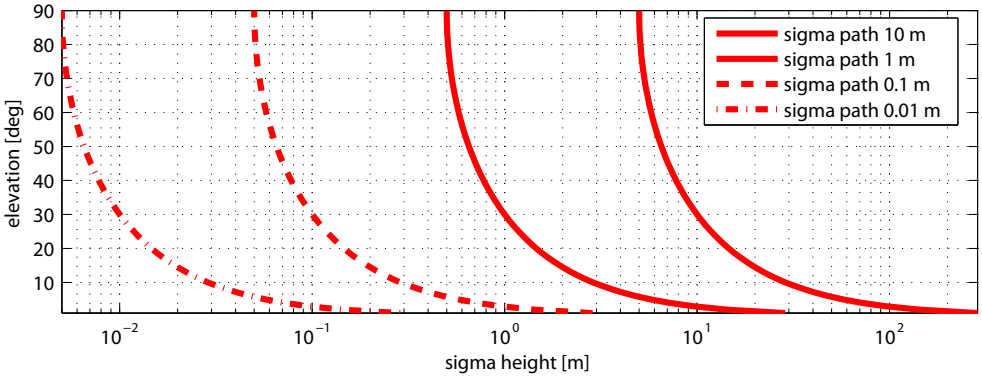

Fig. 3.6: *Dependency between elevation angle and height error σ_h in path length determination*

with

$$M = \frac{a(1-e^2)}{\sqrt{(1-e^2\sin^2\Phi_{rcv})^3}} \quad \text{and} \quad N = \frac{a}{\sqrt{(1-e^2\sin^2\Phi_{rcv})}}. \tag{3.16}$$

The values for the Earth's semi major axis a and eccentricity e are taken as defined by WGS-84 [ICD-GPS-200, 2003].

The positions of receiver R, transmitter T and of the specular reflection point P all lie in one plane which is equal to the paper plane in Fig. 3.7 and Fig. 3.8. The receiver and transmitter position coordinates (x,y) are transformed to the reflection point horizontal system (x',y') (see Fig. 3.7) to express more easily the condition for specular reflection, according to Snell's Law:

$$\frac{x'_t}{y'_t} = -\frac{x'_r}{y'_r}. \tag{3.17}$$

With the following relationship between (x,y) and (x',y') for R and T

$$\begin{pmatrix} x' \\ y' \end{pmatrix} = \begin{pmatrix} \cos\gamma & \sin\gamma \\ -\sin\gamma & \cos\gamma \end{pmatrix} \begin{pmatrix} x \\ y \end{pmatrix} - \begin{pmatrix} r_E \\ 0 \end{pmatrix}, \tag{3.18}$$

Eq. 3.17 can be expressed as

$$\frac{x_t\cos\gamma + y_t\sin\gamma - r_E}{-x_t\sin\gamma + y_t\cos\gamma} = -\frac{x_r\cos\gamma + y_r\sin\gamma - r_E}{-x_r\sin\gamma + y_r\cos\gamma}. \tag{3.19}$$

Eq. 3.19 can be transformed into

$$\begin{aligned} 2(x_t x_r - y_t y_r)\sin\gamma\cos\gamma - \\ (x_t y_r + y_t x_r)(\cos^2\gamma - \sin^2\gamma) - \\ r_E\,(x_t + x_r)\,\sin\gamma + r_E\,(y_t + y_r)\,\cos\gamma \quad = 0. \end{aligned} \tag{3.20}$$

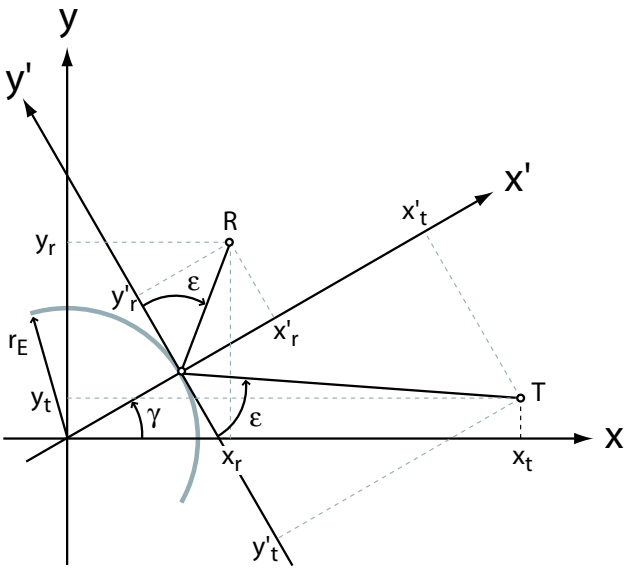

Fig. 3.7: *Reflection point local horizon system (x',y') to express more easily the condition for specular reflection, according to Snell's Law.*

DOI: 10.2312/GFZ.b103-08104

With the substitute

$$t = \tan\frac{\gamma}{2} \tag{3.21}$$

Eq. 3.20 changes to

$$\begin{aligned} & 2(x_t x_r - y_t y_r)\frac{2t}{1+t^2}\frac{1-t^2}{1+t^2} - \\ (x_t y_r + y_t x_r) & \left[\left(\frac{1-t^2}{1+t^2}\right)^2 - \left(\frac{2t}{1+t^2}\right)^2\right] - \\ r_E \frac{2t}{1+t^2}(x_t + x_r) + r_E & \frac{1-t^2}{1+t^2}(y_t + y_r) \quad = 0. \end{aligned} \tag{3.22}$$

With Eq. 3.21 and the coefficients

$$c_0 = (x_t y_r + y_t x_r) - r_E\,(y_t + y_r) \tag{3.23}$$
$$c_1 = -4(x_t x_r - y_t y_r) + 2r_E(x_t + x_r) \tag{3.24}$$
$$c_2 = -6(x_t y_r + y_t x_r) \tag{3.25}$$
$$c_3 = 4(x_t x_r - y_t y_r) + 2r_E(x_t + x_r) \tag{3.26}$$
$$c_4 = (x_t y_r + y_t x_r) + r_E\,(y_t + y_r) \tag{3.27}$$

the equation for the specular point calculation can finally be written as spherical mirror equation

$$c_4 t^4 + c_3 t^3 + c_2 t^2 + c_1 t + c_0 = 0. \tag{3.28}$$

In the following the rotated and translated coordinate system (x',y') is choosen in such a way that the receiver is located along the y-axis at an altitude of H meters above the Earth surface. Now the position vector of the receiver $\vec{r}_r$ can be expressed as

$$\vec{r}_r = \begin{pmatrix} x_r \\ y_r \end{pmatrix} = \begin{pmatrix} 0 \\ r_E + H \end{pmatrix}. \tag{3.29}$$

Using the geometry of Fig. 3.8, the position vector of the transmitter $\vec{r}_t$ can be expressed in terms of the elevation angle ϵ above the local horizon plane at the receiver location:

$$\vec{r}_t = \begin{pmatrix} x_t \\ y_t \end{pmatrix} = \begin{pmatrix} r_t\,\cos(\epsilon+\tau) \\ r_t\,\sin(\epsilon+\tau) \end{pmatrix}. \tag{3.30}$$

τ is the angle enclosed by the triangle R-T-0 and can be written in terms of ϵ by using the sine theorem:

$$\frac{\sin(\frac{\pi}{2}+\epsilon)}{r_t} = \frac{\sin\tau}{r_E + H}. \tag{3.31}$$

Finally the position vector of the transmitter can be expresses by

$$\begin{pmatrix} x_t \\ y_t \end{pmatrix} = \begin{pmatrix} r_t\,\cos(\epsilon)\sqrt{1 - \frac{(r_E+H)^2}{r_t^2}\cos^2\epsilon} - (r_E + H)\sin\epsilon\cos\epsilon \\ r_t\,\sin(\epsilon)\sqrt{1 - \frac{(r_E+H)^2}{r_t^2}\cos^2\epsilon} + (r_E + H)\cos^2\epsilon \end{pmatrix}. \tag{3.32}$$

With the known height H of the receiver above the Earth surface, the Earth radius r_E calculated with Eq. 3.15, and the known elevation angle ϵ of the transmitter at the receiver position, the spherical mirror equation Eq. 3.28 can be solved for a solution of the angle γ. An iterative scheme based on the modified Newton-method [Bronštein et al., 1993] is used to solve the spherical mirror equation and find the specular reflection point where the angle of incidence equals the angle of reflection. Starting with an estimate $\gamma_0 = \frac{\pi}{2} - \frac{1}{3}\gamma_{rt}$ the following values t_n,t_{n+1}, and K_n are calculated

$$t_n = \tan\frac{\gamma_n}{2} \tag{3.33}$$
$$t_{n+1} = t_n - \frac{f_n}{f_n'} \tag{3.34}$$
$$K_n = \left|\frac{f_n''}{f_n'}\right| \tag{3.35}$$

DOI: 10.2312/GFZ.b103-08104

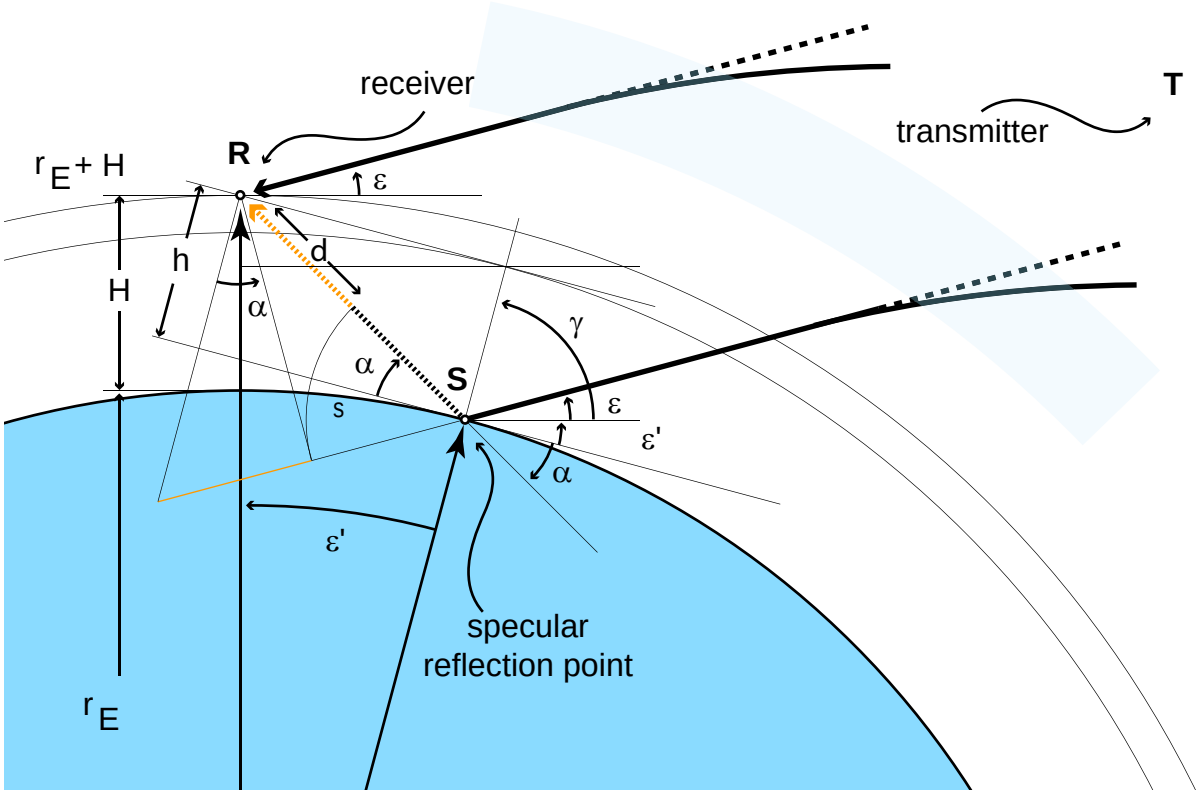

Fig. 3.8: *Geometry used to calculate the position of the specular refl ection point S in terms of the known receiver position R with receiver height H above the osculating sphere and the GPS satellite elevation angle ϵ. h denotes the height variations normal to the tangential plane at P.*

with

$$f_n = c_4 t_n^4 + c_3 t_n^3 + c_2 t_n^2 + c_1 t_n + c_0 \quad (3.36)$$

$$f_n' = 4c_4 t_n^3 + 3c_3 t_n^2 + 2c_2 t_n + c_1 \quad (3.37)$$

$$f_n'' = 12c_4 t_n^2 + 6c_3 t_n + 2c_2. \quad (3.38)$$

γ_{rt} describes the angle between the vectors $\vec{r}_r$ and $\vec{r}_t$. While the conditions $f_n' \neq 0$ and $K_n < 1$ are fulfi lled, n is iterated as long as$|\gamma_{n+1} - \gamma_n|$ is larger than the chosen tolerance ($1 \cdot 10^{-8}$ [rad]). With a solution for γ the position vector of the specular refl ection point P can be derived as

$$\begin{pmatrix} x_p \\ y_p \end{pmatrix} = \begin{pmatrix} r_E \cos(\gamma) \\ r_E \sin(\gamma) \end{pmatrix}. \quad (3.39)$$

Knowing the position vector of the specular refl ection point P, the arc length$s$ from the sub receiver point to the specular refl ection point can be calculated as

$$s = \left(\frac{\pi}{2} - \gamma\right) r_E. \quad (3.40)$$

In Fig. 3.9 six different receiver heights have been considered for plotting the relation between the elevation of the transmitter and the sub receiver point distance to the specular refl ection point. A receiver at an altitude of 5, 50, and 100 m above the refl ecting plane can be considered as a typical site height of a GPS tide gauge receiver. A height of 800 m refl ects the situation of a receiver on a mountain top and a height of 400 km is a GPS altimetry receiver fl ying on board a Low Earth Orbiter (LEO) satellite like CHAMP. A height of 1350 km represents a receiver fl ying on board a satellite like Jason-1.

DOI: 10.2312/GFZ.b103-08104

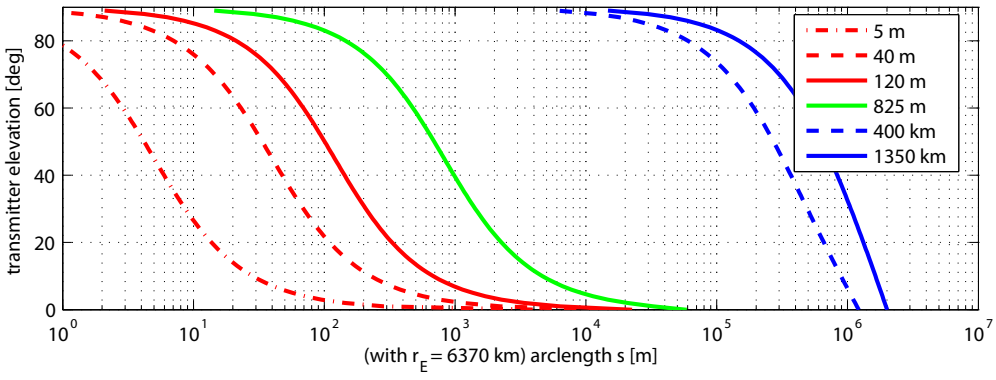

Fig. 3.9: *Receiver foot point surface distance s to the specular reflection point depending on transmitter elevation for different receiver heights*

3.7 GPS C/A-code Altimetry

The C/A-code pseudo range measurement r_{pseudo} results from the time delay between the transmission time T_s at the satellite and the reception time T_r of the GPS signal at the receiver:

$$r_{pseudo} = c(T_r - T_s) \tag{3.41}$$

The local satellite time T_s and local receiver time T_r have to be corrected for the satellite and receiver clock errors Δt_s and Δt_r to give the transmission and reception time t_s and t_r in GPS time.

$$T_s = t_s + \Delta t_s \text{ and } T_r = t_r + \Delta t_r \tag{3.42}$$

Now Eq. 3.41 can be expressed by

$$\begin{aligned} r_{pseudo} &= c(t_r + \Delta t_r - t_s - \Delta t_s) && (3.43)\\ &= c(t_r - t_s) + c\Delta t_r - c\Delta t_s. && (3.44) \end{aligned}$$

The range $r = c(t_r - t_s)$ between satellite and receiver can now be written as

$$r = r_{pseudo} - c\Delta t_r + c\Delta t_s. \tag{3.45}$$

The reflected GPS signal ray path is longer compared to the direct GPS signal ray (Fig. 3.1). Thus, the reflected GPS signal arrives with a time delay Δt at the antenna of the receiver in comparison to the direct GPS signal. In GPS altimetry the difference δ between the range of the direct signal $r1$ and the range of the reflected signal $r2$ is measured and using $\Delta t2_r = \Delta t1_r$ and $\Delta t2_s = \Delta t1_s$ results from

$$\begin{aligned} \delta = r2 - r1 &= r2_{pseudo} - c\Delta t2_r + c\Delta t2_s - r1_{pseudo} + c\Delta t1_r - c\Delta t1_s && (3.46)\\ &= r2_{pseudo} - r1_{pseudo} && (3.47)\\ &= c(T2_r - T1_s) - c(T1_r - T1_s) && (3.48)\\ &= c(T2_r - T1_r). && (3.49) \end{aligned}$$

Thus, the time delay $T2_r - T1_r$ is the quantity to be measured by GPS C/A-code based altimetry and it does not depend on the local clock errors of the receiver or satellite.

When the correlation between the received GPS signal and the model (replica) signal is done, besides the peak of the direct signal a second peak can be observed in case of a reflection event (Fig. 3.12, 3.10). The altimetric height can be derived from the time delay $\Delta T = \frac{\delta}{c}$ between the first peak of the direct signal at time $T1_r$ and the second peak of the reflected signal at time $T2_r$. Fig. 3.10, panel B, shows the time delay between the direct signal, recorded with a RHCP antenna (blue), and the reflected signal, recorded with the LHCP antenna (red). Using a sampling frequency of $f_s = 5.714395$ MHz and with the velocity of light c the reflected signal arrives with a delay of

$$\Delta T = T2_r - T1_r = 15 \text{ samples} = 15\,\frac{1}{f_s}\,\text{sec} = 2.625\ \mu\text{sec} \tag{3.50}$$

DOI: 10.2312/GFZ.b103-08104

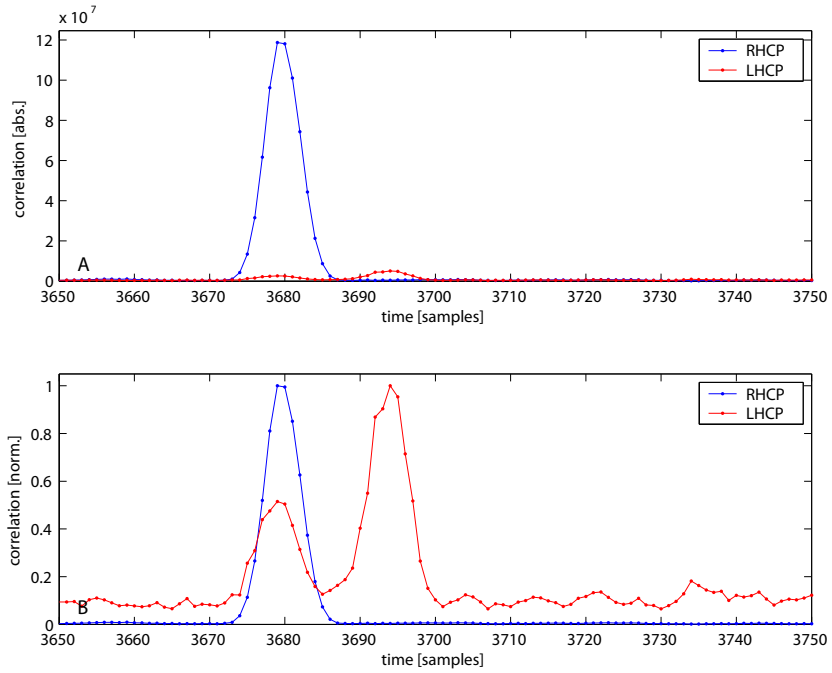

Fig. 3.10: *Panel A and B show the correlation between the replica code for PRN 11 and the recorded GPS 2-bit data stream of the RHCP antenna (blue) and the LHCP antenna (red) with the COMNAV receiver. In Panel A the absolute correlation power (correlation sum during 20 msec) is shown while in Panel B the correlation power is normed to the maximal occurring peak power. See also Fig. 2.5 on page 22.*

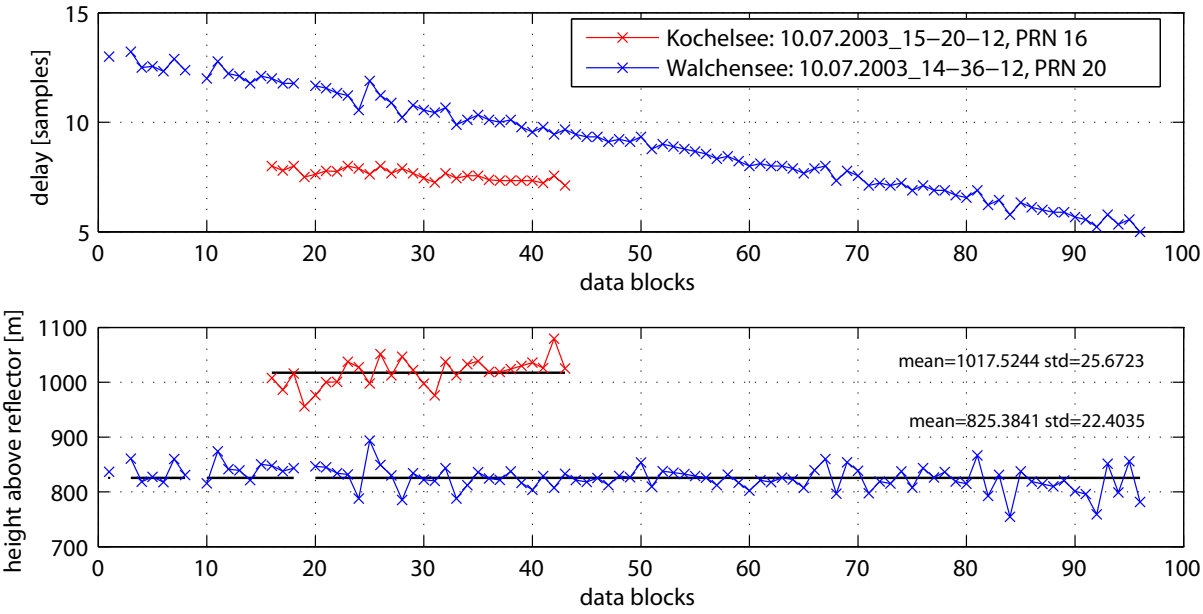

Fig. 3.11: *Results of GPS C/A-code altimetry with the COMNAV receiver on July 10, 2003 at the Fahrenberg location. Data (M. Nitschke, pers. communication)*

at the receiver. This results in an excess path length of

$$\delta = c(T2_r - T1_r) = 786.9 \text{ m}. \tag{3.51}$$

The accuracy of the derived height is limited to several meter due to the wavelength of the used C/A-code. Fig. 3.11 shows the results of GPS altimetry (M. Nitschke, pers. communication) with pseudo ranges from a measurement campaign conducted with the COMNAV receiver. The STD of the calculated heights of the reflecting lake surface is larger than 20 m.

3.8 GPS L1 Carrier Phase Altimetry

The transmitter generates a carrier phase signal Φ_s which increases linearly with time and which grounds on the internal clock of the satellite. The carrier phase – expressed in units of full cycles –

DOI: 10.2312/GFZ.b103-08104

can be described as a function of carrier frequency f and satellite transmission time T_s:

$$\Phi_s = f \cdot T_s. \tag{3.52}$$

T_s includes all clock variations. For simplification we neglect effects like Doppler and assume a constant frequency. The phase signal travels from the transmitter to the receiver. The receiver has no information about the number of full wavelength n when receiving the carrier phase signal Φ:

$$\Phi = \Phi_s - n = f \cdot T_s - n. \tag{3.53}$$

The satellite carrier phase signal arrives at T_r at the receiver. The receiver generates with the internal clock a local reference carrier phase signal Φ_r which can be expressed by

$$\Phi_r = f \cdot T_r. \tag{3.54}$$

Now the phase measurement Φ – the difference between reference phase of the receiver and phase signal of the satellite – can be expressed by

$$\Phi = \Phi_r - \Phi_s = f \cdot (T_r - T_s) + n. \tag{3.55}$$

Multiplying the phase with the carrier wavelength $\lambda = \frac{c}{f}$ results in the range observation equation

$$\begin{aligned} r_{phase} &= \lambda(\Phi_r - \Phi_s) && (3.56)\\ &= c(T_r - T_s) + n \cdot \lambda && (3.57)\\ &= r + c\Delta t_r - c\Delta t_s + n \cdot \lambda. && (3.58) \end{aligned}$$

The phase range observation r_{phase} differs from the code range observation r (see Eq. 3.45) by the term $n \cdot \lambda$, which includes the ambiguity n. In case the receiver looses track of the signal, the receiver cannot continuously count the incoming full carrier phase wave cycles. Thus, an unknown number n of jumps of one carrier wavelength is introduced in the phase measurement. These so called cycle slips have to be fixed during data processing.

Ionosphere and troposphere cause signal delays $\Delta\rho_{iono}$ and $\Delta\rho_{tropo}$ which have to be corrected. Thus, the actual geometric distance ρ between satellite and receiver differs from the measured path length r traveled by the signal. Additionally, relativistic corrections $\Delta\rho_{rel}$, multipath influence $\Delta\rho_{mul}$ and measurement errors ϵ have to be accounted for. An improved model of the geometric distance ρ [Rothacher and Zebhauser, 2000] can be described by

$$\rho = r_{phase} - \Delta\rho_{tropo} - \Delta\rho_{iono} - \Delta\rho_{rel} - \Delta\rho_{mul} - c\Delta t_r + c\Delta t_s - n \cdot \lambda - \epsilon. \tag{3.59}$$

In GPS altimetry the difference between the range $\rho 1$ of the direct signal and the range $\rho 2$ of the reflected signal is the target quantity. Thus, the reflected signal itself has to be tracked and a carrier phase range observation has to be performed. In general the signal strength of the reflected signal is weak and its quality is degraded. Hence, continuous tracking of reflected signals is difficult because of intensity fluctuations in the reflected signal component. In order to increase the SNR measurements with a LHCP high gain antenna are required.

3.9 Open-Loop Tracking

This study favors open-loop tracking in order to use carrier phase-delay observations of reflected GPS signals. Open-loop tracking ensures insensitivity with respect to intensity fluctuations of the reflected signal component. At the same time open-loop tracking takes advantage of the sub-centimeter resolution offered by the GPS carrier phase signal.

During open-loop tracking one receiver channel – the master channel – keeps track of the direct GPS signal. A second channel – the slave channel – measures the reflected GPS signal (see Fig. 3.12). The carrier and code tracking loops of the slave channel are opened and synchronized to the master channel. In the code loop feed-back of the slave channel, however, the estimated delay of the reflected signal is inserted. The estimated delay is calculated from Eq. 3.4 and Eq. 3.51. Open-loop tracking is

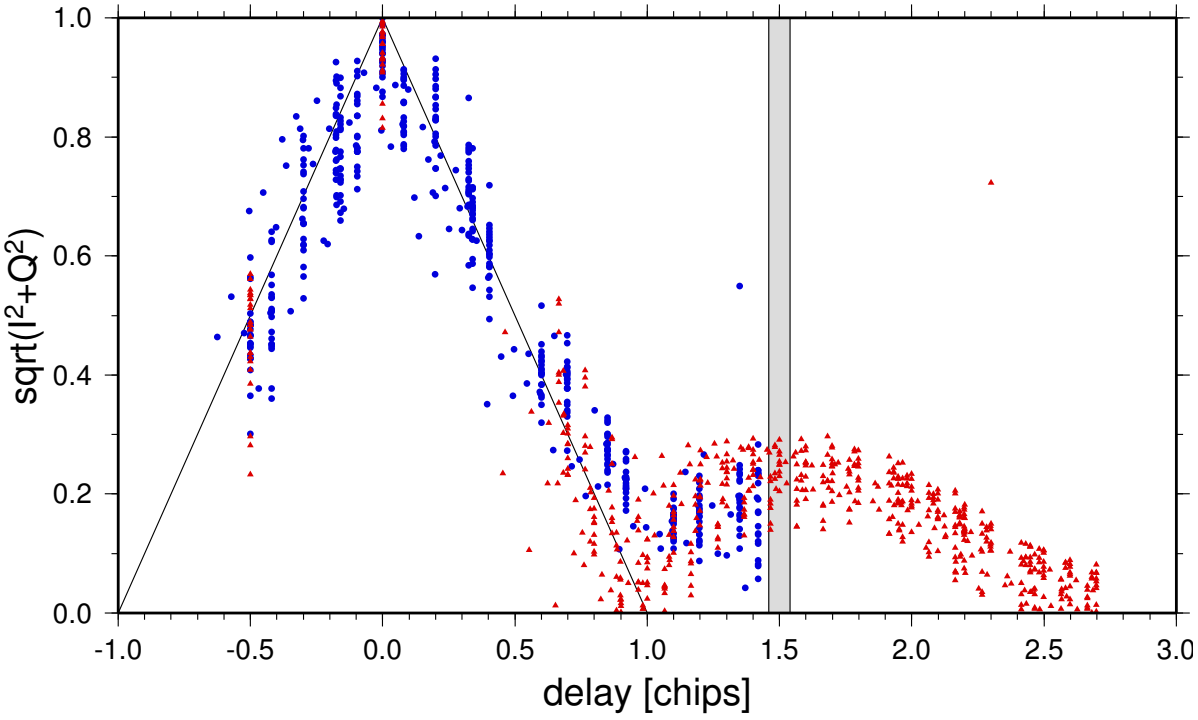

Fig. 3.12: *Delay mapped waveform of a reflection event (PRN 16) measured with the OpenGPS receiver at 13:34:17 GPST 8 July 2003, antenna oriented toward Kochelsee. The delay is given in relation to the maximum peak of the direct signal. Blue circles and red triangles indicate 2 measurements (0.5-second duration) starting 120 (blue) and 267 (red) seconds after the start of the measurement. In the second case (red) the 2-chip-wide interval of covered chip code offsets is centered at the maximum of the reflected signal. The points reveal the measured waveform of the direct and reflected correlation signal. The thin black triangle marks the theoretical C/A code correlation function of the direct signal. The gray box marks the maximum of the reflected signal.*

explained in more detail in section 4.3.1 and 4.3.2 on page 50. The reflected GPS signal is measured by recording the in-phase and quadrature-phase components of the reflected signal which is marked by a gray box in Fig. 3.12.

In the following sections 3.11 and 3.12 open-loop tracking and interferometric techniques are used in order to derive highly accurate altimetric phase measurements from the recorded in-phase and quadrature-phase data.

3.10 In-Phase and Quadrature-Phase Signal Component

The received signal $x(t)$ with the instantaneous carrier frequency ω in radians per second can be represented by

$$x(t) = A\,\cos(\omega t + \varphi). \tag{3.60}$$

The receiver determines the unknown instantaneous amplitude A and instantaneous phase offset φ by multiplying the signal by a pair of reference signals. The reference signals are orthogonal. Thus, they are 90° out of phase to each other or in phase quadrature. We obtain the in-phase and quadrature-phase (or quad-phase) signal components I and Q, respectively. I and Q can be represented after Kelley and Baker [2006b] by

$$I = \frac{1}{2}A\,\cos(\varphi) \;\text{ and }\; Q = \frac{1}{2}A\,\sin(\varphi). \tag{3.61}$$

Hence, I is maximized when the unknown signal is phase-aligned with $\cos(\omega t)$ and Q is maximized when the unknown signal is phase-aligned with $\sin(\omega t)$. The amplitude of the received signal is determined using the vector magnitude of the I and Q components by

$$A = 2\sqrt{I^2 + Q^2}. \tag{3.62}$$

DOI: 10.2312/GFZ.b103-08104

The phase can be determined by the four-quadrant arctangent with

$$\varphi = \tan^{-1}(\frac{Q}{I}). \tag{3.63}$$

3.11 GPS L1 Interferometric Frequency Altimetry

As already mentioned in sections 3.2 and 3.7 the reflected GPS signal ray is longer compared to the direct ray. The observed path difference δ can be expressed (see Eq. 3.4) as a function of receiver height h and elevation angle ϵ at the specular reflection point. Due to the relative change of the position of receiver and transmitting satellite, the time delay and path difference between the direct and the reflected signal slightly changes with time. At the receiver antenna both signals superpose each other. If both signals are coherent and if the path length difference δ between direct and reflected signal has a value of multiples of half the carrier wavelength λ_{L1}, constructive or destructive interference can be observed. Thus, direct and reflected signals interfere at the time of arrival of the reflected signal and cause varying fluctuations in the amplitude of the received signal. These amplitude variations are recorded by the receiver.

During a reflection event one can observe an interference frequency f_i in the amplitude time series of the reflected signal. The excess path δ can be expressed as a function of the time-varying phase φ by

$$\delta = \lambda_{L1}\,\varphi + n\,\lambda_{L1} \tag{3.64}$$

with n representing the generally unknown number of full wavelength λ_{L1}. The time variation of δ can be expressed with Eq. 3.64 by

$$\frac{d\delta}{dt} = \lambda_{L1}\frac{d\varphi}{dt} \tag{3.65}$$

$$= \lambda_{L1}\,f_i. \tag{3.66}$$

Coherence of both signals is mandatory. It might be possible that due to the different signal paths one of the signals is degraded by, e.g., local atmospheric or ionospheric effects, minimizing or destroying coherence.

With the time derivative of Eq. 3.4 one obtains

$$\frac{d\delta}{dt} = \frac{d\,(2\,h\,\sin\epsilon)}{dt}$$

$$= 2\,h\,\cos\epsilon\,\frac{d\epsilon}{dt}. \tag{3.67}$$

and with 3.66 and 3.67

$$\lambda_{L1}\,f_i = 2\,h\,\cos\epsilon\,\frac{d\epsilon}{dt}, \tag{3.68}$$

$$h = \frac{\lambda_{L1}\,f_i}{2\,\cos\epsilon\,\frac{d\epsilon}{dt}}, \tag{3.69}$$

Eq. 3.69 provides the observable height h. From the exact measurement time and the known position of receiver and transmitter ϵ and $\frac{d\epsilon}{dt}$ can be calculated. The interferometric frequency f_i is determined by a spectral analysis of the amplitude time series of the received signal.

Up to now the Earth shape was assumed to be a plane. Results from experiments show that the flat Earth model has to be extended by accounting for the bending of the Earth. For a simplified calculation the Earth shape is approximated in the following by a sphere.

In the reflection point local horizon system (see Fig. 3.7) Eq. 3.4 transforms into

$$\delta = 2\,h\,\sin\alpha. \tag{3.70}$$

DOI: 10.2312/GFZ.b103-08104

The location of the specular reflection point is calculated by solving the spherical mirror equation 3.28 and with Eq. 3.21 a solution of γ can be found. α can be expressed by

$$\alpha = \epsilon - \gamma + \frac{\pi}{2}. \tag{3.71}$$

h can be expressed by

$$h = (H + r_E)\,\sin\gamma - r_E. \tag{3.72}$$

Eq. 3.70, with Eq. 3.71 and Eq. 3.72, transforms to

$$\begin{aligned} \delta &= 2\,[(H + r_E)\,\sin\gamma - r_E]\,\sin(\epsilon - \gamma + \frac{\pi}{2}) \\ &= 2\,(H + r_E)\,\sin\gamma\,\cos(\epsilon - \gamma) - 2\,r_E\,\cos(\epsilon - \gamma). \end{aligned} \tag{3.73}$$

With ϵ and γ as time-dependent quantities we differentiate Eq. 3.73 with respect to time and receive

$$\begin{aligned} \frac{d\delta}{dt} &= 2\,(H + r_E)\,\cos\gamma\,\frac{d\gamma}{dt}\cos(\epsilon - \gamma) - \\ &\quad 2\,(H + r_E)\,\sin\gamma\sin(\epsilon - \gamma)\,\left(\frac{d\epsilon}{dt} - \frac{d\gamma}{dt}\right) + \\ &\quad 2\,r_E\,\sin(\epsilon - \gamma)\,\left(\frac{d\epsilon}{dt} - \frac{d\gamma}{dt}\right). \end{aligned} \tag{3.74}$$

With Eq. 3.66 and Eq. 3.74 the following equation can be solved

$$\begin{aligned} \lambda_{L1}\,f_i &= 2\,(H + r_E)\,\left[\cos\gamma\,\frac{d\gamma}{dt}\cos(\epsilon - \gamma) - \right. \\ &\quad \left. \sin\gamma\sin(\epsilon - \gamma)\,\left(\frac{d\epsilon}{dt} - \frac{d\gamma}{dt}\right)\right] + \\ &\quad 2\,r_E\,\sin(\epsilon - \gamma)\,\left(\frac{d\epsilon}{dt} - \frac{d\gamma}{dt}\right) \end{aligned} \tag{3.75}$$

and H can be written as

$$H = \frac{\lambda_{L1}\,f_i - 2\,r_E\,\sin(\epsilon - \gamma)\,\left(\frac{d\epsilon}{dt} - \frac{d\gamma}{dt}\right)}{2\,\cos\gamma\,\frac{d\gamma}{dt}\cos(\epsilon - \gamma) - 2\,\sin\gamma\sin(\epsilon - \gamma)\,\left(\frac{d\epsilon}{dt} - \frac{d\gamma}{dt}\right)} - r_E. \tag{3.76}$$

In case of small rates of change of γ and with $\gamma \ll \epsilon$, the term $\frac{d\gamma}{dt}$ can be neglected and Eq. 3.76 can be simplified to

$$H = \frac{\lambda_{L1}\,f_i - 2\,r_E\,\sin(\epsilon - \gamma)\,\frac{d\epsilon}{dt}}{-2\,\sin\gamma\sin(\epsilon - \gamma)\,\frac{d\epsilon}{dt}} - r_E. \tag{3.77}$$

The accuracy of the derived height H generally depends on the accuracy of the determination of the interferometric frequency f_i which is limited by the time resolution of the recorded amplitude data.

3.12 GPS L1 Interferometric Carrier Phase-Delay Altimetry

Similarly to the situation discussed in the previous Section 3.11 the time delay and path difference between the direct and reflected signal slightly change with time. If the path length difference δ between direct and reflected signal has a value of multiples of half the carrier wavelength λ_{L1}, both signals superpose each other. If the direct and reflected signal are coherent, constructive or destructive interference can be observed. Both signals interfere. Variations in the signal amplitude and correlation power can be observed at the delay time of the reflection event. The changing path length difference δ between direct and reflected signal causes the phasor to rotate with an interference frequency f_i. The phasor is calculated from the measured in-phase (I) and quad-phase

DOI: 10.2312/GFZ.b103-08104

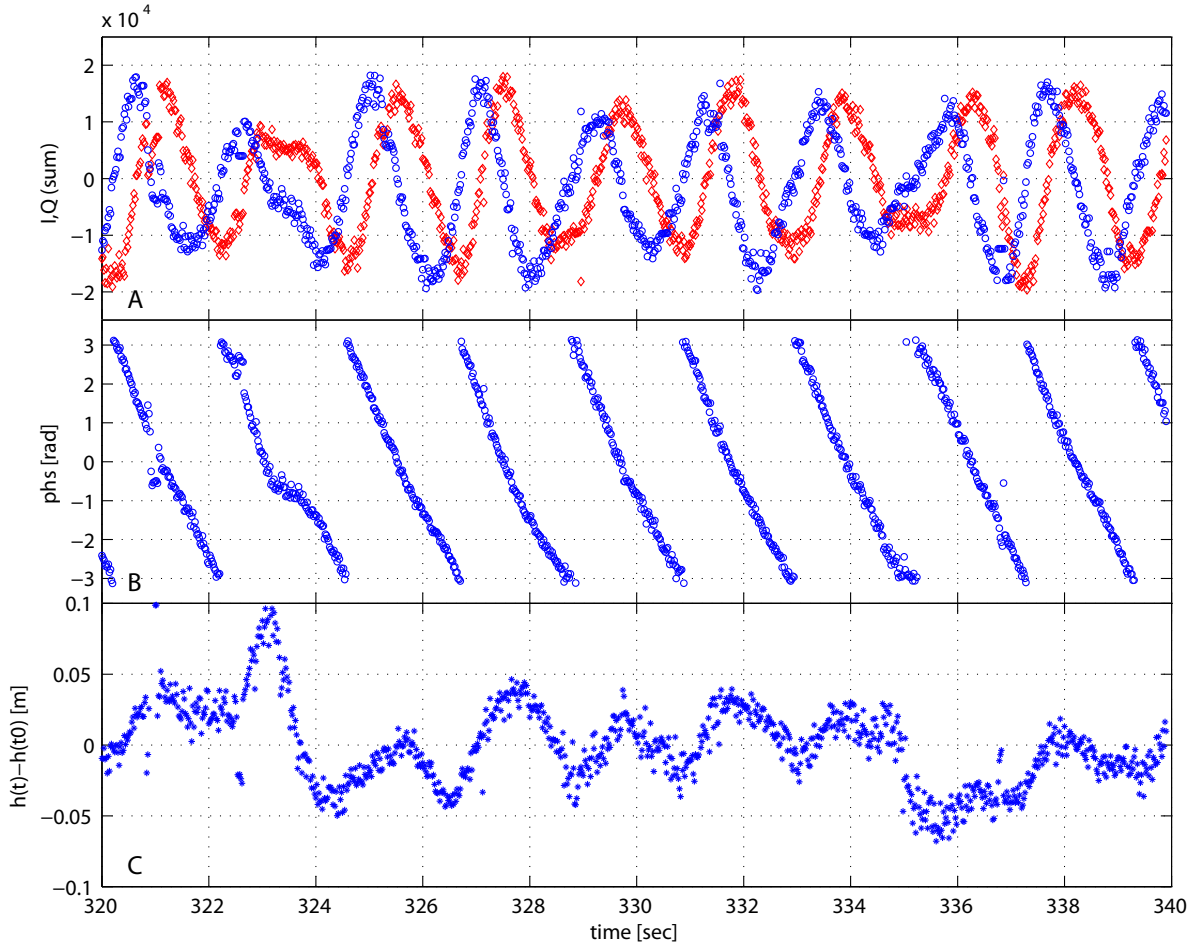

Fig. 3.13: *Panel A shows the demodulated reflected in- and quad-phase data $\tilde{I}_r$ (blue circles) and $\tilde{Q}_r$ (red diamonds) as a function of time since measurement start. With Eq. 3.79 the phase ϕ (Panel B) and from Eq. 3.83, 3.85 and 3.86 the relative height $h(t) - h(t_0)$ is calculated (Panel C), with $H(t_0)$ set to 599.9 m.*

(Q) correlation sums of the reflected signal. With the derived phase time series and the known geometry of receiver, transmitter and reflection point (Fig. 3.1 and Fig. 3.8 on page 36) the relative height change of the specular reflection point can be calculated.

From all in-phase and quad-phase correlation sum values I_r and Q_r of the slave channel the navigation message bits have to be removed according to

$$\begin{aligned} \tilde{I}_r &= \text{sign}(I_d)\, I_r \\ \tilde{Q}_r &= \text{sign}(I_d)\, Q_r, \end{aligned} \tag{3.78}$$

where I_d denotes the in-phase value of the master channel. The phase ϕ (Fig. 3.13 B) is calculated from the four quadrant arctangent

$$\phi = \text{atan2}(\tilde{Q}_r, \tilde{I}_r) \tag{3.79}$$

and is unwrapped by adding $\pm 2\pi$ when the difference between consecutive values exceeds π, resulting in the accumulated phase ϕ_a. The optical path length difference δ between direct and reflected signal is calculated from the accumulated phase ϕ_a and the L1 carrier wavelength $\lambda_{L1} = 0.1903$ m at the observation time t by

$$\delta(t) = \frac{\phi_a(t)}{2\pi}\, \lambda_{L1}. \tag{3.80}$$

From the geometry in Fig. 3.8 the following expression for the optical path length difference δ can be derived:

$$\delta(t) = 2\, h(t) \sin \alpha(t). \tag{3.81}$$

DOI: 10.2312/GFZ.b103-08104

δ changes with time because the geometry changes with time due to satellite, receiver and reflector movement. In this study the receiver is always fixed to the ground. δ changes with time according to

$$\delta(t) - \delta(t_0) = 2\,h(t)\sin\alpha(t) \;-\; 2\,h(t_0)\sin\alpha(t_0) \tag{3.82}$$

and solve Equation 3.82 for $h(t)$:

$$h(t) \;=\; \frac{\delta(t) - \delta(t_0) + 2\,h(t_0)\,\sin\alpha(t_0)}{2\,\sin\alpha(t)} \tag{3.83}$$

With the relation taken from the geometry in Fig. 3.8 and using $\cos(\frac{\pi}{2} - \gamma) = \sin(\gamma)$ results in

$$\sin\gamma(t) = \frac{h(t) + r_E}{H(t) + r_E} \tag{3.84}$$

and thus $h(t)$ can be expressed by

$$h(t) = (H(t) + r_E)\sin\gamma(t) - r_E. \tag{3.85}$$

In this way height H is linked with height h in the rotated coordinate system. Height h is normal to the tangent plane at the reflection point. Starting with a height estimate $H(t_0)$, the temporal evolution of the altimetric height variation $h(t) - h(t_0)$, normal to the tangent plane at the reflection point P, is calculated from Eq. 3.83 and with $h(t_0)$ expressed as function of γ:

$$h(t_0) = (H(t_0) + r_E)\sin(\gamma(t_0)) - r_E. \tag{3.86}$$

γ is calculated by solving the spherical mirror equation 3.28 for the appropriate elevation angle ϵ. Now α and ϵ can be calculated according to

$$\alpha \;=\; \epsilon + \frac{\pi}{2} - \gamma \tag{3.87}$$

$$\epsilon \;=\; \epsilon_{eph} + \Delta\epsilon_{tropo}, \tag{3.88}$$

assuming an infinite distance to the GPS transmitter. ϵ_{eph} is calculated from the broadcast ephemeris data [GPS SPS], the correction $\Delta\epsilon_{tropo}$ accounts for effects caused by atmospheric refractivity. The tropospheric correction is derived from a geometric ray tracing calculation using a refractivity profile obtained from meteorological models provided by the ECMWF. The position of the specular reflection point P as function of γ (Fig. 3.8) is calculated using the equations given in Martín-Neira [1993].

Fig. 3.13 shows measured data of PRN 16 made at the Fahrenberg location on 8 July, 13:35:47 GPST at elevations ranging from $10.83°$ to $10.78°$ (with the antenna oriented towards the Kochelsee). Panel A shows the demodulated reflected in- and quad-phase data $\tilde{I}_r$ (blue circles) and $\tilde{Q}_r$ (red diamonds) as a function of time since measurement start. With Eq. 3.79 the phase ϕ (Panel B) and from Eq. 3.83, 3.85 and 3.86 the relative height $h(t) - h(t_0)$ is calculated (Panel C), with $H(t_0)$ set to 599.9 m.

Thus, the altimetric height change of a reflecting surface derived with a GPS receiver above the reflecting surface is determined from the carrier phase difference between the direct and reflected GPS signal (Fig. 3.13 C). The accuracy of the derived height can be at the centimeter-level due to the wavelength of the used GPS L1 carrier frequency.

DOI: 10.2312/GFZ.b103-08104

4 Data Aquisition and Processing

4.1 OpenGPS Receiver

The OpenGPS receiver used in this study is a 12-channel single-frequency (L1) software receiver implemented with the Zarlink GP2015/GP2021 chip set. OpenGPS means that the OpenGPS project is dedicated to developing open source GPS software for the GP2021 chipset, the most important of which is that the receiver source code is openly available.

The Zarlink GP2015/GP2021 chip set constitutes a quite old design compared to actual, commercially available chip sets, e.g., Sirf III [SiRF, 2005] and was introduced as GP1010/GP1020 by GEC Plessey Semiconductor in the early 1990's. However, GEC Plessey was acquired by Mitel Semiconductors in 1998and since 2001 belongs to Zarlink Semiconductors. Thus, the chip set is the only one commercially available that permit open and free published and documented access down to correlator level. The OpenGPS receiver is an implementation for a Peripheral Component Interconnect (PCI)-bus interface (Fig. 4.1, left) realized by Beyerle [2003] based on Kelley et al. [2002]'s OpenSourceGPS [Kelley and Baker, 2006a]. The OpenGPS receiver PCI-card is hosted in a standard PC which is controlled and operated by the real-time operating system RTAI-Linux.

The OpenGPS software receiver can operate in several acquisition modes. In navigation mode the receiver acts like a standard 12-channel GPS receiver which can track up to 12 GPS satellites simultaneously [Kelley and Baker, 2006b]. The navigation message is decoded and stored and the position of the receiver is calculated.

For altimetric measurements the OpenGPS receiver can operate in two different modes. In open-loop mono reflection mode all 12 correlator channels are tuned to the same GPS satellite. Thus, only one reflection event can be tracked at a time but it is possible to register the waveform of the reflected signal (Fig. 3.12). Operating in open-loop multi reflection mode the OpenGPS receiver allows the tracking of up to 8 direct GPS signals for navigation plus the autonomous open-loop tracking of up to 4 independent reflected GPS signals simultaneously. Hence, a maximum of 4 independent altimetric height measurements can be achieved simultaneously. In both reflection measurement modes, in-phase (I) and quad-phase (Q) correlation sums of each correlation channel are integrated over 20 msec and registered together with C/A-code and L1 carrier phases. During each reflection event the data time series are stored to hard disk at a rate of 50 Hz (every 20 msec).

Fig. 4.1: *Left: OpenGPS PCI-card with TTL logic interface board and Zarlink GPS receiver board attached. Right: Standard RHCP patch antenna mounted on a tilt- and turnable mount fixed to a geodetic tripod. The antenna is 54 mm in diameter and has a hemispheric field-of-view.*

DOI: 10.2312/GFZ.b103-08104

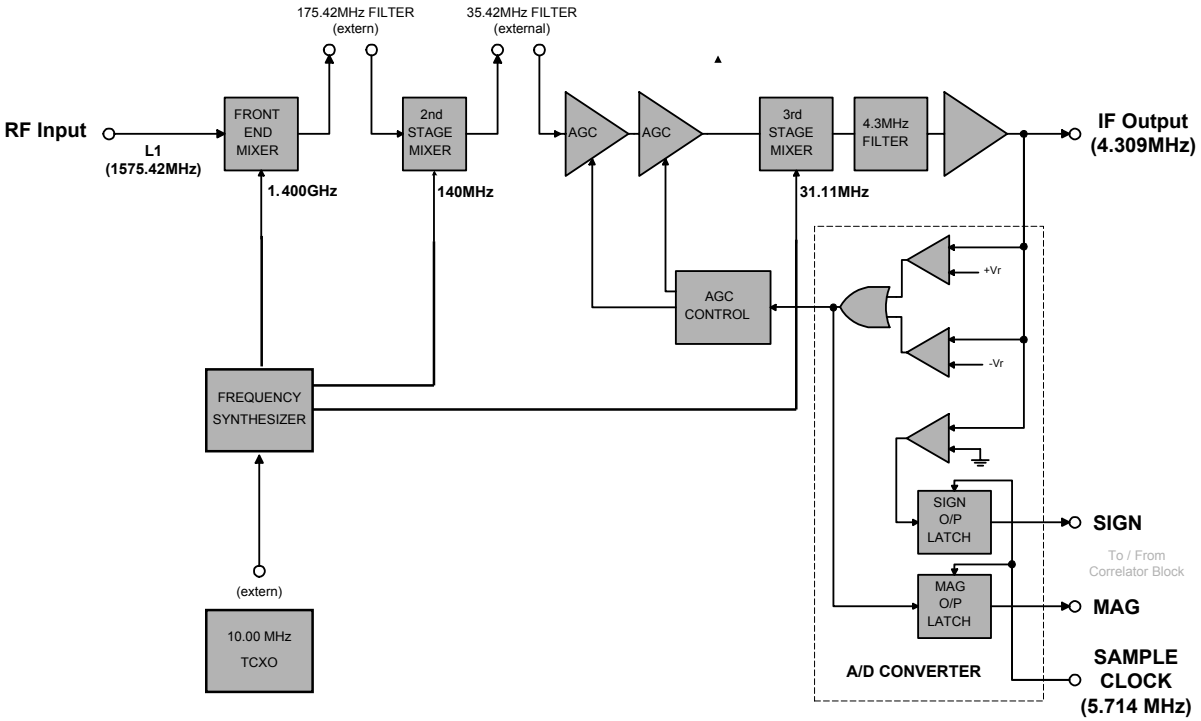

Fig. 4.2: *GP2015 RF frontend block diagram (after [ZARLINK, 2001])*

4.2 OpenGPS Receiver Hardware Design

The OpenGPS receiver hardware is based on a modified CMC Superstar GPS module. The unmodified SUPERSTAR is a complete 12-channel GPS OEM receiver that provides 3D navigation on a single compact board. The SUPERSTAR has the same architecture as the ALLSTAR which is based on the GEC Plessey GPS chip set. The 12-channel single-frequency (L1) GPS receiver board houses a GP2015 GPS receiver RF front end chip [ZARLINK, 2002a] and a GP2021 chip [ZARLINK, 2001] which is a 12 channel C/A code baseband hardware correlator. The ARM60 32-bit RISC processor chip, which usually controls the correlator chip and provides 3D navigation information, has been carefully unsoldered. The free pin connections at the ARM60 board are now used as communication interface between correlator chip and the OpenGPS software.

The next generation Superstar II GPS module [NovAtel, 2005] uses the GP4020 GPS baseband processor [ZARLINK, 2005]. The GP4020 combines the GP2021 correlator with an ARM7 microprocessor in a single device. Thus, with the GP4020 chip it is not possible anymore to access the correlator directly.

The free pin connections at the ARM60 board are used to connect the GP2021 correlator chip via a fast switching TTL logic interface to the PROTO-3 PCI prototyping board from Kolter Electronics (Fig. 4.1, left). The connection cables are twisted to gain better signal shielding. The PROTO-3 PCI card is working in a standard PC equipped with an Intel Pentium 4, 2.4 GHz CPU with 512 MB RAM and 120 GB hard disc. A single unmodified standard RHCP patch antenna (Fig. 4.1, right), namely the AT575-70C from AeroAntenna Technology Inc. (`http://www.aeroantenna.com`) with an integrated low-noise pre-amplifier with 4 dBic gain is used for reception of the direct and the reflected signal. The antenna is directly attached to a shielded HF-cable with a length of 5 m which is connected via a Sub-Miniature-A (SMA) female connector to the GPS receiver board.

4.2.1 GP2015 RF Front End

The GP2015 GPS receiver RF front end chip [ZARLINK, 2002a] receives the analog GPS L1 RF signal, converts it down to a lower frequency and digitizes the down-converted analog signal. Fig. 4.2 illustrates the signal flow. The RF input of the GP2015 chip receives the analog 1575.42 MHz GPS L1 signal and converts it in a threefold mixing, gaining and filtering process down to a 4.309 MHz

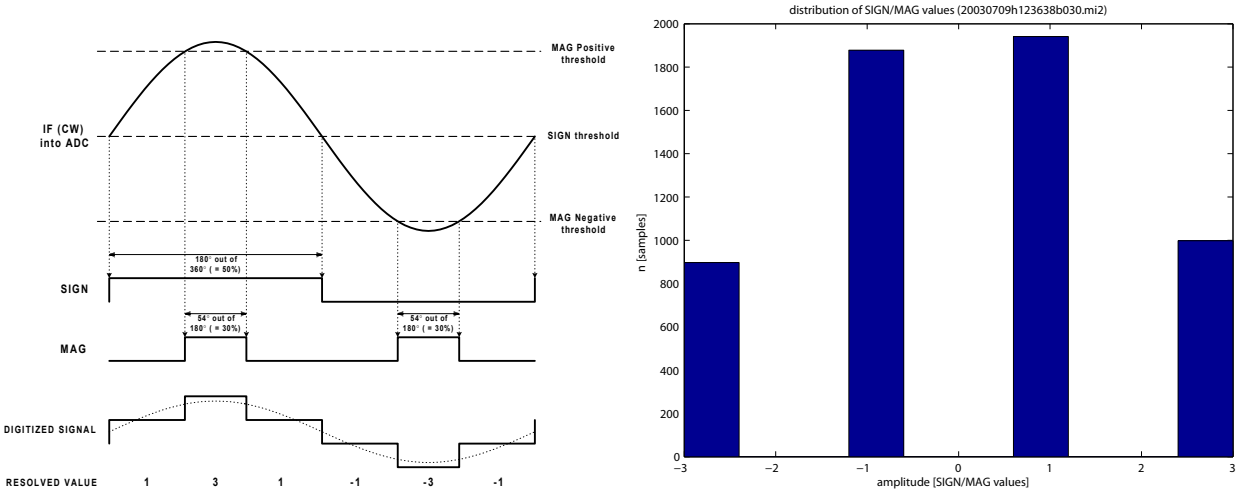

Fig. 4.3: *Right: Digitizing the analog signal with a 2-bit quantisizer (after [ZARLINK, 1999]). Left: Distribution of SIGN/MAG values of 2-bit raw GPS data (Fig. 2.3 on page 20) recorded by the COMNAV receiver which is also based on the GP2015 GPS receiver RF front end.*

Intermediate Frequency (IF). The RF signal is mixed with a lower frequency signal to produce a down-converted IF signal. All frequency signals are generated by a frequency synthesizer which is fed by an external 10.00 MHz Temperature Controlled Crystal Oscillator (TCXO).

For such a low-side mixing, a positive phase change of the RF signal results in a positive phase change of the IF signal. This triple-conversion design improves image rejection and permits user-designed filters to be installed between the conversion stages. Here a simple bandpass filter between the first and second stage and a Surface Acoustic Wave (SAW) filter between the second and third stage is used.

In a fourth down-conversion step the IF output is fed into a 2-bit quantisizer which provides Sign (SIGN) and Magnitude (MAG) outputs (Most Significant Bit (MSB) and Least Significant Bit (LSB)) as shown in the following table.

SIGN	MAG	Digitized Signal Values
0	1	3
0	0	1
1	0	-1
1	1	-3

The magnitude data controls the Automatic Gain Control (AGC) loop, such that on average 30% of the time the magnitude bit is set (Fig. 4.3). The SIGN and MAG data with an IF of 4.309 MHz are sampled with a frequency of 5.714 MHz. The so-called oversampling is a high-side mixing process and results in a digital 2-bit output datastream with an IF centered on 1.405 MHz. High-side mixing produces a phase reversal. Thus, positive phase changes of the input RF signal result in negative phase changes at the output IF, and vice versa.

4.2.2 GP2021 Correlator

The GP2021 chip [ZARLINK, 2001] is a 12-channel GPS C/A-code baseband hardware correlator which processes the down-converted and digitized GPS signal coming from the GP2015 receiver RF front end. In order to extract a specific satellite signal and determine time delay and Doppler values of the signal, the input signal is correlated with an internally generated replica of the satellite code to be received. Individual codes for each channel may be selected independently to enable acquisition and tracking of up to 12 different satellite signals simultaneously. The unit consists of a clock generator, a timebase generator, a sample latch, a set of 12 identical tracking modules, status registers and a data bus interface (Fig. 4.4).

DOI: 10.2312/GFZ.b103-08104

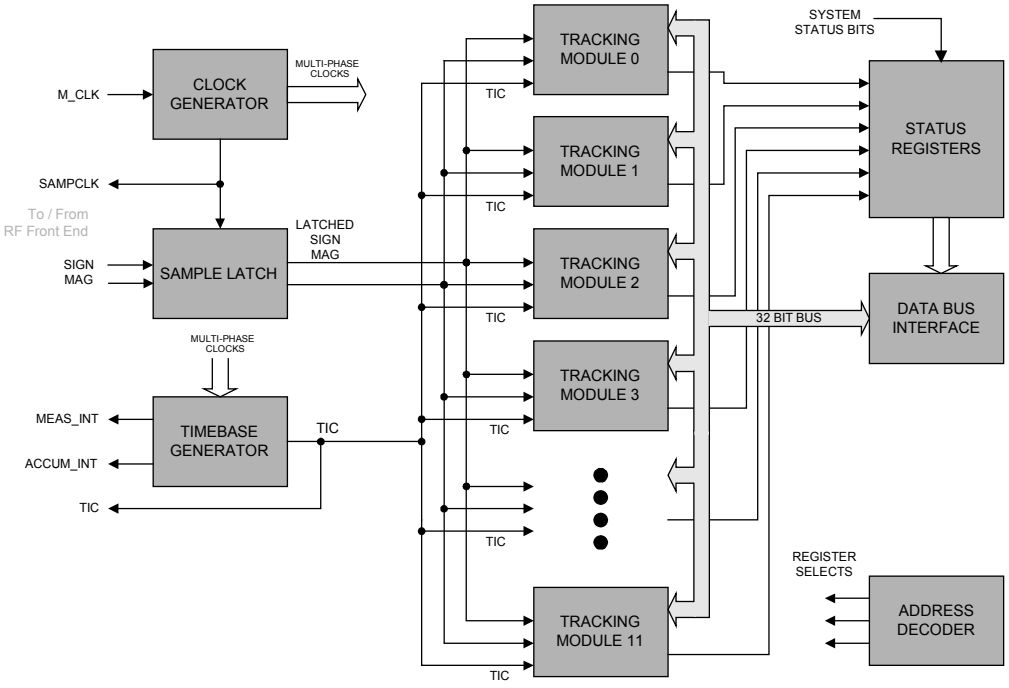

Fig. 4.4: *GP2021 Correlator block diagram (after [ZARLINK, 2002b])*

The clock generator delivers the necessary sampling frequency of 5.714 MHz for the GP2015 GPS receiver RF front end chip which is described in the previous section. The timebase generator produces four important timing signals: ACCUM_INT, TIC, MEAS_INT and TIMEMARK. The timing signal named ACCUM_INT is used to control data transfer between the tracking modules and the PC interface. The ACCUM_INT interrupt occurs every 0.50505 msec. The Time Interval Counter (TIC) interrupt is used to latch the measurement data of all 12 tracking modules at the same instant and is set every 0.0999999 sec (100 msec). A description of MEAS_INT and TIMEMARK can be found in ZARLINK [2001]. The sample latches synchronize the 2-bit input signal coming from the GP2015 RF frontend to the internal SAMPLECLK. The synchronized data are then distributed to the 12 tracking modules. The tracking modules consist of 12 identical signal tracking channels numbered CH0 to CH11. Each tracking channel can be individually programmed. The data bus interface controls the transfer of data between each tracking module connected to the internal 32-bit data bus and the external 16-bit data bus which is connected to the PCI bus. The OpenGPS receiver software directly controls the 12 signal tracking channels. The communication with the GP2021 chip is realized via the PCI bus by reading and writing into a set of about 100 status registers.

Fig. 4.5 shows a block diagram of a single tracking module. Here the final fifth down-conversion stage is realized. The synchronized 2-bit input signal is sampled by the software-controllable carrier Digital Controlled Oscillator (DCO) clock. The carrier DCO is used to generate a set of two digital 3-bit quantisized local oscillator reference signals. The two reference signals I and Q (see section 3.10) are orthogonal and bring the input signal to baseband in the mixer block. The frequency of the carrier DCO must be adjusted to react on Doppler shift and reference frequency errors. The nominal value of 1.405396825 MHz of the carrier DCO can only be set indirectly by altering the DCO frequency with a value stored into the 26-bit increment register (CH*_CARRIER_DCO_INCR). The smallest possible step in the carrier increment register represents 42.57475 mHz. This very fine resolution is required to ensure that the carrier DCO stays in phase with the satellite signal for an adequate time.

The C/A-code generator generates the selected Gold code [GPS SPS, Gold, 1967] for a GPS satellite. Two types of output are generated to give both a PROMPT and a TRACKING signal. The TRACKING signal can be set to four modes: EARLY (The EARLY correlator is fixed to one half chip before the PROMPT correlator), LATE (the LATE correlator is fixed to one half chip behind the PROMPT correlator), DITHERED (the generator toggles between EARLY and LATE every 20 ms) or EARLY-MINUS-LATE (the signed difference). Fig. 2.6 on page 23 illustrates the C/A-code correlation process with EARLY, PROMPT and LATE correlator. The code search pattern is simply a slewing of the PRN code generator by adding an extra chip of delay after each correlation sample. Thus, after 1023

DOI: 10.2312/GFZ.b103-08104

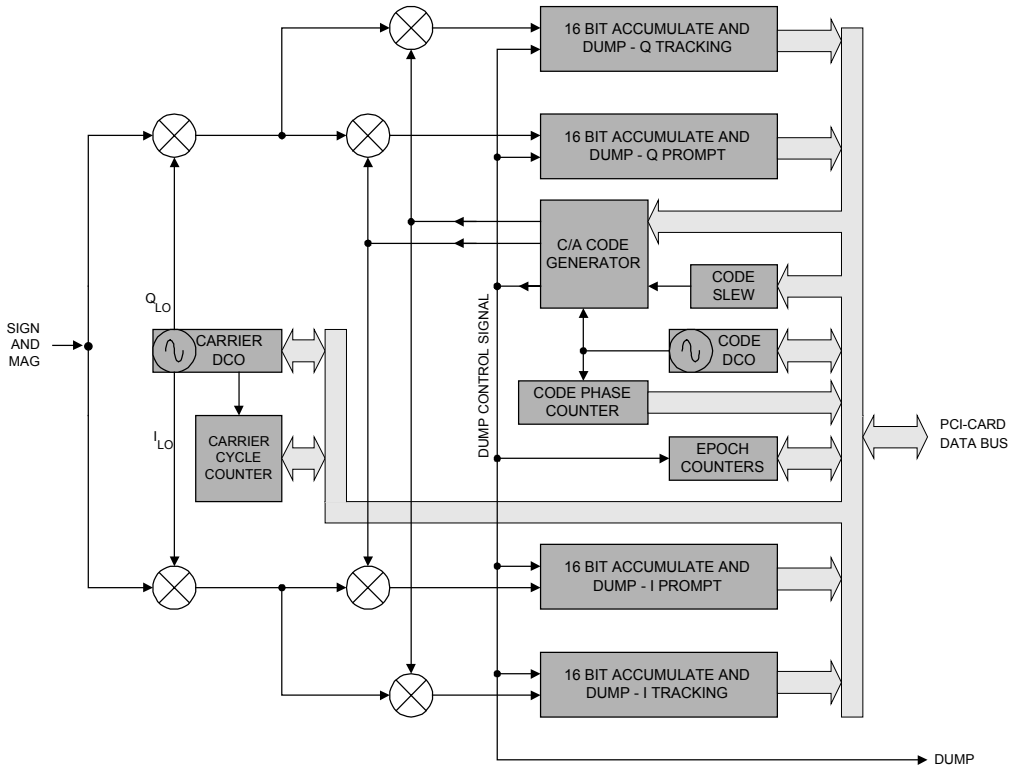

Fig. 4.5: *GP2021 Correlator: Single tracking module block diagram (after [ZARLINK, 2002b]) showing the 4 16-bit ACCUMULATE AND DUMP blocks Q TRACKING, Q PROMPT, I TRACKING, and I PROMPT, respectively.*

samples, every 1/2 chip in C/A-code space has been searched. At the end of every code sequence with a length of 1023 chips a DUMP signal is generated to latch the accumulated data for use by the signal tracking software. Each channel is latched separately, because the satellite signals are not received in phase with each other. Also the frequency of the code DCO must be adjusted in order to stay in phase with the satellite signal. Similarly to what has been previously described the nominal code frequency of 1.023000000 MHz has to be changed through the 25-bit increment register (CH*_CODE_DCO_INCR). The smallest possible step in the code increment register represents 85.14949 mHz. CH*_CODE_DCO_PHASE contains the ten more significant bits of the Code DCO phase accumulator sampled at a TIC event. It is an unsigned integer valid from 0 to 1023.

The 16-bit ACCUMULATE AND DUMP blocks (Q TRACKING, Q PROMPT, I TRACKING, I PROMPT) integrate the mixer output over a complete code period of nominally 1 ms. These 4 accumulators represent the correlation sums of the I and Q signals with the PROMPT and TRACKING codes over an integration time of 1 ms.

4.3 OpenGPS Receiver Software Design

The OpenGPS receiver software is written in C [Beyerle, 2003, Kelley et al., 2002] and compiled with GNU Compiler Collection (GCC), version 3.3. The software consists of several different subroutines which are time-critical. Thus, the software operates under the real-time operation system RTAI, version 24.1.10. RTAI is an open-source real-time extension to the Linux kernel. It is implemented as a set of patches which are designed to be applied to a standard Linux kernel released by Linus Torvald. The patches can be downloaded from `http://www.rtai.org` and the kernels can be found at `http://www.kernel.org`. The real-time optimized design of RTAI offers very low-latency interrupt responsiveness together with the possibility to execute threads at regular intervals necessary to execute the time-critical code of the OpenGPS receiver software. The time-critical processes are assigned to the real-time space while all other processes are assigned to the user-space of the RTAI operating system.

The following time-critical processes are assigned to the real-time space: The communication between the OpenGPS software receiver and the GP2021 correlator chip is performed every 0.505 msec by reading from and writing to the relevant GP2021 status registers via the PROTO-3 PCI data bus. Each correlator channel is updated with the relevant tracking parameters. Second-order PLLs [Tsui, 2000] are implemented. The code PLL parameters damp ratio, loop gain and bandwidth are set to 0.7010678, 0.01 and 2.0, respectively. The carrier PLL parameters damp ratio, loop gain and bandwidth are set to 0.7010678, 0.01 and 25.0, respectively. The OpenGPS receiver checks if a DUMP event has occurred in each correlator channel and collects the in-phase and quad-phase correlation sums of the PROMT and TRACKING (normally set to EARLY mode) correlator arm. A DUMP event occurs at each channel after 1 msec. The DUMP events of the 12 correlator channels are not synchronized. Every 100 msec at a TIC event the actual carrier and code phases are extracted for all 12 correlator channels simultaneously. The OpenGPS receiver extracts the time information from the sub frame headers of the decoded navigation message (preamble).

All non-time-critical processes are running in the user-space of the RTAI operating system. The tracking loops of each tracking module are updated according to the actual warm or cold acquisition state, confirmation state, pull-in state, normal tracking state or open-loop tracking state of the receiver, respectively. The navigation solution is calculated. The navigation message is decoded and almanac and ephemeris data are stored. The measured data is written to hard-disk. User commands are processed and data displayed on screen.

The data exchange and communication between the real-time and the user-space is realized with shared-memory regions and two First In First Outs (FIFOs) data queues. One FIFO transmits the navigation data, the other FIFO transmits the correlation data.

4.3.1 Open-loop mono reflection mode

Operating in open-loop mono reflection mode all 12 correlator channels – each consisting of a PROMPT and EARLY correlator arm – are tuned to the same GPS satellite. Thus, only one satellite signal and one reflection event can be tracked at a time, respectively.

One channel – declared as master channel – acquires, confirms and finally holds track of the direct signal of the target satellite. The target satellite has to be specified by the user by the associated PRN number at the beginning of a measurement. Similarly to normal tracking state the tracking loops are aligned with a navigation data bit and integrate during 20 msec and 1 msec to track C/A-code phase and carrier phase, respectively.

The 11 remaining channels – declared as slave channels – are synchronized to the master channel. Thus, the carrier and code tracking loops of the slave channels are synchronized to the master channel. All slave channel carrier loops operate with zero carrier phase offset with respect to the master channel. Each channel of the implemented hardware correlator offers 2 tracking arms, the PROMPT arm and the TRACKING arm. In open-loop mode the TRACKING arm is generally set to EARLY mode. Thus, the now called EARLY arm is 0.5 chips ahead of the PROMPT arm. The TRACKING mode cannot be set individually but only to all 12 TRACKING channels.

In open-loop mode the code loops of all slave channels are opened. In the code loop feed-back, however, $11 \cdot 2 = 22$ different delays are inserted with an adjustable mean offset delay toward the PROMPT arm of the master channel. In total a fixed time interval of 2 chips (about 2 msec) is covered around the given mean offset by the set of slave correlator arms. The 22 correlator arms are evenly distributed in the fixed time interval. The mean code offset delay of the 11 slave channels can be interactively changed by the user during the measurement. Thus, by recording the correlation power for different delays, the waveform of the correlation peak of the direct signal and of a reflected signal can be recorded.

Fig. 3.12 on page 40 shows such a waveform which was registered in open-loop mono reflection mode. In blue the correlation power of all channels is plotted with a mean offset delay of about 0.3 chips after the PROMPT of the direct signal. The typical triangular form of the correlation peak can be seen. The second set of data are plotted in red. The time interval covered by the slave channels is shifted with a mean delay of about 1.5 chips with respect to the direct signal. Only the PROMPT and the EARLY arm of the master channel are positioned at 0.0 chips and -0.5 chips delay, because

DOI: 10.2312/GFZ.b103-08104

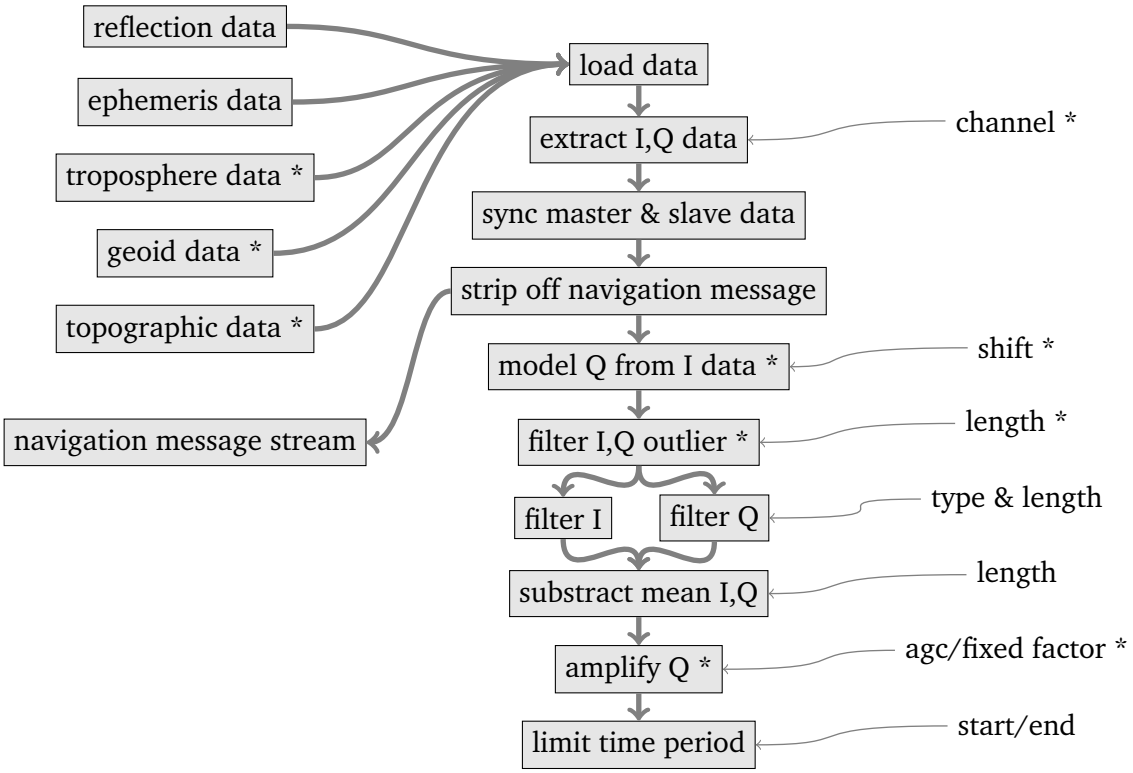

Fig. 4.6: *Level 0 and level 1 processing flow for output data type sdat3. Steps marked with * are optional.*

the master channel is still tracking the direct signal. A second correlation peak can be observed, the delayed reflected signal.

4.3.2 Open-loop multi reflection mode

The open-loop mono reflection mode has been extended for autonomous tracking of more than one reflection event. Operating in open-loop multi reflection mode the OpenGPS receiver allows tracking of up to 8 direct GPS signals for navigation and autonomous open-loop tracking of up to 4 independent reflected GPS signals simultaneously for altimetry.

The user specifies a reflection event mask which is specified by a satellite elevation and azimuth interval. From ephemeris data possible reflection events at the receiver location are predicted. In case a predicted reflection event hits the reflection event mask and the direct signal of the target satellite is already tracked by a channel the receiver automatically switches to open-loop mode. The tracking channel becomes the master channel and a second channel is set as slave channel. The carrier and C/A-code tracking loops are opened and synchronized to the master channel. The master channel continues to track the direct signal. The carrier loop of the slave channel operates with zero carrier phase offset with respect to the master channel. The delay of the reflected signal is calculated by an estimated reflector height and the known geometry. The delay is calculated from Eq. 3.4 and Eq. 3.51. In the code loop feed-back, however, the estimated delay of the predicted reflected signal is inserted. Up to 4 master-slave correlation channel pairs can be set to track and record 4 independent reflection events.

4.4 OpenGPS Data Processing

The processing software, named open2005, version 1.11, is used to extract and process the data recorded with the OpenGPS receiver. This software was developed in the frame of this study and is written in C++ and compiled with GCC, version 3.3 . Different output quantities can be extracted and processed, e.g. header information, 50 Hz navigation data stream, raw in-phase and quad-phase correlation sum data of each channel, different outputs for altimetric height determination. The

DOI: 10.2312/GFZ.b103-08104

following description is confined to the derivation of altimetric height profiles from interferometric carrier phase-delay observations.

For GPS altimetry the OpenGPS receiver can operate in two different modes, the open-loop mono reflection mode and the open-loop multi reflection mode. Hence, two different OpenGPS output data formats exist for OpenGPS reflection data. Version 1 contains the data output in case the receiver operates in mono reflection mode (see section 4.3.1). The mono reflection mode was used during the Fahrenberg experiment and allows only one reflection observation at a time. The data format is described in D.1 on page 159. Version 2 is used in all follow-on experiments and contains the data output if the receiver operates in multi reflection mode (see chapter 4.3.2). The data format is described in section D.2 on page 160. Fig. 4.6 shows an overview of the level 0 and the level 1 processing flow which is described in more detail in the following sections.

4.4.1 Level 0

During level 0 preprocessing the different input data versions are converted to one shared data format. For data version 1 one slave channel has to be selected to accompany the master channel. Thus, the following processing chain can be applied to both data formats in the same manner.

4.4.2 Level 1

During the OpenGPS data registration process it can happen that master and slave correlation sum time series are not related to the same time tag. It is possible that there exists one sample offset between master and slave time series. Thus, master and slave channel data have to be synchronized. Therefore the 50 Hz navigation message is extracted from the first 5000 in-phase data samples from both data time series. The correlation sum between the master and slave navigation message is calculated three times, with a sample offset of n= 0, -1 and +1. The highest correlation value indicates the existing sample offset. In case of a sample offset n=1, one sample is stripped of at the beginning of the master data set and vice versa and synchronisation between master and slave channel data is achieved.

The navigation message is demodulated from the slave channel in-phase and quad-phase time series by multiplying each sample with the sign of the corresponding in-phase value of the master channel (Eq. 3.78, page 43). Only the in-phase and quad-phase time series of the slave channel are processed further on.

The delay of the reflected signal with respect to the direct signal depends on the geometry of receiver, satellite and reflector position. The delay of the slave correlator is set manually (mono reflection mode) or automatically (multi reflection mode) during the data recording. The receiver tracking loop sets and keeps the master correlator (with zero delay) to the correlation peak of the direct signal.

In case of a delay of the reflected signal near or larger than one chip length like in the Fahrenberg experiment the portion of the direct signal in the slave channel data is neglectable and both components, the in-phase and the quad-phase correlation sums can be directly used for calculating the phase according to Eq. 3.79. Fig. 4.7 illustrates how the interferometric pattern (top, panel D) caused by the reflected signal evolves with increasing code offset (top, panel A) of the slave channel. The data shown was recorded at Kochelsee on July 10, 2003, starting at 13:31:18 GPST. While the fraction of the direct signal in the in-phase component (panel B, blue curve) decreases with increasing code offset, the peak power and SNR of the frequency of the interferometric pattern increases. Beginning with a code offset of 1 after about 93 sec, the correlation energy of the direct signal drops to zero. The phase (top, panel C) starts to develop continuously according to the geometry which changes with time. Thus, the rotating phasor describes circular graphs which can be seen in the bottom graph of panel C.

In most ground-based experiments like, e.g., Mercure Hotel, Königsstuhl and Merzbachersee, the delay of the reflected signal is much smaller than a C/A-code chip length. Hence, the correlation energy of the direct signal superimposes the correlation energy of the reflected signal. In order to separate the energy of the direct signal from the desired reflected energy pattern the local mean

DOI: 10.2312/GFZ.b103-08104

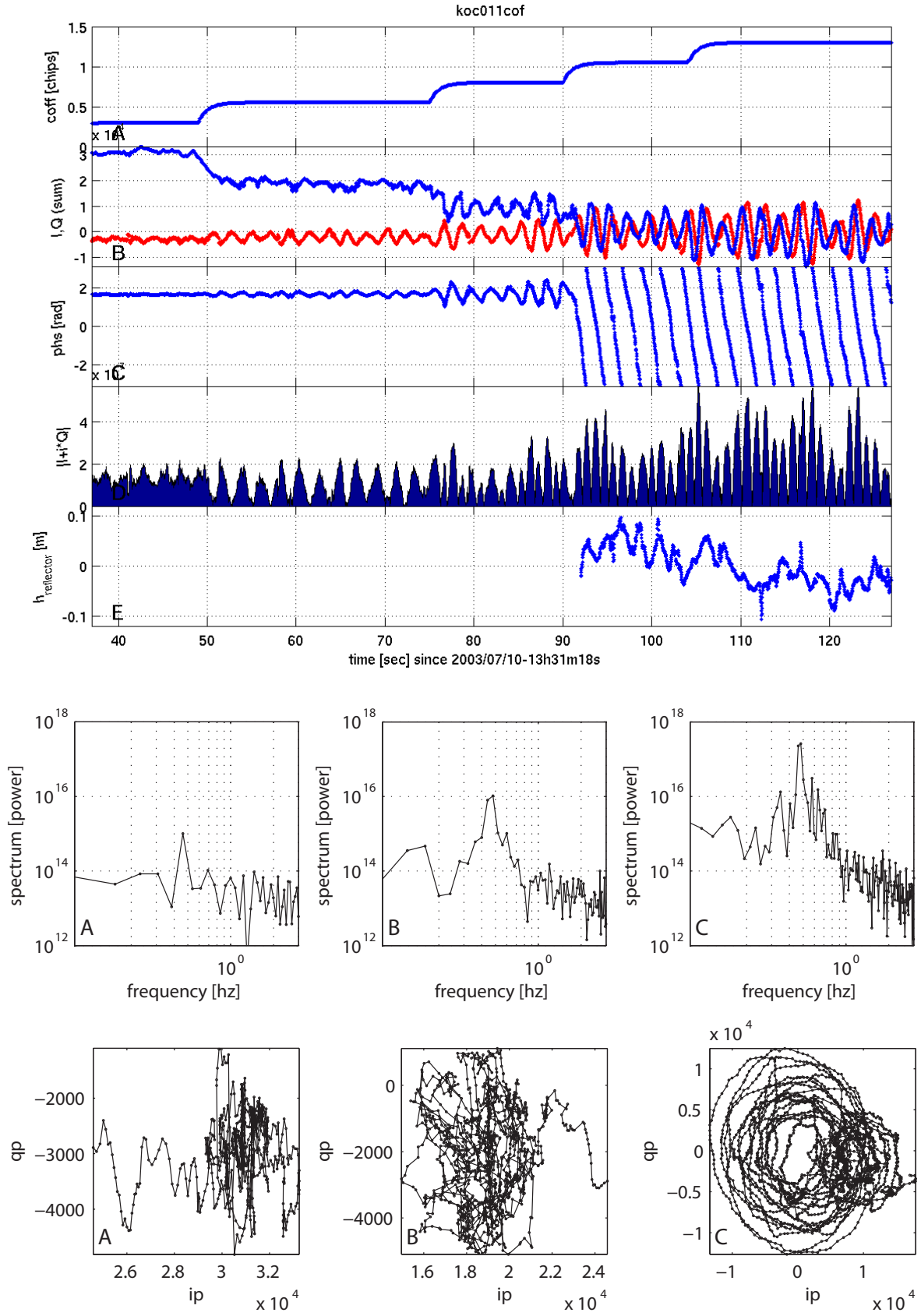

Fig. 4.7: *Reflection event at Kochelsee on July 10, 2003. Top: With increasing code offset of the slave channel (panel A) the correlation energy of the direct GPS signal decreases (see blue in-phase component (red quad-phase) in panel B). The phase starts to evolve (panel C) and the typical interferometric pattern can be observed in the amplitude of the recorded signal (panel D). Panel E shows the calculated and detrended height time series. Center: Panels A, B and C show the appropriate frequency spectrum of the complex correlation data during period 35–50 sec, 50–90 sec and 90–130 sec. Bottom: Panels A, B and C show a cross plot of I and Q during the same time periods as above.*

DOI: 10.2312/GFZ.b103-08104

energy of each in-phase and quad-phase component is calculated and subtracted. The filtering is realised by applying a running mean filter with a length of 1500 samples or 30 seconds to each in-phase and quad-phase component. As a result of this filtering the resulting correlation sums of both in- and quad-phase components oscillate around zero level.

The receiver tracking routine influences the recorded reflected signal at low elevations and small delays, respectively. The tracking routine is programmed to keep the in-phase component of the direct signal to maximum power and the quad-phase component near to zero. Thus, in case the reflected signal has a small delay, the quad-phase component data often contains no or only a weak fraction of the reflected signal. Different processing strategies have been tested to process the measured data (see Fig. 5.32–5.35 on pages 90–91) but best results can be obtained by the following method: The measured quad-phase data is not used because the tracking routine keeps the power of the quad-phase component near to zero. Thus, the quad-phase is modeled using the in-phase data which has maximum power and therefore contains the full reflection signal information. The quad-phase is simply modeled by copying and shifting the in-phase data with a fixed phase offset. The fixed phase offset has to be specified as input parameter of the processing. The phase offset Q_{shift} depends on the observed interferometric frequency f_{interf}. As the quad-phase per definition follows the in-phase with 90° phase offset, the shift (specified in samples) is calculated by

$$Q_{shift} = \frac{12.5}{f_{interf}}. \tag{4.1}$$

The direction or sign of the phase offset depends on whether the observed GPS satellite is rising or setting in relation to the fixed receiver position.

In case of sporadic data spikes or outliers, both in-phase and quad-phase data streams can be treated by applying a short running median filter of length 3–10 samples to each data set. The median filter is much more stable against outliers than the mean filter. The median $\tilde{X}_{\text{median}}$ of a dataset $(X_1, X_2, \cdots, X_n)$ which has been sorted according to their values is calculated after Press et al. [2002] with

$$\tilde{X}_{\text{median}} = \begin{cases} X_{\frac{n-1}{2}} & n \quad \text{odd} \\ \frac{1}{2}(X_{\frac{n}{2}-1} + X_{\frac{n}{2}}) & n \quad \text{even} \end{cases}. \tag{4.2}$$

The in-phase and quad-phase data streams can be independently filtered with a running mean or median filter with variable length. The length of the filters have to be adjusted carefully. In case of large filter lengths high frequency signal content can get lost smoothing the resulting height profile. Additionally further cycle slips/height jumps can be introduced. Fig. 4.8, Fig. 4.9, Fig. 4.10, and Fig. 4.11 illustrate the impact of the chosen filter and filter length. Fig. 4.8, top panel, shows the unfiltered in- and quad-phase data (panel A), unwrapped phase (panel B), reflection signal power (panel C) and derived reflector height (panel D). Fig. 4.8, bottom panel, and both panels of Fig. 4.9 show the impact of a running mean filter with a length of 10, 20 and 50 samples. Up to a filter length of 20 samples the noise in the height data drops. Beginning with a mean filter with 50 samples length a significant loss of high frequency content becomes obvious. For running mean filter lengths 0, 5, 10, 20, 50 and 100 samples the STD is given by 0.0306, 0.0285, 0.0279, 0.0271, 0.0244 and 0.0367, respectively. Fig. 4.10, and Fig. 4.11 show the impact of a running median filter with a length of 10, 20, 50 and 100 samples. A median filter of 20 or more samples length significantly transforms the in- and quad-phase data by flattening the high peaks of the measured correlation sums. Thus, the derived height data gets corrupted. For running median filter lengths 0, 5, 10, 20, 50 and 100 samples the STD is given by 0.0306, 0.0285, 0.0279, 0.0277, 0.0277 and 0.0403, respectively. Fig. 4.12 and Fig. 4.13 show the phasor, derived from the mean and median filtered in- and quad phase data, respectively.

While the mean filter shows good filtering results until the smoothing effect becomes too strong at a filter length of 50 samples, the median filter corrupts the data already starting at a 10 samples filter length. The corrupting effects of the median filter can be seen in the phasor plots of Fig. 4.13. In most conducted experiments a running mean filter with a length of 20 samples or 0.4 sec provides the best relation between noise filtering and high frequency information loss.

In order to minimize edge effects caused by the running mean/median filters the limitation of the dataset to a certain time interval is done after all filtering has been applied to the data.

DOI: 10.2312/GFZ.b103-08104

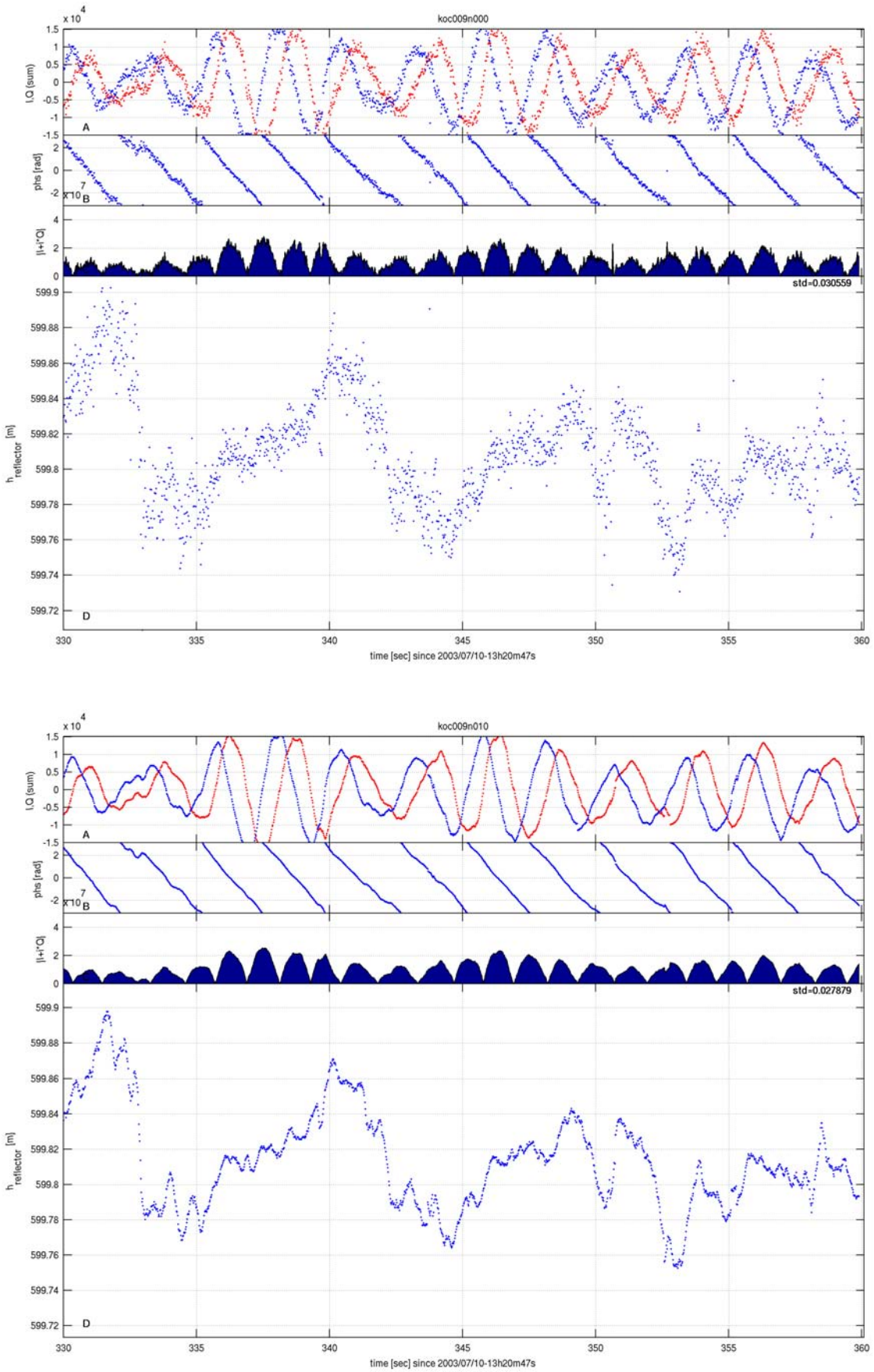

Fig. 4.8: *Unfiltered and mean filtered I,Q data (panel A), unwrapped phase (panel B), reflection signal power (panel C) and derived reflector height (panel D) for a mean filter of a length of 0 and 10 samples, respectively.*

DOI: 10.2312/GFZ.b103-08104

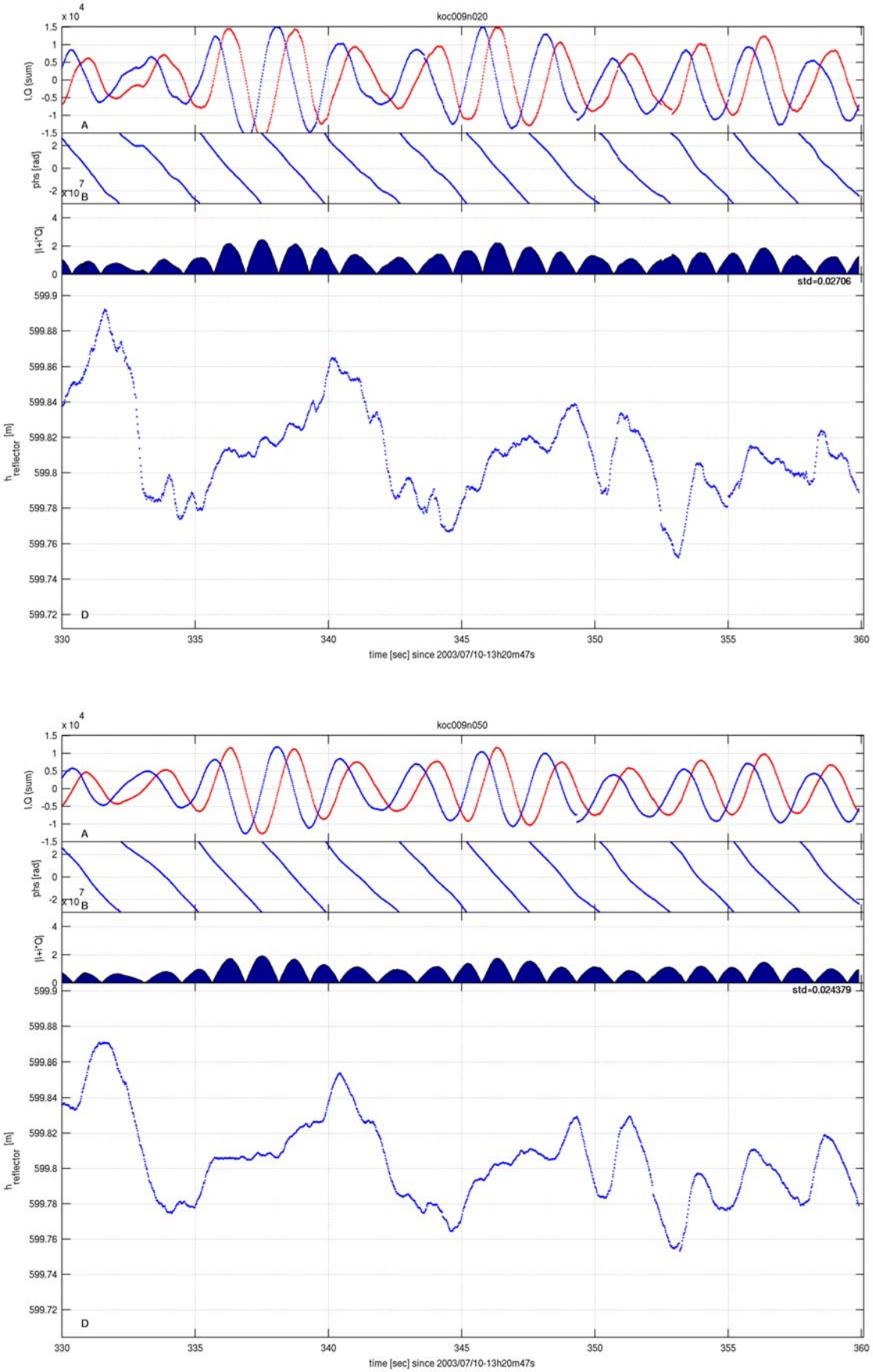

Fig. 4.9: *Mean filtered I,Q data (panel A), unwrapped phase (panel B), reflection signal power (panel C) and derived reflector height (panel D) for a mean filter of a length of 20 and 50 samples, respectively.*

DOI: 10.2312/GFZ.b103-08104

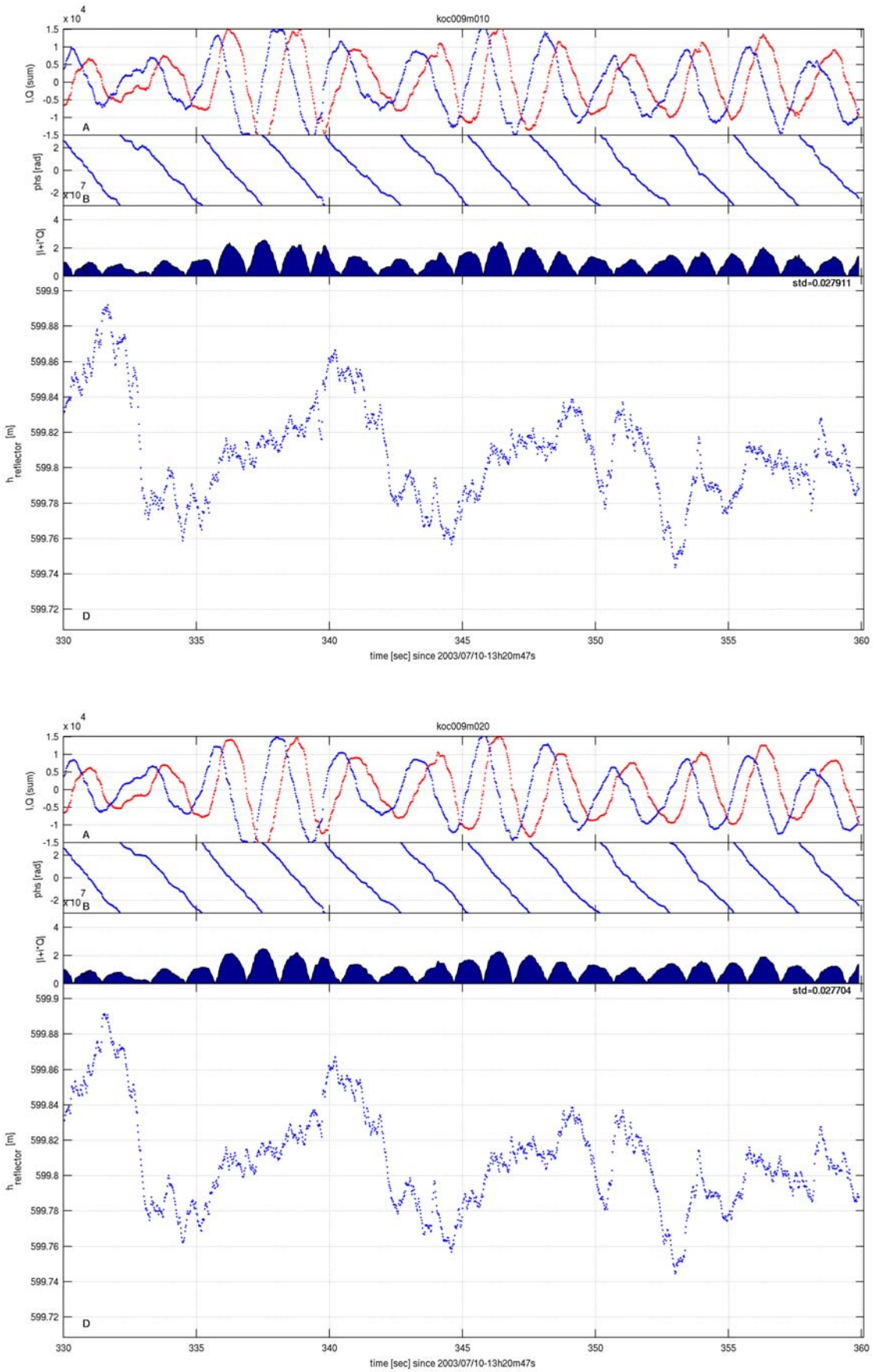

Fig. 4.10: *Median filtered I,Q data (panel A), unwrapped phase (panel B), reflection signal power (panel C) and derived reflector height (panel D) for a median filter of a length of 10 and 20 samples, respectively.*

DOI: 10.2312/GFZ.b103-08104

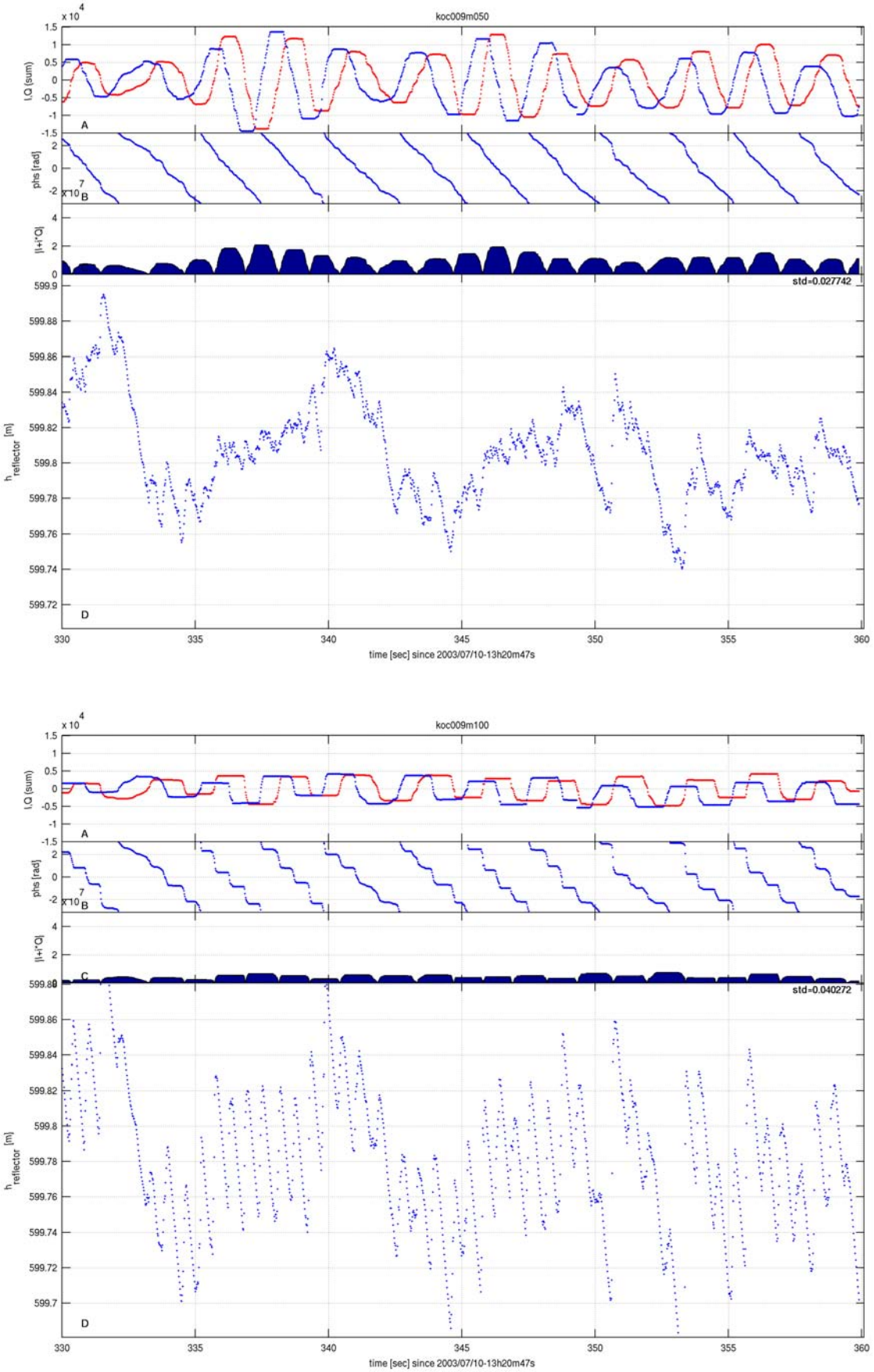

Fig. 4.11: *Median filtered I,Q data (panel A), unwrapped phase (panel B), reflection signal power (panel C) and derived reflector height (panel D) for a median filter of a length of 50 and 100 samples, respectively.*

DOI: 10.2312/GFZ.b103-08104

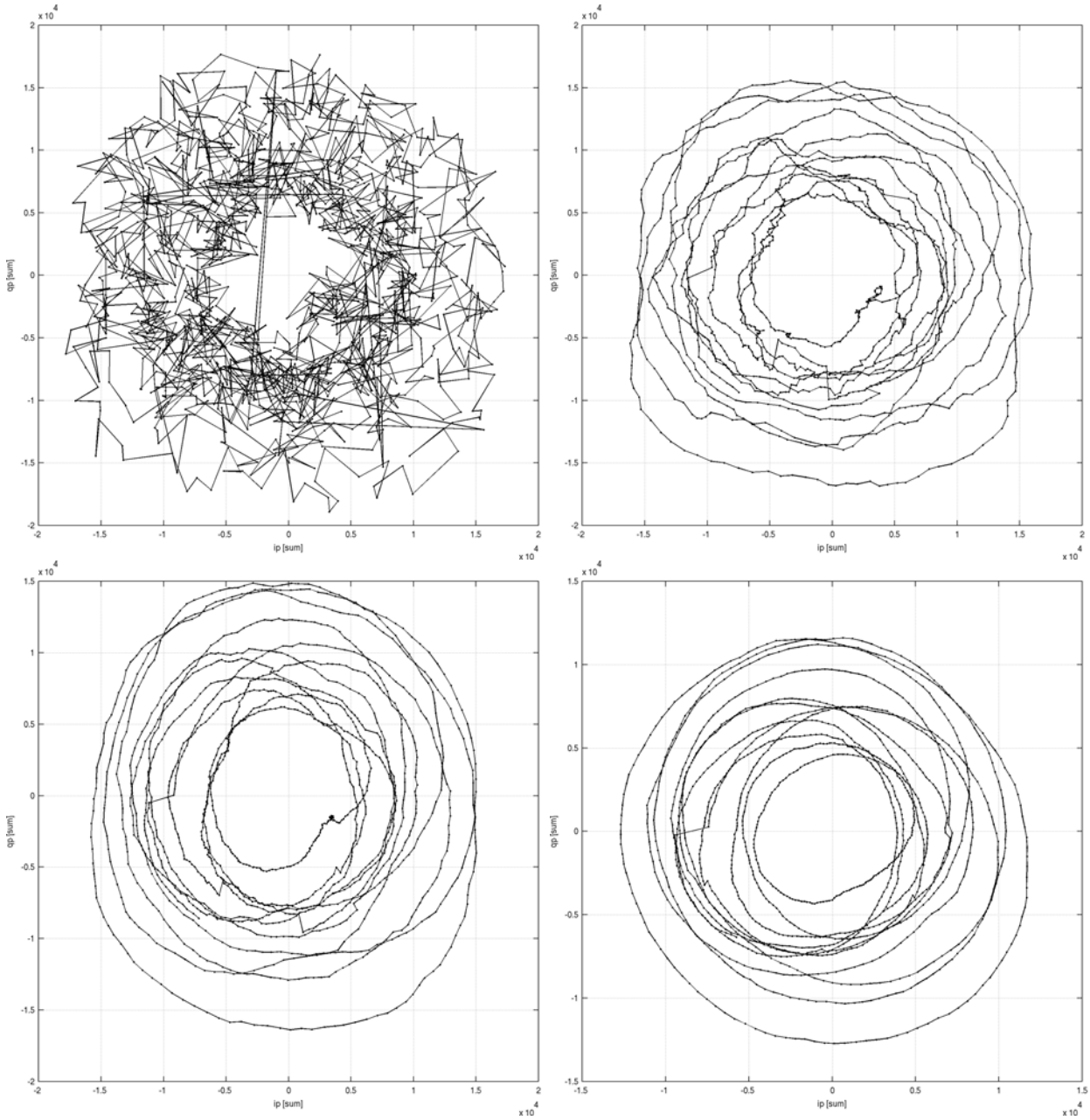

Fig. 4.12: *The different cross plots show the rotating phasor of filtered I,Q data for mean filters of a length of 0, 10, 20, and 50 samples. The filter length increases from top left to lower right panel.*

4.4.3 Level 2

The in-phase and quad-phase data of the slave channel is now filtered and prepared for the following processing steps. Fig. 4.14 shows an overview of the level 2 processing flow. The phase is calculated (Eq. 3.79) and unwrapped by adding $\pm 2\pi$, when the difference between consecutive values exceeds π, resulting in the accumulated phase. The optical path length difference δ between direct and reflected signal is calculated from the recorded phase data following Eq. 3.80.

The location of the specular reflection point is calculated in the next step. The position of the observed GPS satellite is calculated with the orbit parameters derived from the ephemeris file at the time according to the time tag of each recorded data sample. The elevation angle is calculated under which the GPS satellite can be observed at the receiver location. The elevation angle has to be corrected for the bending effect caused by the influence of the local troposphere (see section 4.4.5). The tropospheric deflection correction angle is interpolated from a lookup table which has been calculated beforehand. The lookup table is obtained from a geometric ray-tracing calculation of the specific satellite and time span using a local refractivity profile of the troposphere. The refractivity

DOI: 10.2312/GFZ.b103-08104

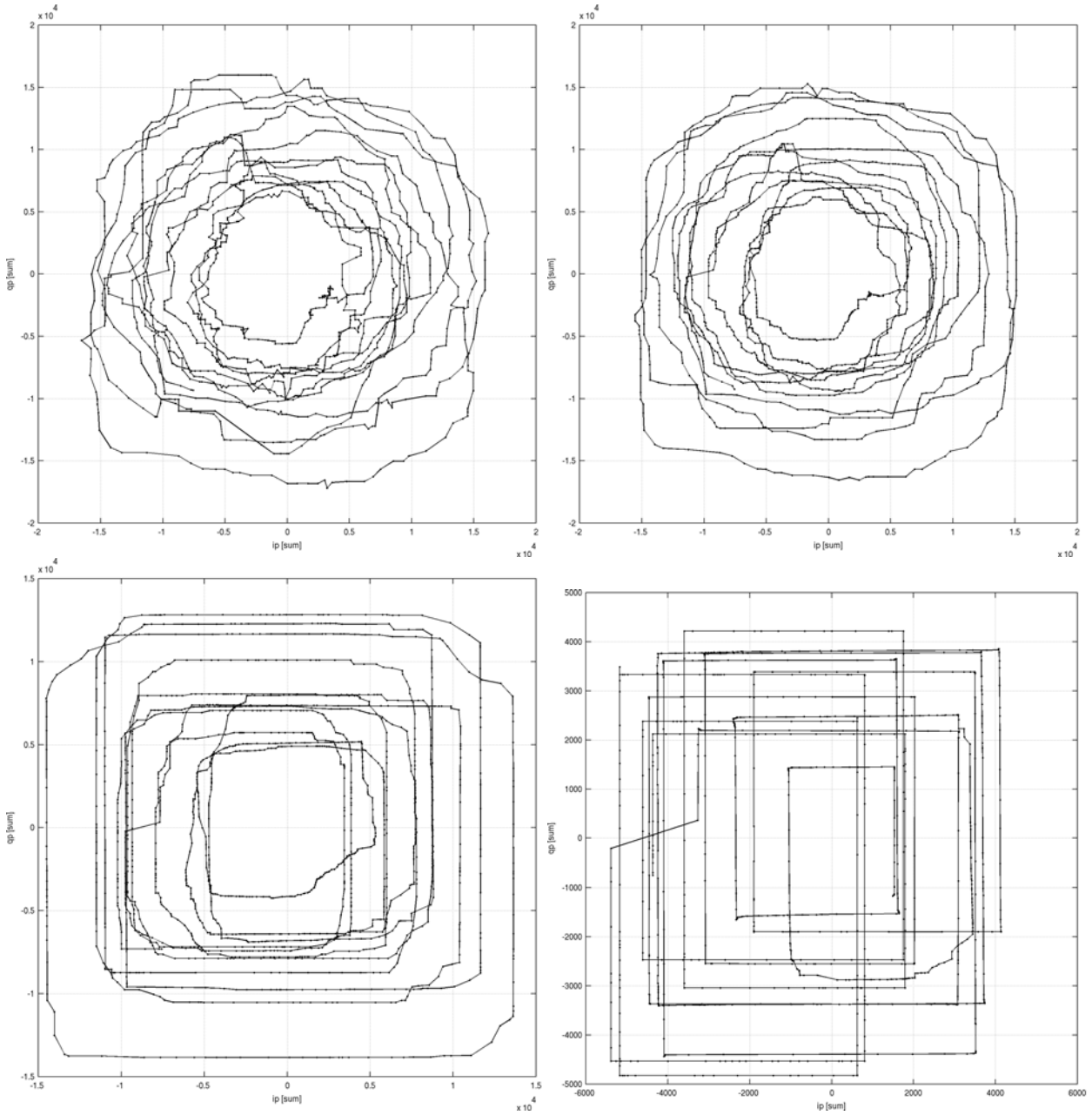

Fig. 4.13: *The different cross plots show the rotating phasor of filtered I,Q data for median filters of a length of 10, 20, 50 and 100 samples. The filter length increases from top left to lower right panel.*

profile is obtained from the nearest local subset of the global ECMWF dataset at 12:00 GPST of the day of the data recording, as most reflection data recordings in this study took place during daytime. In other cases the ECMWF data sets can be confined to the appropriate time of the data in steps of 6 h.

From the known receiver position and the estimated constant reflector height a first estimate of the location of the reflection point is calculated assuming a spherical Earth (see section 3.6). A reflector slope correction is performed (see section 4.4.4). The appropriate geoid correction values at the reflection point location are interpolated bilinearly from the preloaded geoid grid data. Optionally, topographic correction data can be derived in the same manner from a defined topographic grid data file. The location of the reflection point is calculated again, but now with geoid and optional topographic corrections applied to the estimated reflector height profile. While geoid heights vary only within the range of several centimeters in a small area, the height estimate of the reflector itself can vary in the range of several meters. Thus, the position of the reflection point can vary, especially the distance to the GPS receiver which has to be kept in mind when analyzing the resulting height profiles.

DOI: 10.2312/GFZ.b103-08104

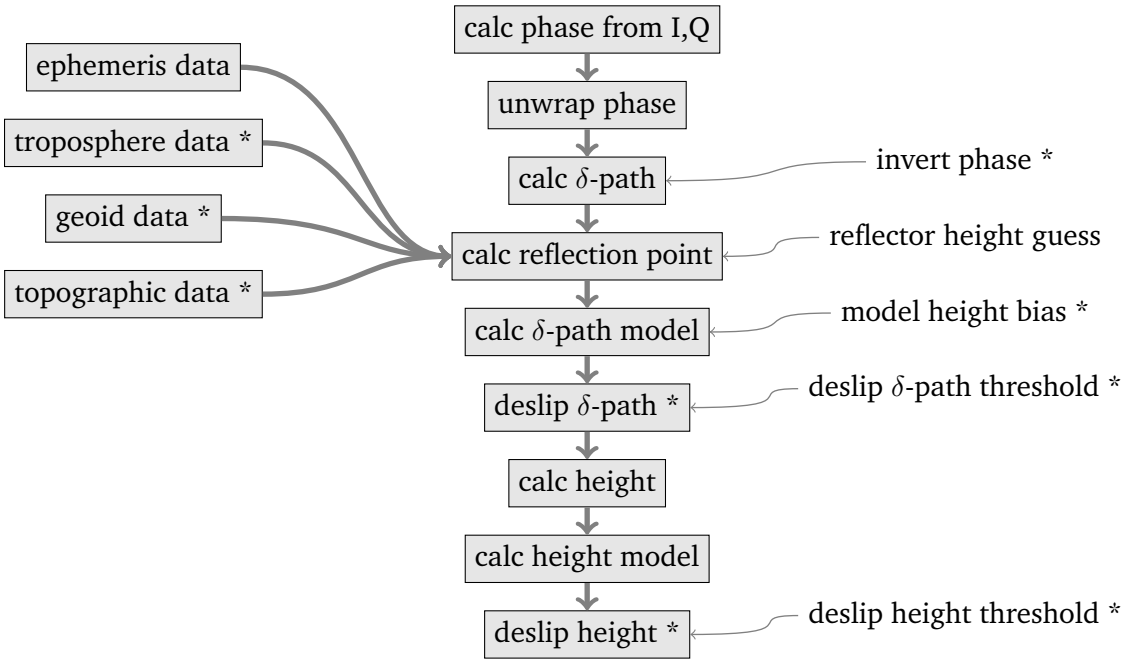

Fig. 4.14: *Level 2 processing flow for output data type sdat3. Steps marked with * are optional.*

A model optical path length difference δ_m can be calculated for each data time tag from Eq. 3.73 and the established geometrical situation. The same troposphere and geoid corrections are applied to the model data δ_m as to the measured data δ. This is done because the model is used later on as a guiding model to handle cycle slips in the real data.

Different to the direct GPS signal, the reflected GPS signal passes two times the atmospheric layer which is situated between the reflector height and the location of the GPS receiver. This lower atmospheric layer introduces an additional delay to the reflected signal which has to be corrected for. This additional delay can cause an additional optical path length of about one meter (see Fig. 5.25). The additional delay is estimated by comparing the optical excess path caused by the local troposphere at the height of the receiver and of the reflector. The optical excess path length is obtained for both heights from a geometric ray-tracing calculation of the specific satellite and time span using a local refractivity profile of the troposphere. The difference between the excess path length at the height of the reflector and at the height of the receiver is taken and stored into a lookup table for every calculated time interval. This additional tropospheric path correction can be optionally applied to the measured and model optical path length differences δ and δ_m. The path correction is applied to the data with factor two because the reflected GPS signal passes two times through the lower atmospheric layer as described above.

The optical path length difference δ is analysed for data jumps or cycle slips. Two methods can be applied to the δ data set. The first method relies on the data itself and compares the actual δ value with the mean value of the preceding and following data block of 20 samples or 0.4 seconds length. In case the difference exceeds the user defined threshold, the necessary amount of multiples of the full carrier wave length λ_{L1} is applied or subtracted from the actual δ value. The threshold factor itself can be given in fractional parts (threshold factor$*\lambda_{L1}$) in order to control the sensitivity when applying slip corrections. In contrary to the threshold factor the applied corrections itself are always applied in multiples of full carrier wave lengths

$$\delta_{deslipped} = \delta \pm (n_{\text{slip}} * \lambda_{L1}). \tag{4.3}$$

The second method compares the measured optical path length difference δ with the modeled path difference δ_m. In case the difference exceeds the user defined threshold, the necessary amount of multiples of the full carrier wave length λ_{L1} are applied or subtracted from the actual δ value. Again the threshold factor itself can be given in fractional parts to allow controlling the sensitivity when applying slip corrections. As mentioned in the first method, the applied corrections itself are always applied in multiples of full carrier wave lengths. The wavelength λ_{L1} is corrected for the actual L1

DOI: 10.2312/GFZ.b103-08104

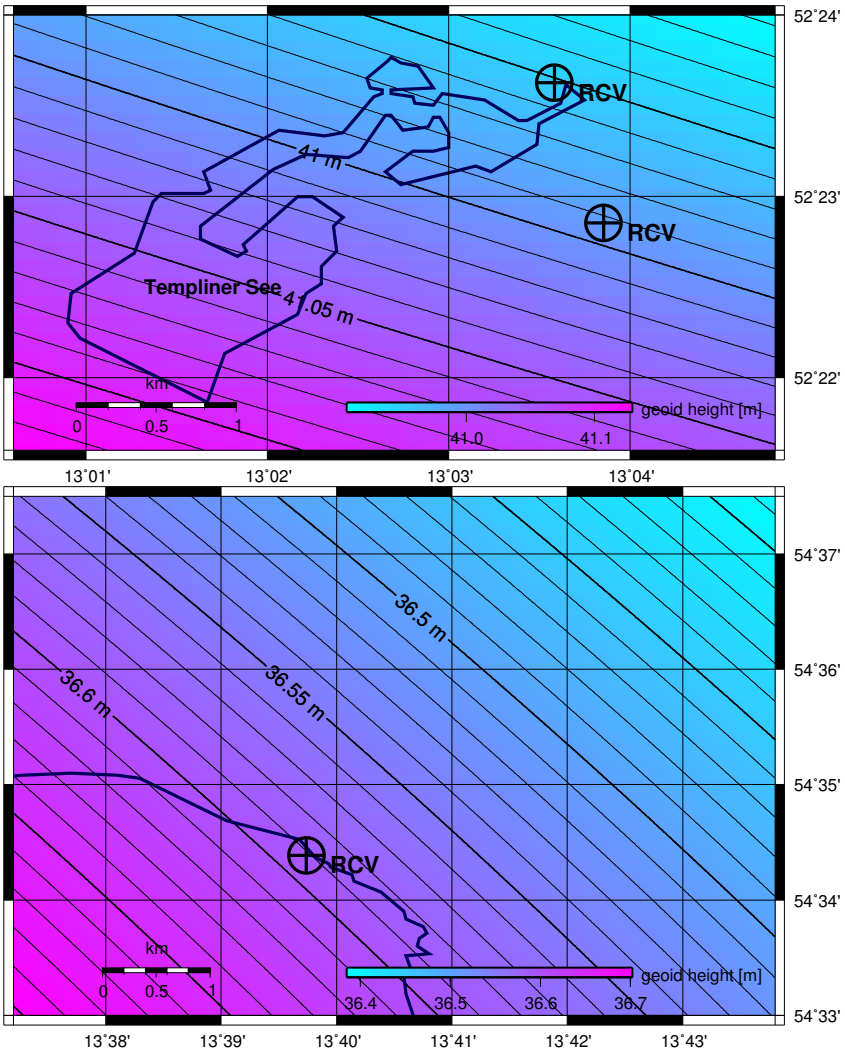

Fig. 4.15: *Height anomalies are shown for the locations Potsdam (Mercure Hotel) and Königsstuhl.*

carrier Doppler frequency. Method 2 showed the best results in the experiments and much longer profiles could be handled with method 2 compared to method 1 (compare Fig. 5.19 and Fig. 5.11).

The height $h(t)$ is normal to the tangent plane of the local specular reflection point and is calculated with Eq. 3.83 for each recorded and corrected δ datum. The height $H(t)$, which is related to the unrotated coordinate system, is calculated by solving Eq. 3.85. Optionally, the appropriate geoid height correction is applied to each height datum.

For comparison, an appropriate model height is calculated from the modeled optical path length difference δ_m. This time δ_m is calculated without applying geoid or tropospheric corrections to the model. Optionally, the model height can be modulated with a user-defined frequency and amplitude.

4.4.4 Reflector Slope Correction

Relative height changes of the specular reflection point can be derived from GPS carrier phase-delay observations using GPS altimetry with L1 interferometry. In order to derive an absolute height profile of the reflector and applying the detrending method described in 3.12, the reflecting surface has to be flat or a known surface slope has to be corrected.

During processing an additional height offset can be added to each height datum of the height profile, depending on the geo-location of the specular reflection point. The height corrections are derived from a 2-dimensional Network Common Data Form (netCDF) [Rew et al., 1997] grid file. The user-specified grid file can contain topographic data obtained from other sensors, or as in this study, geoid data. The slope of the known geoid data is used in this study to detrend the mean slope of the

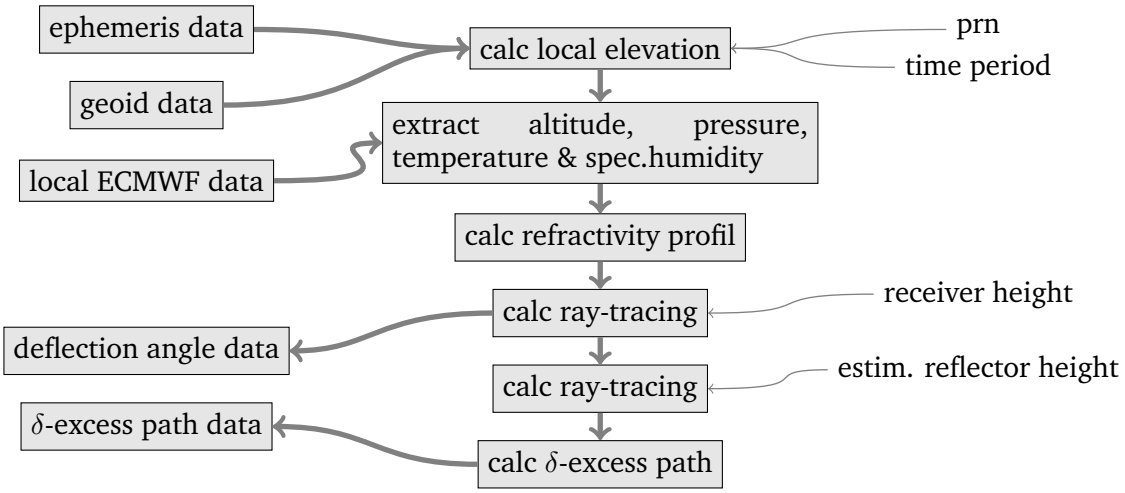

Fig. 4.16: *Calculation of the local tropospheric deflection*

water surface which follows the geoid. Fig. 4.15 shows height anomalies for the locations Potsdam (Mercure Hotel) and Königsstuhl and are calculated from the EIGEN-CG01C gravity model [Reigber et al., 2006]. Fig. 5.23 on page 83 shows height anomalies for the Fahrenberg location which are calculated from a local geoid model of Gerlach [2003].

4.4.5 Tropospheric Refraction Correction

Signal attenuation, scintillation and delay are caused by the local state of the troposphere. Additionally, these effects vary with elevation angle of the observed GPS satellite because lower elevation angles lead to a longer path length through the troposphere between satellite and receiver. The effect of tropospheric refraction has to be corrected for. Otherwise the delay caused by the troposphere results in an additional height signal superposed on the measured altimetric height profile. The tropospheric effect is a function of local temperature, pressure and humidity.

A geometrical ray-tracing analysis (Beyerle and Hocke [2001], G. Beyerle, personal communication) is performed to calculate the influence of the troposphere on the bending angle and the optical path lengths of direct and reflected GPS signals. Tropospheric correction look-up tables are generated for each single reflection event which state, in GPS time, every 10 sec the estimated deflection angle and excess optical path caused by the troposphere. GPS time is given in GPS weeks and Time of Week (TOW). The processing flow of the ray-tracing analysis is shown in Fig. 4.16. The ray-tracing simulation utilizes GPS orbit parameters calculated from ephemeris data (ftp://cddisa.gsfc.nasa.gov) and geoid data to calculate the geometry of transmitter and receiver and the local elevation. From the global ECMWF data set, as provided for the CHAMP/GRACE processing, a subset is extracted (T. Schmidt, personal communication) which covers the receiver location and observation time of the reflection event. From the ECMWF data subset the values of pressure, temperature and specific humidity are extracted as function of altitude. From pressure and specific humidity the partial pressure of water is calculated. The dry pressure is calculated from the difference between pressure and the partial pressure of water. Now a refractivity profile can be calculated as function of temperature, dry pressure and the partial pressure of water at the receiver location and observation time. Fig. 4.17 shows a temperature (panel A) and refractivity height profile (panel B) at the Fahrenberg location. The refractive index field is assumed to be spherically symmetric with respect to the center of the Earth surface curvature. Ray-tracing calculations yield the troposphere-induced excess optical path length (panel C) and deflection angle (panel D) as a function of satellite elevation. The two point boundary value problem of finding the ray originating from the GPS satellite and reaching the position of the receiver within a predefined radius is solved numerically by Newton-Raphson iteration [Press et al., 1992]. Panel E of Fig. 4.17 illustrates the correlation between excess optical path length and deflection angle (panel E.). The results from ray-tracing analyzes are compared to the simple troposphere models which are described in Eq. 2.7 and Eq. 2.8. Panel F of Fig. 4.17 shows that the largest model differences are expected at elevations below 7°.

DOI: 10.2312/GFZ.b103-08104

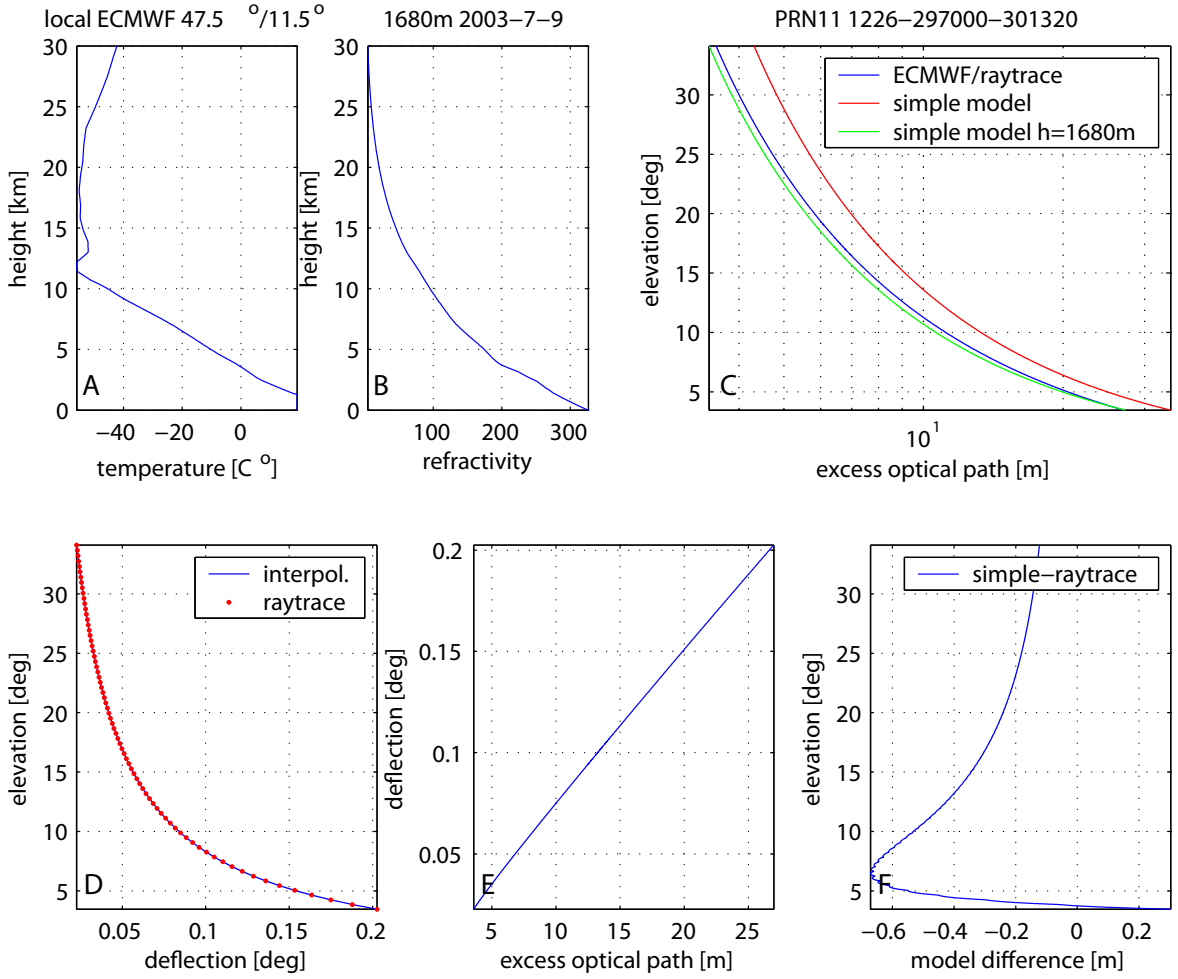

Fig. 4.17: *Tropospheric corrections calculated from ray-tracing analysis with local ECMWF data at the Fahrenberg location.*

An additional tropospheric correction parameter is generated for the tropospheric correction look-up table. In comparison to the direct GPS signal the reflected signal travels twice through the atmospheric layers between the height of the reflecting surface and the receiver location. This lower layer with a thickness equal to the height of the receiver above the reflector introduces an additional delay of the reflected signal which has to be corrected for. The excess optical path caused by the troposphere is calculated at the height of the reflector and compared to the values calculated at the height of the receiver. The resulting excess optical path differences are plotted for data observed at the Fahrenberg location in Fig. 5.25 on page 85 (panel C and panel D).

Toward grazing angles more complex mechanisms begin to play a role. Beside the already discussed tropospheric refraction, shadowing (see Fig. 5.28), diffraction, multiple scattering, and trapping by atmospheric ducts and waves influence the signal propagation [Valenzuela, 1978]. These effects must be taken into account in future studies, but are not considered in this study.

DOI: 10.2312/GFZ.b103-08104

5 Experiments

5.1 Motivation

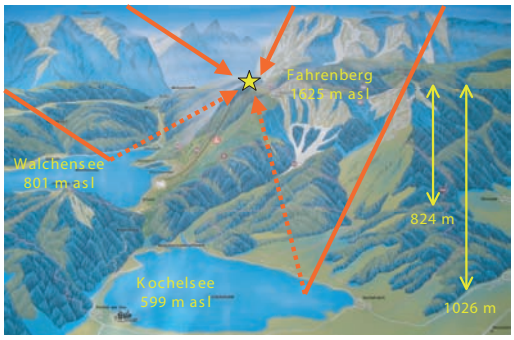

Fig. 5.1: *The OpenGPS receiver is situated on the mountain top of Fahrenberg. From the receiver location an unobstructed view is available to lake Kochelsee to the north and lake Walchensee to the south.*

The Fahrenberg experiment verifies the proof-of-concept of GPS altimetry with the OpenGPS receiver using carrier phase-delay observations of reflected GPS signals. At the Fahrenberg location the receiver is situated 824 m and 1026 m above the lakes Walchensee and Kochelsee (Fig. 5.1). Hence, the signals, which are reflected at the lake surface, arrive at the receiver with a delay greater than 1 C/A-code chip (Fig. 3.2). Thus, the signals of the direct and reflected signal can clearly be distinguished in the received waveform (see Fig. 3.12). Additionally, the reflected signal strength is high because both lakes show smooth water surface conditions (Fig. 5.7, 5.8). The OpenGPS receiver is working in open-loop mono reflection mode which allows to track single reflection events and register the reflected waveform.

In comparison to the Fahrenberg experiment the geometry of the Mercure hotel experiment differs significantly. The receiver is situated on the roof of the Mercure hotel. Due to the low observation height of about 63 m of the receiver above the Havel river water surface, the reflected GPS signals arrive at the receiver antenna only with a comparably small delay after the direct signal. Thus, the direct and reflected signal superpose each other. The data processing is enhanced in order to separate both signals. The new implemented OpenGPS receiver open-loop multi reflection mode was tested which allows an automatic registration of up to 4 reflection events in parallel.

In contrast to the experiments ”Fahrenberg” and ”Mercure Hotel” the reflecting water surface was not smooth anymore during the Königsstuhl experiment. At all days wave heights in the range of the observation wavelength λ_{L1} and larger could be observed (Fig. 5.43 to f-waterpics-koe5). The Königsstuhl experiment evaluates at which conditions coherent phase-delay observations are possible at low observation heights. The influence of the troposphere at low observation heights is discussed.

Fig. 5.2: *Panoramic view on June 11, 2004 from Mercure hotel, Potsdam, looking in south direction*

DOI: 10.2312/GFZ.b103-08104

Fig. 5.3: *The OpenGPS experimental setup at the Königsstuhl location with GPS patch antenna mounted on top a 2.7 m high aluminum tripod 118 m above the baltic sea-surface.*

Fig. 5.4: *Merzbacher lake on August 6 (left) and August 9 (middle), 2004. Photo by Marc Roussel. Right: Bridge destroyed by the 2005 dam break. Photo by Alexander Petlenko.*

The glaciated Tianshan mountain chains of Kyrgyzstan represent the main reservoir of water supply of large parts of Central Asia. The regression of glaciation in this area, observed since the last two decades, caused changes in the dynamics of the glaciers. This led to an accumulation of mud slide and fl ow events and dam failures of glacier lakes in the Kirgisian high mountain area (Fig. 5.5). Especially at the largest glacier lake of Central Asia – the Merzbacher Lake – the number of dam failures rose dramatically and caused massive damage to the infrastructure of the regions situated below the glacier outfl ow. Recent dam failures occurred on: July 27/28, 2001; August 1/2, 2002; July 22/23, 2003; August 6/7, 2004 (Fig. 5.4) and July 13/15, 2005. During such a dam failure event the lake water level is expected to decline several meter. Thus, the massive height change of the water surface is expected to generate a noticeable height signal in the GPS signals which are refl ected from the lake's water surface. The experiment evaluates the potential of GPS refl ectometry and the OpenGPS instrumentation for a natural hazard monitoring scenario under rough environment conditions.

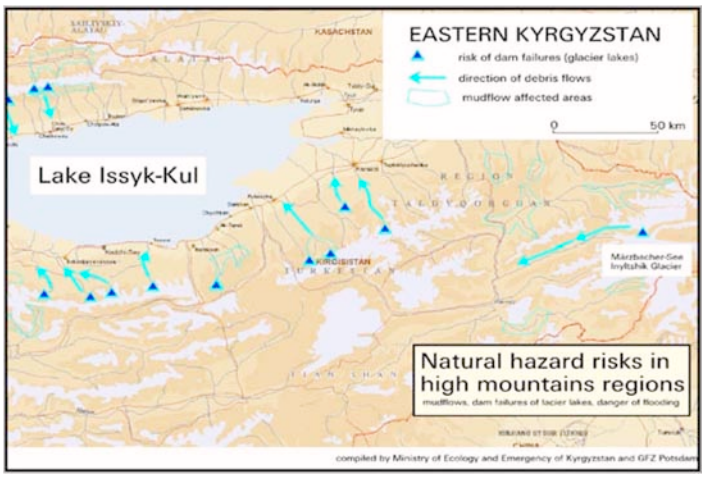

Fig. 5.5: *Risk of dam failures in eastern Kyrgyztan (H.-U. Wetzel, personal communication).*

For each experiment the experimental setup, data acquisition and data processing is described. The measured data are analyzed and discussed. The results of each experiment are summarized in Section 6.

DOI: 10.2312/GFZ.b103-08104

5.2 Fahrenberg Experiment

5.2.1 Experimental Setup and Data Acquisition

The experiment was conducted during daytime on 8–10 July 2003, 50 km south of Munich, Germany, in the Bavarian alpine upland at the mountain top of Fahrenberg (47.61°N, 11.32°E) at a height of about 1625 m above sea level. Mount Fahrenberg belongs to the Karvendel mountains and from the mountain top an unobstructed view is available to lake Kochelsee to the north and lake Walchensee to the south. Kochelsee has a surface area of 5.96 km^2, a maximum depth of 65.9 m, a maximum length of 5.1 km, a maximum width of 1.2 km, a volume of 184.7 $\cdot 10^6$ m^3 and a mean water level of 598.8 m above sea level. The higher situated, much larger and deeper Walchensee has a surface area of 16.27 km^2, a maximum depth of 189.5 m, a maximum length of 8.0 km, a maximum width of 2.0 km, a volume of 1324 $\cdot 10^6$ m^3 and a mean water level of 800.8 m above sea level [Wasserwirtschaftsamt Weilheim, 2004]. An artificial subsurface water channel (Kesselbergstollen) drains the Walchensee water into the Kochelsee. The hydro power is used by the Walchensee power plant which is situated in the south of the Kochelsee. The natural inflow of the Walchensee of about 3 m^3/s has been increased by artificial inflows from the Isar and Rissbach rivers by about 25 m^3/s and 12 m^3/s at a maximum. During winter months the winning of hydro power can cause the Walchensee water level to drop by a maximum of 6.6 m. During the measurement campaign the lake level raised only about 6 cm at Walchensee and dropped about 15 cm at Kochelsee. The lake level heights at Walchensee and Kochelsee (Fig. 5.6) are drawn from daily local tide gauge readings (Mr. Kremer, Walchensee Power plant, Kochel, Germany, personal communication). Calm water surface conditions could be observed from the lakes shoreline during morning and afternoon hours with estimated wave heights of not more than 5 cm throughout the whole day. Fig. 5.7 and Fig. 5.8 show photos from the surface conditions at Kochelsee and Walchensee, respectively.

Every day the single RHCP patch antenna was remounted on a geodetic tripod in a height of about 1.93 m above the ground. The antenna was tilted about 45° toward the horizon. Following a schedule of predicted GPS reflection events, the receiver antenna was manually turned toward the lake surface of the Kochelsee or Walchensee. The OpenGPS receiver was working in open-loop mono reflection mode (see section 4.3.1) in which all 12 correlator channels are tuned to the same GPS satellite. The PRN number of the satellite has been manually set before the measurement was initialized. During measurement the code offset of the 11 slave channels was manually adjusted during measurement to the estimated actual time delay of the reflection event. The correlation sums of each channel together with code and carrier phases were stored to hard disk at a rate of 50 Hz until the OpenGPS receiver lost the tracking of the direct signal.

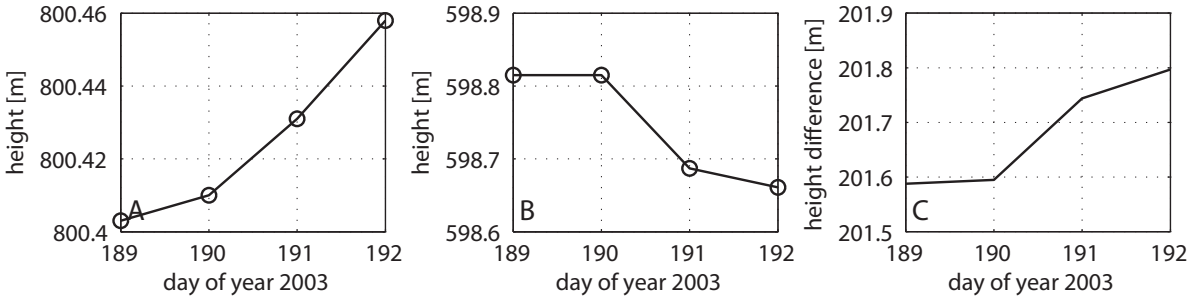

Fig. 5.6: *Daily lake level heights during the measurement capaign at Walchensee and Kochelsee from local tide gauge readings.*

5.2.2 Data Analysis and Discussion

During all 3 days several reflection events with different GPS satellites were observed from both lake surfaces, indicated by a clearly visible waveform (see Fig. 3.12 on page 40). With the antenna oriented in northeast direction (35° azimuth) reflection events took place only in the eastern region of the lake surface of Kochelsee (Fig. 5.9, left). The reflection events occurred in a distance between 4900–6000 m to the receiver at satellite elevations between 9.5° and 11°. With the antenna oriented

DOI: 10.2312/GFZ.b103-08104

Fig. 5.7: *Photos taken at Kochelsee (from top to bottom: at 08:40 on July 8, at 16:40 on July 9 and 08:30 on July 10, 2003) showing the lakes surface conditions in the morning and afternoon hours.*

DOI: 10.2312/GFZ.b103-08104

Fig. 5.8: *Photos taken at Walchensee (from top to bottom: at 17:00 on July 8, at 16:20 on July 9 and 17:10 on July 10, 2003) showing the lakes surface conditions in the morning and afternoon hours.*

DOI: 10.2312/GFZ.b103-08104

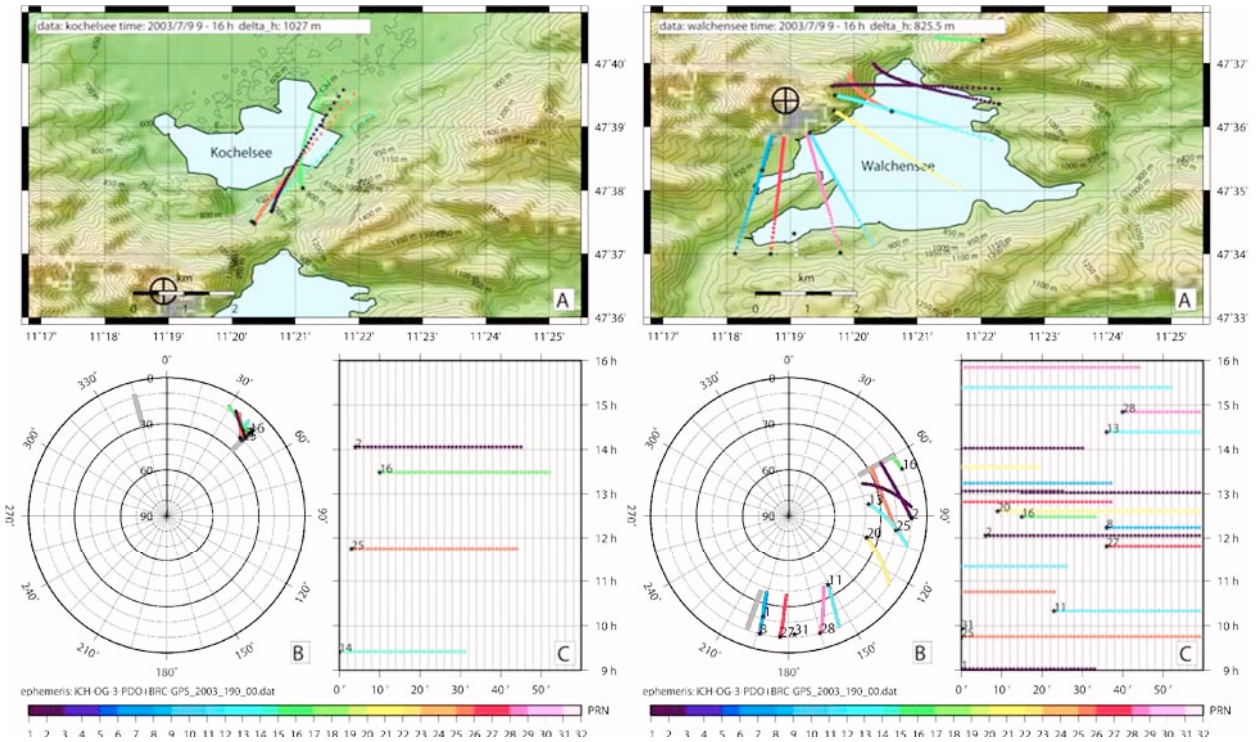

Fig. 5.9: *Schedule of reflection events at Kochelsee(left) and Walchensee (right): Panel A shows the possible location of specular refl ection points of visible GPS satellites (PRN) which can be observed on 9 July 2003 at the Fahrenberg receiver location (marked by a circle with a cross). Panel B shows the position of the satellites. Panel C shows the time schedule of satellite visibility. Calculations are based on ephemeris data.*

in south southeast direction (140° azimuth) several refl ection events could be observed from the Walchensee lake surface (Fig. 5.9, right). At Walchensee the refl ection events could be registered at distances between 1800–4600 m to the receiver at satellite elevations between 11° and 25°.

Fig. 5.10 illustrates a typical Fahrenberg measurement in open-loop mono reflection mode with unfiltered data. Fig. 5.10, panel A, plots the development of the code delay of each correlator channel with the measurement time. While the PROMPT and EARLY arms (see section 4.2.2) of the master channel constantly stay at 0 and -0.5 code chips offset, all slave channels are evenly distributed in the code offset space at about 60 sec after the measurement was initialized. Beforehand, in the time between 30–60 sec, each slave channel was independently set to the target code delay in a step-by-step adjustment. Beginning at 64 sec, the code offset of all slave channels was enlarged by the user in several steps in order to cover the code delay region of 1.5 chips, the estimated delay of the refl ection event. Fig.5.10, panel B reveals the measured waveform of the direct signal at 0 code chip delay and the delayed waveform of the refl ected signal at 1.5 chips. The peak power of the refl ected signal still reaches about 18% of the power of the direct signal. This shows that at elevations of about 10° a reasonable fraction of the LHCP refl ected signal can be obtained by theRHCP patch antenna used. Panels C and D of Fig. 5.10 show the behavior of the in-phase (blue) and quad-phas (red) correlation-sums for the 2 different slave channels 6 and 1. After pulling-in on a code offset of 1 chip, channel 6 starts capturing the interferometric pattern which evolves between the refl ected signal and the model replica of the direct signal. The amplitude of the pattern reaches at about 70 sec a maximum at a delay of 1.5 chips. With increasing delay – forced by the user – the amplitude of the pattern drops to noise level. Starting at 45 sec, channel 1 (Fig. 5.10, panel D) measures the in-phase and quad-phase correlation-sums of the direct signal. After the receiver locks the signal, the in-phase sum is kept to a maximum while the quad-phase component is hold to a minimum. At the moment the code offset of the slave channel is increased, the correlation energy of the direct signals linearly drops to zero at about 80 sec. Starting at a code offset of 0.5 chips or at 70 sec the interferometric pattern starts to evolve. This shows that the interferometric pattern occurs not only with maximum amplitude at the exact code delay of the refl ection but can be observed with an almost unreduced amplitude within a range of about +/- 1 code chip delay around the target delay. Thus, the channel observing the refl ection does not have to be positioned at the exact code delay.

DOI: 10.2312/GFZ.b103-08104

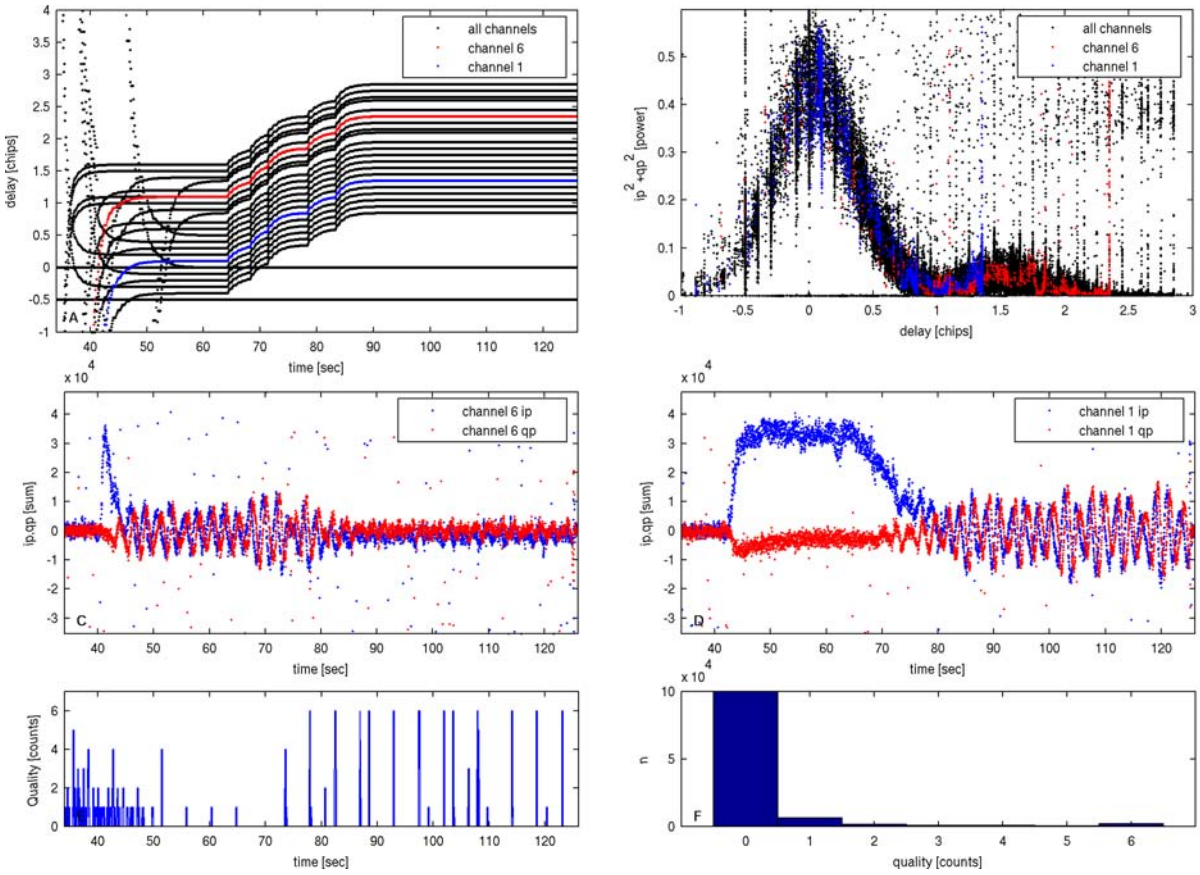

Fig. 5.10: *Typical raw in- and quad-phase data at the Fahrenberg location with antenna orientated at 35° azimuth to Kochelsee lake surface*

Nominally, 5 data samples are expected to be registered during a 100 ms long data interval. The number of data samples can deviate at the beginning of a measurement before every slave correlation channel is set to the defined code offset and at sporadic events throughout the whole measurement (Fig. 5.10, panel E). The first 10 sec of a data set are cut and 100 ms data blocks are deleted which deviate from the nominal 5 samples. The histogram in Fig. 5.10 illustrates the number of data blocks which deviate from 0 to 6 samples from the nominal 5 samples. Fig. 5.10 shows that most of the time 5 data samples (0 quality) are recorded.

Several outliers can be observed in all Fahrenberg data records. Most likely they are caused by overheating of the hardware correlator chip [S. Esterhuizen, University of Colorado, personal communication, 2003]. In a first attempt, outliers are removed in the following way: a predicted value is calculated by linear extrapolation from the last 3 recorded samples of in-phase correlation sums. If the difference between predicted and actual value exceeds a threshold (20000-22000), the extrapolated value replaces the measured actual value. The same is applied to the quad-phase data. Additionally cycle slips – sporadic height jumps of about λ_{L1} m in adjacent data points – can be observed in the calculated optical path length difference $\delta(t)$. The distortion of the data by cycle slips was minimized by applying the same method as above to $\delta(t)$. Continuous data segments without cycle slips were calculated up to a maximum length of 200 sec. Fig. 5.11 shows the achieved relative height time series of Kochelsee (A–C) and Walchensee (D–F). All observations were taken on different days, using the signals of PRN 16 and 25 at Kochelsee and PRN 11 and 20 at Walchensee. The height varies in a range of about $\pm$5 cm with a STD of about 3.1, 3.9 and 2.6 cm (Kochelsee) and about $\pm$2.5 cm with a STD of about 1.5, 1.7 and 1.4 cm (Walchensee).

The mean receiver height above the lake surface is not expected to change during the short analyzed time periods. From topographic maps (scale 1:25000, Bayerisches Landesvermessungsamt, 1987) the heights $H(t_0)$ are estimated to be 1026 m $\pm$ 5 m (Kochelsee) and 824 m $\pm$ 5 m (Walchensee), respectively. By minimization of the linear trend of $h(t) - h(t_0)$ within the time interval of a maximum length of 200 sec we obtain a $H(t_0)$ of 1023.5 m (Kochelsee) and 825.5 m (Walchensee). The estimated absolute height of the receiver above the reflecting lake surface H(to) deviates from

DOI: 10.2312/GFZ.b103-08104

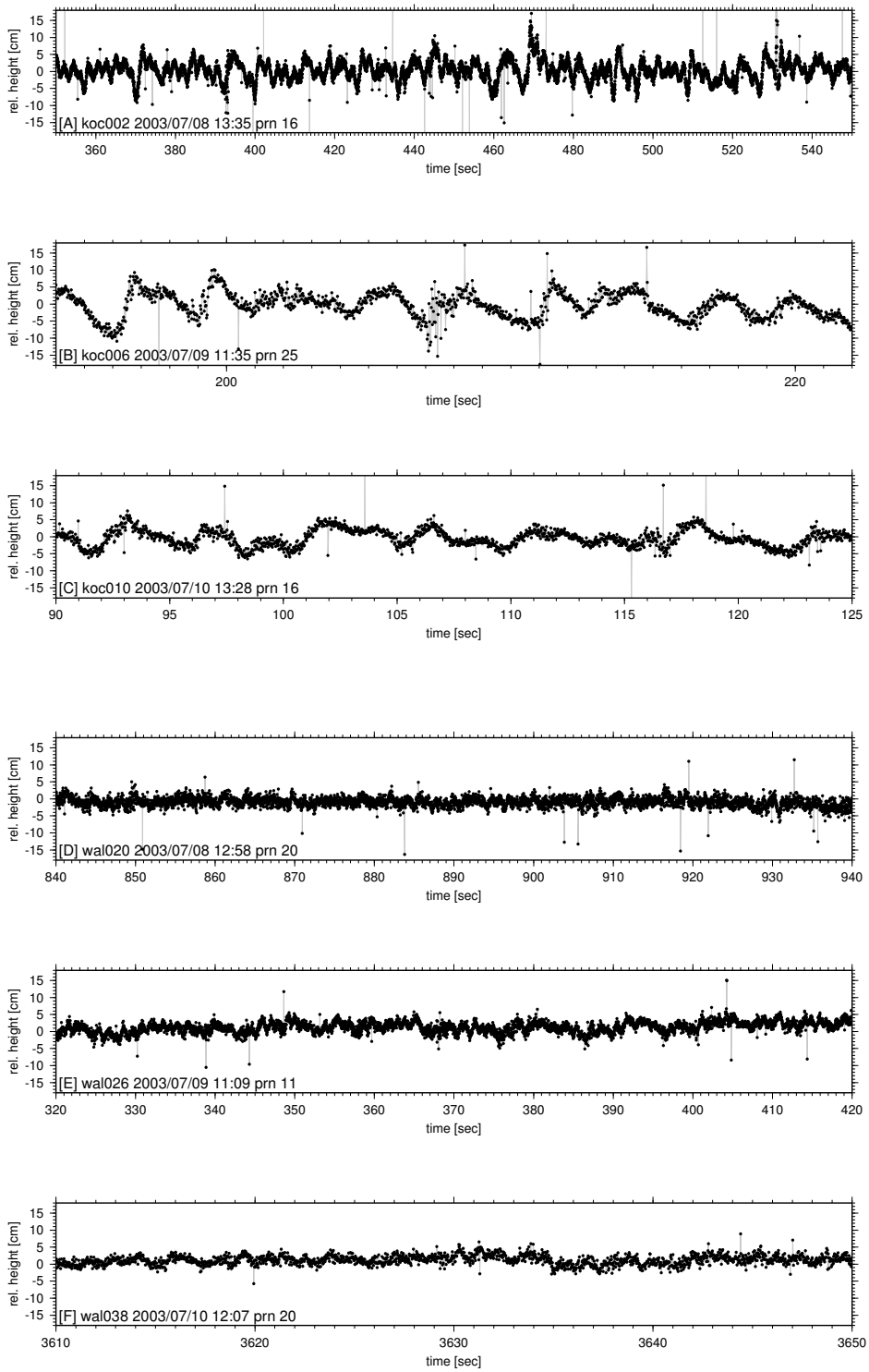

Fig. 5.11: *First version of processed relative height measurements at Kochelsee (panel A,B,C) and Walchensee (panel D,E,F)*

the expected values by 1 m at Walchensee and 3 m at Kochelsee. If the tropospheric correction is neglected, this error will rise to several meter.

Depending on the chosen data segment and time period the resulting height $H(t_0)$ can change significantly. Because of this reason the processing has undergone major changes to achieve much longer continuous height time series without interrupting cycle slips. Analyses show that outliers are best treated in the further processing by a running mean filter with a length of 20 samples (0.4 sec) which have been applied to both in-phase and quad-phase correlation-sum time series. Cycle slips are best

DOI: 10.2312/GFZ.b103-08104

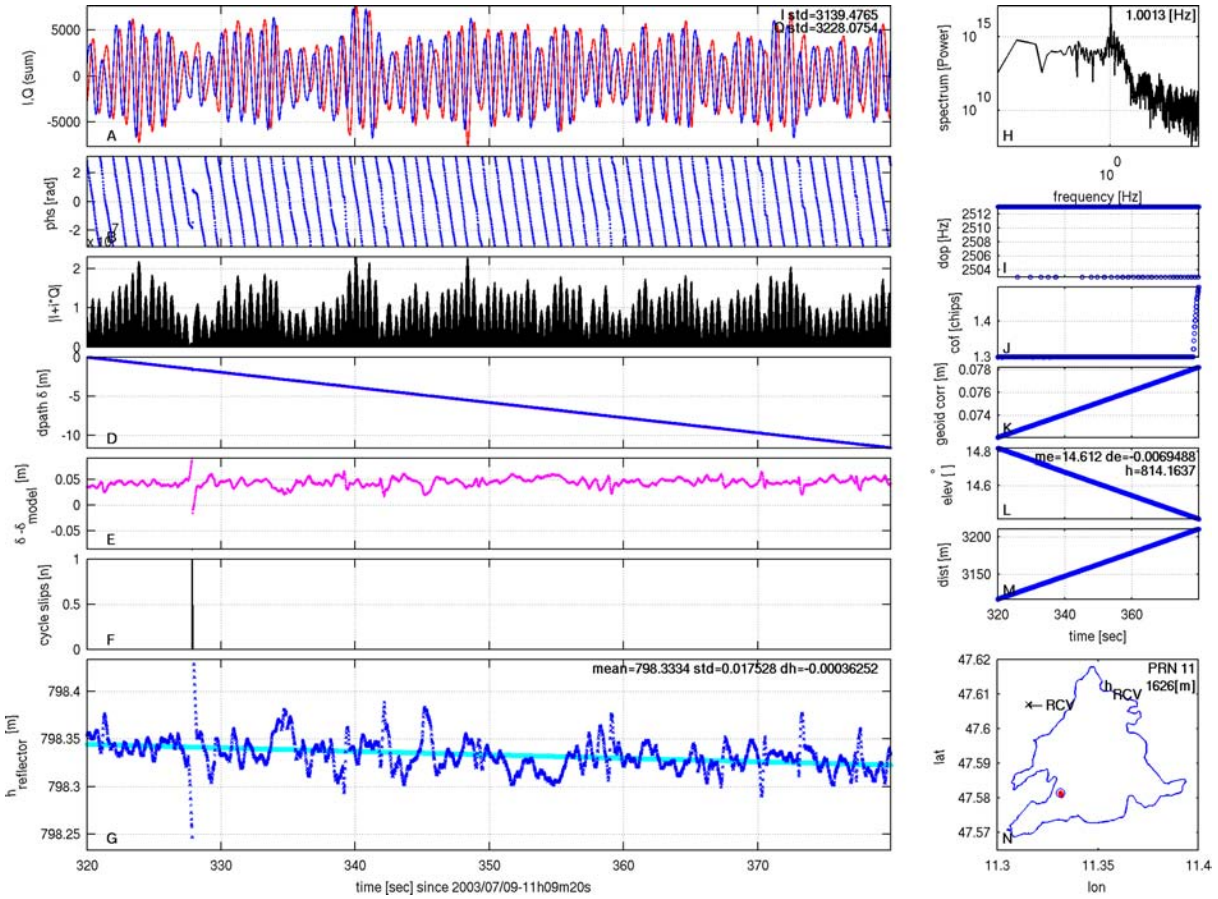

Fig. 5.12: *Details of Walchensee reflection event of PRN 11 starting at 11:09:20 GPST after 320 sec*

treated by comparing the measured dpath data δ with calculated model dpath data δ_{model}. In case the measured data exceeds a previously defined offset from the target model data, n multiples of λ_{L1} are inserted or taken away from the measured δ data until the offset is minimized. With the enhanced post processing much longer height profiles can be extracted from the Fahrenberg data with durations up to 15 min and covering a height profile of about 1700 m length (Fig. 5.19).

Fig. 5.12 shows details of a 60-sec segment of reprocessed data of a Walchensee reflection event of PRN 11 on July 9, 2003. Panel A shows the filtered in- and quad-phase data, panel B the derived phase, panel C the power of the signal and panel D the derived δ (blue) and model δ_{model} (pink). The deviation of δ from the model is plotted in panel E. At about 328 sec there is a phase inconsistency caused by a cycle slip. The δ data exceeds the offset from the target model until $n = 1\ \lambda_{L1}$ cycle is inserted into the data (panel F). Thus, the derived height profile has no height jumps and varies with a STD of 1.7 cm around a mean height of 798.33 m reflector height. The dominant frequency in the spectrum of the measured in- and quad-phase data is about 1.0013 Hz, shown in the spectrum on panel H. The Doppler of the carrier frequency stays constant at a value of 2512 Hz (panel I) and also the code offset of the measuring slave correlator channel keeps to a value of 1.3 chips (panel J). The applied geoid correction varies between 7.4–7.8 cm (panel K) while the elevation drops from 14.8° to 14.4° (panel L). With the mean elevation and the elevation change rate an absolute height of 814 m of the reflector can be estimated with the peak frequency 1.0013 Hz of the observed interferometric pattern. The distance of the specular reflection point from the receiver is increasing as the observed satellite is setting (panel M). Panel N shows the geo-location of the reflection point with respect to the lake's shoreline.

Fig. 5.13 and Fig. 5.14 compare selected height measurements from Kochelsee and Walchensee on July 8 (top), July 9 (middle) and July 10 (bottom), 2003. 60 sec long extracts of filtered I,Q data (panel A), unwrapped phase (panel B), reflection signal power (panel C) and derived reflector height (panel D) are plotted at the same scale for each measurement. All lake measurements are processed with the same reflector height guess of 599.9 m (Kochelsee) and 798.2 m (Walchensee). On July 8 the calmest conditions can be observed on both lake surfaces with a STD of 2.1 cm on Kochelsee and

DOI: 10.2312/GFZ.b103-08104

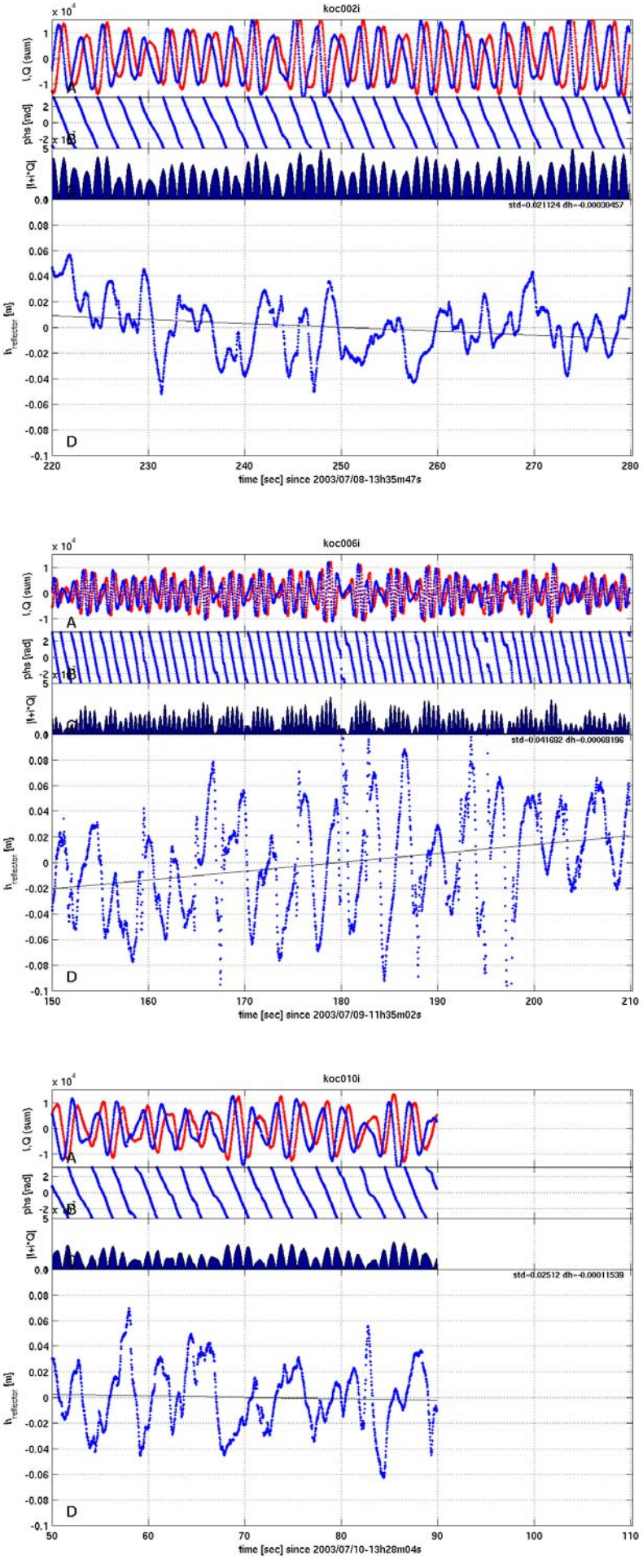

Fig. 5.13: *Selected height measurements from Kochelsee on July 8 (top), July 9 (middle) and July 10 (bottom), 2003 are shown. Extracts of filtered I,Q data (panel A), unwrapped phase (panel B), reflection signal power (panel C) and derived reflector height (panel D) are plotted for each measurement.*

DOI: 10.2312/GFZ.b103-08104

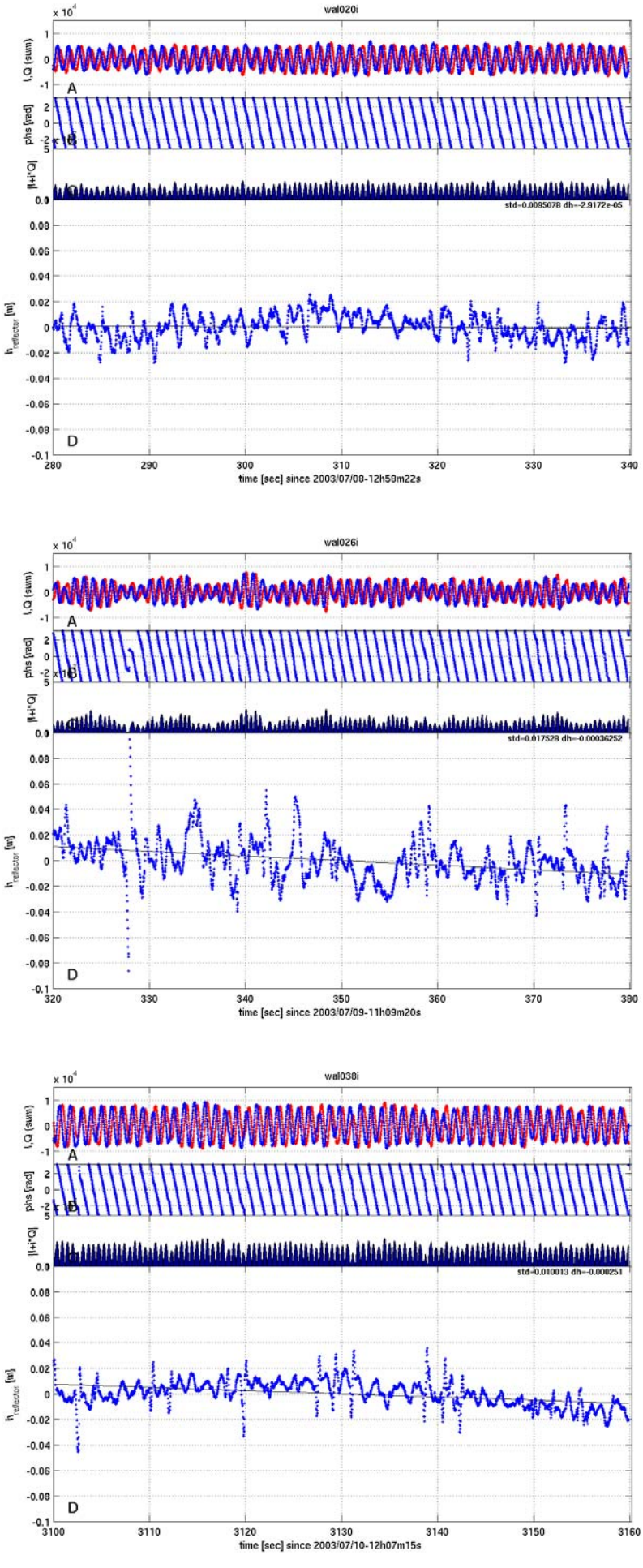

Fig. 5.14: *Selected height measurements from Walchensee (right) on July 8 (top), July 9 (middle) and July 10 (bottom), 2003 are shown. Extracts of filtered I,Q data (panel A), unwrapped phase (panel B), reflection signal power (panel C) and derived reflector height (panel D) are plotted for each measurement.*

DOI: 10.2312/GFZ.b103-08104

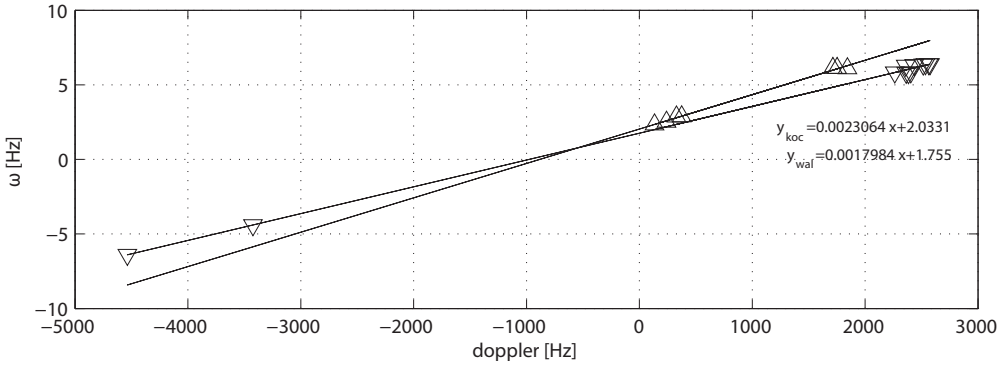

Fig. 5.15: *Dependency between measured Doppler frequency shift of the carrier frequency and observed interferometric frequency ω.*

0.8 cm on Walchensee. On July 9 on both lake surfaces the STD increased to 4.2 cm at Kochelsee and 1.8 cm at Walchensee. Several phase inconsistencies can be observed at 180 sec and 195 sec in the Kochelsee data and 328 sec in the Walchensee data, where cycle slips had to be corrected. On July 10 the observed STD drops down again to 2.5 cm on Kochelsee and 1.0 cm on Walchensee. The signal power received from Kochelsee is much higher compared to the signal received from Walchensee. This can be explained by the lower mean elevations at which the Kochelsee data was recorded (11.0°, 10.2°, 11.3°) compared to the Walchensee data (17.7°, 14.6°, 16.1°). On July 8 and 10 a much lower interferometric frequency can be observed in the Kochelsee data. This lower frequency is caused by the low Doppler of 240–250 Hz of the carrier for the selected data sets. All other selected data sets have Doppler values in the range of about 1700–2500 Hz. A linear dependency between Doppler and observed interferometric frequency is shown in Fig. 5.15, where all Fahrenberg datasets have been taken into account.

To analyse how the reflected signals change during a day, Fig. 5.16 shows selected 60 sec long data sets from Walchensee, recorded on July 8 and starting at 09:20, 11:05, 12:58 and 13:17 GPST. The first two data sets show reflections from PRN 11, the following two data sets show reflected signals from PRN 20. The height signal does not significantly change throughout the day and when changing the observed satellite. The height signal varies within centimeter range with a STD of about 1.0 cm in case the data is not corrupted by inconsistent phase gaps causing cycle slips. The low signal power of the first data set shown should be mentioned. Here the reflection occurred at a comparably high elevation of about 24.4°. All subsequent measurements occur at a lower mean elevation of 17.3°, 14.6° and 11.8°, respectively.

Fig. 5.17 shows in detail what happens in case the OpenGPS receiver temporally looses track of the signal and the slave correlator has to be positioned again. The signal power of the derived reflected signal drops to a low level. During the pull-in process of the receiver, the slave correlator approximates the code offset of the reflected signal and the interferometric pattern again regains strength (in the time interval from 125 to 130 second).

A first attempt to determine the absolute altimetric height of the reflector can be made with the help of the observed interferometric frequency, elevation and elevation change rate. From the Kochelsee data sets shown in Fig. 5.13 the heights 655.4 m, 618.6 m and 670.9 m were calculated, giving only a very rough estimate of the reflector height. From the Walchensee data sets shown in Fig. 5.14 816.4 m, 814.2 m and 820.5 m were calculated for the reflector height. During July 8 the following heights could be calculated from the data sets seen in Fig. 5.16: 816.6 m, 814.7 m, and 816.4 m. Taking all 7 usable data sets into account, for Kochelsee a mean height of 641.3 m with a STD of 26.0 m can be achieved (Fig. 5.21, panel A). For Walchensee a mean height of 816.1 m with a STD of 3.5 m can be calculated from 8 selected data sets (Fig. 5.21, panel B).

The absolute height of the reflecting surface can be additionally derived from the carrier phase based relative height measurements. The following constraint has to be made: The reflecting water surface has to be horizontal, or known slopes have to be corrected beforehand. Slopes can be caused e.g. by wind set-up, water currents or gravitational forces caused by topographic or bathymetric excess masses. Thus, the relative height profile has to be detrended by using the starting height $H(t_0)$ as tuning parameter. $H(t_0)$ has to be varied until the slope of the resulting height profile is as close to zero as possible. The final value of $H(t_0)$ represents the height of the reflector. Using the shown data sets (Fig. 5.13) 599.78 m, 599.88 m and 599.82 m mean height could be calculated for Kochelsee

DOI: 10.2312/GFZ.b103-08104

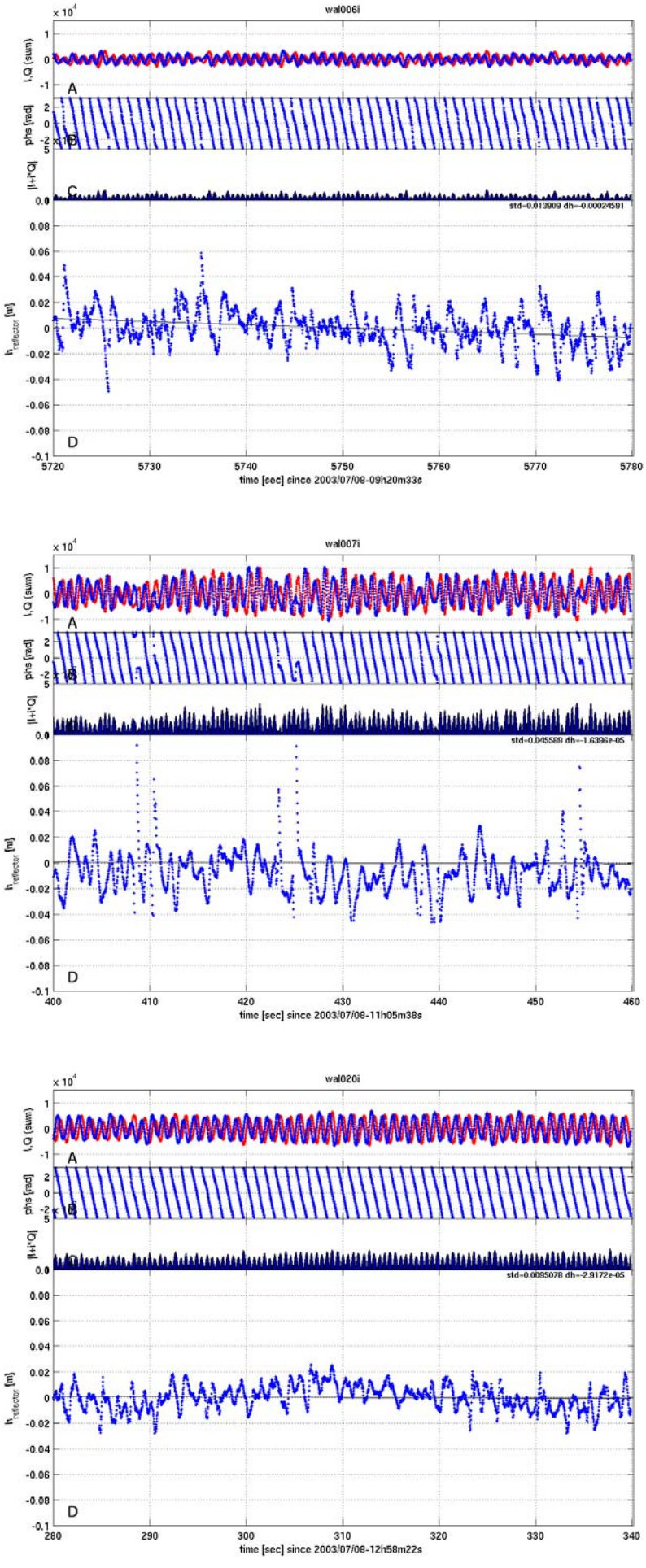

Fig. 5.16: *Selected data sets from Walchensee are shown, recorded on July 8 and starting at 09:20, 11:05, and 12:58 GPST. Extracts of filtered I,Q data (panel A), unwrapped phase (panel B), reflection signal power (panel C) and derived reflector height (panel D) are plotted for each measurement.*

DOI: 10.2312/GFZ.b103-08104

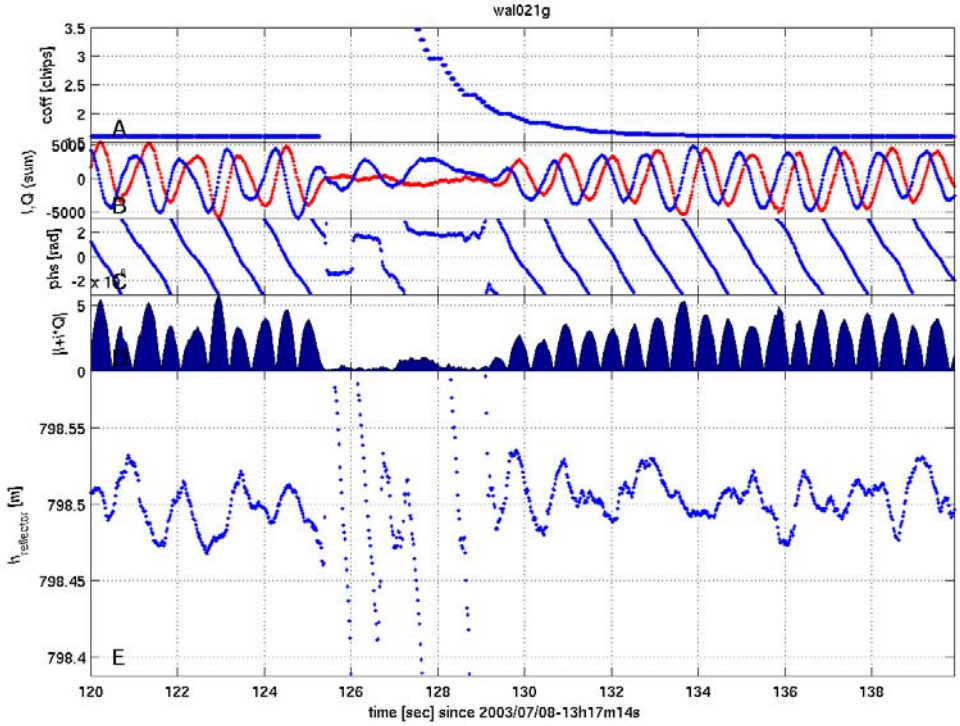

Fig. 5.17: *The OpenGPS receiver temporally looses track of the signal and the slave correlator has to be positioned again.*

and 798.39 m, 798.52 m and 798.38 m was measured for Walchensee. Taking all 7 usable data sets into account, for Kochelsee a mean height of 599.74 m with a STD of 0.10 m can be achieved (Fig. 5.21, panel C). For Walchensee a mean height of 798.43 m with a STD of 0.11 m can be calculated from 8 selected data sets (Fig. 5.21, panel D). The different heights between both lakes during the 3 observed days (198.61 m, 198.64 m and 198.56 m) are compared with the local tide gauge readings (Fig. 5.6) and a height offset of about 3 m can be noticed. Additionally, the rising height difference toward July 10, reported by the tide gauge readings cannot be reproduced in the GPS altimetry data.

The different height variations at both lakes can be explained by different local wind and wave height conditions. Lake Walchensee is completely surrounded by mountains. Thus, waves are mainly driven by local, thermally induced winds which mainly occur at noon. Lake Kochelsee is open to the north, so longer lasting winds can build up waves on the lake surface. Additionally, a longer lasting wind force is able to generate a slope in the Kochelsee lake surface.

In the following the 60 sec data sets are extended to the complete, continuous and consistently processed height profiles. All measurements are processed with the same reflector height guess of 599.9 m (Kochelsee) and 798.2 m (Walchensee). The selected height guess was tuned to achieve the smallest slope on all lake height profiles. At each lake 2 height profiles were selected that are composed of several continuous data recordings. The ground tracks of the selected observations are plotted in Fig. 5.18.

In Fig. 5.19 the derived height profiles are plotted against the ground distance to the OpenGPS receiver. Panel 1 and 2 show the Kochelsee height profiles track-1 and track-2. Panel 3 and 4 show Walchensee track-1 and track-2 height data. All plots use the same height scale for the y-axis but differ in the x-axis scale used for the distance.

At Kochelsee the track-1 data (koc006a and koc008a) show a good agreement and differ only very slightly over more than 300 m profile length (Fig. 5.20, top). A mean height of 599.73 m and 599.74 m with a STD of 5.0 cm and 4.5 cm were achieved. From the observed interferometric frequency of 0.97565 Hz and 0.97078 Hz an absolute height of 610.54 m and 616.21 m can be calculated. The longest data take (koc001a) at Kochelsee with a length of about 800 m results in a mean height of 599.96 m with a STD of 5.5 cm. The height differs from the previous stated measurements by a bias of about 22 cm, which could be explained by an undetected cycle slip. From the observed interferometric frequency of 0.97524 Hz an absolute height of 600.89 m can be calculated. Taking into account the limited accuracy of the frequency determination, both heights

DOI: 10.2312/GFZ.b103-08104

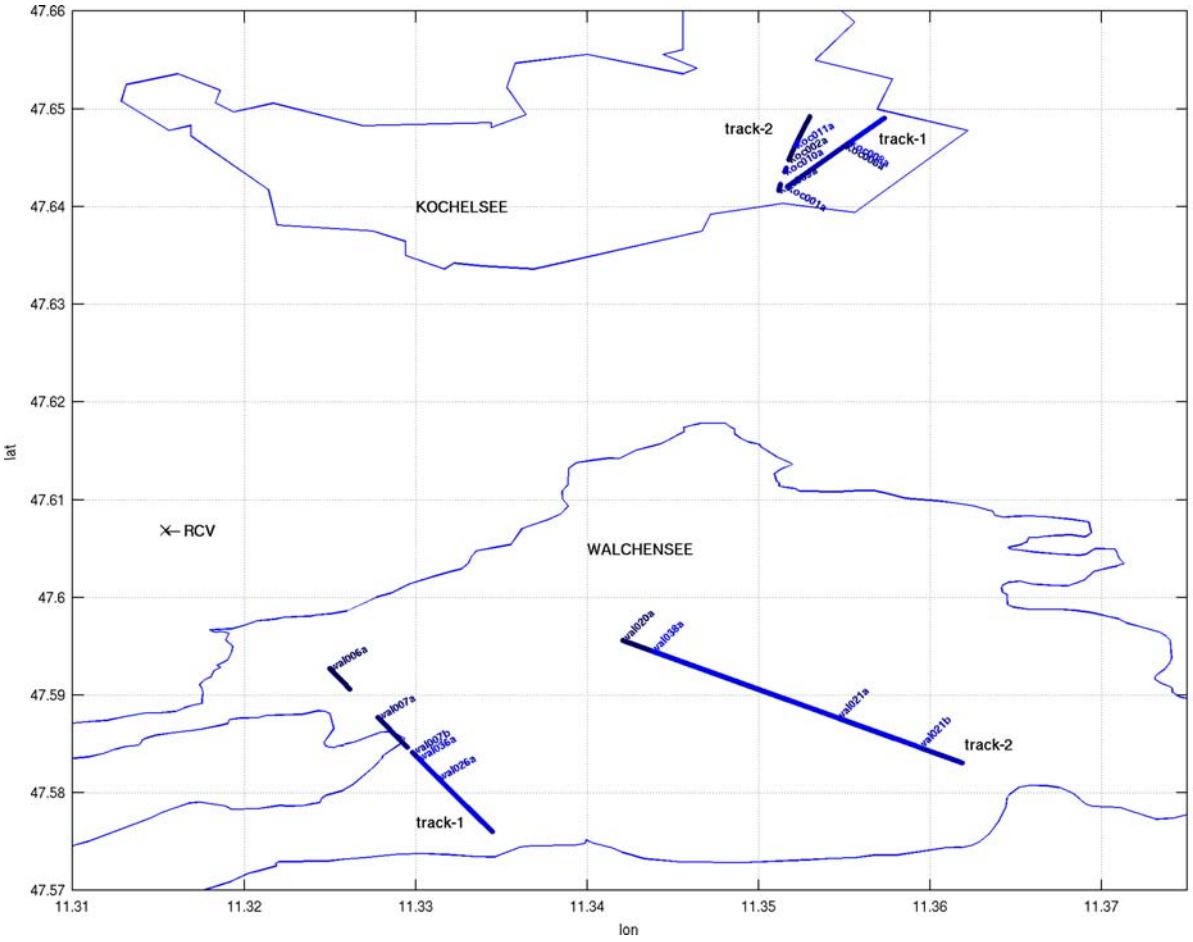

Fig. 5.18: *Ground tracks of the specular reflection point for four different reflection events at Kochelsee and Walchensee (Fig. 5.19 on page 80)*

are in good agreement. Starting at a distance of 5200 m, a small slope can be observed in the data.

At Kochelsee with track-2 data, a height bias between the data sets can be observed which again can be explained by an uncorrected cycle slip. The measurement koc002a, with a length of about 500 m, has a negative slope which could not be minimized without changing the reflector height guess significantly. Noisy data cannot explain this effect because, compared to track-1 data, here the data is less disturbed by corrupted phase data causing cylce slips. A height of 652.42 m is derived from the interferometric frequency of 0.457725 Hz.

At Walchensee, track-1, all height profiles show a small negative slope in the range of about -2 cm/100 m. The slope increases at greater distances starting from 2800–3200 m and reaches a value of about -6 cm/100 m. At the same starting height Walchensee track-2 data show nearly no slope except data take wal021b. Profiles wal021a and wal021b deviate by a height bias of about 15–23 cm and, starting at a distance of 4100 m, a negative slope of about 5 cm per 100 m can be observed. Profiles wal021a and wal021b are calculated from the same data recording, but use different correlator channels for different time intervals. The principle can be seen in Fig. 5.10, where channel 6 and 1 are used to extract all possible reflection data. Data take wal020a overlaps with wal038a at a length of about 900 m and the derived heights show a very good agreement (Fig. 5.20, bottom). The height data of wal038a consistently covers a profile of about 1700 m length. Here a mean height of 798.45 m with a STD of 2.9 cm could be achieved although the dataset was interrupted twice by severe signal loss (at a distance of about 3150 m and 3800 m). Additionally, an absolute height of 798.92 m can be calculated from the interferometric frequency of 0.93007 Hz which is in good agreement with the previously derived height, based on carrier phase measurements. For wal020a the STD of the height data could be improved to a value of 2.0 cm with the same mean height of 798.45 m. From the observed interferometric frequency of 0.92759 Hz an absolute height of 798.08 m was calculated.

DOI: 10.2312/GFZ.b103-08104

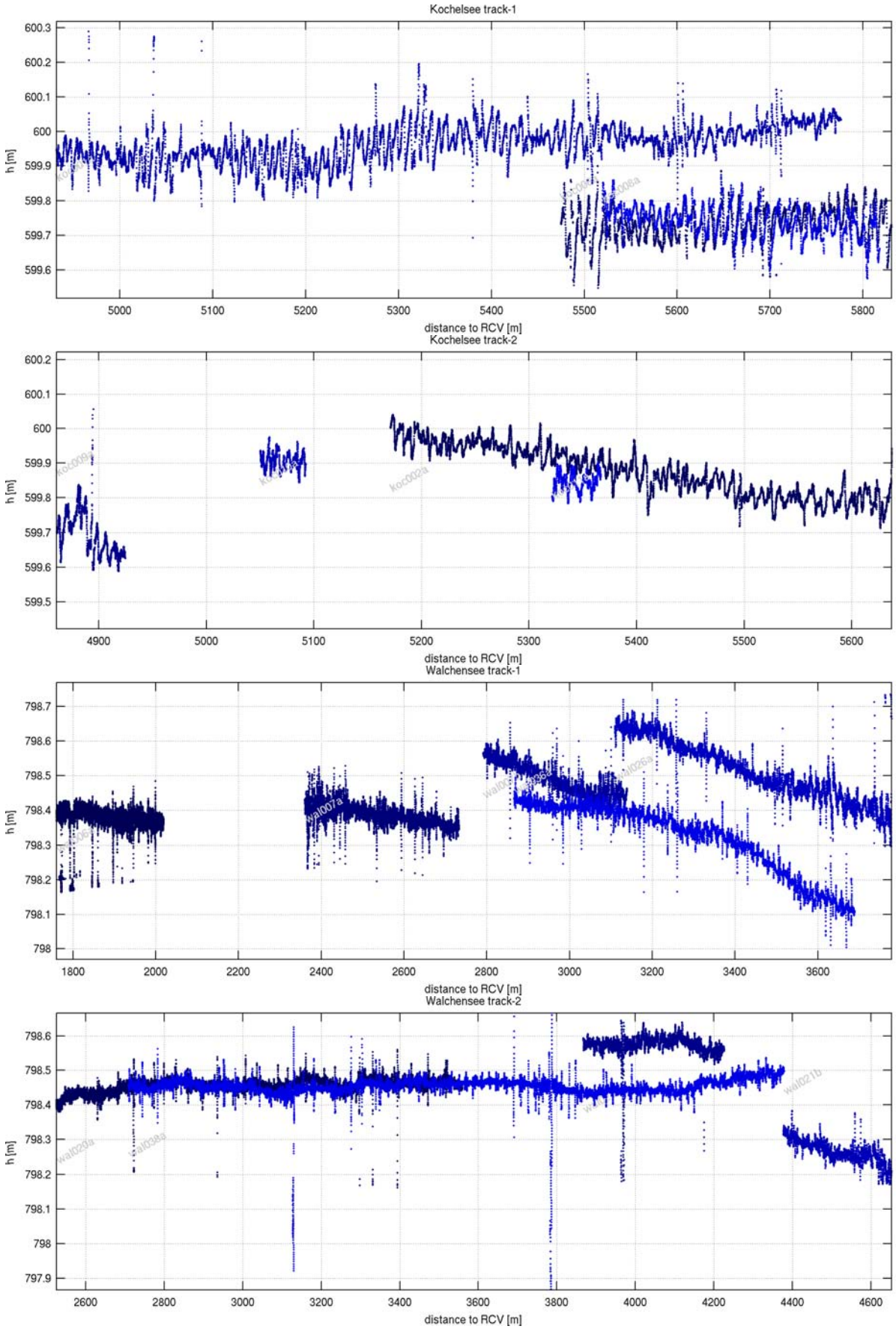

Fig. 5.19: *Derived height profiles at Kochelsee (panel 1 and 2) and Walchensee (panel 3 and 4), location of the ground tracks are plotted in Fig. 5.18 on page 79.*

DOI: 10.2312/GFZ.b103-08104

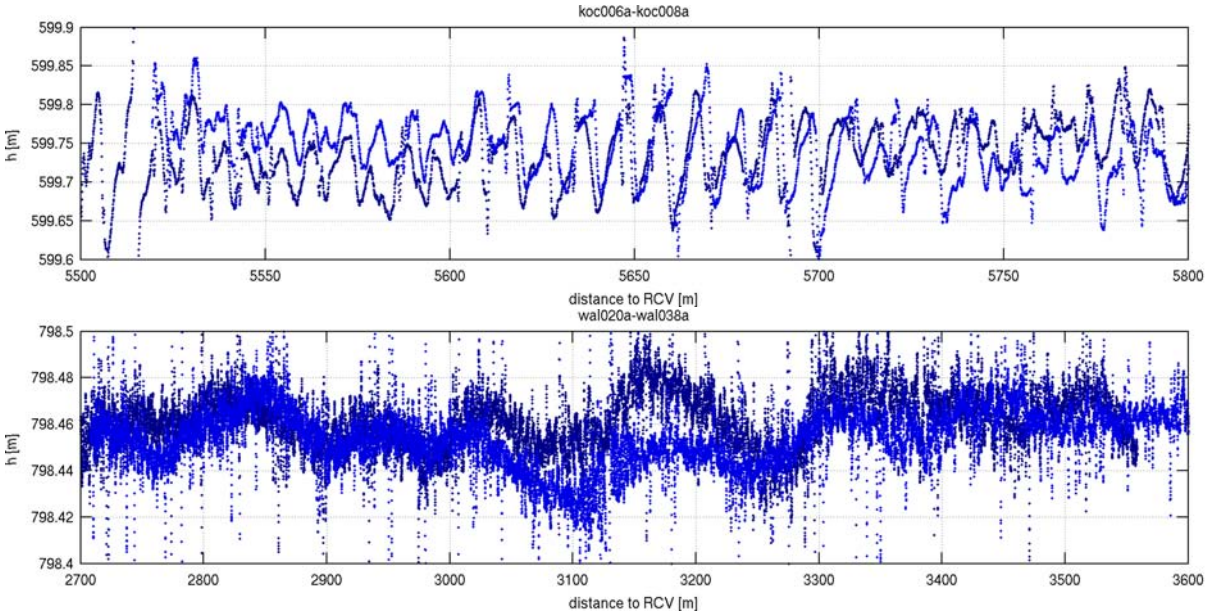

Fig. 5.20: *Details of derived height profiles at Walchensee, location of the ground tracks are plotted in Fig. 5.18 on page 79.*

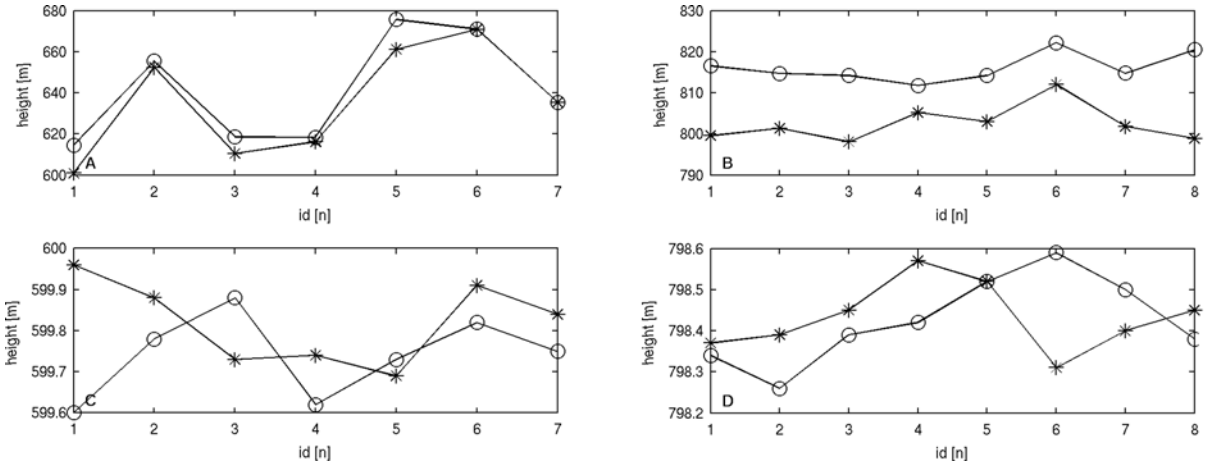

Fig. 5.21: *Derived absolute heights from Kochelsee (left) and Walchensee (right): Absolute reflector heights have been calculated from interferometric frequency (panel A and C) and from detrended relative height measurements calculated from carrier phase measurements (panel C and D). Data points related to 60 sec long data are marked by a circle. Stars mark heights derived from full range data sets.*

The absolute height estimate derived from the interferometric frequency significantly improves with longer data sets and comes much closer to the expected height value. Taking all 7 full data sets into account for the Kochelsee a mean height of 635.35 m with a STD of 27.0 m can be achieved (Fig. 5.21, panel A). For the Walchensee a mean height of 802.1 m with a STD of 4.5 m can be calculated from 8 selected data sets (Fig. 5.21, panel B). Longer data sets directly improve the accuracy/resolution of the interferometric frequency estimate which is derived from spectral analysis, but still the accuracy persists in the range of several meter. Analysing the selected detrended long relative height data sets, only a slight improvement can be observed with the 8 selected Walchensee data sets and the overall STD drops to a value of 0.08 m (Fig. 5.21, panel D). The necessary process of detrending the relative height data sets increases the sensitivity to slopes the more data samples are involved. Thus, longer data sets require much more manual tuning of the involved process parameters. Additionally, long, consistent and continuous data sets can clarify the influence of the applied correction models.

In the following the longest, continuous reflection profile wal038a is selected to illustrate the influence of different processing parameters on the derived absolute height. Fig. 5.22 shows the resulting height from 10 processing runs with different time, height trend and troposphere corrections (p0 - p4, p9) and varying reflector height estimation at measurement start (p5 - p8): Run p0 applies a

DOI: 10.2312/GFZ.b103-08104

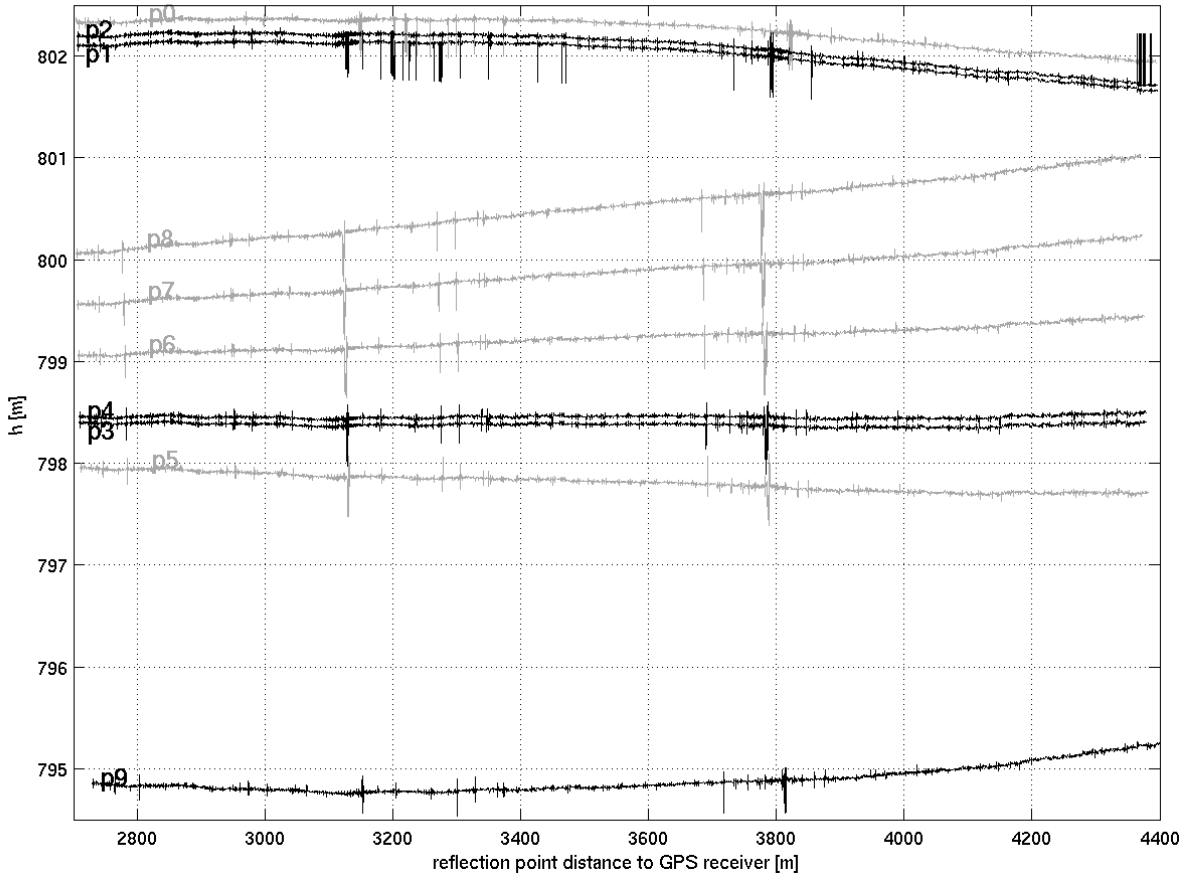

Fig. 5.22: *Influence of processing parameters on absolute height determination at Walchensee (PRN 20 (wal038) data extract between July, 10, 2003 12:57:15 and 13:13:55 GPST).*

wrong time offset of -15 sec to the data causing a height offset of about 23 cm in comparison to run p1 data. For run p1 neither a trend correction nor a tropospheric correction has been applied to the measured data. The reflector height estimate at measurement start ($H(t_0)$) was varied until the trend of the resulting height data was minimized up to a distance of 3450 m from the GPS receiver. At greater distances a negative trend can be observed.

Run p2 adds a trend correction derived from the local geoid surface of Gerlach [2003] which varies from -3 cm to 4 cm at the track of the reflection point. This correction is necessary to fulfill the assumption of a flat water surface and to achieve the correct height after the necessary detrending process. The mean lake surface is influenced by the local gravity field as shown in Fig. 5.23. Here the geoid gradient is plotted at the Fahrenberg location. Caused by the gravity field, a positive slope southwards of about 10 cm/km at Kochelsee and about 6 cm/km at Walchensee can be observed. At Walchensee the gradient increases towards the south lake shore to about 10 cm/km. The local geoid must be expected to be locally much more inhomogeneous. The used local geoid relates only to a few supporting measurement points in the area of the lakes [Gerlach, 2003]. Additionally, Walchensee has a strong varying bathymetry with up to 190 m depth. A rough estimate of the topographic influence is shown in Fig. 5.24 and from the center of the lake towards the shoreline an increase of about 20 mGal has been calculated. The surrounding topography was modeled with the program grav2dc (`http://www.rockware.com`). The lake water was set to a density of 1 g/cm^3 and the lake body was set to a strike length of 3000 m to each side. The surrounding bedrock was set to a typical value of 2.7 g/cm^3 for limestone and had a strike length of 5000 m to each side.

For run p2 no tropospheric correction is applied to the measured data. $H(t_0)$ was varied until the trend of the resulting height data was minimized up to a distance of 3450 m from the GPS receiver. Besides the remaining constant negative trend, an almost constant height bias of about 8 cm can be observed. A change of $H(t_0)$ always introduces a bias in the calculated distance/position of the reflection point.

DOI: 10.2312/GFZ.b103-08104

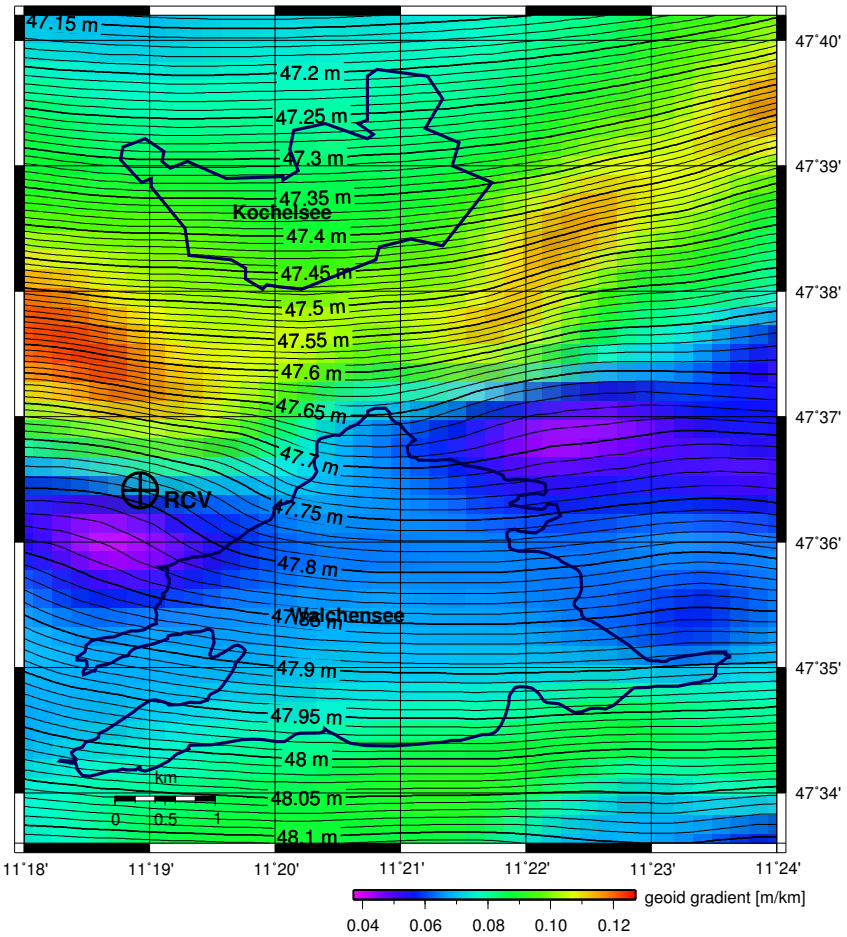

Fig. 5.23: *Surrounding gravity anomalies can cause possible height trends. Above height anomalies are shown for the location Fahrenberg and are calculated from a local geoid from Gerlach [2003].*

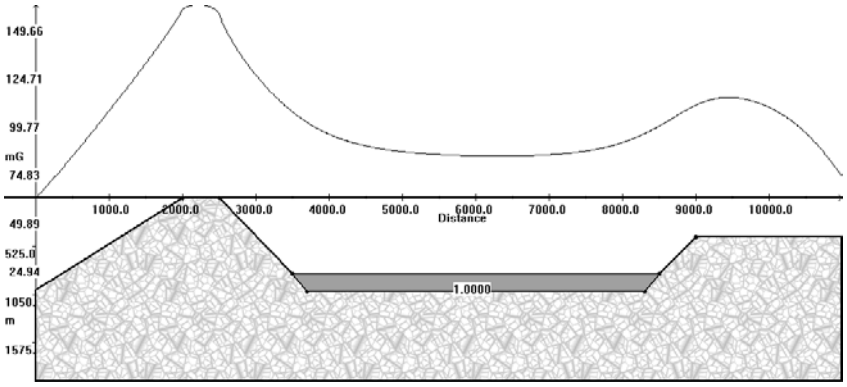

Fig. 5.24: *Simple model of the gravity anomalies at Walchensee location caused by the local topography.*

The tropospheric refraction has been corrected in the following runs (p3-p9) using correction data derived from ray-tracing calculations with local ECMWF meteorological data. During run p3 only the bending effect of the troposphere was corrected for, influencing the elevation angle of the observed satellite. In comparison to the previous processing a large height bias of more than 2.5 m is observed. Additionally, no remaining trend can be observed anymore.

Fig. 5.25, panel A, shows the derived tropospheric elevation angle correction – the deflection angle $\delta\varepsilon$ – for a selected set of Fahrenberg measurements. Especially for long data recordings like wal038 – when the observed elevation (panel E) decreases from 17° to 11° – the influence of the atmosphere increases and the deflection angle rises from 0.05° to 0.08°. Thus, the optical path length increases from 7 m to 11 m (panel B). Typically, the troposphere delays GPS signals by about 8 ns, i.e., cause an additional path length of 2.4 m in case the signal is received from zenith direction.

In comparison to the direct signal the reflected signal travels twice through the atmospheric layer between the reflection point at lake level and the receiver location. This lower layer with a thickness of about 800 m at the Walchensee location and about 1000 m at the Kochelsee location introduces an additional delay of the reflected signal which has to be corrected for. From ray-tracing calculations with local ECMWF meteorological data this tropospheric path delay is estimated and applied to the

measured data in the following runs p4–p8. The excess optical path caused by the troposphere is calculated at the height of the reflector and compared to the values calculated at the height of the receiver. The GPS signal has to travel a longer path through the troposphere to reach the reflector. Thus, the excess optical path and the deflection angle $\delta\varepsilon$ are always larger than the values at receiver height. The resulting differences are plotted in Fig. 5.25(panel C and panel D). In the following the differential excess optical path δ is taken as additional tropospheric correction to respond to the delay caused by the atmospheric layer between receiver and reflector. The correction value is multiplied by the factor 2, as the reflected signal travels twice through the atmospheric layer.

For run p4 the height bias – observed in p3 – is minimized when an additional constant mean tropospheric correction value of $2 \cdot 0.998 = 1.996$ m is applied to the δ data. For run p9 the changing correction values – derived from the ray-tracing analysis – introduce an additional slope to the data. This slope introduced by the additional varying tropospheric correction causes a large height offset after the data has been detrended. Additionally, the resulting height profile has remaining slopes and dips.

Looking only at the resulting height profiles, p3 and p4 seem to be the most reasonable height profiles which one would expect from a lake surface. From the geophysical point of view, p4 should be preferred, as the most dense atmospheric layer definitely introduces an additional delay in the reflected signal. The additional trend added to the height data for run p9 interferes with the detrending process. Thus, the resulting mean height of about 794.87 m deviates by several meters from the most reasonable height values of Walchensee and the height of 798.92 m, extracted from the interferometric frequency of 0.93007 Hz from the p9 data set.

Runs p5–p8 illustrate the sensitivity of the derived height profile to the selected height estimate $H(t_0)$. Runs p5–p8 are processed in the same manner as p4. $H(t_0)$ of run p4 and run p5 differ by 0.3 m and the most obvious difference between both height profiles is the resulting height bias of about 0.5 m. For run p6, and for p7 and p8 with greater variations in $H(t_0)$ the resulting height bias increases and the overall trend in the height profile becomes larger and can be easily noticed in the height profiles. During all processing runs the parameters used for the dpath comparison model had to be adjusted to minimize occurring cycle slips in case of greater changes of $H(t_0)$. All measurements were performed with the same measurement channel (correlation channel 2). Only once, for p2, the measurement channel had to be switched from channel 2 to 0.

A negative slope can be observed in Walchensee track-1 data wal036a and wal026a toward larger receiver distances beginning at 3200 m (Fig. 5.19, panel 3). In the following the negative slope is discussed again. In Walchensee track-2 data wal021a,b a similar slope can be observed at a distance beginning at 4100 m (Fig. 5.19, panel 4). No independent reference height data is available to connect the observed slope to a defined source. The applied geoid correction model may be erroneous due to the local gravitational forces. An increasing slope toward the south lake shoreline can already be seen in the geoid model used (Fig. 5.23). Reflection observations at larger distances from the receiver are the result of GPS signals from satellites at low elevations. At low elevations the lower part of the atmosphere heavily affects signal propagation. Local in-situ meteorological observations should be integrated into the tropospheric correction model as known from handling classical geodetic microwave ranging. With no meteorological data available, only a mean estimate of the path delay can be obtained from ray-tracing calculations with a model atmosphere. Here the meteorological data closest to the Fahrenberg location are taken from daily ECMWF model data at noon (12:00 GPST). The meteorological situation around Walchensee and Kochelsee may deviate from the model estimate. Especially at the Walchensee location large deviations can be expected. Here the local meteorological situation can change rapidly during the day which is typical for mountaineous areas like the Alps.

Fig. 5.26 illustrates how the atmospheric parameters pressure (panel A), temperature (panel B) and refractivity (panel C) vary for July 8–10, 2003 at 12:00 GPST. The data are extracted from the ECMWF model data at location 47.5°N, 11.5°E, 800.5 m above sea level. Fig. 5.27 evaluates what height variations can be expected by applying a wrong tropospheric correction to the data. Here we derived the tropospheric corrections from ECMWF model data from July 8, 9 and 10, 2003 at 12:00 GPST and applied the corrections to the data measured between July, 10, 2003 12:57:15 and 13:13:55 GPST. The temperature (Fig. 5.26, panel B) of the ECMWF model data showed the largest variations (several degrees) between 4 km and 16 km height within the analysed 3 days. Refractivity (Fig. 5.26, panel C) shows the largest variations in the height region between 3 km and 6 km.

DOI: 10.2312/GFZ.b103-08104

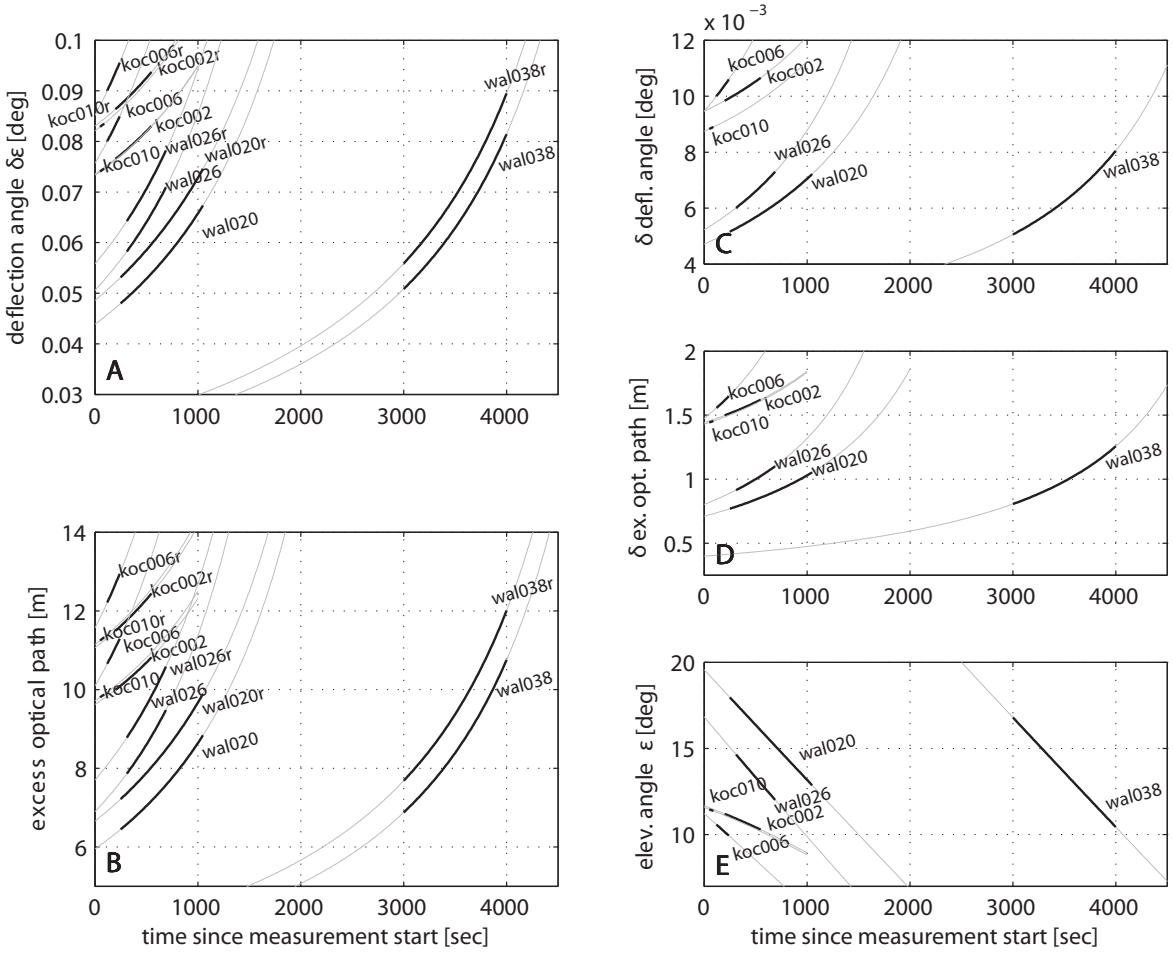

Fig. 5.25: *Influence of the troposphere on observed elevation and extended optical path length for the observed Fahrenberg data.*

Another effect is caused by the surrounding high mountains. At low elevations the GPS signal can be shadowed by the mountain tips. Fig. 5.28 analyses the situation at Walchensee track-1 (panel B). Panel A shows the topographic heights derived from the Shuttle Radar Topography Mission (SRTM) C-SAR data along with respect to the reflection profile. At 6 different distances the geometric signal path is plotted (red) without taking atmospheric bending effects into account. The distances are marked as red dots in panel E. Panel C plots the power of the reflected signal, panel D the code offset of the measuring correlator towards the direct signal and panel E the derived heights versus the distance to the receiver. Firstly, the height profile illustrates the difficulty to detrend such a relative height profile. Secondly, a linear decrease of signal power can be observed starting at a distance of about 3400 m. The signal finally fades away at a distance of 3800 m, where the geometric signal path hits the mountain ridge near the peak of Altlacher Hochkopf.

5.2.3 Footprint Size Estimation

In order to estimate the size of the footprint of the reflected signal, the signal behavior is analysed at the transition zone between water and land in the following section. Panel A, B, C and D of Fig. 5.29 show the measured in- and quad-phase data, the calculated phase, the power of the reflected signal and the derived detrended relative height, respectively. The extract of data take koc001 has been recorded at the northwest shoreline of Kochelsee (panel E). No guiding height model was applied to the data and no cycle slips corrected. Up to 488 sec the reflected signal seems to be quite undisturbed. Starting from 492 sec the peak signal power decreases by about 30%. Several phase anomalies can be observed. Starting at 510 sec the deviations from the model (blue flat line) increase and a cycle slip can be observed near the marked point at 513 sec. Starting at about 522 sec the derived height increases with a rate of about 15 cm/sec. Panel F – an extract of the map in panel E – shows the

DOI: 10.2312/GFZ.b103-08104

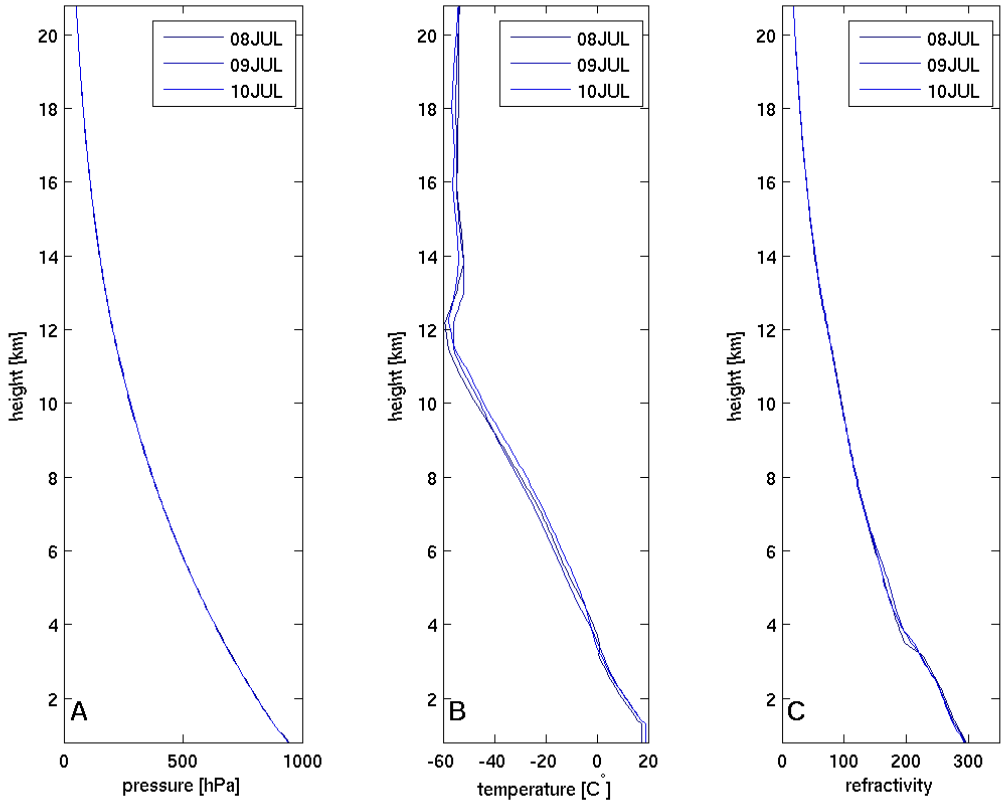

Fig. 5.26: *Variation of the atmospheric parameters at 47.5°N, 11.5°E, 800.5 m above sea level from July 8–10, 2003 at 12:00 GPST. The data were extracted from ECMWF model data.*

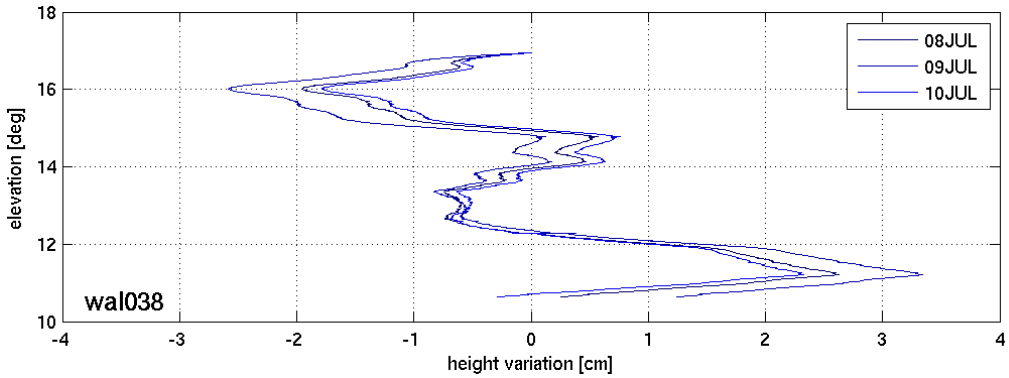

Fig. 5.27: *Height variation plotted versus satellite elevation. The height variation is caused by applying different tropospheric corrections based on ECMWF data of July 8, 9 and 10, 2003 at 12:00 GPST to the data measured between July, 10, 2003 12:57:15 and 13:13:55 GPST.*

first Fresnel zones at the marked measurement times 513 sec and 519 sec. The red line indicates the reflection point profile and the blue line indicates the shoreline of Kochelsee. It is difficult to identify exactly where the height signal changes from water signature to land signature, but it seems that after 519 sec the height signal is dominated by the land signature. Hence, the footprint size seems to be of the order of the plotted first Fresnel zone. Up to 513 sec the footprint is fully covering water and starting with 519 sec the footprint is fully covering land. In the time period in-between the higher conducting water surface seems to dominate the derived height signal.

A more complicated situation is illustrated in Fig. 5.30. Panel A, B and C of Fig. 5.30 show the measured in- and quad-phase data, the power of the reflected signal and the derived detrended relative height, respectively. The extract of data take wal027 has been recorded at the western

DOI: 10.2312/GFZ.b103-08104

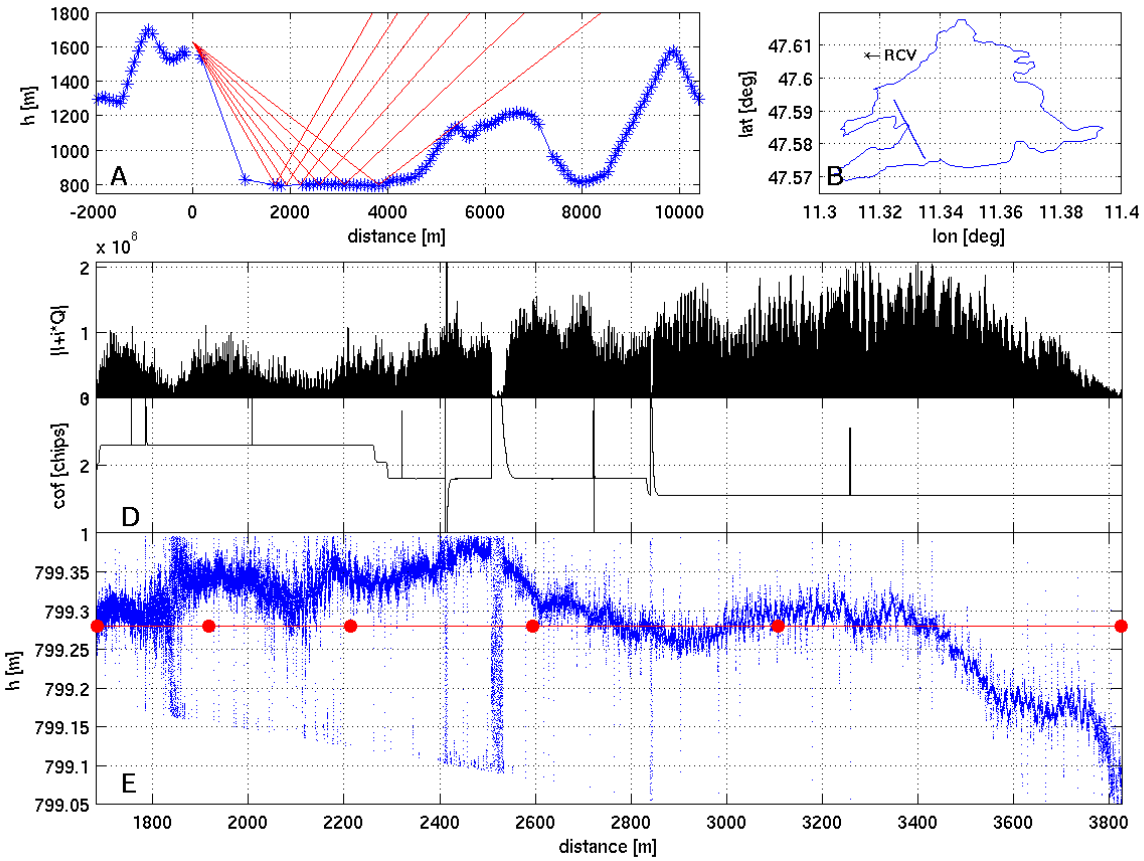

Fig. 5.28: *At low elevations the GPS signal can be shadowed by the mountain tips.*

shoreline of Walchensee with the village Walchensee in the north and a peninsula in the south (panel D). The lake bight has a width of about 200 m. Again no guiding height model was applied to the data and no cycle slips corrected. In-between the marked time period from 450 sec to 710 sec a powerful oscillation can be observed continuing with decreasing power.

DOI: 10.2312/GFZ.b103-08104

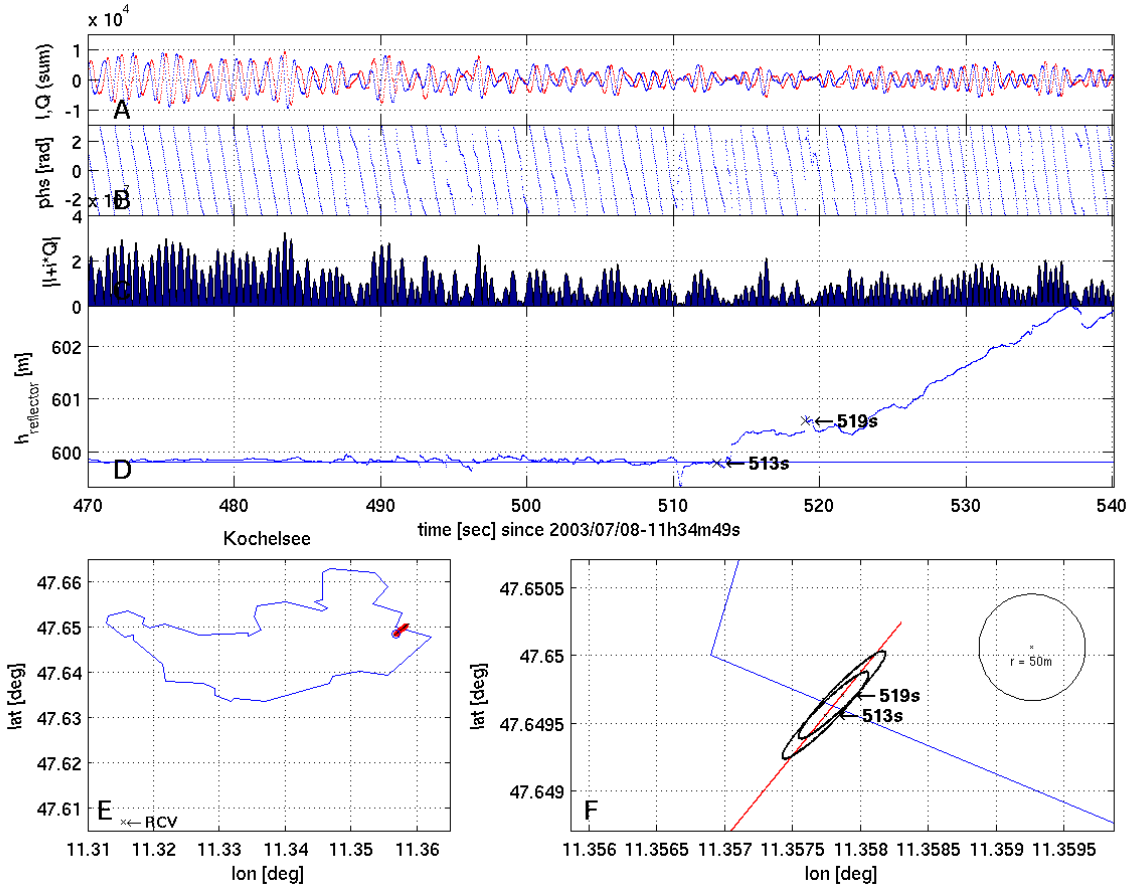

Fig. 5.29: *Footprint size estimation at the northwest shoreline of Kochelsee*

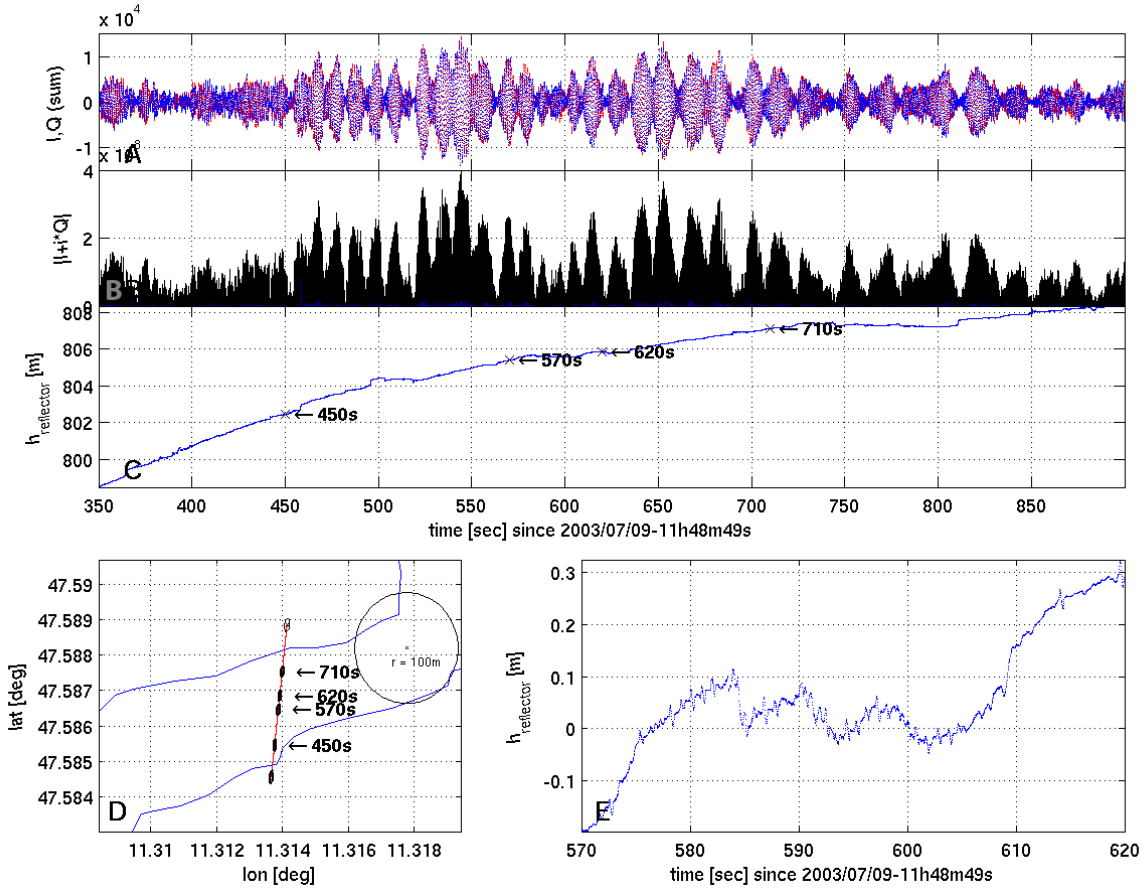

Fig. 5.30: *Footprint size estimation at the western shoreline of Walchensee with the city Walchensee in the north and a peninsula in the south*

DOI: 10.2312/GFZ.b103-08104

5.3 Mercure Hotel Experiment

5.3.1 Experimental Setup and Data Acquisition

The experiment was conducted on 11 June, 2004, on the roof of Mercure Hotel, Potsdam (52.39°N, 13.06°E). The receiver antenna was fixed to the balustrade and orientated southwards with unobstructed view to the Havel river surrounding Hermannswerder island (see Fig. 5.2 on page 65). The RHCP antenna was tilted 45° and had a height of about 63 m above the river water level which served as reflector. The OpenGPS receiver was working in open-loop multi reflection mode (see chapter 4.3.2) which allows the autonomous tracking of 4 independent reflected GPS signals simultaneously. Calculations based on ephemeris data show that 2–4 refl ection events can be observed in parallel at the Mercure Hotel receiver location throughout the day (Fig. 5.31, panel C). Between 09:08 and 14:26 GPST on June 11, 2004, 19 refl ection events could be recorded from southwest, south and southeast direction.

5.3.2 Data Processing

In comparison to the Fahrenberg experiment the geometry of the Mercure Hotel experiment differs signifi cantly. Due to the low observation height of about 63 m of the receiver above the refl ector, the refl ected GPS signal has to travel an extended path length of 17.5 m. Thus, the signal will arrive at the receiver antenna only with a comparably small delay of 58.5 nsec or 0.06 code chips after the direct signal for an observed GPS satellite at an elevation of 8°. The correlation signal of the refl ected signal cannot be separated from the correlation triangle of the direct signal. Thus, the correlation signals of direct and refl ected signal superpose each other. Additionally, the receiver tracking routine is infl uenced by the refl ected signal for the observed small signal delays. The tracking routine is programmed to keep the in-phase component to maximum power and the quad-phase component

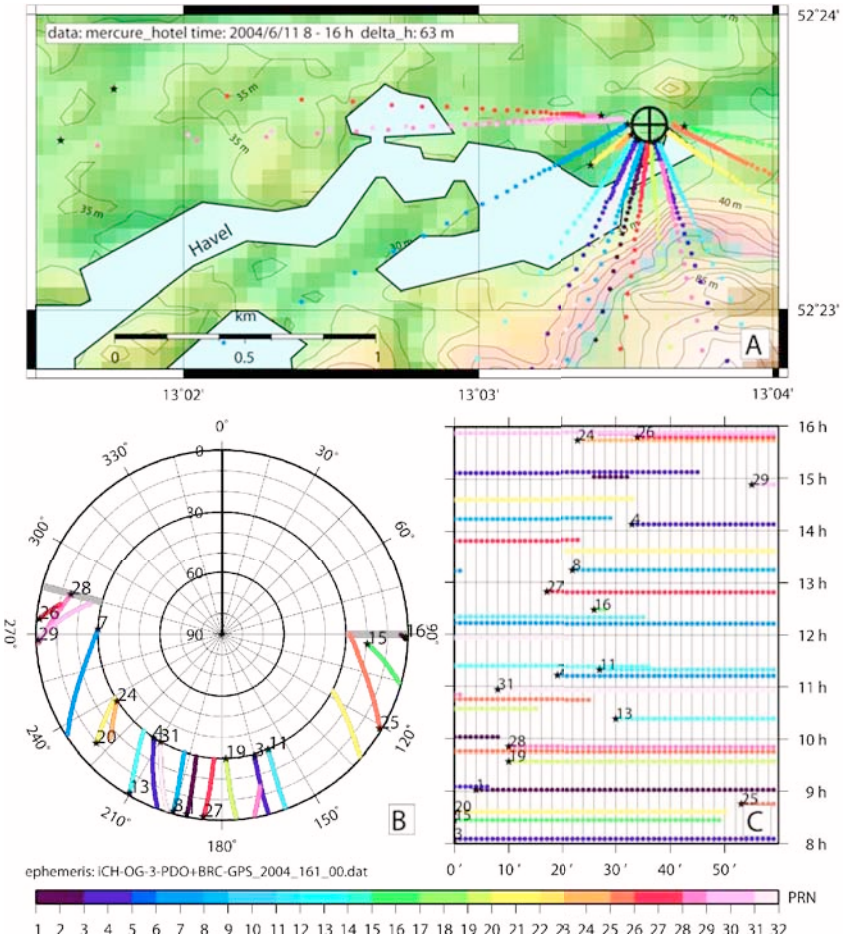

Fig. 5.31: *Schedule of refl ection events at the Mercure Hotel in Potsdam: Panel A shows the possible locations of specular refl ection points of visible GPS satellites (prn's) which can be observed on June 11, 2004, at the receiver location on top the hotel building (marked by a circle with a cross). Panel B shows the position of the satellites in a skyplot. Panel C shows the time schedule of satellite visibility. Calculations are based on ephemeris data.*

DOI: 10.2312/GFZ.b103-08104

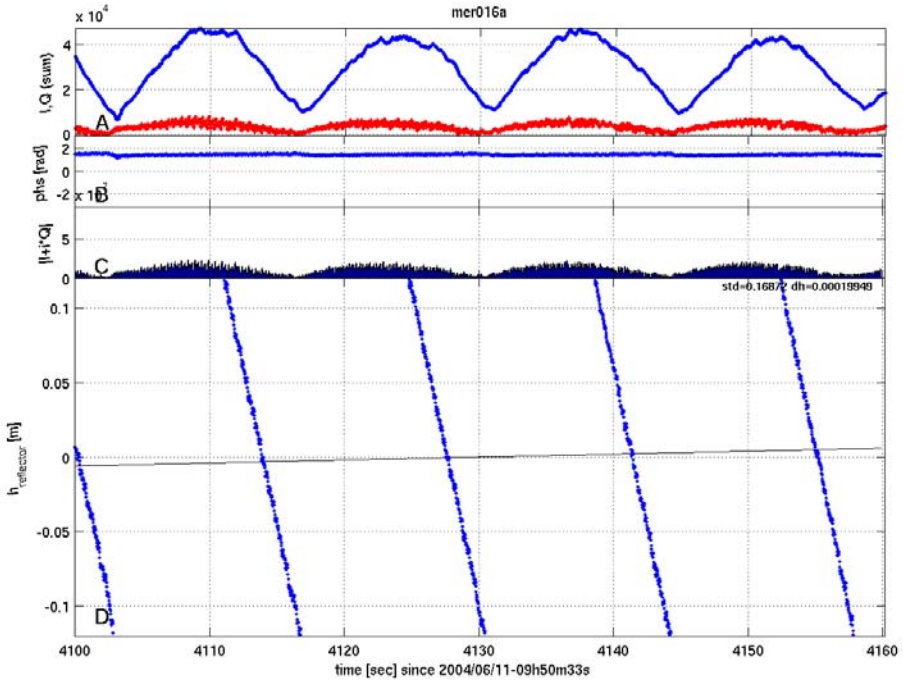

Fig. 5.32: *Strategy 1 to process the measured in- and quad-phase correlation data (panel A, blue and red curve) for phase (panel B) and relative height (panel D) calculation, respectively. Panel C shows the amplitude of the processed data.*

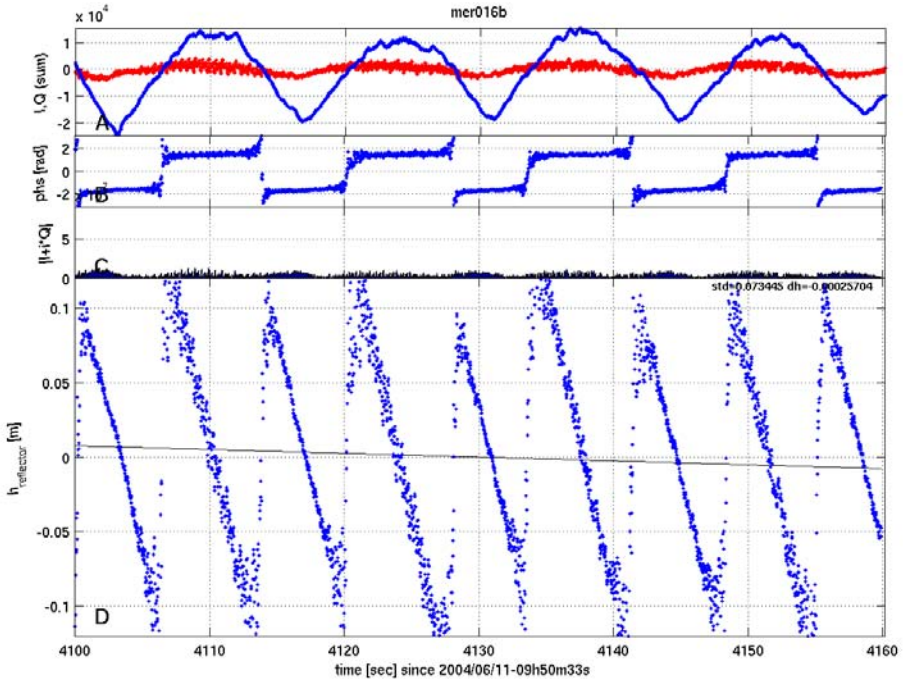

Fig. 5.33: *Strategy 2 to process the measured in- and quad-phase correlation data (panel A, blue and red curve) for phase (panel B) and relative height (panel D) calculation, respectively. Panel C shows the amplitude of the processed data.*

near to zero. Thus, at low receiver elevations, like in the Mercure Hotel experiment, the quad-phase component data often contain no or only a weak fraction of the reflected signal.

Different strategies have been tested to extract the altimetric information from observations made at low receiver elevations. Fig. 5.32,Fig. 5.33,Fig. 5.34, and Fig. 5.35 show the results of 4 strategies to process the measured in- and quad-phase correlation data (panel A, blue and red curve) for phase (panel B) and relative height (panel D) calculations, respectively. Panel C shows the amplitude of the processed data. A 60 sec long extract of the data set recorded at Mercure Hotel on June 11, 2004 beginning at 09:50:33 GPST is used.

The first strategy (Fig. 5.32) only applies a short running mean filter of 20 samples to both the in- and quad-phase data. A strong interferometric pulsating signal can clearly be observed in the in-phase component. The in-phase component contains a strong fraction of the correlation energy of the direct signal because the in-phase component oscillates around a mean correlation sum of about 3000. The quad-phase component also contains the pulsating signal, but with very low intensity and

DOI: 10.2312/GFZ.b103-08104

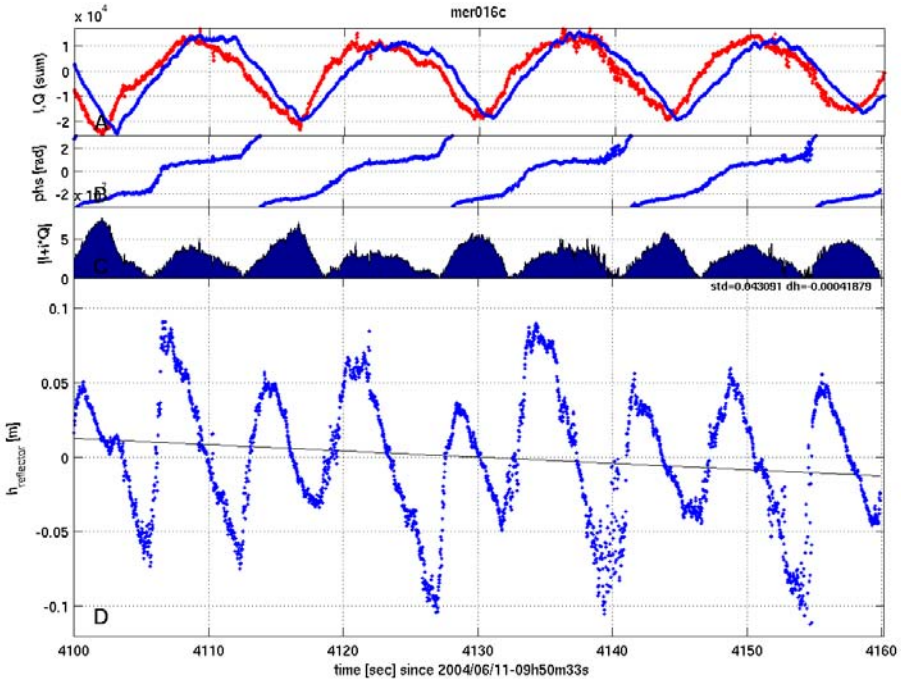

Fig. 5.34: Strategy 3 to process the measured in- and quad-phase correlation data (panel A, blue and red curve) for phase (panel B) and relative height (panel D) calculation, respectively. Panel C shows the amplitude of the processed data.

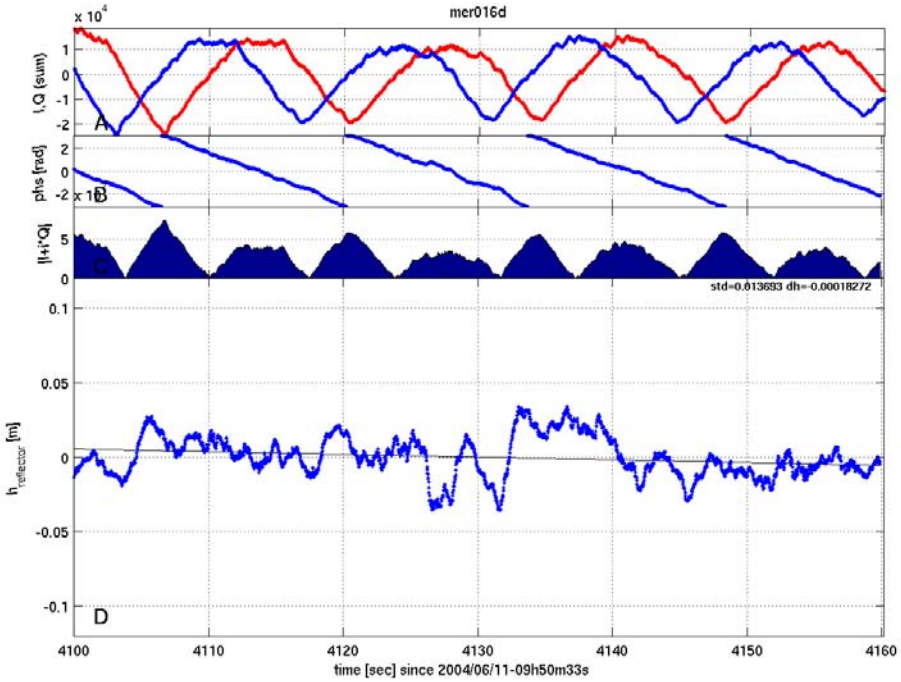

Fig. 5.35: Strategy 4 to process the measured in- and quad-phase correlation data (panel A, blue and red curve) for phase (panel B) and relative height (panel D) calculation, respectively. Panel C shows the amplitude of the processed data.

high noise level. A suitable phase and height cannot be calculated from both components.

The second strategy (Fig. 5.33) calculates a long running mean filter of 1500 samples or 30 sec length and subtracts the mean fraction from both components to suppress the fraction of the direct signal. Now the interferometric pulsating signal of both components oscillates around zero and a developing phase can be calculated from the data. A reasonable height cannot be derived from the in- and quad-phase data, because the energy of the interferometric signal is asymmetrically distributed to both components I, and Q. The in-phase component still contains the main fraction of the interferometric signal. To achieve a symmetric energy distribution, the third strategy (Fig. 5.34) amplifies the quad-phase component with a running Automatic Gain Control (AGC) filter of 30-sec length to the energy level of the in-phase component. Beforehand the short running mean filter applied to the quad-phase data was increased from 20 samples to a length of 50 samples. An increasing phase can be calculated and a reasonable height profile can be derived from the data. Two points militate against the third strategy. The elevation of the observed GPS satellite is decreasing from 9.4° to 9.0°. Thus, the phase

DOI: 10.2312/GFZ.b103-08104

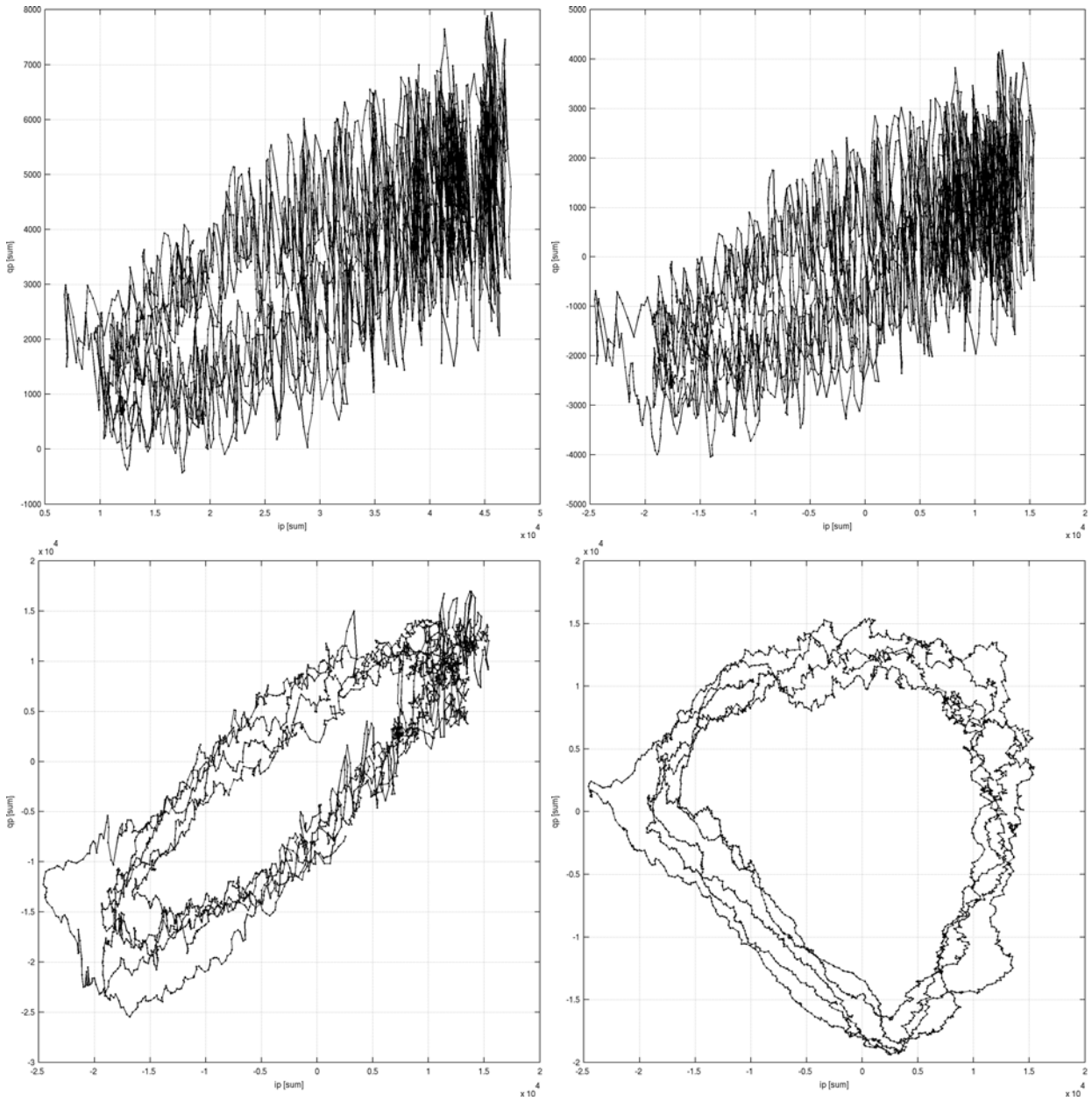

Fig. 5.36: *Results of strategies 1-4 to process the measured in- and quad-phase correlation data (see Fig. 5.32-5.35). Cross plot of in- and quad-phase data.*

should decrease as the path length, the reflected signal has to travel, decreases with setting elevation. The Havel wave heights are visually estimated to be much lower (in the range of about ± 5 cm) than the heights derived from the third strategy data.

The problem can be solved by modeling the quad-phase component from the in-phase data which contains the full fraction of the reflected signal. Fig. 5.35 shows the results of the processing strategy finally applied. The recorded quad-phase data is neglected and the quad-phase component is modeled from the in-phase data and the observed interferometric frequency, as already discussed in section 4.4.2 on page 54. Following Eq. 4.1 and using the observed interferometric frequency of 0.07 Hz, the in-phase data is shifted 179 samples back in time (delayed) and represents the new quad-phase model data. The calculated phase develops as expected and a height time series can be calculated which is consistent with the visually observed Havel wave heights.

Fig. 5.36 illustrates the behavior of the phasor depending on the applied strategy in the corresponding graphs . Only the phasor of the fourth strategy shows a quasi-circular behavior (left graphs, bottom right) or helical structure if the phasor is plotted versus time (see Fig. C.1, bottom right). An interesting feature can be seen in the phasor plots of the fourth strategy: The circular behavior is lost

DOI: 10.2312/GFZ.b103-08104

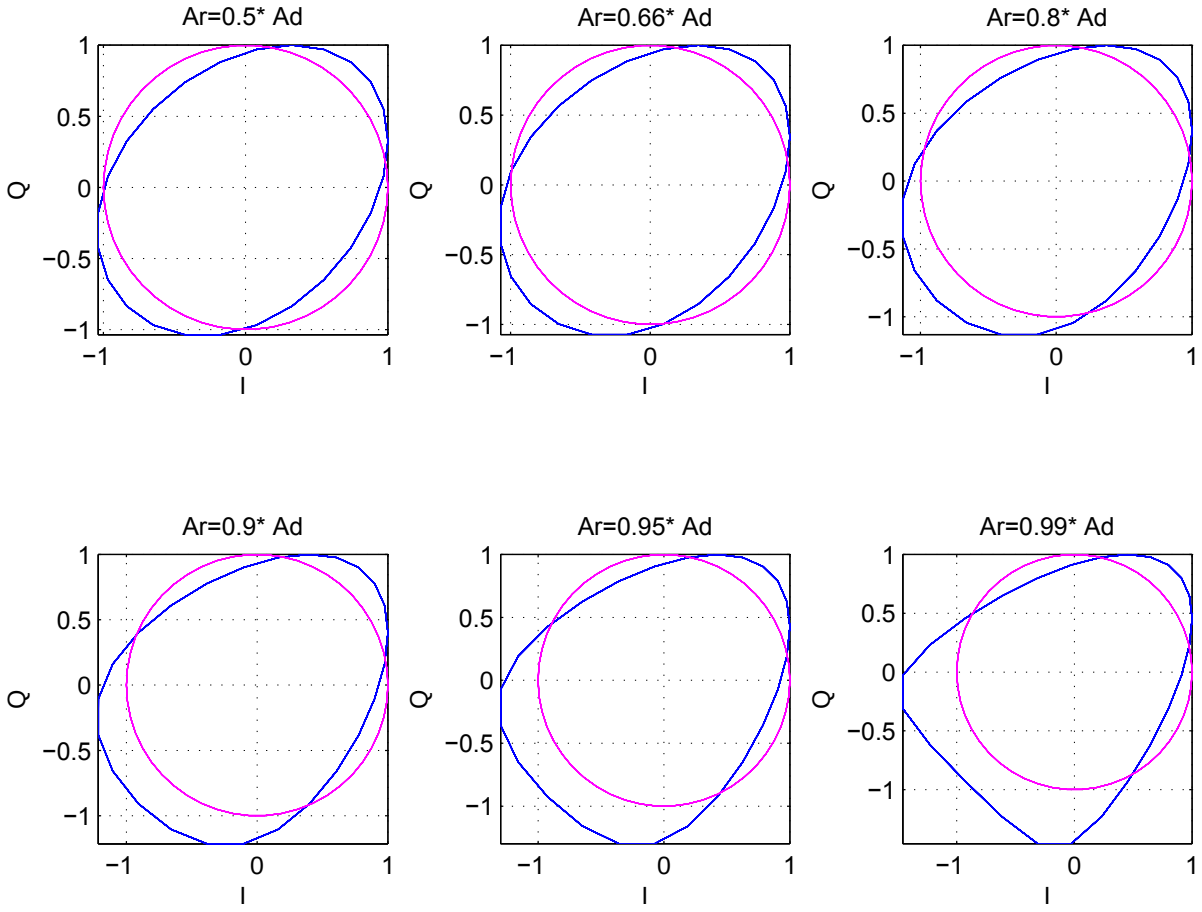

Fig. 5.37: *Rotational behavior of the I,Q vector (blue) for 6 different relationships between the signal amplitudes of direct and reflected signal. For comparison a circular behavior is plotted in magenta.*

in the lower left quadrant of the phasor plot. Hence, the reflection height information is lost during the measurement which might be a shadowing effect. A similar effect could not be observed in the Fahrenberg data (see Fig. 4.13 on page 60) or the Königsstuhl data (see Fig. 5.50 on page 102).

A numerical simulation was performed in order to see how the signal which arrives at the receiver reacts on different amplitude relationships between the direct and reflected signal. The resulting signal is a composite of the direct signal and the reflected signal, each signal with a specific amplitude and a phase. In the simulation the sampling frequency was set to 50 Hz and the bandwidth of the PLL tracking loop was set to 25 Hz. The amplitude of the reflected signal was set to 0.5, 0.66, 0.8, 0.9, 0.95 and 0.99 fractional parts of the amplitude of the direct signal. Fig. 5.37 shows the rotational behavior of the I,Q vector (blue) for the different relationships between the signal amplitudes of direct and reflected signal. In case the reflected signal has an amplitude of 0.9 to 0.99 in relation to the direct signal, the simulated I-Q vector describes a non-circular movement. For comparison a circular behavior is plottet in magenta. This indicates that the tracking loop cannot follow the signal fast enough so that this non-circular behavior is generated like it is observed in the measured data.

5.3.3 Data Analysis and Discussion

Fig. 5.38 shows the extended dataset of the previously discussed reflection event of PRN 31 starting at 09:50:33 GPST. Panel A plots the filtered in- and modeled quad-phase data, panel B the derived phase, panel C the power of the signal and panel D the derived dpath (blue) and model dpath (pink). The deviation of dpath from the flat mirror-like reflector model is plotted in panel E. No large phase inconsistency can be observed which might cause a cycle slip. Thus, the dpath data does not exceed the offset from the target model and no multiples of λ_{L1} have to be inserted into the data (panel F). Thus, the derived height profile has no height jumps and varies with a STD of 4.3 cm around a mean height of 29.0 m reflector height. The dominant frequency in the spectrum of the measured

DOI: 10.2312/GFZ.b103-08104

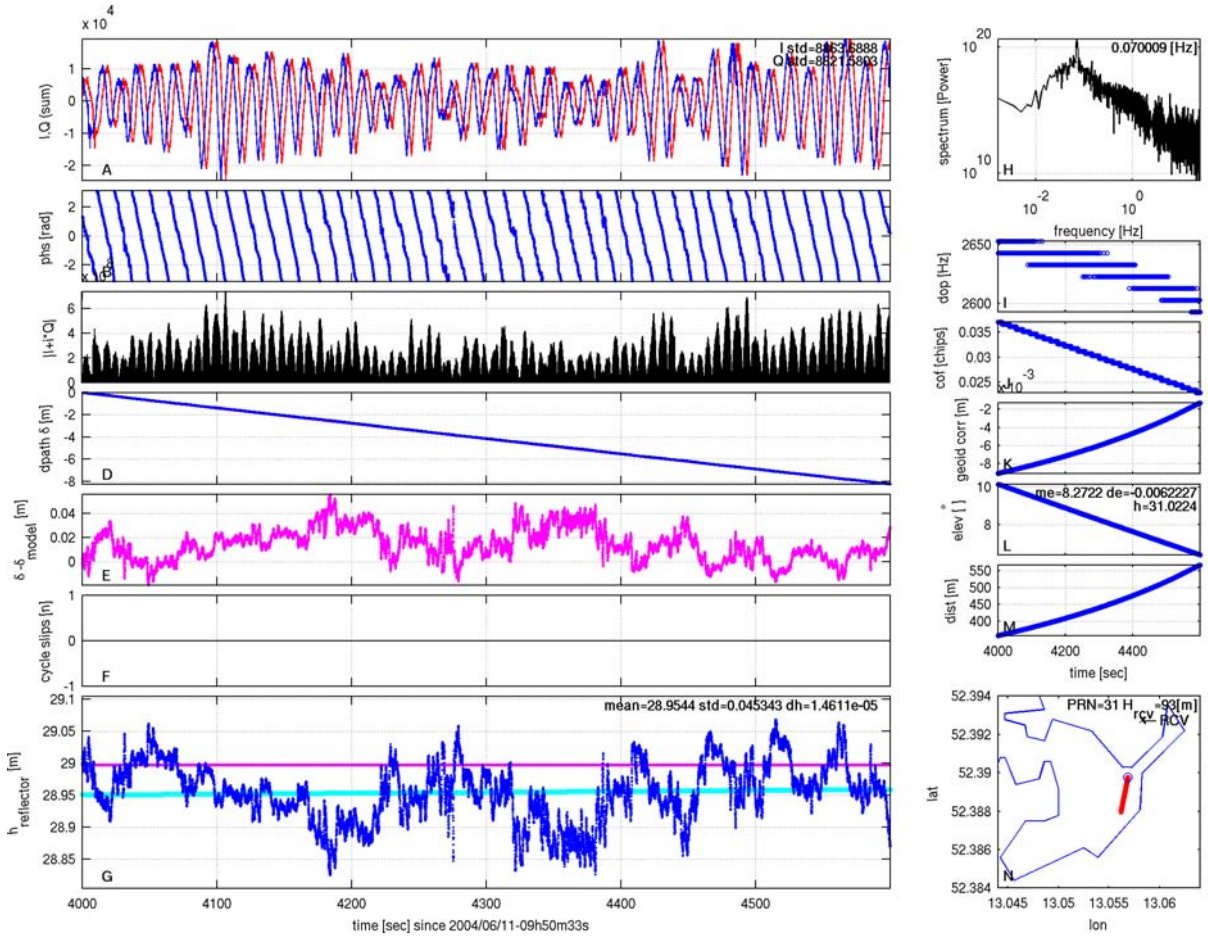

Fig. 5.38: *Reflection event of PRN 31 starting on June 11, 2004 at 09:50:33 GPST, recorded at Mercure Hotel about 63 m above the Havel river used as reflector.*

in- and quad-phase data is about 0.0700 Hz, shown in the spectrum in panel H. The Doppler of the carrier frequency varies slightly from 2650 Hz to 2600 Hz (panel I). The code offset of the measuring slave correlator channel decreases from 0.036 to 0.023 chips (panel J). The applied geoid correction varies from 1.3 to2.1 cm (panel K) while the elevation drops from 10° to 6° (panel L). With the mean elevation and the elevation change rate an absolute height of 31.0 m of the reflector can be estimated with a peak frequency of 0.0700 Hz for the observed interferometric pattern. The distance from the specular reflection point to the receiver is increasing from 356 m to 565 m as the observed satellite is setting (panel M). Panel N shows the geo-location of the reflection point with respect to the river shoreline.

Fig. 5.39 illustrates the good consistency of the recorded reflection data on June 11, 2004. In panel A the derived height profile is plotted versus time and panel B geo-locates the estimated specular reflection point. The top and middle panels show a parallel recording of the reflection event of PRN 1 and 19, both starting at 09:08:56 GPST. The bottom panel shows the recording of the reflection event of PRN 13, starting at 10:25:56 GPST. Although recorded at slightly different times and locations, all height profiles vary with an SNR of 4–6 cm around a mean reflector height of 29.00 m, 29.03 m and 29.04 m. Using the observed interferometric peak frequencies 0.0800 Hz, 0.0800 Hz and 0.0767 Hz and the appropriate mean elevation and elevation change rates, the absolute height estimates result in 31.56 m, 30.92 and 31.22 m, respectively.

Taking all 4 measurements into account, a mean height of 29.01 m ± 0.04 m can be derived from the detrended relative height observations (Fig. 5.40, panel A). The calculated SNR values change only slightly between the different observations (Fig. 5.40, panel B) and can be interpreted as a mean wave height estimate. The mean SNR value of 0.05 m ± 0.01 m shows good agreement with the visual observations. The absolute height estimates show good agreement between the single measurements (Fig. 5.40, panel C) and result in a mean absolute height estimate of 31.18 m ± 0.28 m. Obviously all measurements have a height offset of 2.17 m compared to the

DOI: 10.2312/GFZ.b103-08104

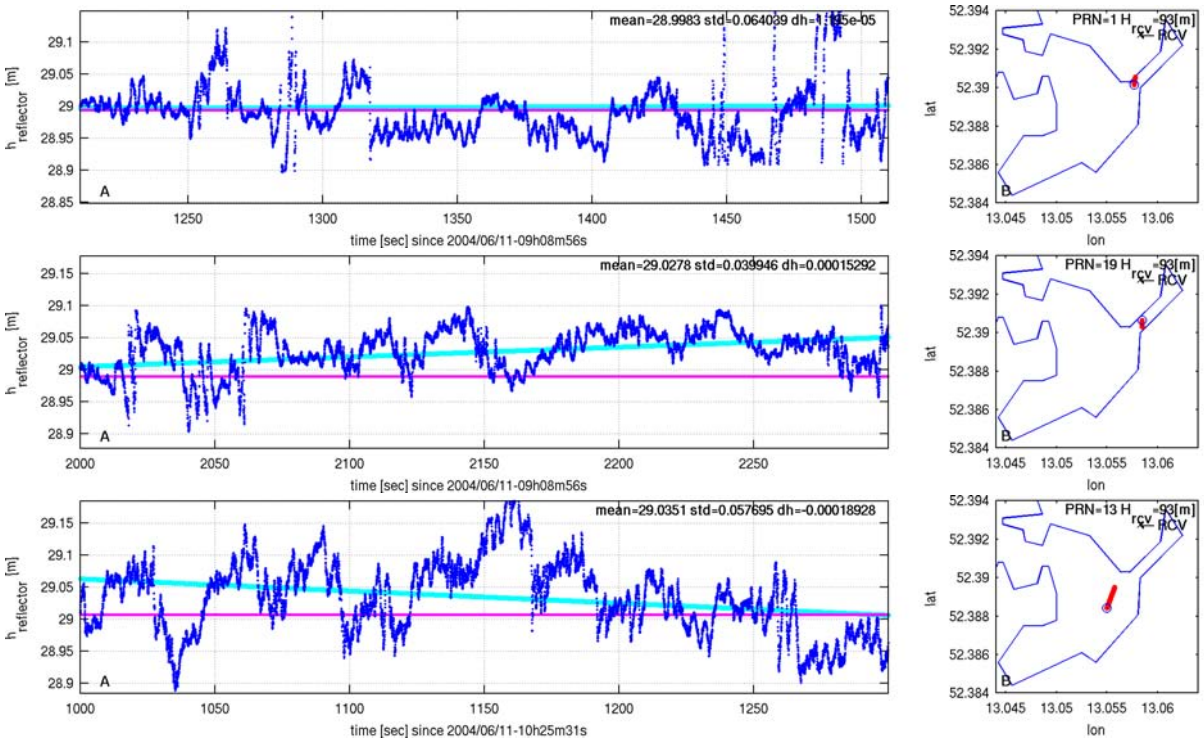

Fig. 5.39: *Top and middle: Parallel recordings of reflection event of PRN 1 and 19, both starting at 09:08:56 GPST. Bottom: Reflection event of PRN 13, starting at 10:25:56 GPST on June 11, 2004.*

detrended relative height measurements in Fig. 5.40, panel A. The height offset can be caused by the limited spectral resolution when estimating the interferometric peak frequency. More likely, the offset is caused by uncorrected tropospheric influences. Although the appropriate mean elevation and elevation change rates used during calculation are corrected for the bending effect caused by the troposphere, the troposphere typically causes an excess path of about 2.3 m in zenith direction.

Analysing the data of PRN 1 (Fig. 5.39, top), several processed cycle slips, e.g. at 1285 s, 1449 s and 1485 s and an increased SNR value can be observed (Fig. 5.40, panel B, id 1). The increase in the number of cycle slips occurring towards the end of the reflection recording can be explained by the approach of the reflection point toward the river shore-line. In the following section the footprint size is estimated at the water/land transition zone.

5.3.4 Footprint Size Estimation

Fig. 5.41 shows the further extended dataset of the previously discussed reflection event of PRN 31, starting at 09:50:33 GPST. Panel A plots the filtered in- and modeled quad-phase data, panel B the derived phase, panel C the power of the signal and panel D the derived detrended reflector height estimate versus the recording time. This time, the cycle slip correction was switched off. Between 4000 sec and 4670 sec a strong reflection can be identified with the harmonically oscillating in- and

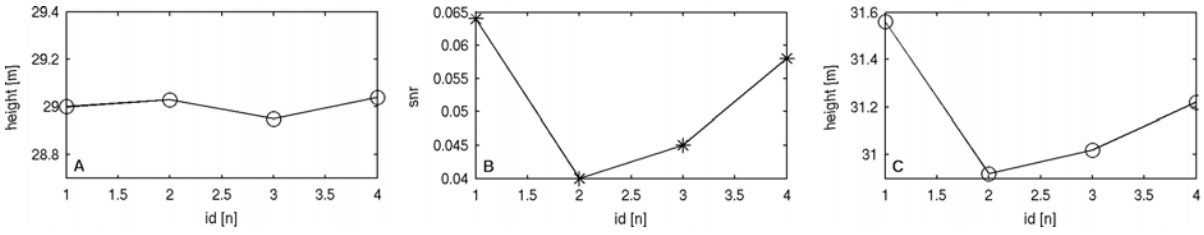

Fig. 5.40: *Altimetric heights of the Havel reflector, derived from detrended relative height observations (panel A) with the observed SNR values (panel B). Panel C shows the absolute heights calculated from the observed interferometric peak frequency and mean elevation and elevation change rates.*

DOI: 10.2312/GFZ.b103-08104

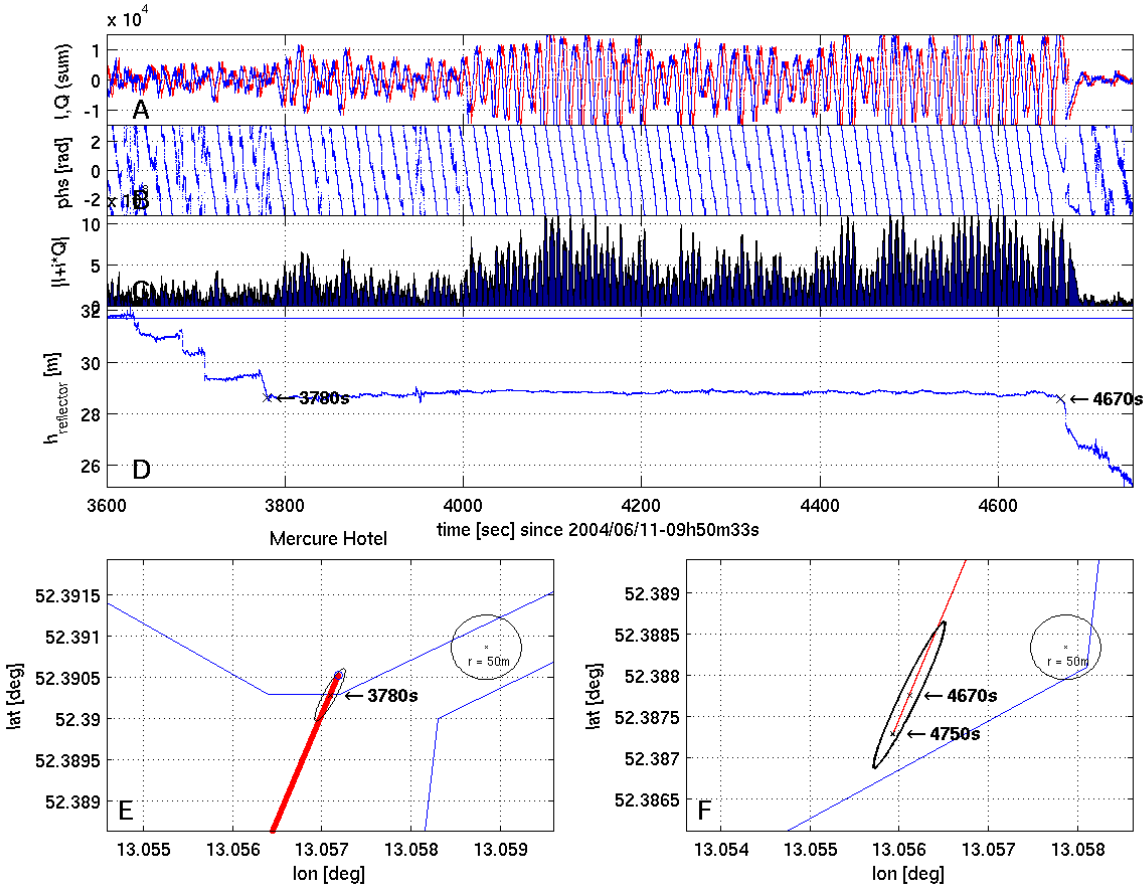

Fig. 5.41: *Extended dataset of reflection event of PRN 31 starting at 09:50:33 GPST. In- and quad-phase data (panel a), phase (panel B), signal amplitude (panel C) and reflector height (panel D) are plotted versus the time. Panel E and panel F show the geolocated reflection point (red) at the marked time 3780 s and 4670 s at the beginning and end of the height profile. The marked points are surrounded by an ellipse (black), representing the first fresnel zone.*

quad-phase data (panel A), a clearly growing phase (panel B) and a strongly fluctuating amplitude data (panel C). After 4670 sec an abrupt amplitude drop can be observed, several cycle slips occur and the noise level of in- and quad phase data rises significantly. The specular reflection point approaches the south shoreline of the Havel and the first Fresnel zone nearly touches the shoreline (panel F). The fact that the reflection stops before the reflection point reaches the south shoreline can be explained by the local geometry. High trees are growing directly at the shoreline. Thus, the GPS satellite signal is blocked by the leaves of the trees up to a certain distance from the shoreline.

Between 3780 sec and 4000 sec a slight drop in amplitude can be observed, accompanied with a slight increase of the noise level. At 3780 sec the reflection point is exactly at the transition zone between land and water of the north Havel shoreline (panel E). Thus, already with part of the Fresnel zone touching the water reflector surface, a stable reflection signal can be acquired. When the reflection point travels over land during the time before 3780 sec, the noise level is further increased and the amplitude has further decreased. The phase becomes temporally unstable and several cycle slips are introduced. Panel E and F are plotted with the same scale. The increase of the first Fresnel zone area with setting elevation can be seen at 3780 sec with 11.5° elevation and at 4670 sec with 5.9° elevation.

In the following the dataset is analysed with wavelet techniques using the continuous wavelet transform. The continuous wavelet transform [Torrence and Compo, 1998] of a discrete sequence is defined as the convolution of the sequence with a scaled and translated version of a function, called the mother wavelet. By varying the wavelet scale and translating along the localized time index, one can construct a two-dimensional picture showing both, the amplitude of any features versus the scale and how this amplitude varies with time [Helm et al., 2004]. The result represents the wavelet energy spectrum. In this study the Morlet wavelet has been used. The relationship between wavelet

DOI: 10.2312/GFZ.b103-08104

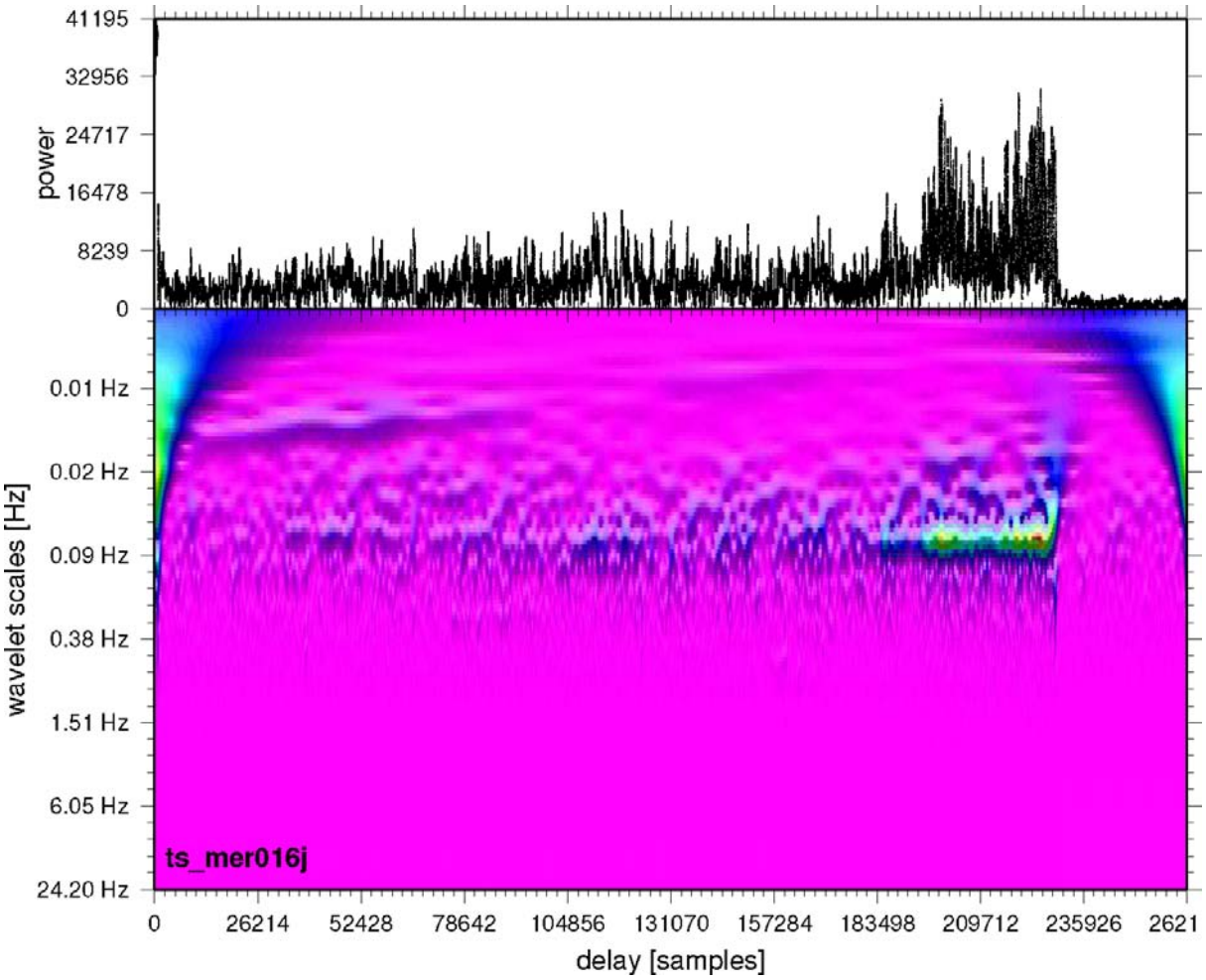

Fig. 5.42: *Top: The power of the complex phasor $I + iQ$ is plotted after subtracting a 30 sec running mean in order to suppress the energy of the direct signal. Bottom: The energy distribution of the complex phasor in the wavelet domain is shown.*

scale and Fourier frequency depends on the wavelet function used and can be derived analytically for a particular wavelet function. In the wavelet spectrum, signals with constant frequency appear as horizontal lines or as line segments, if the signal occurs only sporadically.

Fig. 5.42 shows the resulting power of the in- and quad-phase data taken as complex phasor $I + iQ$ (top panel). In order to suppress the energy of the direct signal, a 30-sec running mean has been subtracted from the in- and quad-phase data. In the lower panel the energy distribution of the complex phasor in the wavelet domain is shown. Beside the energy caused by the edge effects at very low frequencies a clear signal at about 0.08 Hz can be seen between the samples 200000 and 230000. The signal identified in the wavelet domain is accompanied by a strong increase in reflection power by a factor of 3. At earlier times a much weaker signal can sporadically be observed in the same frequency range. Additionally, a lower frequency shift can be observed at the beginning of the measurements, starting at about 0.015 Hz and lowering down to 0.01 Hz. Thus, with wavelet techniques not only strong, but also weak reflection signatures can be identified and localized in the recorded height time series.

DOI: 10.2312/GFZ.b103-08104

5.4 Königsstuhl Experiment

5.4.1 Experimental Setup and Data Acquisition

The experiment was conducted on September 20–24, 2004, during daytime at the Königsstuhl chalk cliff top in the Jasmund national park on Rügen island,Germany. Fig. 5.43, Fig. 5.44, Fig. 5.45, Fig. 5.46, and Fig. 5.47 show photos from the surface conditions at the coastline of Königsstuhl.

The Königsstuhl is an exposed Cretaceous chalk cliff developed from a sea extension during the Liturina transgression which took place between 6000 and 10000 a.D. . From the Königsstuhl cliff top (54.57°N, 13.66°E) at a height of about 118 m above sea level an unobstructed view (Fig. 5.3) to the baltic sea is available from about -30° to 120° azimuth. Every day a single wide field-of-view RHCP patch antenna was positioned on top of an aluminium tripod, which had to be reestablished every day due to security reasons. Hence, the antenna height varied from 2.71 to 2.65, 2.64 and 2.68 m on September 21, 22, 23 and 24, respectively. On September 20 the tripod had a height of 4.98 m, but caused by wind stress the antenna oscillated by about 1 cm. Thus, the tripod height was reduced on the following days and wind-induced movements of the antenna could be reduced significantly. The antenna was tilted by 45° toward the horizon and directed to 50° azimuth. On September 21 between 09:00 and 16:00 tests were conducted with a tilt angle of 90°. The OpenGPS receiver was protected against weather conditions by an aluminium box housing. The power supply could be maintained by AC main power.

Simulation calculations based on ephemeris data of September 20, 2004, illustrate the area of the baltic sea which can be covered with specular reflection monitoring points (Fig. 5.48, panel A). In the simulation data shown the satellite observations were limited to elevations between 0° and 45° and -45° and 120° azimuth (Fig. 5.48, panel B). With a simulated antenna height of 120 m above the reflector 2–6 reflection events can be expected in parallel at the Königsstuhl location throughout the day (Fig. 5.48, panel C).

The OpenGPS receiver was working during all days in open-loop multi reflection mode (see section 4.3.2). This mode allows the tracking of up to 8 direct GPS signals for navigation and open-loop tracking of up to 4 independent reflected GPS signals simultaneously for altimetry. The measurement mask of the receiver was set to reflection events between -90° and 180° azimuth. Reflection observations were recorded up to elevations between 45° and 85°. During a reflection event the OpenGPS receiver recorded the in-phase and quad-phase correlation data with a rate of 50 Hz into binary data files.

217 data sets could be recorded between September 20, 15:10 GPST and September 24, 10:48 GPST. Small data sets with file sizes lower than 1 MByte were discarded. The file size of the remaining data sets varied between 2.5 MByte and 20 MByte. The file size of a 4-hour long record was 60 MByte.

5.4.2 Data Processing

Due to the low observation height of about 118 m of the receiver above the reflector, the reflected GPS signals arrive at the receiver antenna only with a comparably small delay after the direct signal. Thus, the correlation signal of direct and reflected signal superpose each other. Like in the Mercure experiment different strategies have been tested for a measured dataset to extract the altimetric information. The dataset used was recorded at Königsstuhl on September 21, 2004, beginning at 12:41:19 GPST, using the signals of PRN 8. Fig. 5.49, Fig. 5.50, Fig. 5.51, and Fig. 5.52 show the results of different data processing strategy tests for phase and relative height calculations, respectively.

In the first strategy (Fig. 5.49) no filtering is applied to the data. A strong interferometric pulsating signal can be clearly observed in the in-phase component. The in-phase component contains a strong fraction of the correlation energy of the direct signal because the component oscillates around a mean correlation sum of about 3000. The quad-phase component also contains the pulsating signal, but with much lower intensity and a high noise level. A suitable phase and height cannot be calculated from both components. Thus, no development in the calculated phase can be observed (panel B). The sawtooth structure of the derived height profile (panel D) results from the applied cycle slip correction algorithm, which forces the relative height signal to a certain distance from the modeled

DOI: 10.2312/GFZ.b103-08104

target height. The interferometric pulsating – caused by the reflected signal – can be sensed already in the amplitude of the signal (panel C). Fig. 5.53, top right, illustrates the behavior of the complex phasor with time. Noise is dominant and no rotational behavior can be seen.

In the second strategy (Fig. 5.50) a long running mean of 1500 samples or 30 sec length was calculated and subtracted from each in- and quad-phase time series to minimize the fraction of the correlation energy of the direct signal. Hence, the interferometric pattern caused by the reflection results in harmonic oscillations around zero for both components. A short running mean filter was applied to both data components to lower the noise level, using a filter length of 50 samples for the in-phase data and 100 samples for the quad-phase data. Beforehand, the quad-phase component was amplified with an AGC filter, which was programmed to amplify the quad-phase data to the amplitude of the in-phase data. A continuously growing phase development can be observed and a reasonable height profile can be derived from geometry and phase data. Like in the Mercure Hotel experiment 2 points militate against this strategy: Firstly, the elevation of the observed GPS satellite PRN 8 is setting from 3.3° to 2.9°. Thus, the phase is expected to decrease as the path length, the reflected signal has to travel, decreases with setting elevation. Secondly, the derived heights vary in a range of several decimeter while, from visual observation, baltic sea wave heights near the coast vary in the range of about ± 20 cm. In Fig. 5.53, bottom right, a rotational, but asymmetric behavior of the phase can be seen, which is limited to one diagonal of the square.

Fig. 5.43: *Photo taken on September 20, 2004, at 17:00, showing the daily sea-surface conditions at the coastline of Königsstuhl.*

Fig. 5.44: *Photo taken on September 21, 2004, at 14:51, showing the daily sea-surface conditions at the coastline of Königsstuhl.*

DOI: 10.2312/GFZ.b103-08104

Fig. 5.45: *Photo taken on September 22, 2004, at 11:47, showing the daily sea-surface conditions at the coastline of Königsstuhl.*

Fig. 5.46: *Photo taken on September 23, 2004, at 16:03, showing the daily sea-surface conditions at the coastline of Königsstuhl.*

Fig. 5.47: *Photo taken on September 24, 2004, at 08:12, showing the daily sea-surface conditions at the coastline of Königsstuhl.*

DOI: 10.2312/GFZ.b103-08104

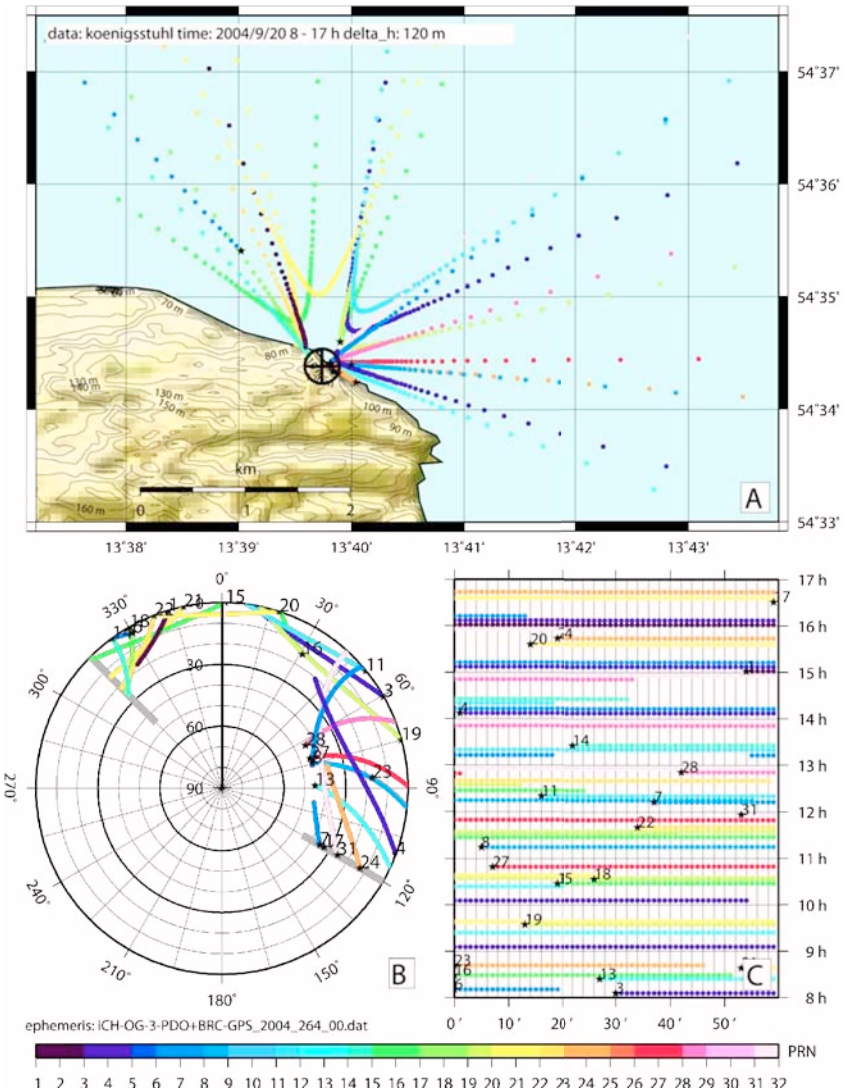

Fig. 5.48: *Schedule of refl ection events at the Königsstuhl on Rügen: Panel A shows the possible location of specular refl ection points of visible GPS satellites (prn's) which could be observed on September 20, 2004, at the receiver location (marked by a circle with a cross). Panel B shows the position of the satellites. Panel C shows the time schedule of satellite visibility. Calculations were based on ephemeris data.*

The third strategy (Fig. 5.51) solves the problem by modeling the quad-phase component from the in-phase data which contains the full fraction of the reflected signal. The recorded quad-phase data, containing only a very small and noisy fraction of the reflected signal, is neglected and the quad-phase component is modeled from the in-phase data and the observed interferometric frequency as already discussed in section 4.4.2 on page 54. Following Eq. 4.1 and using the observed interferometric frequency of 0.124 Hz, the in-phase data is shifted 101 samples back in time (delayed) representing the new quad-phase model data. The phase decreases with setting elevation and a height time series can be calculated that is consistent with the visually observed baltic sea wave heights. Fig. 5.53, top right, shows a circular rotating phasor with a certain noise level superimposed.

The fourth strategy (Fig. 5.52) additionally applies a short running mean filter to both data components to lower the noise level. A fi lter length of 25 samples applied to both components exposes to be the best ratio between noise fi ltering effect and loosing height signal resolution. Fig.5.53, bottom right, shows a circular, rotating phasor with a set of harmonic signals superimposed.

The processing steps of the fourth strategy are chosen as standard processing for all follow-on Königsstuhl data sets: The infl uence of the direct GPS signal is suppressed by subtracting the mean correlation energy from each in-phase and quad-phase component. Hence, a 30-sec running mean filter is applied to the correlation data and subtracted. Additionally, in-phase and the modeled quad-phase data are filtered by a 0.4-sec running mean filter (Fig. 5.54, panel A). Further on the phase is calculated from a four quadrant arctangent and unwrapped (Fig. 5.54, panel B). The path difference δ between the direct and refl ected signal is calculated by multiplying the phase with the wavelength λ_{L1} of the Doppler corrected carrier frequency (Fig. 5.54, panel D). Cycle slips occurring are treated by inserting multiples of λ_{L1} cycles in case the measured path deviates from a modeled path beyond a previously defi ned threshold (Fig.5.54, panel E and F). With the derived and desliped time series

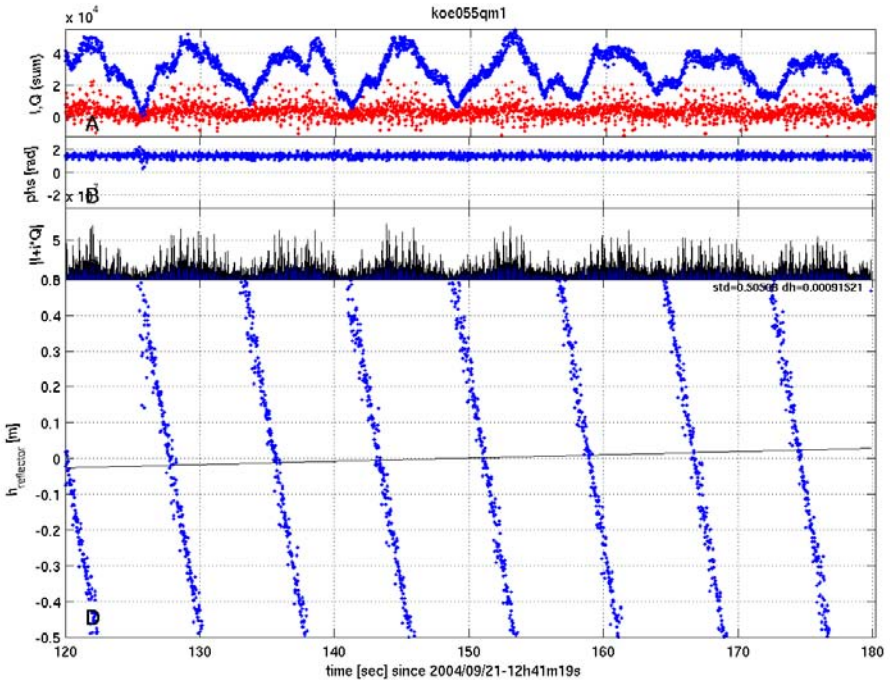

Fig. 5.49: *Processing strategy 1: In-phase and quad-phase correlation sums (panel A), phase (panel B), signal amplitude (panel C) and derived height time series (panel D).*

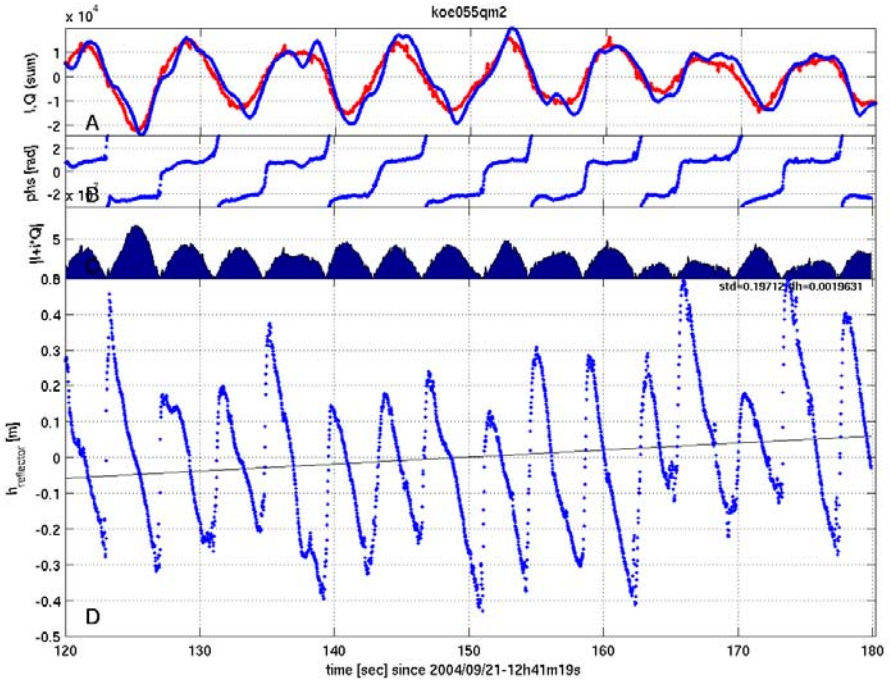

Fig. 5.50: *Processing strategy 2: In-phase and quad-phase correlation sums (panel A), phase (panel B), signal amplitude (panel C) and derived height time series (panel D).*

of δ and the known geometry of receiver, transmitter and reflection point (continuously changing with time), the relative height change of the reflection point can be calculated. By starting with an estimated reflector height and carefully removing the influence of troposphere and known height gradients, an absolute height profile can be generated (Fig. 5.54, panel G). The influence of the troposphere is calculated from ECMWF data and ray-tracing analyses. The relative height gradient is derived from the EIGEN-CG01C geoid.

5.4.3 Data Analysis

At all days the roughness of the observed open sea surface was greater than the carrier wavelength λ_{L1}. Thus, sufficiently strong coherent signals could only be expected at lower elevation angles. Here the sea surface appears smooth enough according to the Rayleigh criterion (Eq. 2.11) to derive carrier phase-delay-based height observations. For low grazing angles the behavior of electromagnetic wave

DOI: 10.2312/GFZ.b103-08104

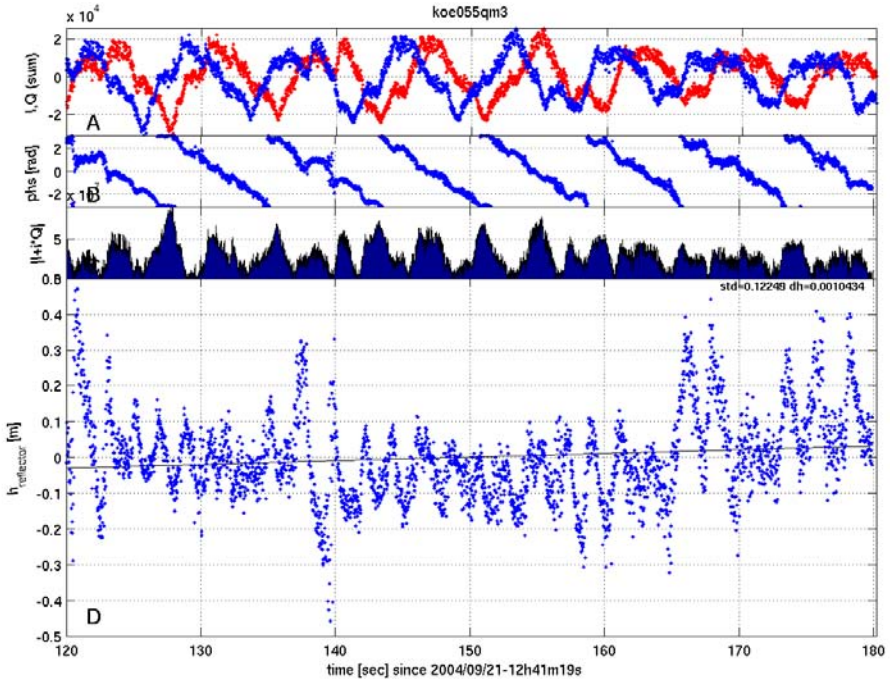

Fig. 5.51: *Processing strategy 3: In-phase and quad-phase correlation sums (panel A), phase (panel B), signal amplitude (panel C) and derived height time series (panel D).*

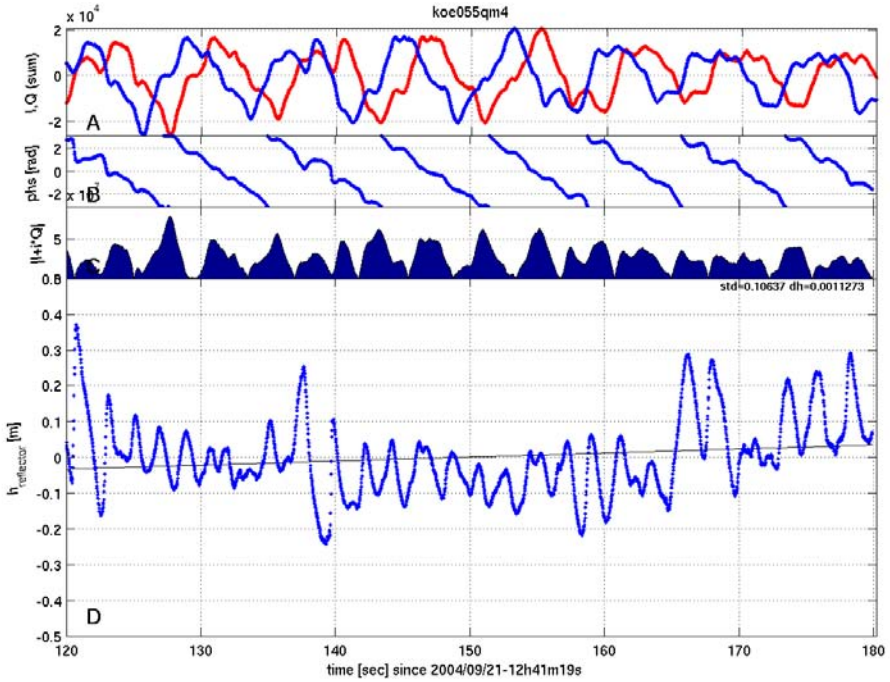

Fig. 5.52: *Processing strategy 4: In-phase and quad-phase correlation sums (panel A), phase (panel B), signal amplitude (panel C) and derived height time series (panel D).*

scattering is described in Voronovich [1994].

Fig. 5.54 shows a 25 minutes long continuous data recording made on September 20, 2004, which started at 15:30:14 GPST. The processing of the 6.4 MByte large binary data file took about 10 sec on an AMD ATHLON64 4000+ processor equipped with standard linux. The observed satellite PRN20 raised from 3.5° to 5.5° elevation (Fig. 5.54, panel L). Thus, the path of the reflected signal is extended by 10 m during the observed time interval (Fig. 5.54, panel D). After 800 sec a decrease in signal quality can be observed in the correlation sums (Fig. 5.54, panel A) and the derived phase (Fig. 5.54, panel B). The decreased quality of the phase data results in numerous cycle slips, which have to be corrected during post-processing. The derived path difference δ (Fig. 5.54, panel D) is compared with a modeled path difference δ_{model}. If the difference between derived and modeled value exceeds a predefined value, the appropriate integer number of cycles is inserted (Fig. 5.54, panel E). Thus, the number of automatically corrected cycle slips (Fig. 5.54, panel F) increased after 800 sec.

DOI: 10.2312/GFZ.b103-08104

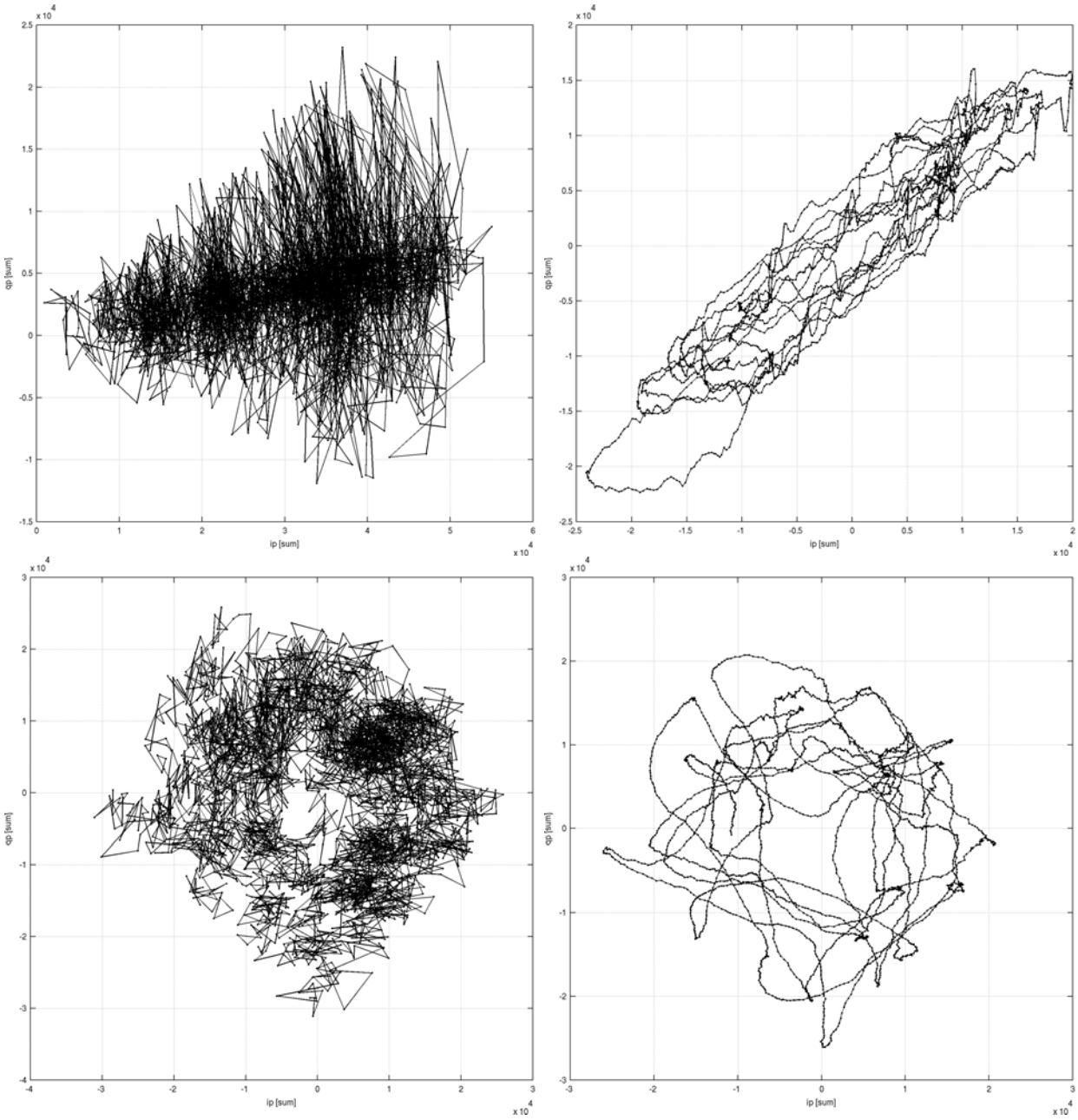

Fig. 5.53: *Different processing strategies. Complex phasor, in-phase data plotted versus quad-phase data. Fig. C.2, right panels show 3D plots of the complex phasor versus time.*

Fig. 5.55 shows a 17 minutes long continuous data recording made on the same day 20 minutes earlier on September 20, 2004, which started at 15:10:46 GPST. The observed satellite PRN31 dropped from 6.7° down to 1.2° elevation (Fig. 5.55, panel L). Thus, the path of the reflected signal abridges by 24 m during the observed time interval (Fig. 5.55, panel D). Here the signal quality improves with time. 400 sec after the start of the measurements, the derived phase data significantly improves in quality and after 700 sec a consistent continuous phase can be calculated from the in-phase and quad-phase data (Fig. 5.55, panel B). No cycle slip can be observed in the data. Therefore, no cycle slip corrections had to be added to the data (Fig. 5.55, panel F) 400 sec after epoch.

From the beginning of the measurement until 700 sec the height signal oscillates as expected around a mean height of 0.516 m (Fig. 5.55, panel G). Between 700 sec and 790 sec an unusual height rise of about 0.5 m can be seen. The height decreases again by 1.0 m when reaching 900 sec. After that, a height rise can be observed again. This height signal can be observed in a dedicated distance of the reflection point between 2400 m and 5700 m (Fig. 5.55, panel M). Firstly, we assumed that at larger distances from the coast, the sea surface is outside the area where the Rügen coast covers

DOI: 10.2312/GFZ.b103-08104

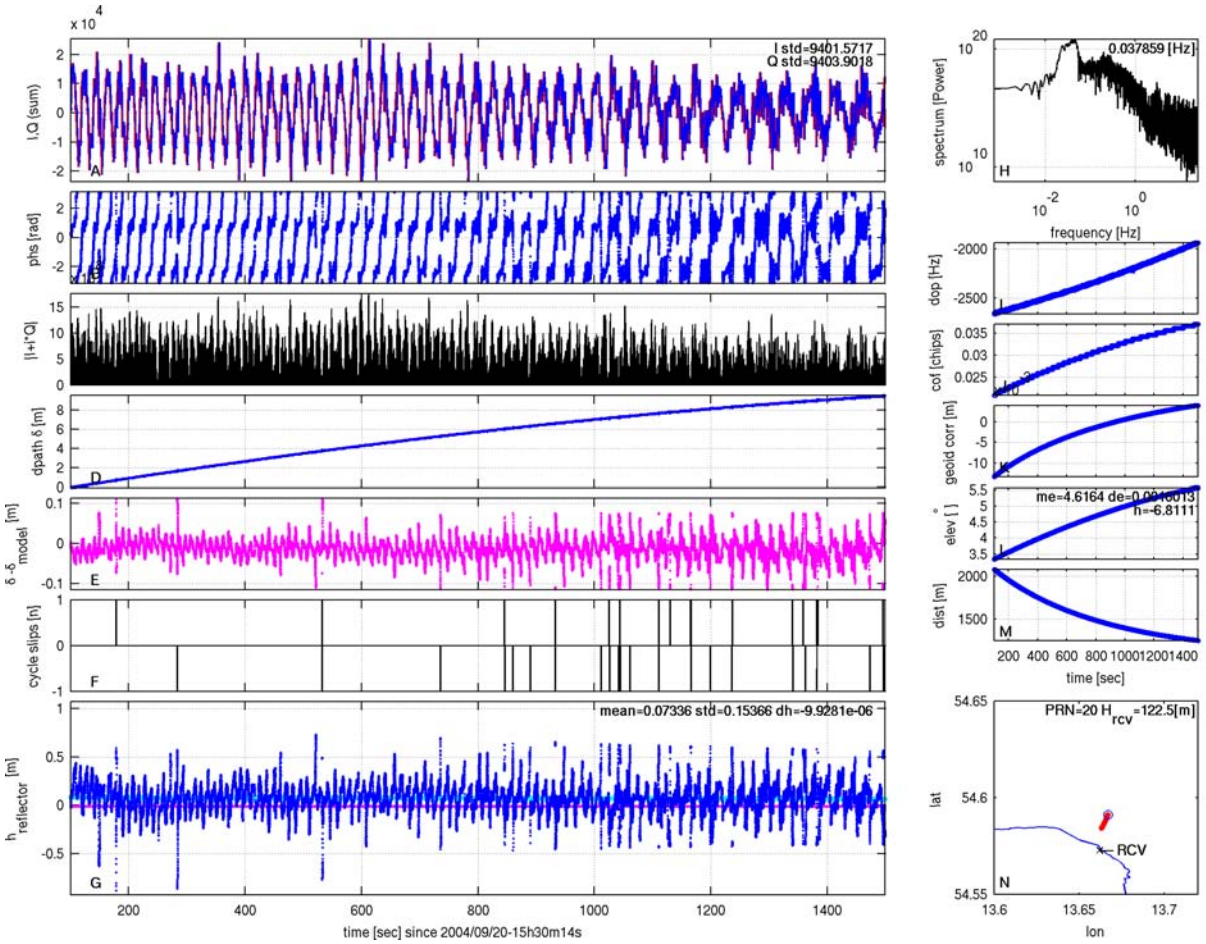

Fig. 5.54: *25 minutes long continuous data recording of PRN20 made on September 20, 2004, which started at 15:30:14 GPST.*

the water surface against the wind force. Thus, at larger distances, the wind can develop full wave heights and the height changes were assigned to oceanic waves of that dedicated height. Influences from the satellite movement can also be excluded, as the measured Doppler changes only linearly from 2850 Hz to 2680 Hz (Fig. 5.55, panel I). Reasonable height correction values between 0 and 0.1 m were applied from the geoid model data (Fig. 5.55, panel K) and cannot be the origin of the height signal. A low frequency signal with an observed period of about 300 sec can be observed in the height signal. This signal cannot be a reasonable oceanographic signal in the area of the baltic sea.

The motion of the ocean surface can be classified by various wave types according to temporal and spatial scales [Harigae et al., 2005]. Ocean waves can consist of wind waves and swells. A wind wave develops at first as a capillary wave. Surface tension is the driving force to continue periodic wave motion. Capillary waves develop into ripples by the effect of gravity. The ripples have a period of about 0.3 sec (3.3 Hz). With the aid of wind forces ripples develop further and their period reaches 10–15 seconds (0.06–0.1 Hz). Wave heights can grow up to 10 m. Wind waves that develop further and move away from their origin are called swells. According to wavelength and period, swells can be divided into three categories: short (wavelength $<$ 100 m, period $<$ 8 sec), middle (wavelength 100–200 m, period 8–12 sec) and long (wavelength 200–400 m, period 12–20 sec).

A spectral analysis of the height time series koe007 discussed before reveals only the low-frequency component, as expected (Fig. 5.56, panel A and B). In order to isolate the frequency band of a reasonable oceanic signal, the height time series was filtered with a digital Butterworth high-pass and low-pass filter at a cut-off frequency of 0.125 Hz. The filter response functions of the applied Butterworth high-pass and low-pass filters are plotted in Fig. 5.57. The high-pass filtered data (Fig. 5.56, panel C) now contains no slow height changes. The calculated Fourier spectrum reveals 3 frequencies at 0.5 Hz, 0.1 Hz and 0.2 Hz around which the energy is distributed (Fig. 5.56, panel D). The low-pass filtered height time series Fig. 5.56, panel E) contains significant components only

DOI: 10.2312/GFZ.b103-08104

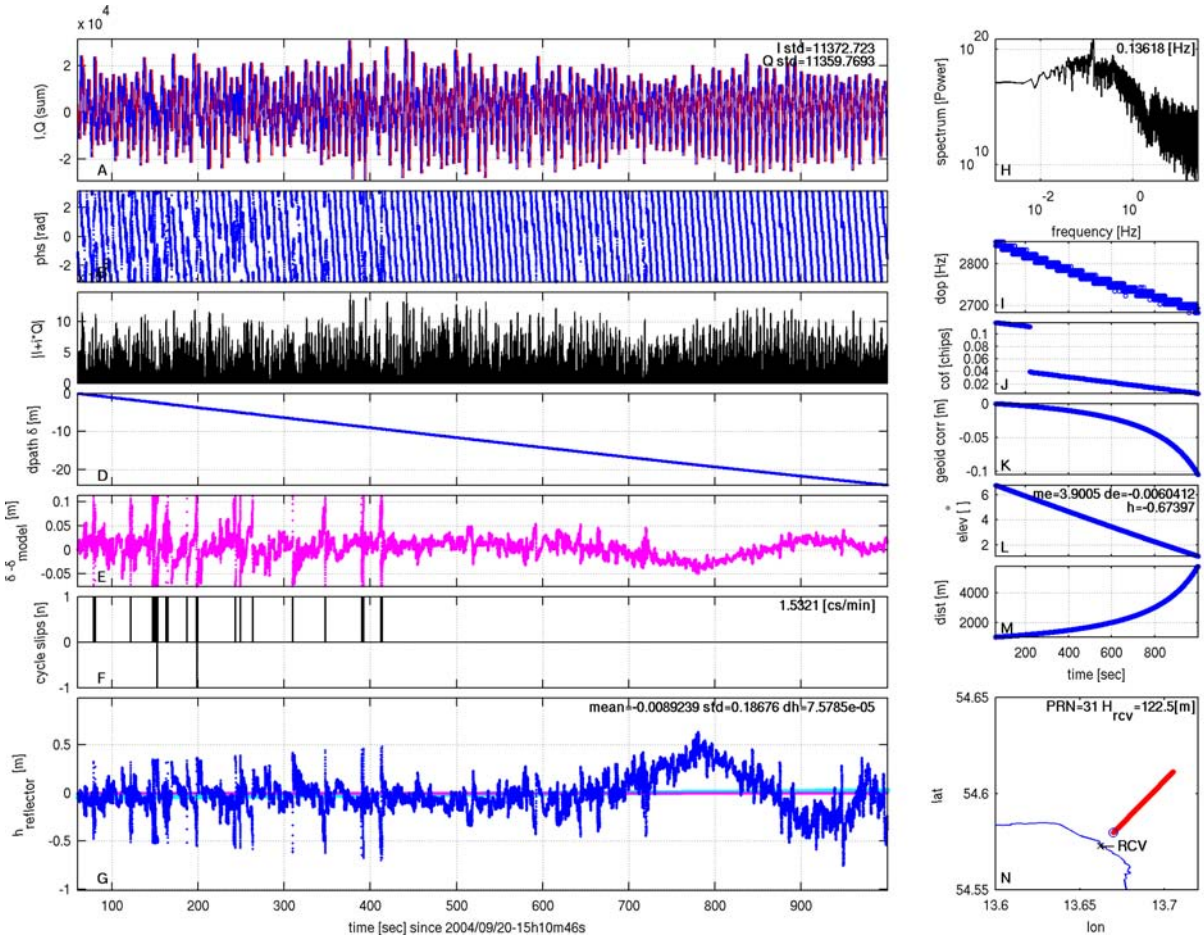

Fig. 5.55: *17 minutes long continuous data recording of PRN31 made on September 20, 2004, which started at 15:10:46 GPST.*

at frequencies lower than 0.008 Hz (Fig. 5.56, panel F).

The most reasonable origin for uncommon height changes is the troposphere. Although the data are already corrected by a tropospheric correction model based on ECMWF model data, it seems reasonable that the local in-situ atmospheric parameters deviate from the ECMWF model, especially at very low elevations. Fig. 5.58 shows the variation of the atmospheric parameters pressure (panel A), temperature (panel B) and refractivity (panel C) at 54.5°N, 13.5°E, 0.0 m above sea level between September 20 and 24, 2004, at 12:00 GPST, extracted from ECMWF model data and which are used for the tropospheric correction model applied.

Similar height fluctuations like those observed in dataset koe007 (Fig. 5.55, 5.56) can sporadically be observed during all measurement days. In Fig. 5.59, for each day, all measured height profiles are low-pass filtered and plotted versus the elevation. At all days it can be observed that the height fluctuations massively occur at elevations lower than 4°. At elevations lower than 2° the height fluctuations can exceed amplitudes of ± 0.4 m. At elevations above 4° the low-pass filtered height changes seldom exceed values of ± 0.1 m.

In order to analyse the sensitivity of the derived height profiles to the chosen tropospheric corrections, the following was performed: The first tropospheric correction file was generated by taking the suitable ECMWF data of the day of the data recording and performing a ray-tracing analysis. The next four virtual tropospheric correction files were generated in the same way except that the wrong ECMWF data of 1 to 4 days earlier or later was taken. Fig. 5.60 shows the influence of the different tropospheric correction sets applied to 4 different data recordings. The top left panel of Fig. 5.60 shows the effect on the dataset koe007, which has previously been discussed in Fig. 5.55 and 5.56. At elevations around 1.5° the differences between the different height time series can be larger than 1.0 m. At elevations larger than 5° the differences do not exceed a value of 0.3 m. Fig. 5.60, top right panel, shows dataset koe008, which was recorded on the same day at 15:10:47 GPST. The profile was taken at higher elevations, starting from 4.7° to 10.8°. At elevations above 5.5° the

DOI: 10.2312/GFZ.b103-08104

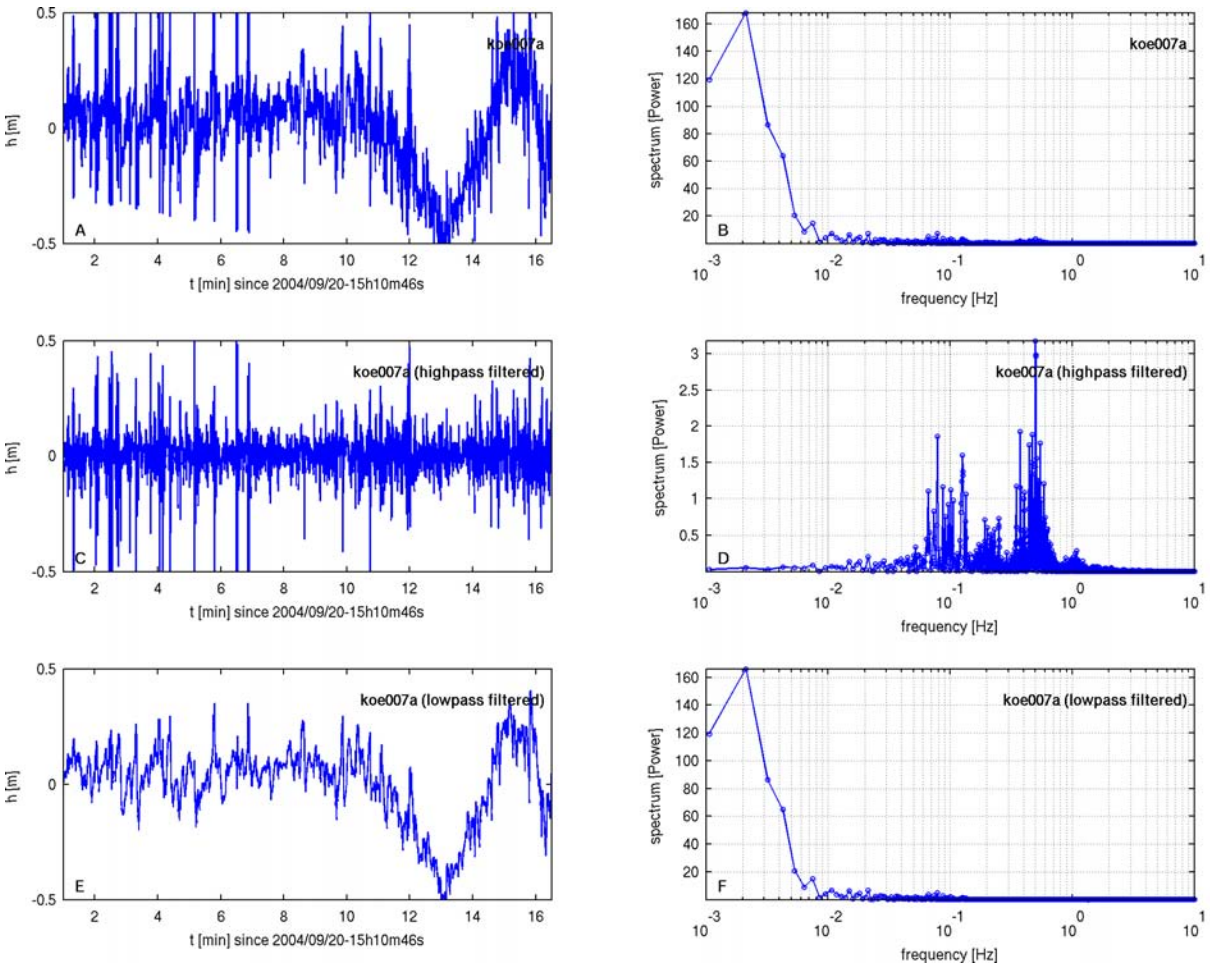

Fig. 5.56: *The measured height time series (panel A) is separated with a digital Butterworth high-pass and low-pass filter. The results are shown in panel C and D. The spectra of each time series are shown on the right side in panel B, D and F.*

differences between the different corrected height time series do not exceed a value of 0.1 m. Dataset koe055 (Fig. 5.60, bottom left panel) was recorded on September 21 at 12:41:19 GPST between 3.7° and 1.0° elevation. At these low elevations all applied tropospheric correction files cause height signals exceeding values of 1.0 m. No large differences between each tropospheric correction can be observed in data recording koe213, which was collected on September 24 at 08:37:49 GPST between 1.8° and 6.2°. Here only a small height bias of 5–10 cm can be observed between each tropospheric correction. It can be concluded that the derived height profiles are very sensitive to the in-situ tropospheric conditions. At high elevations (down to 4°) the tropospheric influence can be treated fairly well by applying a tropospheric correction term derived from ECMWF model data and ray-tracing analyses. At elevations smaller than 4° the in-situ troposphere is not represented accurately enough by the correction data. Thus, low-frequency height artifacts in the range of several decimeter can be observed. Additionally, during the process of detrending, a height bias can be caused by a

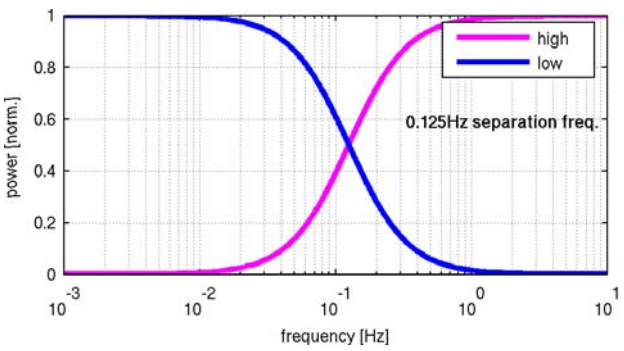

Fig. 5.57: *The filter response functions of a digital Butterworth high-pass and low-pass filter with a separation frequency of 0.125 Hz.*

DOI: 10.2312/GFZ.b103-08104

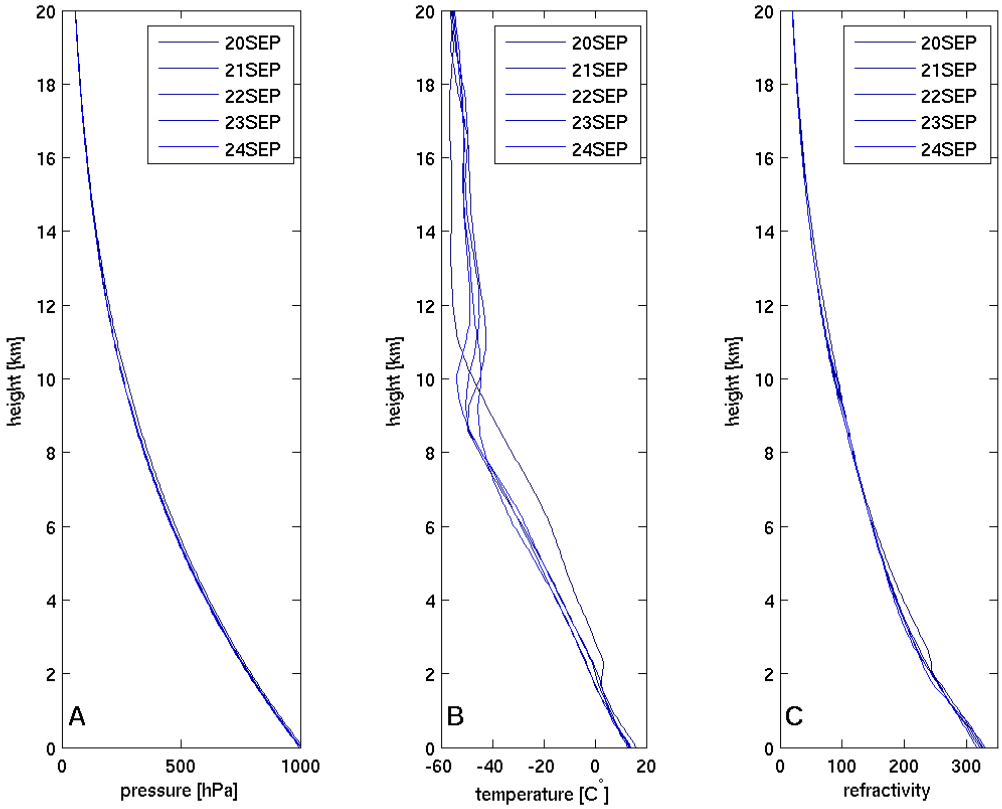

Fig. 5.58: *Variation of the atmospheric parameters pressure (panel A), temperature (panel B) and refractivity (panel C) at 54.5°N, 13.5°E, 0.0 m above sea level between September 20–24, 2004, at 12:00 GPST*

wrong slope estimate for the relative height profile.

5.4.4 Discussion

In the following synopsis (Fig. 5.61, Fig. 5.62, Fig. 5.63, Fig. 5.64 and Fig. 5.65) one selected unfiltered height profile (blue) is presented for each measurement day. The reflector model estimate is plotted in pink and the linear slope of the derived heights is plotted in red color. For better comparison the height profile data are plotted versus time with the same height and time scale (left, panel A). To the right (panel B) the location of the corresponding specular reflection point ground track is shown in red color (In blue the data of the complete dataset is shown which is not represented in the height data of panel A). During the first two observation days September 20 and 21 surface conditions do not change significantly. On the following day September 22 and 23 we observe larger amplitudes in the height profils which indicate an increased surface roughness and higher waves. On September 24 the surface conditioned calmed down again. More selected height profils (blue) for each measurement day are presented in the appendix in Fig. C.3, Fig. C.5, Fig. C.7, Fig. C.9 and Fig. C.11. Additionally, the spectra (blue) of the associated high-pass filtered complete height data are shown in Fig. 5.66 and Fig. C.4, Fig. C.6, Fig. C.8, Fig. C.10 and Fig. C.12. A running mean with a window width of 10 samples was calculated from the spectrum and is overlayed as pink colored curve. The smoothing was done in order to automatically pick the maximum frequency peak more easily.

On September 20, 2004, the first 3 datasets in Fig. C.3 show a homogeneous height profile of PRN 31, 7 and 1 at a mean absolute height of 0.52 m, 0.32 m and 0.56 m. The STD ranges from 0.19 m, 0.13 m to 0.06 m. Only dataset koe016 has a high STD of 0.34 and a mean height of -0.72 m. Here PRN 7 signals were recorded at very low elevations between 1.2° and 0.8°. As previously discussed, the lower local troposphere generates height artifacts ranging to more than ±1 m. Because of the low

DOI: 10.2312/GFZ.b103-08104

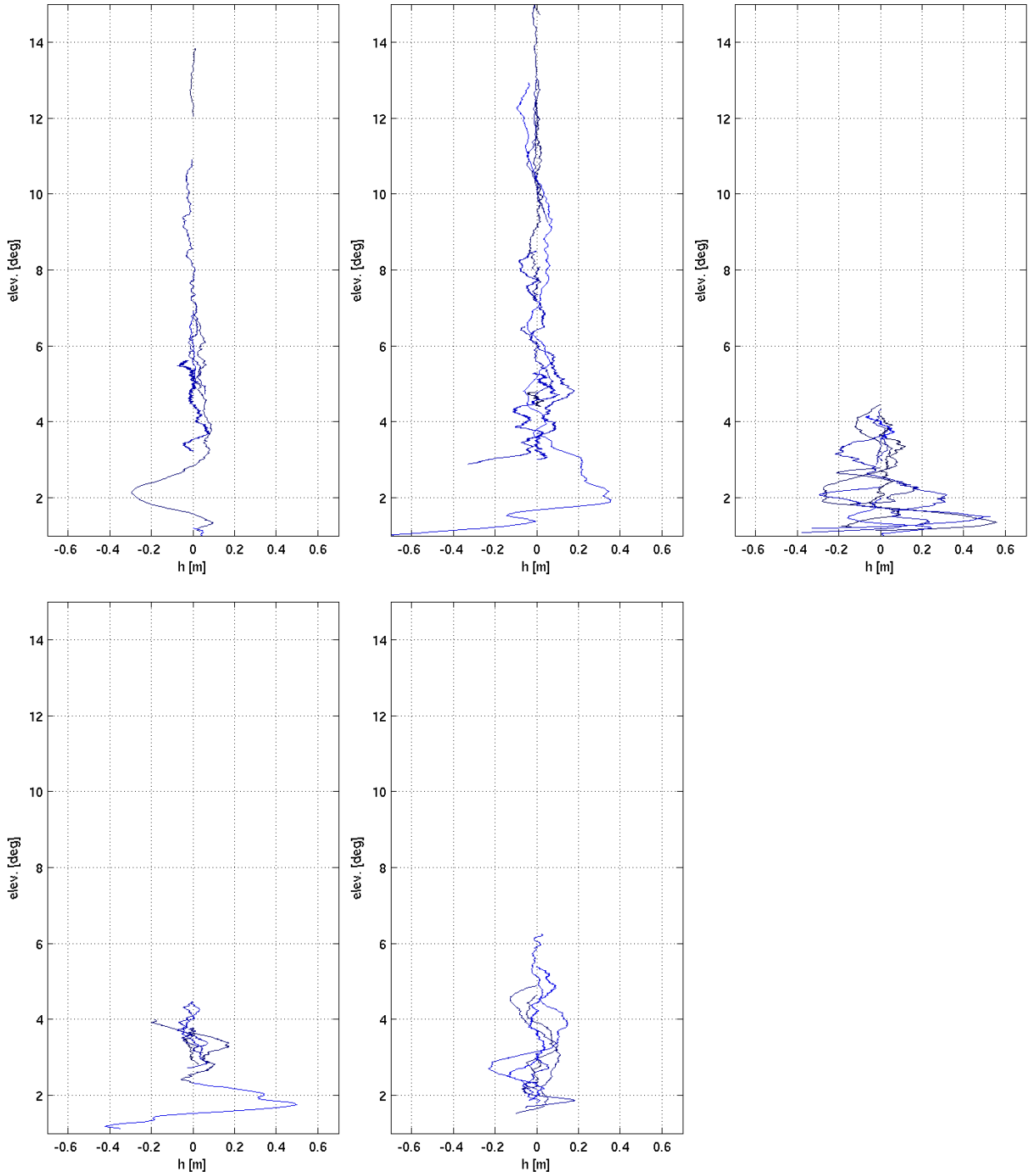

Fig. 5.59: *Below 4° the influence of the local troposphere is not correctly represented in the applied correction model which is based on local ECMWF model and ray-tracing analysis of the specific observed GPS satellite data.*

elevations and the fulfilled Rayleigh criterion, a strong reflected signal can be observed and no single cycle slip correction had to be inserted. For data take koe015 – which was recorded at elevations ranging from 4.9° to 6.9° – a calm reflecting surface could be observed with a mean value of 0.3 cycle slips inserted per minute. Rougher surface conditions can be estimated from data take koe007 with a mean value of 1.7 cycle slips inserted per minute with observations ranging from 6.8° to 1.1°. As can be seen in Fig. 5.55 the cycle slips have to be corrected only at elevations above 4°. Data recording koe008 was taken from 10.9° down to 4.7° elevation. Thus, a lower fraction of coherent reflected signals is expected at higher elevations and 8.5 cycle slips per minute had to be corrected in the data recording. The strongest observed frequency peaks in the spectra – shown in Fig. C.4 – are in a range between 0.42 Hz and 0.52 Hz, representing a reasonable ocean wave with a period between 1.92 sec and 2.38 sec, respectively.

DOI: 10.2312/GFZ.b103-08104

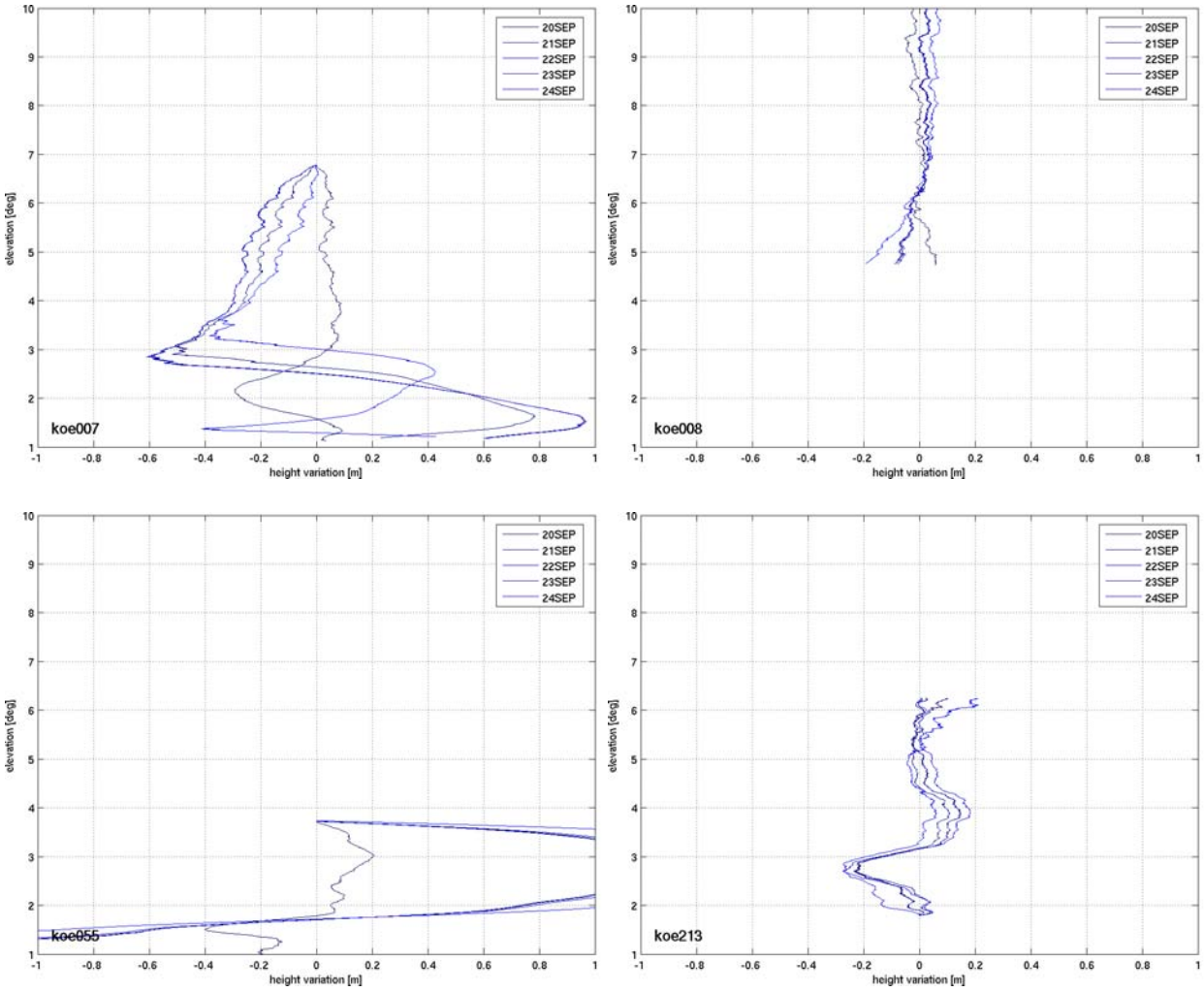

Fig. 5.60: *Sensitivity of derived height profiles to the chosen tropospheric corrections.*

On September 21, 2004, the surface conditions have not changed. Thus, the results from the reflection measurements should not change either. The first 3 selected datasets of PRN 23, 13 and 21 are taken at elevations from 15.1° to 9.5°, 13.0° to 9.3° and 4.6° to 6.5° (Fig. C.5). The mean derived absolute height are given by -0.01 m, 0.05 m and -0.07 m. The STD varies from 0.07 m to 0.08 m and 0.13 m. Cycle slips had to be corrected in a range from a mean value of 4.1 to 8.4 corrections per minute. The high number of cycle slip corrections was necessary for data take koe028 with observations up to 15.1° elevation, where the fraction of coherent reflected signals is expected to be lower. Data take koe055 was made at elevations ranging from 3.7° to 1.0°, measuring signals of PRN 8. At the low elevations a strong signal could be recorded and no cycle slips had to be corrected. A 60-sec long detail of the dataset can be seen in Fig. 5.50. Caused by the uncorrected fraction of the lower troposphere the STD of the height time series increases to an amount of 0.49 m and the mean absolute height is biased to a value of -1.79 m. Data take koe055 illustrates the massive impact of the local in-situ lower troposphere, which is not adequately represented by the model correction data. Additionally, it can be seen, that the detrending process of the measured relative height profiles severely depends on the selected data segment. Taking into account only data in the time interval from 1 min to 6 min results in a different absolute height than that for the data taken from the time interval 2 min to 7 min. In the spectra shown in Fig. C.6 only for dataset koe034 – a measurement near the coast – the dominant frequency is in the range of 0.54 Hz, waves having a period of about 1.85 sec, comparable to the measurements the day before. In the other spectra more energy can be observed in the lower frequency band around 0.28 Hz or 3.57 sec period, 0.39 Hz or 2.56 sec period and 0.09 Hz or 11.11 sec period.

On September 22, 2004, the surface conditions changed. The visually observed wave heights and the roughness of the sea surface increased. This can be seen in Fig. 5.45 by the increased number

DOI: 10.2312/GFZ.b103-08104

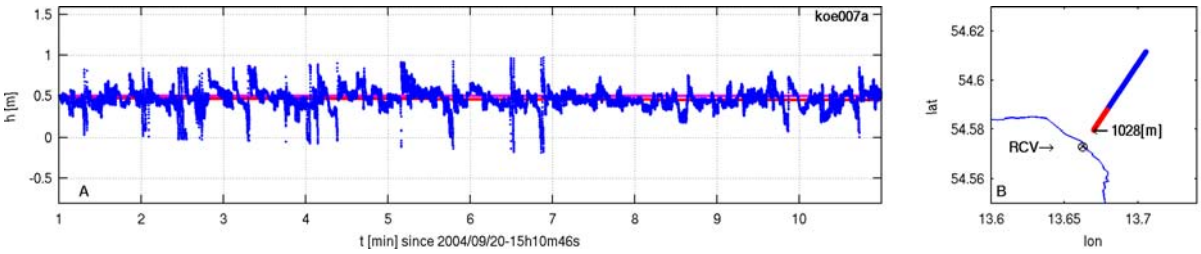

Fig. 5.61: *Height time series (panel A) and the corresponding location of the specular reflection point (panel B) on September 20, 2004.*

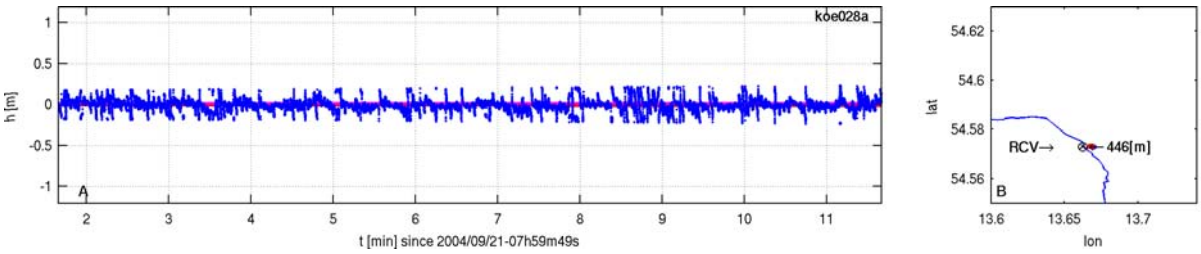

Fig. 5.62: *Height time series (panel A) and the corresponding location of the specular reflection point (panel B) on September 21, 2004.*

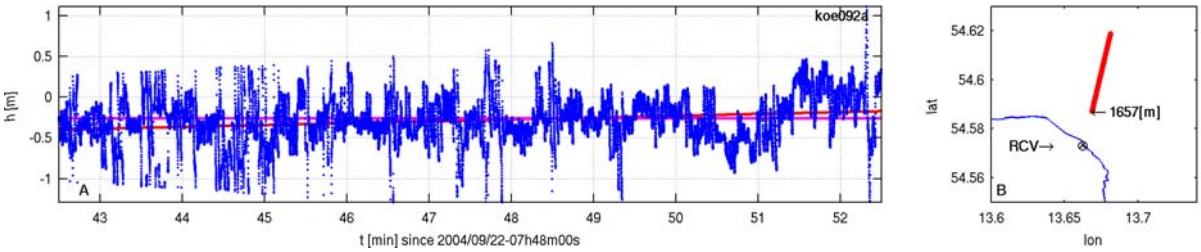

Fig. 5.63: *Height time series (panel A) and the corresponding location of the specular reflection point (panel B) on September 22, 2004.*

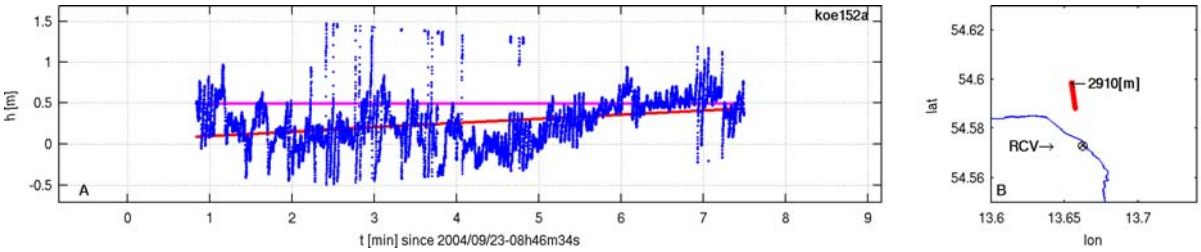

Fig. 5.64: *Height time series (panel A) and the corresponding location of the specular reflection point (panel B) on September 23, 2004.*

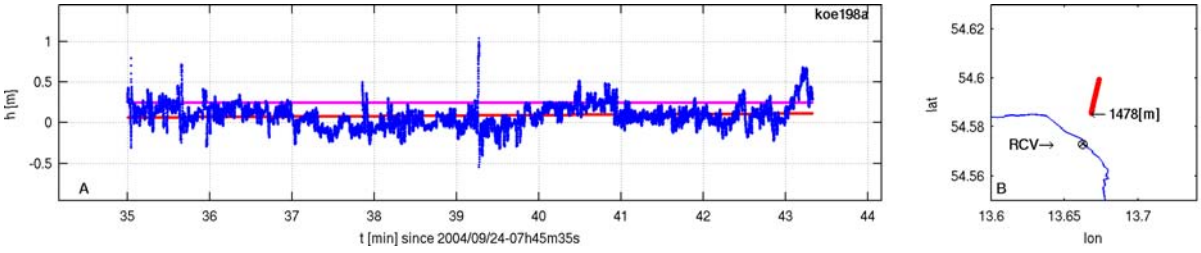

Fig. 5.65: *Height time series (panel A) and the corresponding location of the specular reflection point (panel B) on September 24, 2004.*

DOI: 10.2312/GFZ.b103-08104

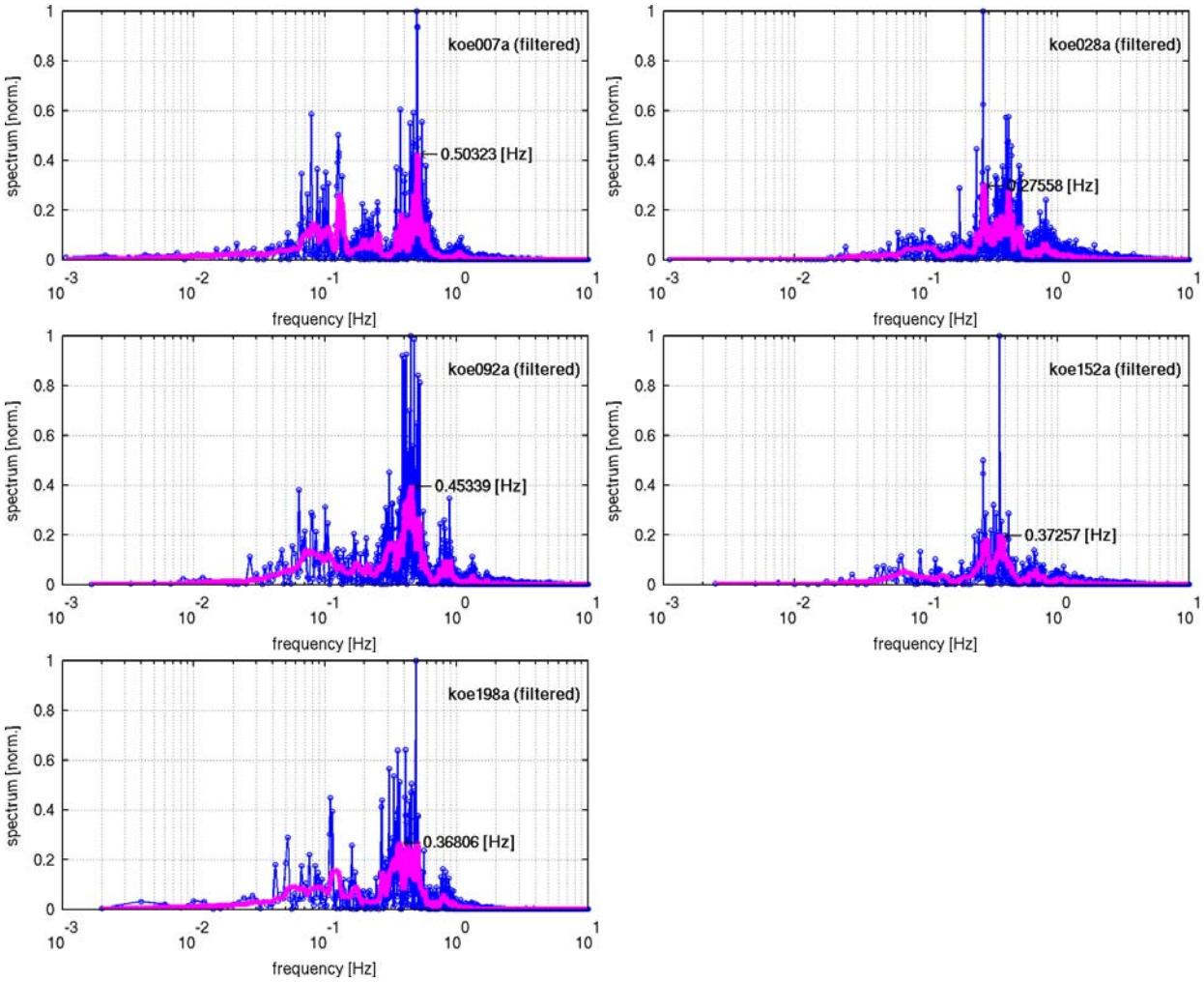

Fig. 5.66: *Fourier spectra of the filtered height time series on September 20–24, 2004.*

of observed white crest waves. Measurements could be made only at lower elevations between 4.1° to 1.2° (PRN 16), 4.5° to 1.1° (PRN 23), 3.7° to 1.1° (PRN 19) and 2.3 to 1.2° (PRN 11) (Fig. C.7). Thus, all height profiles are modulated by low-frequency height changes resulting from the uncorrected fraction of the lower troposphere. The absolute mean height varies between -0.28 m, -0.52 m, -1.19 m and -0.35 m with a possible height bias due to the uncorrected fraction of the lower troposphere. The higher oceanic waves can directly be seen in the larger amplitudes of all derived height profiles. The STD of the height time series vary from 0.29 m, 0.45 m, 0.49 m up to 0.57 m, much higher than the values observed the two days before. Cycle slips had to be corrected for all measurements in a range from 4.4, 0.2, 6.2 and 1.3 corrections per minute. During data take koe093 the receiver lost only twice some phase information. Thus, only 0.2 cycle slips per minute had to be corrected. The Doppler changed only slightly during the data recording from 2280 Hz to 2220 Hz. A clear frequency peak of 0.123 Hz can be observed in the spectrum of the measured correlation data. With a mean elevation of 2.75° and a mean elevation change rate of -0.0055°/sec during the whole data take, a mean absolute height of -0.58 m could be estimated which agrees well with the derived height of -0.52 m from the height profile. The absolute height estimates of the other data takes koe092, koe0110 and koe113 derived from the observed interferometric frequency vary between 1.94 m, 2.57 m and 6.02 m and deviate from the heights estimated from the height profile. Thus, the absolute height gained by the frequency estimate can only be used as a first guess or estimate for the reflector height. The frequency peaks observed in the spectra shown in Fig. C.8 vary between 0.45 Hz, 0.45 Hz, 0.38 Hz and 0.22 Hz. In the koe113 spectrum a strong peak can also be seen at 0.4 Hz, but from automatic processing the 0.22 Hz peak was picked due to the higher energy level accumulated in that frequency band. Thus, mainly waves with a period of 2.22 sec, 2.22 sec, 2.63 sec and 2.50 sec are correlated with the observed height profiles during September 22.

On September 23, 2004, observations could be made at lower elevations between 2.3° to 4.0° (PRN

21), 4.2° to 2.7° (PRN 9), 4.5° to 3.3° and 2.3 to 1.1° (both PRN 28) (Fig. C.9). The relatively high wave amplitudes – observed the day before – decreased by a factor of 50%. STD of the height time series could be observed in a range from 0.29 m, 0.22 m, 0.18 m and 0.66 m. The latter value again is influenced by the low-frequency height fluctuations by the uncorrected fraction of the lower troposphere at low elevations. The absolute mean height derived from the detrended height time series varies between 0.26 m, -1.11 m, 0.33 m and 0.78 m. The mean height of -1.11 m derived from measurement koe154 deviates by more than a meter from all other measurements of the day. The height observation based on the reflected PRN 9 signal better agrees with the PRN 9 observations made the day before where a height of -1.19 m was determined. Cycle slips had to be corrected only at observations higher than 3° elevation, where the mean cycle slip corrections per minute value varied from 3.3 to 5.7. The spectra show distinct frequency peaks at 0.37 Hz, 0.49 Hz, 0.30 Hz, 0.51 Hz and 0.44 Hz (Fig. C.12). Ocean waves with a corresponding period of 2.70 sec, 2.04 sec, 3.33 sec and 2.27 sec are correlated with the height observations measured on September 23.

In the morning of September 24, 2004, observations could be made at lower elevations between 4.6° to 2.2° (PRN 16), 4.9° to 1.5° (PRN 23), 1.8° to 6.2° (PRN 21) and 5.4° to 1.9° (PRN 3) (Fig. C.11). Sea surface conditions further calmed down and STD of the height time series could be observed in a range from 0.15 m, 0.16 m, 0.15 m and 0.17 m. Due to the calmer sea surface a higher fraction of the coherent signal component could be recorded. Thus, fewer cycle slips had to be corrected. The mean cycle slip corrections per minute value varied from 0.4, 0.7, 0.7, and 2.4 , respectively. The influence of the uncorrected fraction of the lower troposphere is much lower than the days before. From detrending each relative height profile a mean absolute height in the range between 0.09 m, -1.28 m, 0.41 m and 0.64 m could be derived. Analysing data take koe199, a mean elevation of 3.171° and a mean elevation change rate of -0.00563°/sec could be calculated. An interferometric frequency of 0.125 Hz can be observed in the appropriate Fourier spectrum of the correlation data. From that data a mean absolute height of -0.56 m can be estimated which fits well to the derived height of -0.58 m from measurement koe093 which uses the same PRN 19 observations two days earlier. From data set koe213 a corresponding absolute height estimate of -0.46 m can be made from an observed interferometric frequency of 0.090 Hz, a mean elevation of 4.058° and an elevation change rate of 0.00496°/sec. Both other data sets koe198 and koe217 of the same day result in absolute height estimates between 1.52 m and -1.59 m and do not agree. The spectra shown in Fig. C.12 reveal frequency peaks at 0.37 Hz, 0.49 Hz, 0.27 Hz and 0.32 Hz, respectively. Waves with a corresponding period of 2.70 sec, 2.04 sec, 3.70 sec and 3.13 sec could be observed in the height profiles measured on September 24.

Taking all processed data sets into account smoothed spectra can be calculated for each single high-pass filtered height profile. They are shown for each day in Fig. 5.67 – Fig. 5.71. On September 20 (Fig. 5.67) most profiles have a frequency peak in the frequency band between 0.4 Hz and 0.5 Hz. On September 21 (Fig. 5.68) the observed frequency peaks are much wider spread over a frequency band starting from 0.09 Hz up to 0.7 Hz. On September 22 (Fig. 5.69) the observed frequency peaks cluster at the already observed frequency band between 0.4 Hz and 0.5 Hz and, additionally, 3 data recordings have peaks around 0.2 Hz. At that day the highest wave conditions within the observation period could be observed. On the following September 23 (Fig. 5.70) all frequency peaks are smeared around the frequency band 0.2 Hz and 0.6 Hz. On September 24 (Fig. 5.71) the observed frequencies appear similar to those the day before but extending to a frequency band of 0.1 Hz and 0.6 Hz.

In Fig. 5.72 all processed unfiltered height profiles are shown for each observation day, heights plotted versus distance to the receiver. Already at distances larger than 2500 m the influence of the uncorrected fraction of the lower troposphere becomes apparent with low-frequency height variations of about ± 0.5 m. At distances larger than 3500 m this influence increases and causes height variations of about ± 1.0 m. While on most days only one measurement could be made at very low elevations, i.e. at large distances, on September 22 (Fig. 5.72, panel Koenigsstuhl 266) several data sets could be measured at distances between 4000 m and 6000 m. Ignoring the height bias between each profile, the observed low-frequency height fluctuations can be correlated with each other. Thus, all measurements were influenced by nearly the same local in situ conditions of the lower troposphere which are not adequately represented in the applied troposphere correction model. The same correlation can be seen in Fig. 5.72, panel Koenigsstuhl 268. Comparing the height profiles at a mean height of -1.0 m in a distance between 2500 m and 4000 m, both profiles follow the same low-frequency height fluctuations.

DOI: 10.2312/GFZ.b103-08104

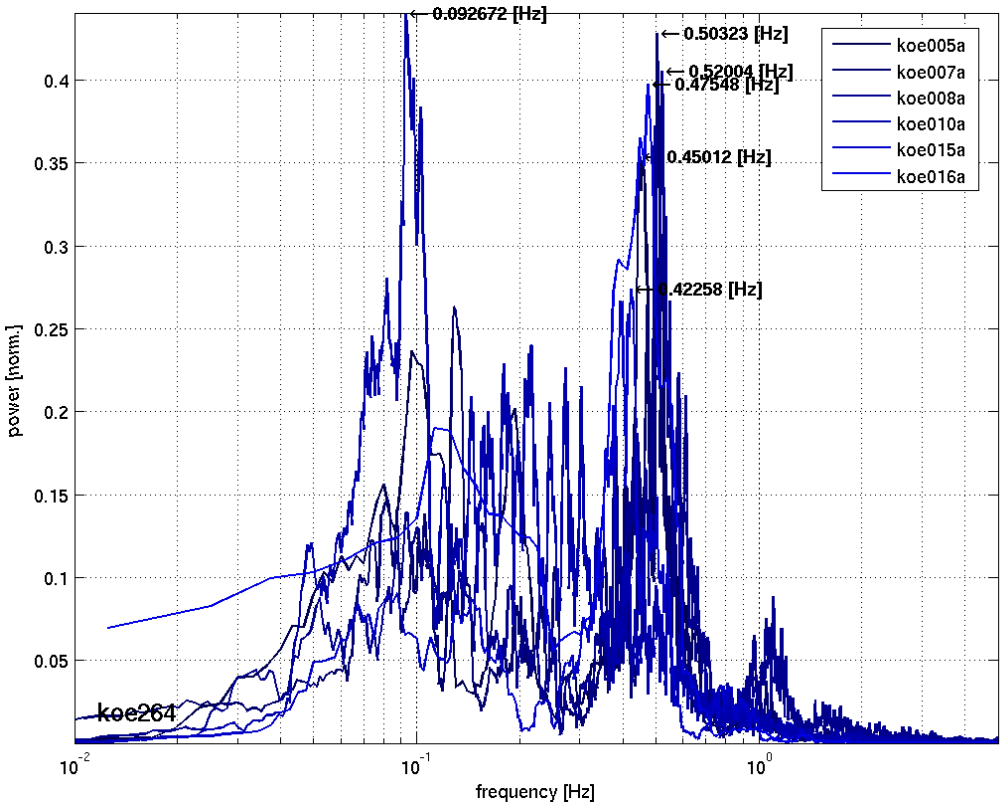

Fig. 5.67: *Smoothed spectra with detected peak frequency on September 20, 2004.*

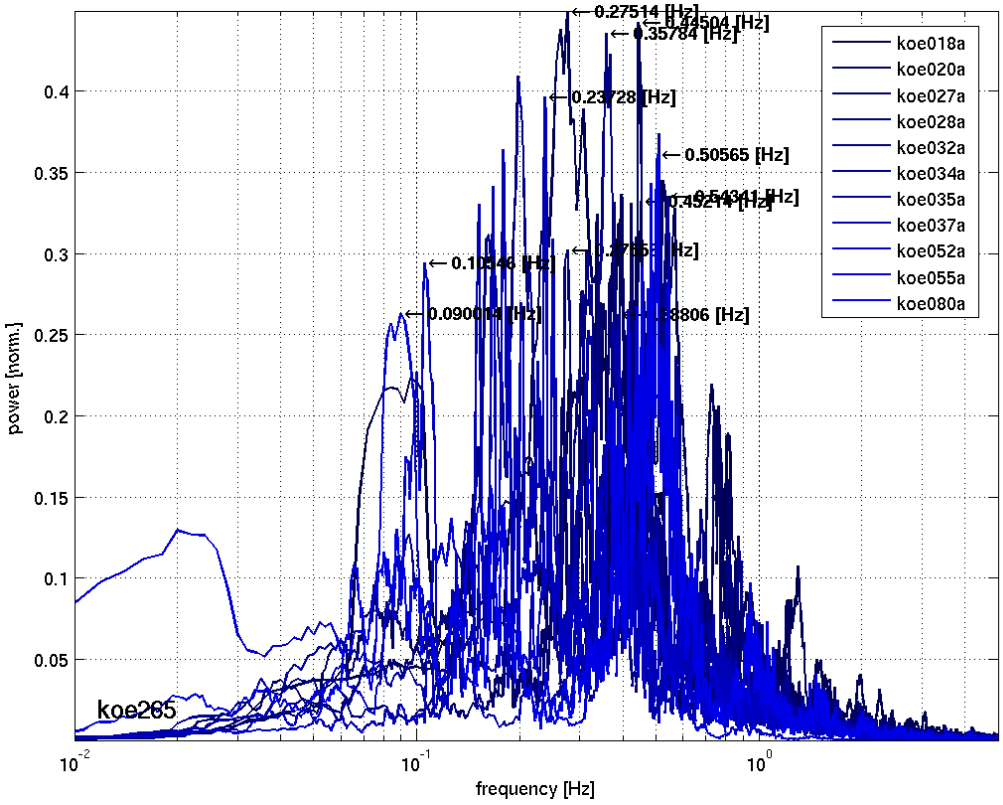

Fig. 5.68: *Smoothed spectra with detected peak frequency on September 21, 2004.*

DOI: 10.2312/GFZ.b103-08104

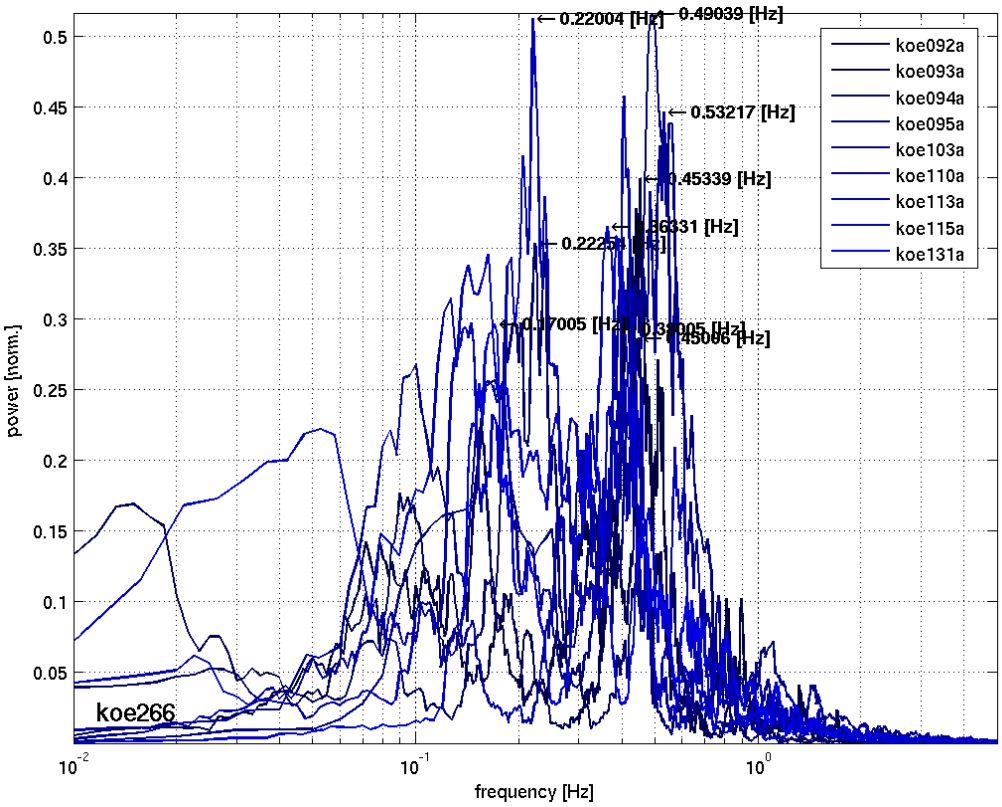

Fig. 5.69: *Smoothed spectra with detected peak frequency on September 22, 2004.*

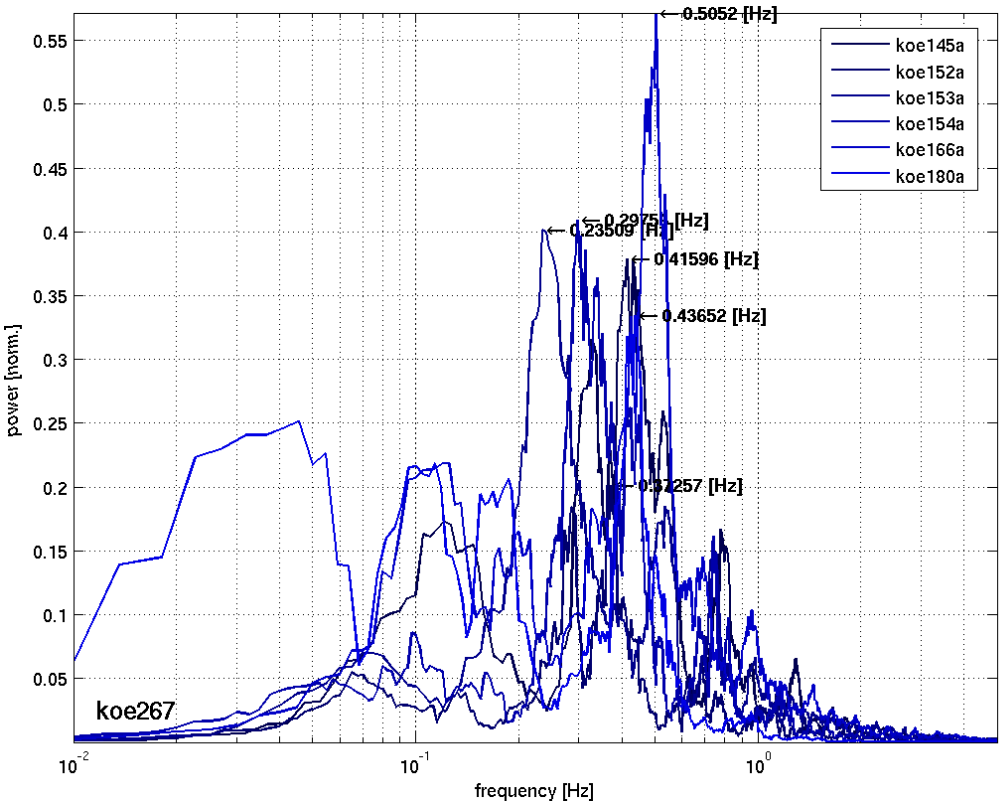

Fig. 5.70: *Smoothed spectra with detected peak frequency on September 23, 2004.*

DOI: 10.2312/GFZ.b103-08104

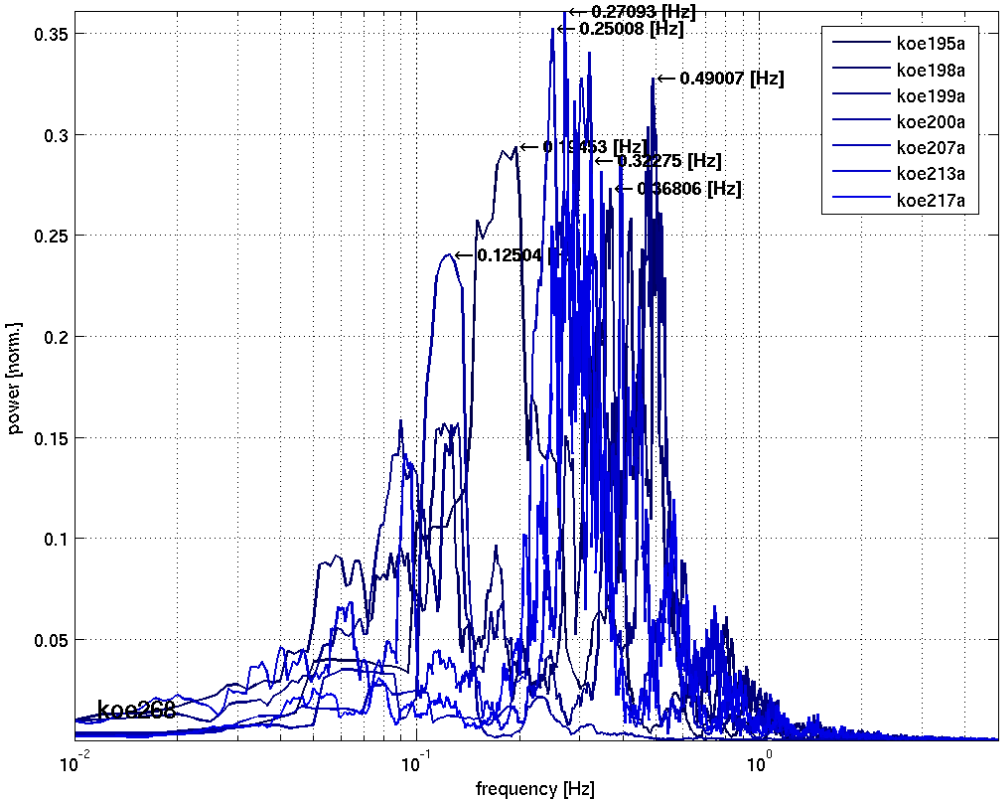

Fig. 5.71: *Smoothed spectra with detected peak frequency on September 24, 2004.*

A height bias of 1 m up to 3 m can exist between single height profiles and can be observed for all days. On September 20, (Fig. 5.72, panel Koenigsstuhl 264) nearly all profiles agree with their derived absolute mean height except for the profile measured at a distance between 5500 m and 8000 m. At the low elevations at which the measurement was recorded the height bias is likely caused by the uncorrected slope caused by the lower local troposphere. The observed height bias of about 1 m in Fig. 5.72, panel Koenigsstuhl 268, cannot easily be explained by the influence of the lower troposphere, because the observations happen at higher elevations. Thus, the fraction of coherently reflected signals decrease and therefore the quality of the measured phase decreases. Hence, cycle slips occur and might not be handled properly during post processing which results in a height bias. A height bias can also be generated by an uncorrected slope of the sea surface which can be caused by long lasting wind forces. In case of an existing linear slope a correlation between the azimuth direction and the height offset should be expected. The following data sets are all measured in the morning of September 24. The data sets koe195, koe198, koe200, koe213 and koe217 are measured in azimuthal direction 350°, 10°, 330°, 350°, and 10°. A corresponding mean height of -0.74 m, 0.09 m, -1.22 m, 0.41 m, and 0.64 m was calculated, respectively. The data sets koe199 and koe207 are measured in perpendicular direction in 100° and 60° azimuth and a mean height of -1.28 m and -1.09 m was calculated, respectively. Thus, no sufficient correlation can be seen in the data. A much denser data set of observations is needed for a reliable statistical statement.

Fig. 5.73 shows the relation between the received power of the coherently reflected signal and the elevation of the signal transmitting satellite. The scatter plot displays the power versus elevation of all recorded data received from the sea surface in the time period from September 20 to September 24, 2004. The mean power versus the mean elevation is plotted as red circles. The strongest signals could be received at elevations between 1° and 8°. Between 10° to 15° the signal power drops by a factor of 2. Around 7°, 9° and 14° a further signal loss can be observed.

Precise height measurements for calibration purposes were conducted with a two-frequency Trimble 4000 geodetic receiver at the OpenGPS receiver antenna position and at the shoreline of the baltic sea. Unfortunately, the phase measurements failed and no accurate height information could be derived. No other dedicated calibration measurements of the sea surface have been performed in parallel. At Sassnitz harbor, data of a local tide gauge could be acquired. The height data is plotted versus time (day of year) in Fig. 5.74, panel A (blue curve). For a comparison the estimated tide

DOI: 10.2312/GFZ.b103-08104

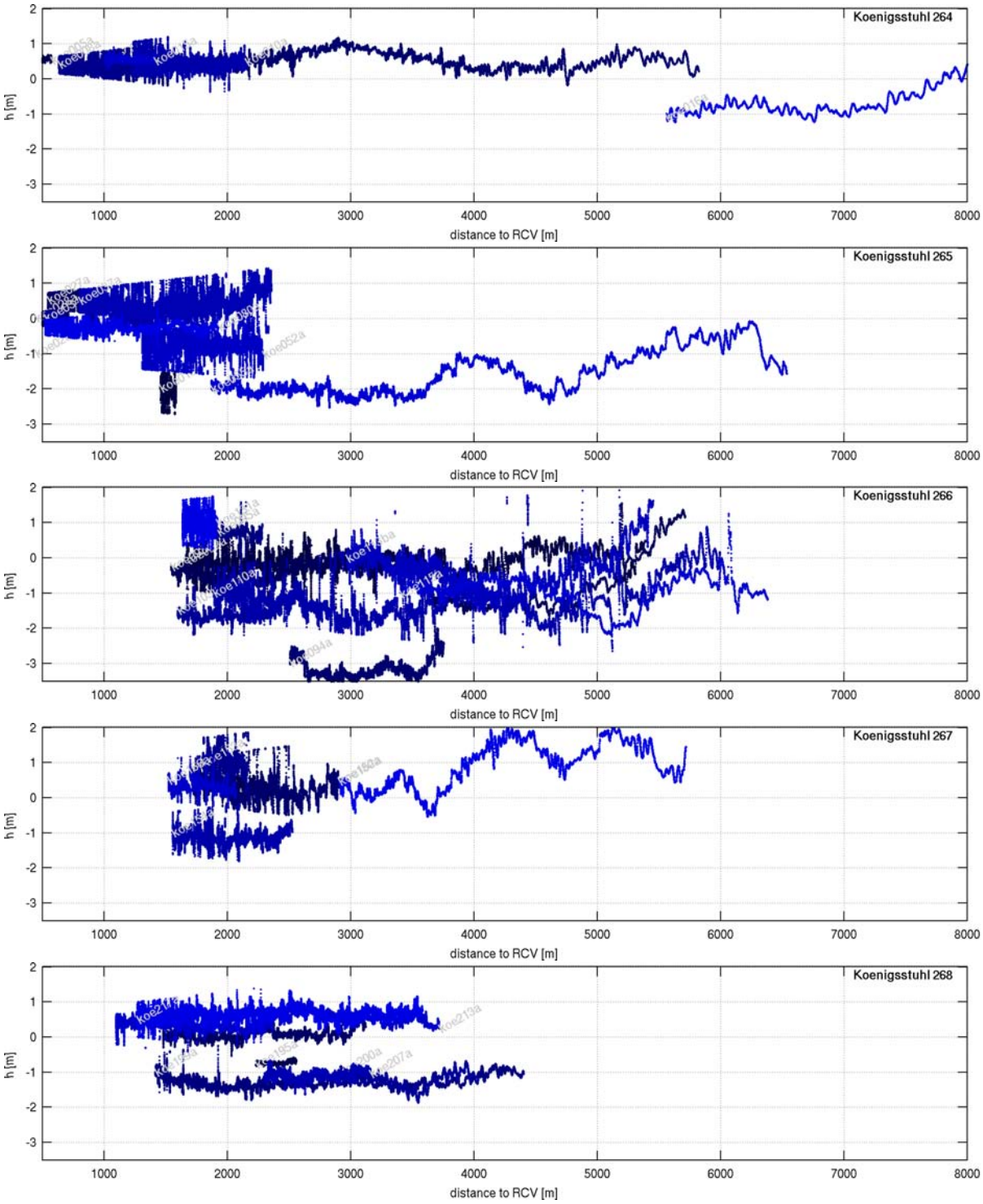

Fig. 5.72: *Unfiltered height profiles versus distance to the receiver.*

signal derived from the NAO99 model is plotted in pink color into the same panel. Although the accuracy of the tide model is expected to be low near Rügen coast, a tidal signal of $\pm$ 0.1 m seems suitable for that area. No daily tidal signal can be seen in the Sassnitz tide gauge recordings. The observed height changes seem to be driven by the changing conditions of the wind setup. Additionally, data from the Arcona buoy could be acquired. In September 2004 the directional wave rider buoy Arkona was positioned at 54.716° N, 13.744° E at a water depth of 40 m and the distance to the OpenGPS receiver position was 16.69 km. On September 20, 2004 (day 264) in the open baltic sea sea waves could be observed with 1 m height which grew up to 2 m height on September 21 and 22 (Fig. 5.74, panel B). From September 22 to 25 the wave heights decreased to heights lower than 1 m again. The wind mainly blew from 300° azimuthal direction, except on September 20, on which

DOI: 10.2312/GFZ.b103-08104

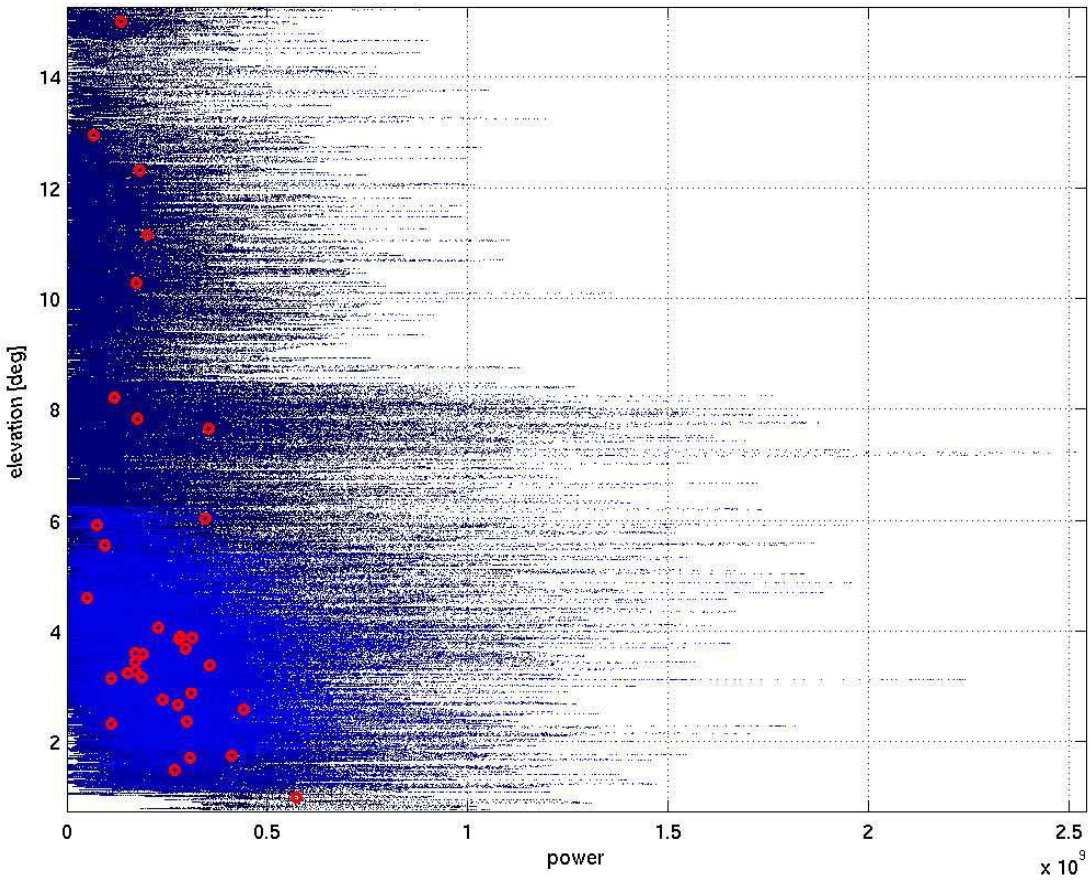

Fig. 5.73: *Scatter plot power versus elevation and mean power versus mean elevation (red circles) of all recorded data received from the sea surface in the time period from September 20 to September 24, 2004.*

the wind was coming from 200° azimuth (Fig. 5.74, panel C). Between September 20 and 21 wave periods grew from 3 sec to 5 sec (Fig. 5.74, panel D). Between September 21 and 22 the periods with the highest wave could be observed with mean values of 5 sec and peak values between 6 sec and 7 sec. The wave periods decreased on the following days and reached periods of 3 sec again on September 25.

The results of all processed OpenGPS data sets are presented versus time (day of year) in Fig. 5.74, panel E, F, G and H. Due to the previously discussed height bias and the influence of the lower uncorrected tropospheric influence the measured mean heights scatter up to several meters around the expected height of the baltic sea surface. A polynomial fitting of degree 3 of the height data varies mainly between 0.0 m and -0.5 m which agrees well with the expected value (Fig. 5.74, panel E). The STD of all height time series are shown in Fig. 5.74, panel F. The STD of the unfiltered height time series is presented by a blue cross. The STD of the low-pass filtered data is marked by a turquoise topside down triangle. The STD of the high pass filtered data is plotted by a red triangle. In the following only the STD of the high pass filtered data is discussed which contains the highest fraction of oceanographic signal from the reflecting surface. On September 20 and 21 the STD varies around a value of 0.1 m and can be interpreted as a $\pm$0.1 m moving ocean surface and wave heights of 0.2 m. On September 22 the highest STD values could be measured, varying from 0.09 m to 0.29 m with a mean value of 0.16 m. On September 23 still a mean value of 0.17 m can be observed which drops down again to a STD of 0.09 m on September 24. These measurements are correlated with the visual observations made (Fig. **??**). On September 22 the highest waves marked by white crest waves could be observed during the observation period. A polynomial fitting of degree 3 through the unfiltered data (blue curve) and high-pass filtered data (red curve) indicate both that the highest waves could be measured between September 22 and 23. The Arcona measurements state the highest waves one day early between September 21 and 22. This effect can only be explained by the different measurement locations. While the Arcona Buoy measures open sea conditions the OpenGPS receiver measures in the coastal zone with shallow water. A temporal behavior of the reflected power which depends on the changing sea surface conditions cannot be seen in the data shown in Fig. 5.74,

DOI: 10.2312/GFZ.b103-08104

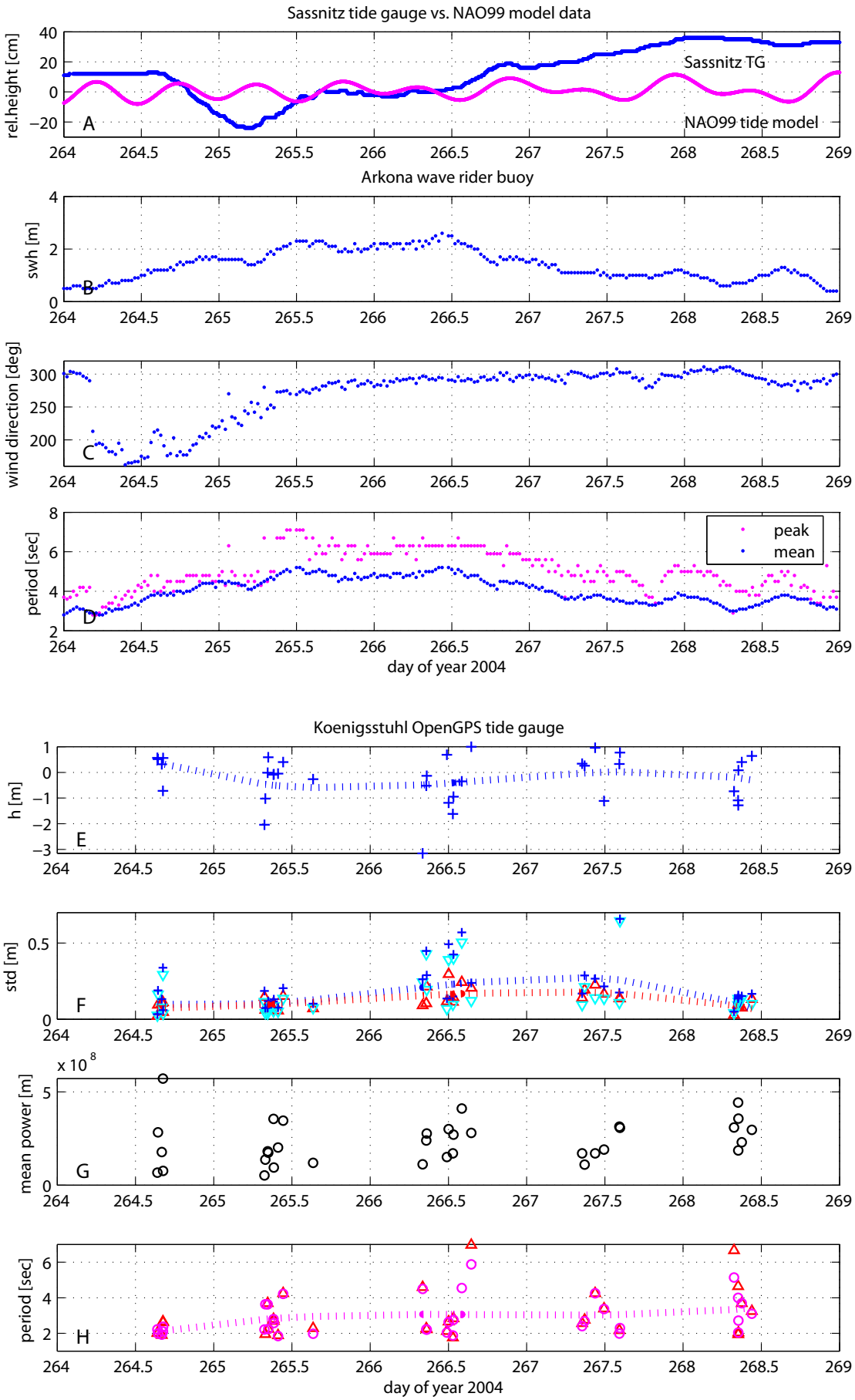

Fig. 5.74: *Water level relative height estimates derived from NAO99 tide model (magenta) and Sassnitz tide gauge data (blue) (panel A) and Arcona wave rider buoy data (panel B–D). Mean absolute height estimate (panel E), STD (panel F), mean power (panel G) and estimated wave period (panel H) of all recorded data received from the sea surface in the time period September 20 (doy 264) to September 24 (doy 268), 2004.*

DOI: 10.2312/GFZ.b103-08104

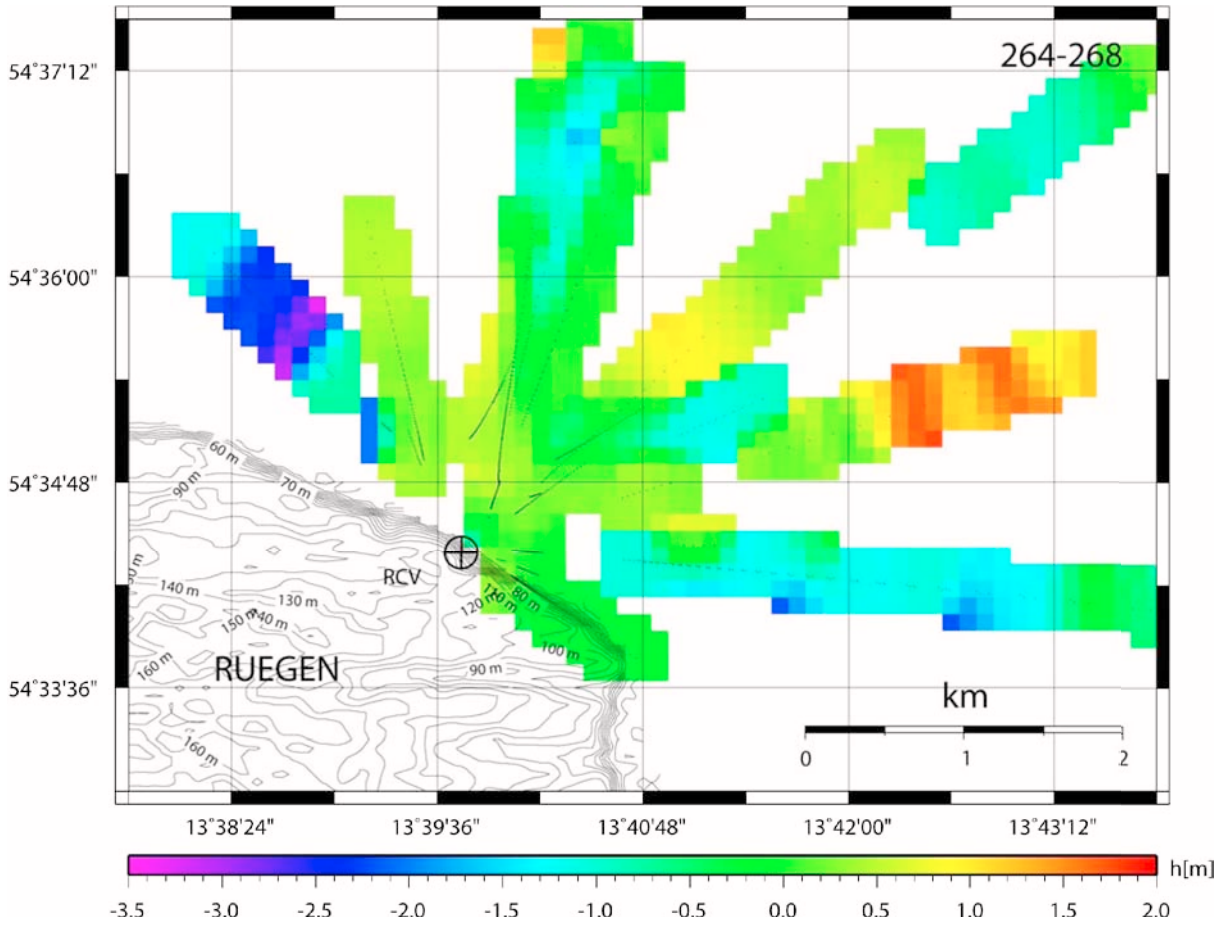

Fig. 5.75: *Spatial coverage of height profiles measured from carrier phase-delay observations of reflected GPS signals during daytime between September 20 and 25, 2004, at the Königsstuhl location on Rügen island, Germany. Colors which deviate from green indicate measurements infl uenced by the local uncorrected troposphere.*

panel G. As shown previously, the power of the refl ected signal is dominated by the infl uence of the elevation of the transmitting satellite.

The most promising results can be achieved by analysing the Fourier spectrum of each high-pass fi ltered height time series. The evaluated frequency peak values of each data set are plotted versus time in Fig. 5.74, panel H. Pink circles represent the peak values derived from the smoothed spectra while red triangles represent the peak values from the untreated spectra. On September 20 the observed periods vary between 2.0 sec and 2.4 sec. On September 21 a mean period of 2.8 sec can be derived from the data, observed values varying between 1.8 sec and 4.2 sec. The highest variations can be observed on September 22. Periods between 1.9 sec and 5.9 sec can be observed with a mean value of 3.0 sec. On September 23 periods vary between 2.0 sec and 4.3 sec with a mean value of 3.0 sec. On September 24 the observed mean period increased to 3.3 sec and scatters around 2.0 sec and 5.1 sec. Keeping the different location of the OpenGPS receiver and the Arcona buoy in mind a reasonable oceanographic signal can be measured by the discussed method.

Fig. 5.75 presents all unfi ltered height measurements made in the time span from September 20 to 24. The specular refl ection point of each measurement is plotted as black dot at an interval of 60 sec. The derived absolut height is color-coded. Green color represents reasonable height estimates of about -0.5 m to 0.0 m above sea level. Colors, which deviate from green, indicate measurements infl uenced by the local uncorrected troposphere. The spatial coverage of height profi les – measured from carrier phase-delay observations of reflected GPS signals during daytime between September 20 and 25, 2004, at the baltic coast – demonstrate that the height data measured by the OpenGPS receiver is not fi xed to one location but covers a comparably large area.

DOI: 10.2312/GFZ.b103-08104

5.5 Inylshik Experiment

5.5.1 Experimental Setup and Data Acquisition

The Merzbacher Lake is located at a height of about 3230 m above sea level and is situated in the borderland and fusion area of two glaciers, the North- and the South-Inylshik Glacier. A map of the Inylshik area – based on an ASTER-Terra image taken on June 25, 2003 – is shown in Fig. 5.78 (H.-U. Wetzel, personal communication). This glacier system, the largest of the Tienshan region, has a total length of more than 65 km and comprises an area of more than 815 km^2. The lake has a length of 4 km, a width of 1 km and a depth of about 130 m. A lake of that size situated in the moraine of a high mountain glacier is a unique natural phenomenon. Caused by this situation, every year a system of cavities develop with a length of 14 km within the South Inylshik Glacier as underground drainage system for the melt water accumulated in the Merzbacher Lake [Wetzel et al., 2005]. Recent dam failures occurred on: July 27/28, 2001; August 1/2, 2002; July 22/23, 2003; August 6/7, 2004 (Fig. 5.4) and July 13/15, 2005. The melt water is fed by the North Inylshik Glacier.

During the Inylshik Expedition conducted between July 22 and August 13, 2005, the OpenGPS experiment was installed at the south-east border of the Merzbacher Lake at a distance of about 500 m from the ice dam of the South Inylshik Glacier. A single RHCP patch antenna was mounted on a geodetic tripod at a height of 1.93 m above the ground. The antenna was tilted 45° towards the horizon and oriented in west direction (azimuth of 260°). Fig. 5.76 shows the OpenGPS instrumentation at the observation site south-west of the Merzbacher Lake. On Fig. 5.77 the OpenGPS antenna and the sensor of the meteorological station can be seen in the foreground. The ice dam of the South Inylshik Glacier can be seen in the background. The picture illustrates the lake surface conditions of Merzbacher Lake on July 30, 2005. Due to an unusually warm summer period in 2005 the expected dam failure already occurred on July 13/15, 2005, unfortunately several days before the expedition arrived at Merzbacher Lake. Thus, the lake water level already had dropped by several meters. In contrast to the expected large open water surface nearly the complete lake surface is covered by floating ice floe and floating and grounded ice bergs. Only a small fraction of the lake surface near the ice dam was temporally ice-free water surface due to small wind forces.

Simulation calculations based on ephemeris data of July 30, 2005, illustrate the area of the Merzbacher Lake which can be covered with specular reflection monitoring points (Fig. 5.79, panel A). In the simulation data shown the satellite observations are limited to elevations between 2° and 75° and -160° and 30° azimuth (Fig. 5.79, panel B). With a simulated antenna height of 45 m above the reflector between 3–6 reflection events can be expected at the Merzbacher Lake location throughout the day (Fig. 5.79, panel C).

Originally, it was intended to conduct the measurements continuously, day and night. Due to envi-

Fig. 5.76: *OpenGPS instrumentation at the observation site southwest and 45 m above the shoreline of the Merzbacher lake.*

DOI: 10.2312/GFZ.b103-08104

ronmental conditions the power supply of the receiver was limited more or less to daytime. Electricity was supplied by a maximum number of 12 x 30 Watt solar panels which effectively generated about 120 Watt during periods of full sunlight. Depending on light intensity, the electrical power was partly used by the receiver (about 55 W) and for battery charging which buffered the power supply for low-light intensity and night time.

The OpenGPS receiver was working during all days in open-loop multi reflection mode (see section 4.3.2). This mode allows tracking of up to 8 direct GPS signals for navigation and open-loop-tracking of up to 4 independent reflected GPS signals simultaneously for altimetry. The measurement mask of the receiver was set to reflection events between -160° and 100° azimuth. Reflection observations were recorded up to 45° elevation. During a reflection event the OpenGPS receiver recorded the in-phase and quad-phase correlation data with a rate of 50 Hz in binary data files.

The OpenGPS receiver monitored the temporal changes of the lake water level during 15 days. 402 data sets could be recorded between July 27, 07:53 GPST and August 10 , 04:23 GPST. Small data sets with file sizes smaller than 1 Mb were neglected. The file size of the remaining data sets mainly varied between 2.5 Mb and 44 Mb. The file size of a 4-hour long record was 60 Mb.

Precise calibration height measurements were conducted in parallel with a Trimble 4000 geodetic receiver at the OpenGPS receiver antenna position (42.196671°N/79.846990°E at 3273.35 m) and at the lake level of Merzbacher Lake on July 30 and August 1, 2005. The local station coordinates were calculated with Trimble Total Control software (Version 2.70 build 306) using the local GPS reference station at Poljana base camp. The Poljana reference station was located at a distance of 4257 m southwest in -145° azimuthal direction of the OpenGPS receiver location. The local reference station Poljana has been connected to the global reference frame with station BIS2 at Bishkek. The long baseline was processed with the Bernese GPS Software (Version 5.0) [Hugentobler et al., 2005, 2001]. Precise ephemeris data from the International GNSS Service (IGS) [Dow et al., 2005] were used. Fig. 5.80 shows the calibration site in the northeastern part of the Merzbacher Lake. Here access to the water and a good GPS signal reception geometry could be found for the calibration measurement. On July 30, 2005 a height of 3228.56 m could be measured at 42.200908°N/79.849443°E (Fig. 5.80). Direct distance observations between antenna and lake surface with a laser meter revealed an uprise rate of the lake water of +4 cm/hour during the afternoon hours between 16:25 and 17:47 GPST+6h. During the afternoon hours the melting process reaches the maximum ablation rates at the North-Inylshik glacier which explains the observed high lake level rise rate. During a repeat measurement on August 1, 2005 at 42.200984°N/79.849418°E a lake level height of 3228.51 m was measured. On August 1 a setting of the water level by -5 cm could be observed with the laser distance meter (Fig. 5.81). On a revisit of the location on August 3, 2005 it was impossible to perform a third lake level calibration measurement. A second dam break occurred and the lake water level dropped several meter (Fig. 5.82). Access to the lake shoreline

Fig. 5.77: *Panorama of the refilled Merzbacher lake during July 30, 2005.*

DOI: 10.2312/GFZ.b103-08104

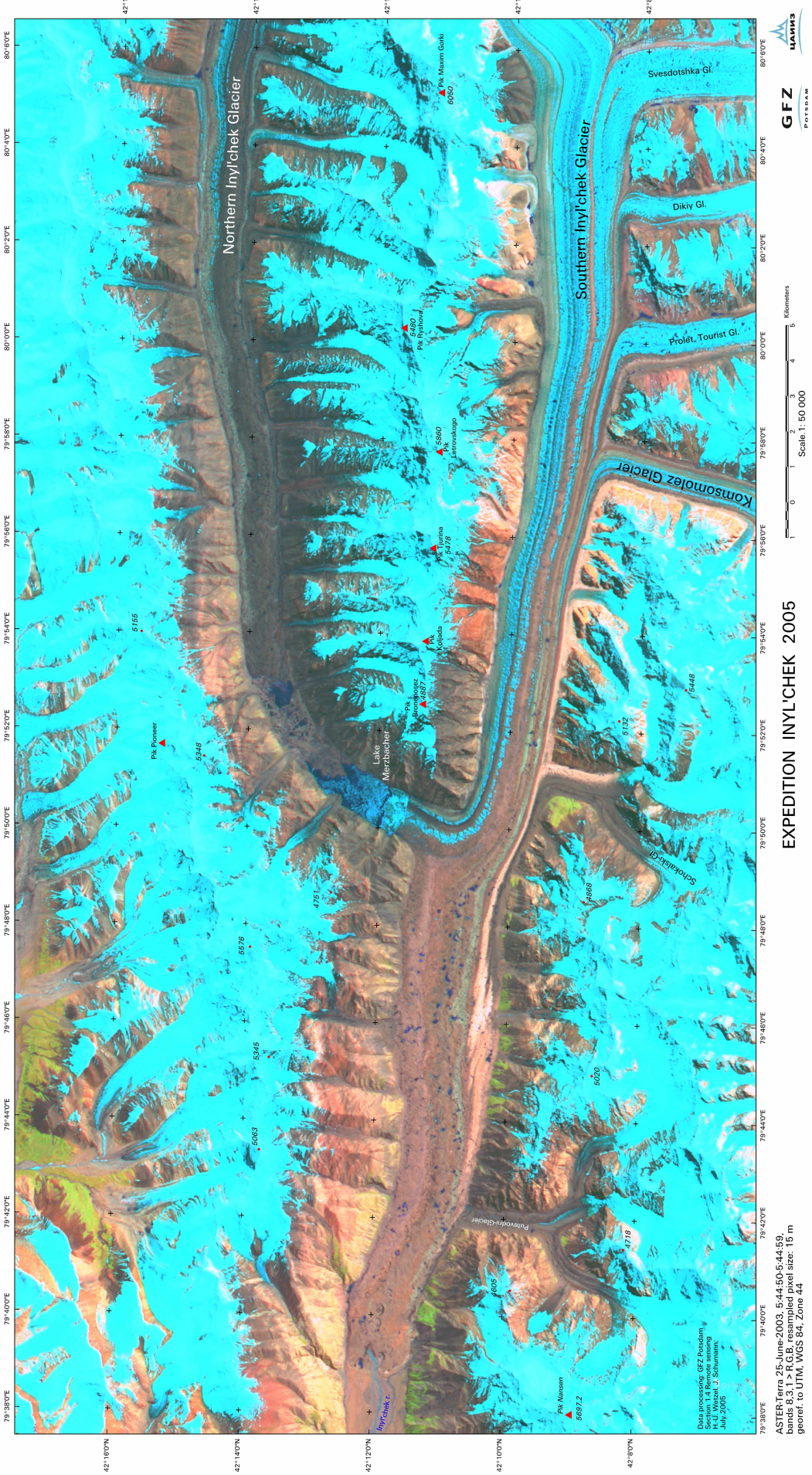

Fig. 5.78: *North and the South Inylshik glacier system (H.-U. Wetzel, personal communication).*

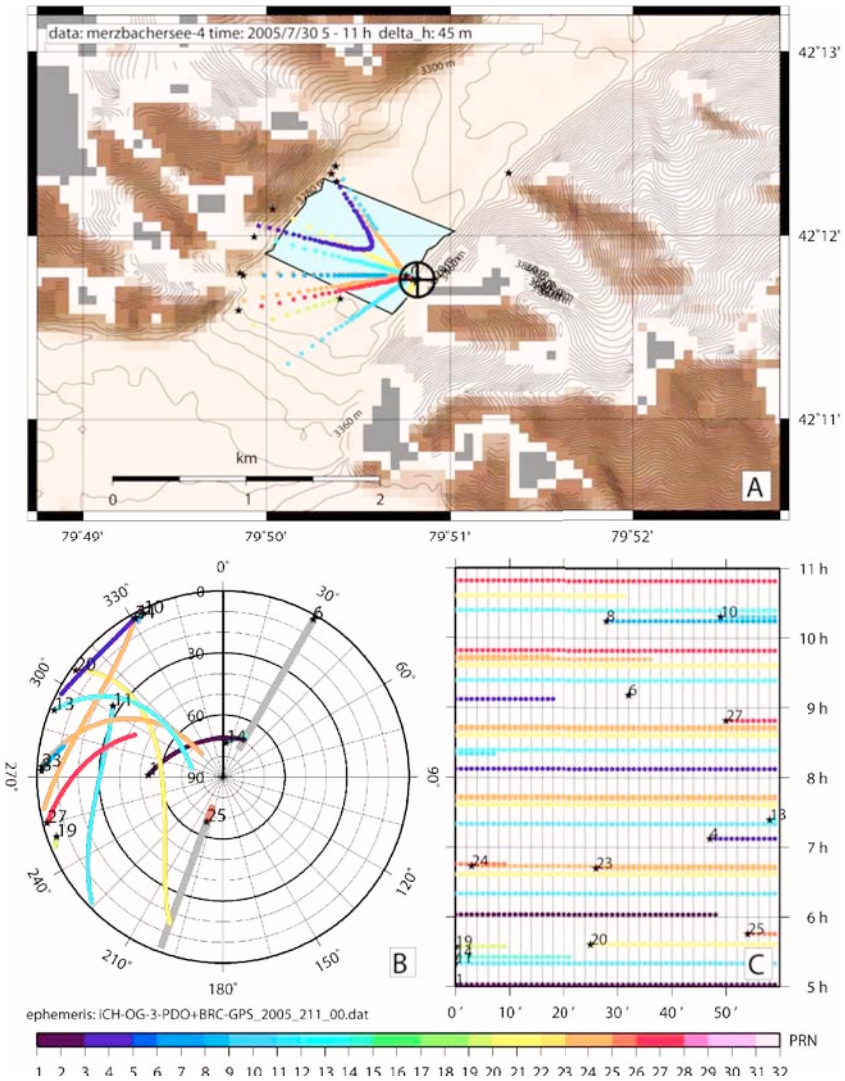

Fig. 5.79: *Schedule of refl ection events at Merzbacher Lake: Panel A shows the possible location of specular refl ection points of visible GPS satellites (prn's) which can be observed on 30 July, 2005, at the Inylshik receiver location (marked by a circle with a cross). Panel B shows the position of the satellites. Panel C shows the time schedule of satellite visibility. Calculations are based on ephemeris data.*

now was impossible without risk of life.

The massive changes of the Merzbacher lake surface – observed from the OpenGPS receiver location – are documented in Fig. 5.83 and Fig. 5.84: The top picture in Fig. 5.83 shows the lake condition until July 30, 2005. Since the reported dam failure on July 13/15 the replenishment of the lake could be observed. Except for a few very large icebergs mostly smaller icebergs and ice fl oes are fl oating. In the background of the picture the height of the maximum water level can be estimated by the visible old shoreline and the grounded small icebergs which can be observed at the north-east shore of the Merzbacher Lake. On August 3 the situation changed dramatically (Fig. 5.83, bottom). The water level dropped massively and grounded icebergs can be observed near the shoreline. At the center of the lake water covered by ice fl oe still dominates the lake surface characteristic. On August 5 (Fig. 5.84, top) the water content which had been stored in the lake, completely vanished. The ice fl oes and icebergs are grounded at the bottom sediments of the lake. During the next days the melt water fl ow – continuously fed by the North Inylshik glacier – generated a continuously growing ice-free river channel. The river channel can be seen in the bottom picture of Fig. 5.84. The set of pictures documents the massive changes of the lake height, topography and surface structure observed during the experiment.

5.5.2 Data Processing

Due to the low observation height of about 43 m of the receiver above the refl ector the refl ected GPS signals arrive at the receiver antenna only with a comparable small delay after the direct signal. Thus, the correlation signal of direct and refl ected signal superpose each other. Like in the Mercure and Königsstuhl experiment the infl uence of the direct GPS signal is suppressed by applying a 30 sec

DOI: 10.2312/GFZ.b103-08104

Fig. 5.80: *Trimble calibration measurement of the lake level of Merzbacher Lake on July 30, 2005, +4 cm/hour rising water level.*

Fig. 5.81: *Repeated calibration measurement of the lake level of Merzbacher Lake on August 1, 2005, -5 cm/hour setting water level.*

Fig. 5.82: *Location of calibration measurement after the second water flooding of the Merzbacher Lake on August 3, 2005, estimated setting water level of about 40cm/hour.*

DOI: 10.2312/GFZ.b103-08104

Fig. 5.83: *Lake level of Merzbacher Lake on July 30, 2005, (top) and on August 3, 2005 (bottom)*

long running mean filter to the correlation data and subtracting the mean value. Additionally, in-phase and quad-phase data were filtered by a 0.4 sec long running mean filter (Fig. 5.87, panel A). As already discussed in the Mercure and the Königsstuhl experiment the quad-phase data had to be modeled from the in-phase data. The phase was calculated from a four quadrant arctangent and unwrapped (Fig. 5.87, panel B). The path difference δ between the direct and reflected signal was calculated by multiplying the phase with the wavelength λ_{L1} of the Doppler-corrected carrier frequency (Fig. 5.87, panel D). In most cases data extracts without cycle slips were selected. Sporadic cycle slips were treated by inserting multiples of λ_{L1} in case the measured path δ deviated from the modeled path δ_{model} by more than a previously defined threshold (Fig. 5.87, panel E and F). With the derived time series δ corrected for cycle slip and the known geometry of receiver, transmitter and reflection point (continuously changing with time), the relative height change of the reflection point was calculated. By starting with an estimated reflector height and carefully removing the influence

DOI: 10.2312/GFZ.b103-08104

Fig. 5.84: *Lake level of Merzbacher Lake on August 5, 2005, (top) and on August 10, 2005 (bottom)*

of troposphere and known height gradients an absolute height profile can be generated (Fig. 5.87, panel G). The influence of the troposphere was calculated from ECMWF data (Fig. 5.85) and ray-tracing analyses. The relative height gradient was derived from the EIGENCG01C geoid [Reigber et al., 2006].

5.5.3 Data Analysis

The OpenGPS receiver recorded 402 data sets between July 27, 07:53 GPST and August 10, 04:23 GPST. In the following extracts from 56 data sets have been manually selected where a clear interferometric signature and undisturbed phase could be observed.

Fig. 5.86 and Fig. 5.87 show the results of data set iny149, measured on July 31, 2005 and starting

DOI: 10.2312/GFZ.b103-08104

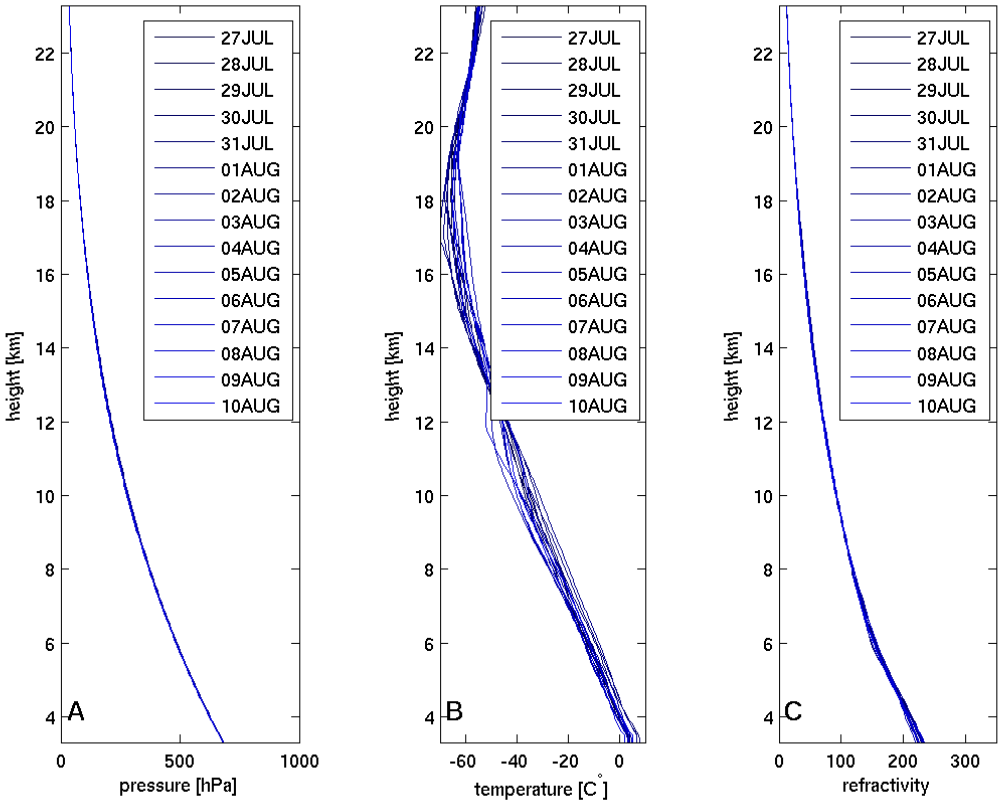

Fig. 5.85: *Variation of the atmospheric parameters pressure (panel A), temperature (panel B) and refractivity (panel C) at 42.0°N, 80.0°E, 3182.0 m above sea level between July 27 and August 10, 2005, at 12:00 GPST. The data are extracted from ECMWF model data.*

at 11:21:11 GPST. The data extract shows the received reflected signals of PRN 8 between 6.9° and 8.4° elevation. For a first height guess the observed interferometric frequency of 0.041 HZ is determined from the Fourier spectrum calculated from the correlation data (Fig. 5.86, panel H). Using the observed interferometric frequency and from the mean elevation of 7.657° and the mean elevation change rate of 0.0050°/sec an absolute height of 3229 m of the reflector has been estimated (Fig. 5.86, panel L). From the interferometric pattern which can be clearly observed in the correlation data (Fig. 5.87, panel A) and the amplitude of the signal (Fig. 5.86, panel C) an undisturbed phase could be calculated (Fig. 5.86, panel B). The predicted path δ of the model deviates from the measured path δ by not more than 0.04 m most of the time (Fig. 5.86, panel E). Thus, no cycle slip had to be corrected (Fig. 5.86, panel F). The detrended height profile states a mean height of 3227.33 m with a STD of 0.05 m. The derived height profile has a length of 18 m and is dominated by sharp saw tooth formed structures, e.g. between a distance of 346 m and 354 m from the receiver. The derived absolute heights deviate by -0.44 m/1.26 m and -0.49 m/1.21 m from the calibration measurements made on July 30 and August 1.

On August 3, 2005, the data set iny246 was recorded, starting at 11:08:20 GPST (Fig. 5.88, C.13). Again the GPS signal of PRN 8 was observed between 4.7° and 6.2° elevation. The correlation data, the phase data and amplitude behavior appear to be quite similar to the data previously discussed. From the interferometric frequency of 0.053 HZ and a mean elevation of 5.424° and the mean elevation change rate of 0.0050°/sec an absolute height of 3215 m of the reflector is estimated. Compared to the previous measurement much smoother height fluctuations can be observed in the derived detrended height profile. The detrended height profile states a mean height of 3213.58 m with a STD of 0.06 m. Thus, based on the reflectometry measurements iny149 and iny246 the lake level dropped by an amount of 14 m or 13.75 m. This large height change agrees with the estimates made during visual observations.

Fig. 5.89 and Fig. C.14 show the data set iny224, recorded at the same day at 04:31:19 on August

DOI: 10.2312/GFZ.b103-08104

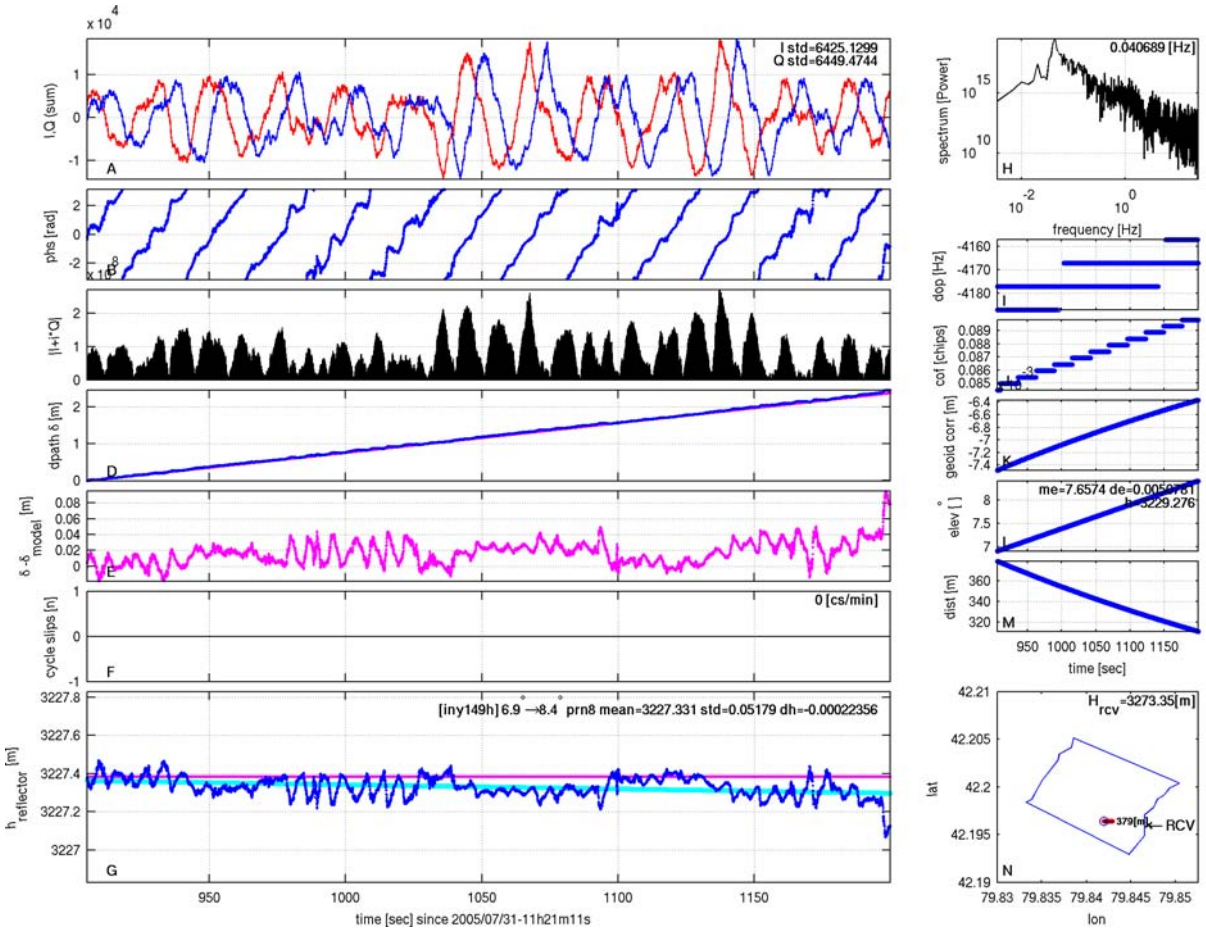

Fig. 5.86: *Height profile of Merzbacher Lake on July 31, 2005, starting at 11:21:11 GPST*

3, 2005. PRN 11 was observed between 29.5° and 28.4° elevation. Again a strong interferometric pattern can be observed in the correlation data and the amplitude (Fig. C.14, panel A and C). From the interferometric frequency of 0.042 HZ and a mean elevation of 28.96° and the mean elevation change rate of -0.0026°/sec an absolute height of 3172 m of the reflector is estimated. A bending of the height profile can be observed in a range of ± 0.2 m between a distance of 188 m and 196 m from the receiver. This complicates the detrending process. The detrended height profile states a mean height of 3167.11 m with a STD of 0.03 m. The derived absolute heights deviate by 56.51 m/61.40 m from the calibration measurement made on August 1. The derived height values underestimate the lake height at August 3. Most probably the recorded signal was reflected by a sloped surface of an iceberg or ice floe. Therefore only a comparably short profile with a length of 8 m could be observed. Thus, the unknown slope could not be corrected and the derived height is biased.

After August 3, 2005, the lake surface conditions changed again and the water which has been stored in the lake, completely vanished. The lake surface now consists of a rough topography of a scattered and inhomogeneously distributed conglomerate of icebergs and ice floes which are grounded in humid fineclastic lake sediment. Only very short data extracts can be found for successful processing.

Fig. 5.90 shows a typical profile recorded on August 6, starting at 04:00:54 GPST. Observations of PRN 19 were used at elevations between 21.4 down to 20.8°. The signal strength of the registered correlation data significantly decreased. A much higher amount of noise can be observed in the correlation data and the derived phase (Fig. C.15, panel A and B). Although a noisy but recognizable phase indicates a reflection, compared to the examples shown before the interferometric pattern is hardly noticeable in the amplitude itself. The predicted model path δ deviates by not more than 0.1 m from the measured path δ for most of the time (Fig. C.15, panel E). But, caused by the noisy and degraded phase data, several cycle slips had to be corrected (Fig. C.15, panel F). From the interferometric frequency of 0.048 Hz and a mean elevation of 21.08° and the mean elevation change rate of -0.0024°/sec an absolute height of 3156 m of the reflector was estimated. The detrended height profile states a mean height of 3148.41 m with a STD of 0.05 m. Again, the derived absolute

DOI: 10.2312/GFZ.b103-08104

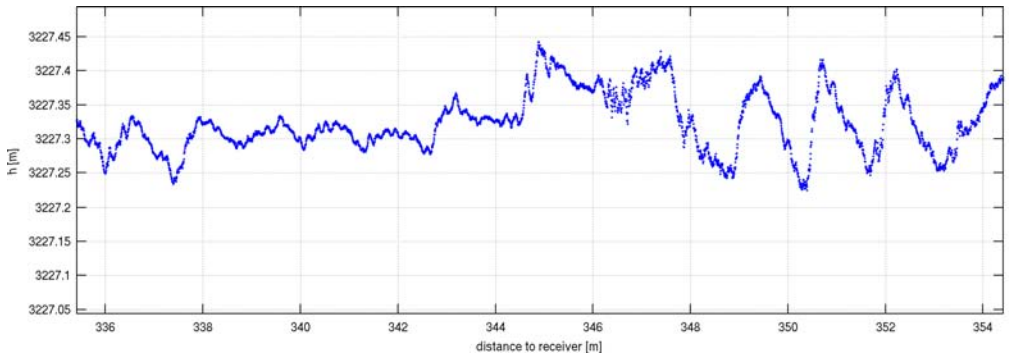

Fig. 5.87: *Height profile of Merzbacher Lake on July 31, 2005, starting at 11:21:11 GPST*

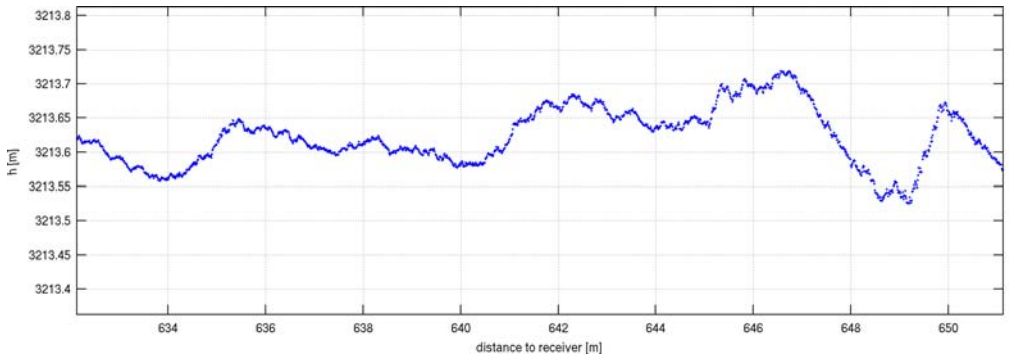

Fig. 5.88: *Height profile of Merzbacher Lake on August 3, 2005, starting at 11:08:20 GPST*

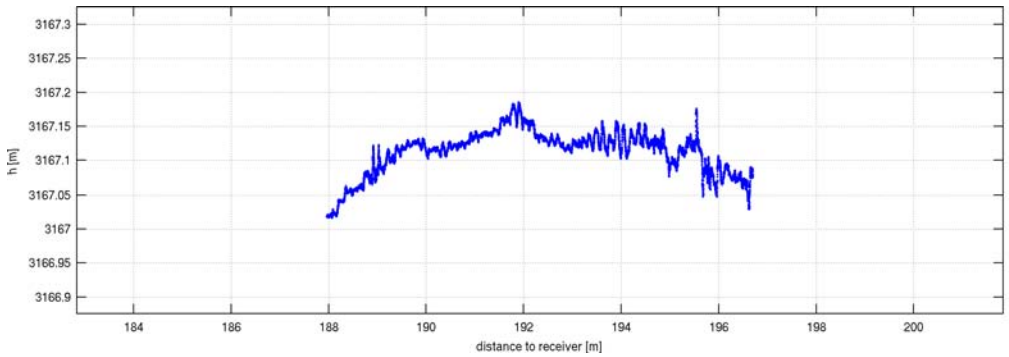

Fig. 5.89: *Height profile of Merzbacher Lake on August 3, 2005, starting at 04:31:19 GPST*

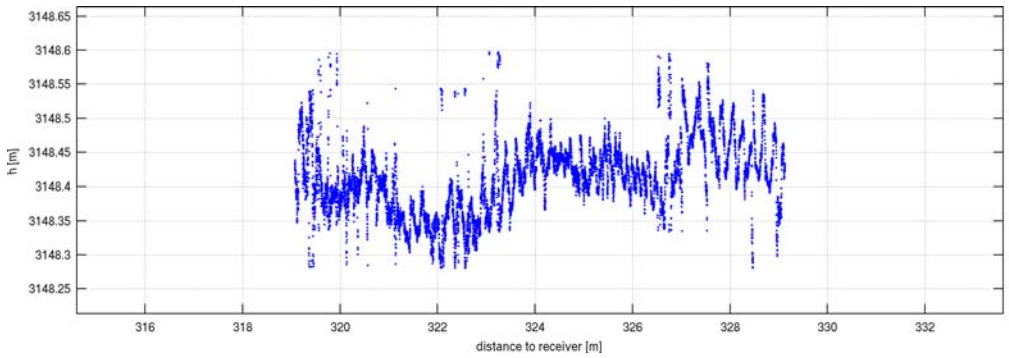

Fig. 5.90: *Height profile of Merzbacher Lake on August 6, 2005, starting at 04:00:54 GPST*

DOI: 10.2312/GFZ.b103-08104

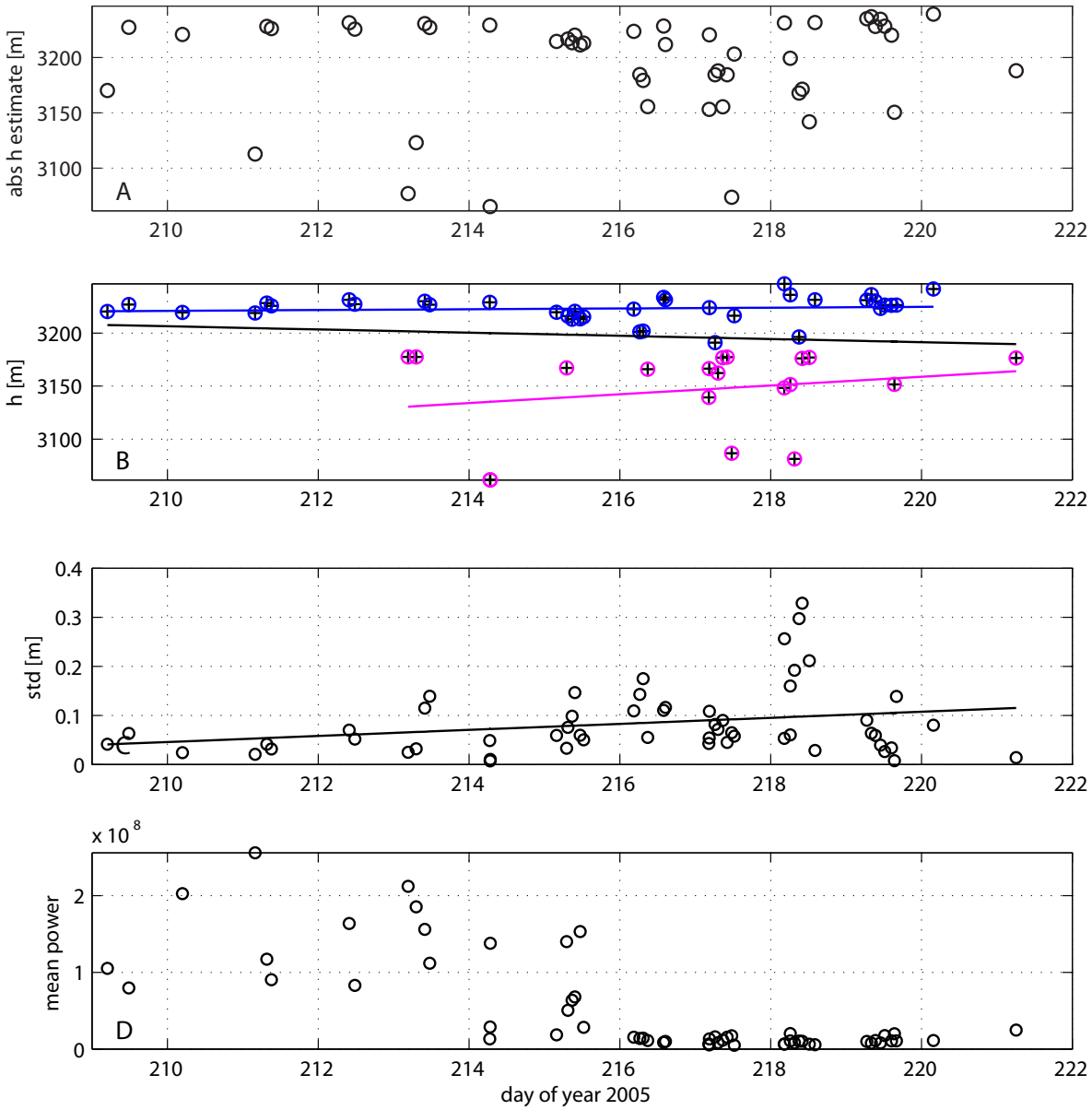

Fig. 5.91: *Mean absolute height calculation from peak frequency estimate (panel A), mean absolute height estimate (panel B), STD (panel C) and mean power (panel D) of all recorded data received from the lake area between July 28 (doy 209) and August 9 (doy 221), 2005.*

heights deviate by 72.51 m/80.10 m from the calibration measurement made on August 1. The derived height values underestimate the lake height on August 3. The recorded signal must have been reflected by a sloped surface of an iceberg or ice floe. Therefore only a comparably short profile with a length of 8 m could be observed. Thus, the unknown slope could not be corrected and the derived height is biased. The specular reflection point of the measured reflected GPS signal is not bound to the horizontal lake surface. The specular reflection point can be situated at any point between satellite and receiver antenna which meets the reflection geometric boundary conditions.

5.5.4 Discussion

In the following the results of all 56 selected and individually processed data sets are discussed. Fig. 5.91, panel A, plots the mean absolute height versus the time of observation between July 28 (doy 209) and August 9 (doy 221), 2005. The mean height is calculated from the peak frequency estimate of each height data set. Beside some outliers far below 3200 m the estimated mean height ranges between 3220 m and 3230 m until August 2 (doy 214). On August 3 (doy 215) all observa-

DOI: 10.2312/GFZ.b103-08104

tions deliver heights between 3211 m and 3220 m. From August 4 (doy 216) on the derived heights uniformly scatter between the extreme values of 3074 m and 3239 m.

Similar results can be seen in Fig. 5.91, panel B. The mean heights shown result from the detrended relative height profiles derived from measured phase observations. Except some outliers on August 1 and 3, the calculated mean height ranges between 3219 m and 3232 m until August 2 (doy 214). On August 3 (doy 215) all observations deliver heights between 3213 m and 3221 m. From August 4 (doy 216) onward the derived heights again uniformly scatter between the extreme values of 3081 m and 3247 m. 3 linear trends are plotted in Fig. 5.91, panel B. The black line represents the trend in case that all heights are considered. As discussed earlier, reflection events stating a height below 3180 m most probably do not result from the horizontal lake surface but from a sloped surface and exhibit a height bias. Thus, the derived heights were classified into heights below (pink colored) and above 3180 m (blue colored) and a linear trend has been calculated for both classes.

Fig. 5.91, panel C, shows the corresponding STD of each single height time series. Until August 1 (doy 213) in most cases the values vary between 0.02 m and 0.07 m. Starting on August 3 (doy 215) the observed STD variation increases to values in the range from 0.03 m to 0.15 m. The peak variation can be observed on August 6 (doy 218) with values ranging from 0.03 m up to 0.33 m.

The mean correlation power (I^2+Q^2) of the reflected signal of each data set is displayed in Fig. 5.91, panel D. Between July 28 (doy 209) and August 1 (doy 213) the recorded data sets result from strong reflected signals with a mean power between $8.2 \cdot 10^7$ and $2.6 \cdot 10^8$. The reflected power drops by a factor of 2 between August 2 and 3 (doy 214 and doy 215). During that period the mean power varies between $1.3 \cdot 10^7$ and $1.5 \cdot 10^8$. From August 4 (doy 216) on the reflected power significantly decreased down to values between $5.0 \cdot 10^6$ and $2.5 \cdot 10^7$.

The most significant changes during the observation period can be seen in the reflected power. During the time period from July 28 to August 1 a comparably slow refilling process took part. The structure and the size of the reflecting lake surface did not significantly change during that time span. The water covered with ice floe reflected a comparably high fraction towards the OpenGPS antenna (see Fig. 5.83, top). During the following 2 days on August 2 and 3 the water discharged. Thus, the area of ice floe-covered water which represents a comparably planar and horizontal, reflecting surface decreased and the number of grounded ice bergs increased (see Fig. 5.83, bottom). The former lake surface starts to transform into a discontinuous surface of small horizontal ice floe-covered areas with inlets of larger ice bergs representing small reflecting surfaces of all possible slopes. From August 4 (doy 216) on, the lake water completely discharged (see Fig. 5.84). Only a small fraction of the GPS signal is reflected from the scattered ice surface. The derived mean height values vary within a large height range as the reflections are originated most probably from different sloped surfaces.

In Fig. 5.92, panel E, the estimated peak period of the height time series is displayed versus the observation time. Red triangles represent the peak periods derived from the Fourier spectrum calculated from the height time series, pink circles represent the mean peak periods derived from the smoothed Fourier spectrum, filtered by a running mean filter of 10 samples length. Calculating a linear trend from the mean peak period reveals a slow decrease from 7.5 sec on July 28 (doy 209) to 4.8 sec on August 9 (doy 221). From August 4 (doy 216) on the reflected power significantly decreased and the variation of the derived peak period increases by a factor of 2. The peak period scatters around values ranging from 1.7 sec to 16.6 sec.

Between July 28 and July 31 the observations were recorded between 13.3° and 20.4° elevation (Fig. 5.92, panel F). The distance of the specular reflection point to the receiver varied between 146 m and 194 m (Fig. 5.92, panel G). On August 1 observations could only be made at lower elevations ranging from 8.4° down to 3.2°. Thus, the reflection point was located at larger distances between 311 m and 740 m. From August 2 onwards the data sets occurred at elevations varying between 3.1° and 40.0° elevation and the reflection took place at distances between 44 m and 978 m.

Fig. 5.93, panel A, shows a scatter plot of all data sets with the mean elevation plotted versus the reflection point distance. The color scale represents the time sequence the data sets were recorded (panel B, C, D, too). Blue circles represent earlier measurements, mainly recorded in July 2005 while green circles represent later measurements, mainly recorded in August 2005. The solid, dashed and dash-dot black curves represent the theoretical relation between elevation and reflection point distance (see Fig. 3.9 on page 37) of a reflector at 3228 m, 3214 m and 3170 m observed by a receiver

DOI: 10.2312/GFZ.b103-08104

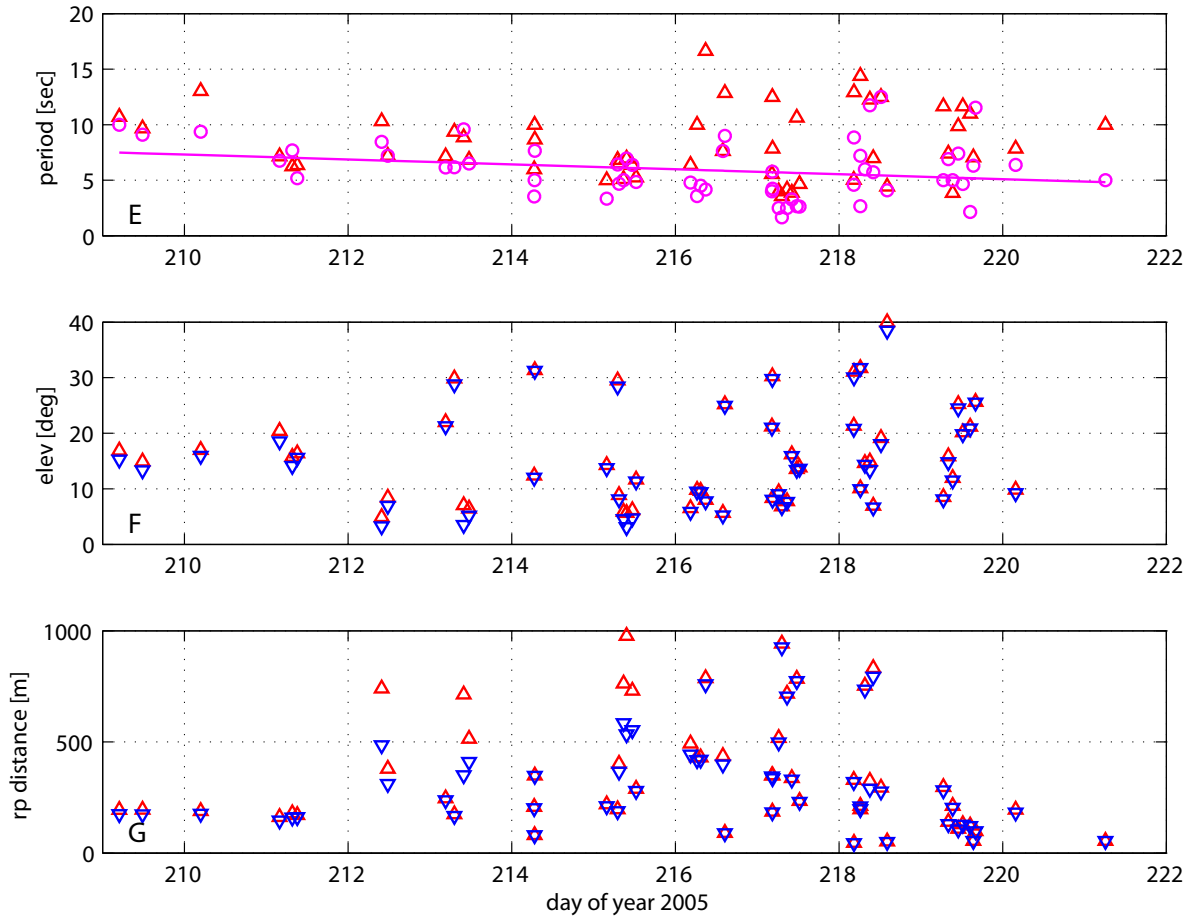

Fig. 5.92: *Estimated peak period (panel E), minimum and maximum observed elevation (panel F) and minimum and maximum distance of the mean reflection point (panel G) of all recorded data received from the lake area between July 28 (doy 209) and August 9 (doy 221), 2005.*

at 3271 m. Most observations lie in the interval given by the 3228 m and 3214 m high reflector model and occur at elevations between 40° and 4°. A second class of observations cluster around the 3170 m model reflector and observations range between 70° and 6° elevation. In Fig. 5.93, panel B, no strong relationship can be seen in the scatter plot between the distance of the specular reflection point to the receiver and the observed mean period within the height time series. The solid black line represents the calculated linear trend of all plotted data. Most observations occur in a distance between 50 m and 400 m with a period between 2.1 sec and 12.5 sec with a mean value of 6.4 sec. The relation between reflection point distance and STD reveals a weak positive linear trend (Fig. 5.93, panel C). The solid black line represents the calculated linear trend of all plotted data. At a distance of 50 m the STD varies between 0.01 m and 0.03 m. At a distance around 110 m the STD varies between 0.02 m and 0.04 m and increases to values between 0.02 m and 0.06 m at a distance of around 180 m. At distances larger than 400 m no STD below 0.06 m can be observed. This effect can be explained by the varying velocity at which the specular reflection point travels over the reflecting surface. At high elevations and low distances the geometry of satellite and receiver changes slowly. Thus, the reflection point travels at a low velocity. At lower elevations the geometry of satellite and receiver changes faster and, within 60 sec, the reflection point can cover a profile of more than 200 m (see Fig. 5.79, panel A). Fig. 5.93, panel D, shows a scatter plot of all data sets with the mean profile height plotted versus the reflection point distance. The solid black line represents the calculated linear trend of all plotted data. A small linear descent can be seen in the data clustering around 3230 m height. Interesting are the 5 measurements at 3177 m height at distances between 54 m and 333 m.

The smoothed Fourier frequency spectrum of nearly all height time series used show a significant signal in the frequency band between 0.1 Hz and 0.2 Hz (Fig. 5.94). The power is normalized to the maximum peak power observed in the unfiltered Fourier frequency spectrum. The color scale repre-

DOI: 10.2312/GFZ.b103-08104

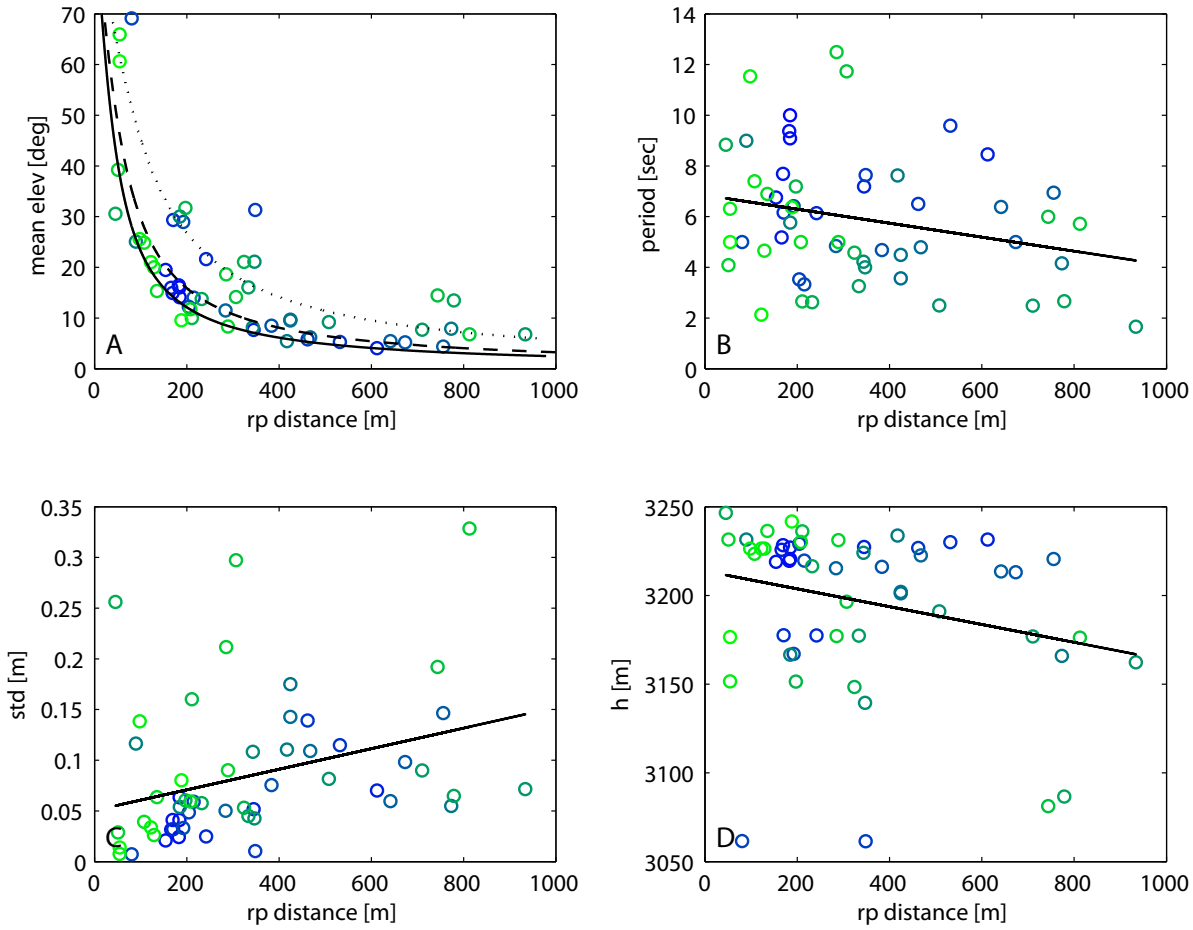

Fig. 5.93: *Scatter plot of mean elevation (panel A), estimated period (panel B), standard deviation (panel C) and height versus the estimated distance of the reflection point.*

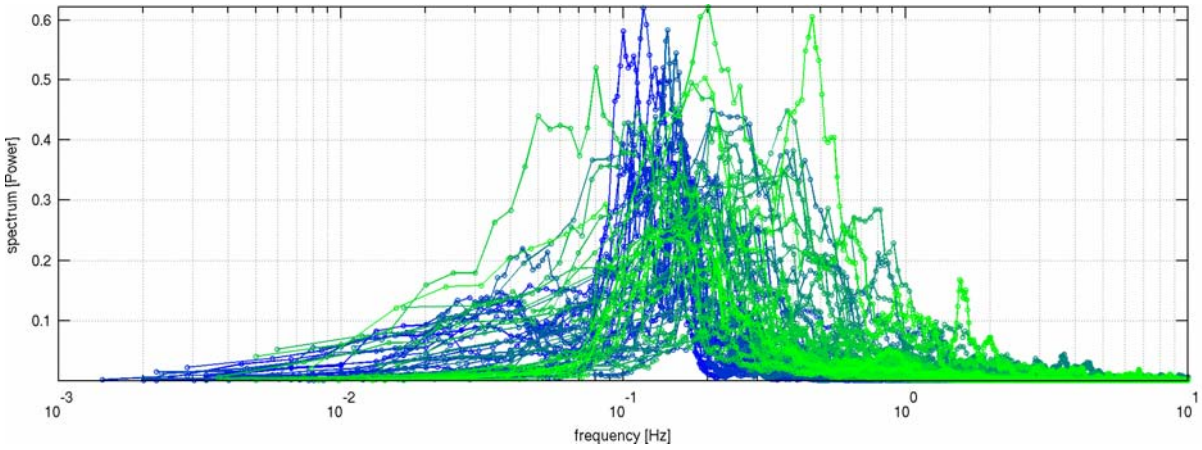

Fig. 5.94: *Smoothed Fourier frequency spectrum of the measured height signal.*

sents the time sequence the data sets were recorded. Blue circles represent earlier measurements, mainly recorded in July 2005 while green circles represent later measurements, mainly recorded in August 2005. Spectra of height time series measured after August 1 (green) tend to have frequency content at higher frequencies from 0.2 Hz to 0.9 Hz.

The top panel of Fig. 5.95 shows all selected datasets geo-located at the Merzbacher Lake location. The estimated coastline of the lake is picked from the ASTER-Terra image which is shown in Fig. 5.78. The south-western coast line – representing the ice-dam – is expected to be incorrect because the ASTER image was already taken in 2003. Each height profile location and length is represented by a black line. The derived mean height is plotted at the mean reflection location and

DOI: 10.2312/GFZ.b103-08104

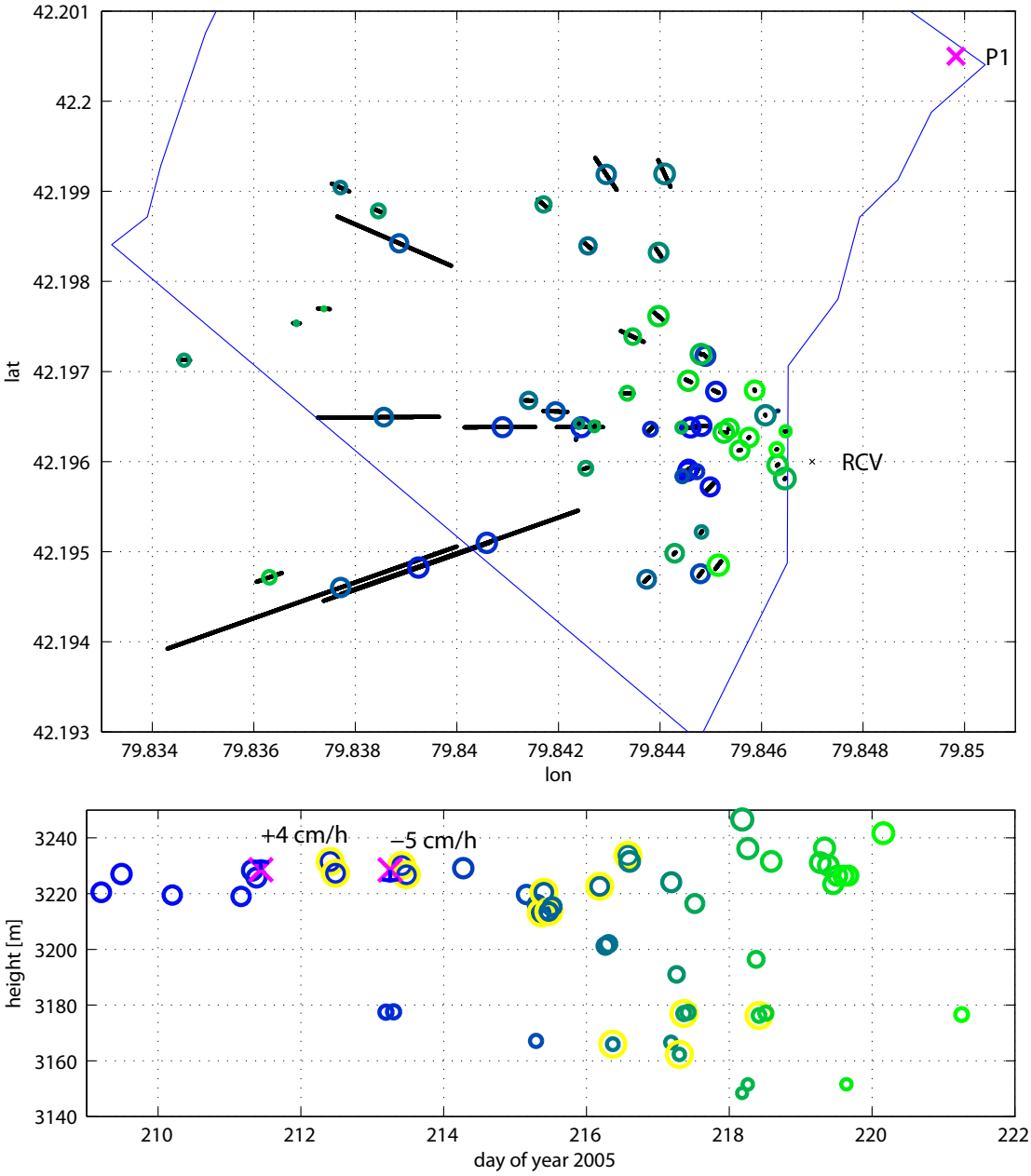

Fig. 5.95: *Top: Mean geographic location and mean absolute height of each evaluated height profile recorded from the lake area between July 28 (doy 209, green color) and August 9 (doy 221, blue color), 2005. Bottom: Mean absolute height of each evaluated height profile. Two Trimble height calibration measurements are marked with red circles with blue arrows indication the estimated water level rise rate.*

represented by a colored circle. The color scale represents the time sequence the data sets have been recorded. Blue circles represent earlier measurements, mainly recorded in July 2005 while green circles represent later measurements, mainly recorded in August 2005. The diameter of the circles represent the derived mean height. A lower reflector height is represented by a small diameter, a higher reflector by a larger diameter. A red cross, marked by P1, assigns the location of the two precise Trimble calibration measurements. The data show a good spatial coverage of the southern part of the Merzbacher Lake surface. No systematic pattern can be seen in the geolocated data. Measurements after August 7 (doy 219) tend to be located near to the receiver. The bottom panel of Fig. 5.95 shows the same measurements as mean heights versus measurement time. The mean heights are represented in the same way as above as colored circles. The two precise Trimble calibration measurements are marked with red crosses and the appropriate rise/decrease rate is stated with +4cm/h on July 30 and -5cm/h on August 1. Heights marked with yellow circles indicate measurements recorded at a mean elevation below 8°, but no systematic pattern can be identified in

DOI: 10.2312/GFZ.b103-08104

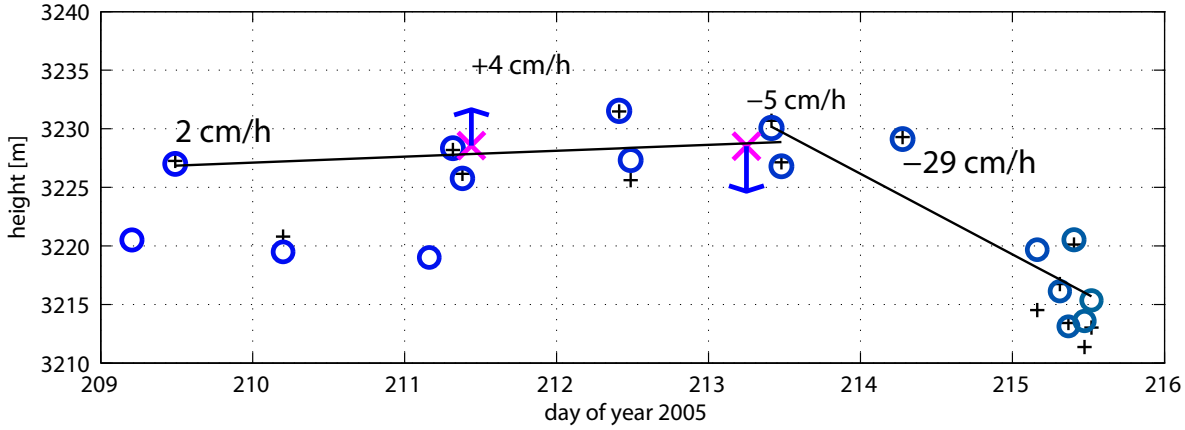

Fig. 5.96: *Mean absolute height of each evaluated height profile recorded from the lake area between July 28 (doy 209, green color) and August 9 (doy 221, blue color), 2005. Two Trimble height calibration measurements are marked as red circles with blue arrows indicating the estimated water level rise rate.*

the yellow marked data.

As already previously discussed in Fig. 5.91, panel B, except some outliers on August 1 and 3, the calculated mean height ranges between 3219 m and 3232 m until August 2 (doy 214). On August 3 (doy 215) all observations deliver heights between 3213 m and 3221 m. From August 4 (doy 216) on the derived heights uniformly scatter between the extreme values of 3081 m and 3247 m. The 3178 m height measurements on August 1 can directly be compared with the parallel calibration measurement. Thus, the reflections cannot be generated by the horizontal ice-covered water of the lake surface. All height profiles stating a height below 3180 m can be categorized as signals which have been reflected by sloped surfaces of icebergs and ice floes or reflectors not located at the water level of the lake. Thus, a height bias is introduced by the fact that the supposed slope of the reflecting surface is not corrected and the assumption of a horizontal reflector is not fulfilled. For lake level monitoring applications this measurements have to be corrected for the slope if possible. Due to the rapidly changing environment of the Merbacher Lake and ice distribution a slope correction was not possible without other independent observations. Therefore the measurements had to be excluded. The remaining measurements are plotted in Fig. 5.96.

Blue circles represent the mean height derived from the detrended relative height profiles. Black crosses mark the appropriate absolute heights derived from the peak frequency estimate. The two calibration measurements are marked by a pink cross. Between July 28 and July 30 three measurements can be observed which state a mean height around 3220 m and are biased by more than 7 m in comparison with the calibration measurement on July 30. Probably they belong to the same reflector which is not located at the water level of the lake. These measurements are excluded from the calculation of the linear height trend of the measurements recorded from July 28 to August 1. A mean rise rate of 2 cm/h or 0.48 m/day can be calculated from the selected height profiles during that time period which show good agreement with the directly measured rate of 4 cm/h at the calibration point on July 30. The higher value can be explained by the higher melting rates expected in the afternoon hours due to the sun radiation during daytime. On August 1 already a decrease rate of -5 cm/h could be directly measured at the calibration point. Between August 1 and August 3 a second linear trend is calculated with a mean decrease rate of -29 cm/h or 7.0 m/day. Obviously much more data is needed in order to come up with a statistically more reliable statement.

GPS positional measurements have been performed directly at the ice dam of the South-Inylshik glacier in order to register the response of the glacier ice dam to the dam break and complete loss of the Merzbachersee water body. The GPS positional measurements show vertical movements of up to 0.8 m/day and vertical motions not related to ablation of up to -15 m/day [Mayer et al., 2006, 2008].

DOI: 10.2312/GFZ.b103-08104

6 Conclusions and Future Work

This study answers the question if carrier phase observations of reflected GPS L1 signals can be successfully used to obtain from a remote position altimetric information about the reflecting surface itself. Focus is put on coherent specular reflections from water surfaces. The conducted ground-based experiments demonstrate that the interferometric amplitude variations of the reflected signal can be recorded with the newly developed OpenGPS receiver. The open-loop tracking technique could be successfully applied to directly record in-phase and quad-phase data of the reflected signal. The recorded GPS L1 carrier phase information allows for measuring the optical path difference between direct and reflected GPS signal. The conducted experiments show that altimetric information about the reflector can be recovered with some centimeter accuracy. Model calculations of the reflection coefficients of an air-water interface based on the Fresnel equations show that toward lower elevations the reflected signal consists of an increasing signal fraction with RHCP polarization. The conducted experiments confirm that for observations below about 20° elevation the new experimental set-up of only one tilted omni-directional standard RHCP patch antenna with 4 dBic gain suffices – depending on the reflectors surface roughness conditions – for direct and reflected signal reception in parallel. Such setup represents a different observation technique to a combined setup of two RHCP and LHCP antennas which focuses on observations for scatterometry. In case the GPS antenna can be positioned high above the reflecting surface, the reflected signal has a sufficient large time delay. Thus, the reflected signal can be recorded without any influence of the direct signal. This mostly is the case in air-borne, space-based scenarios and at the Fahrenberg experiment in the Bavarian alpine upland. At measurement geometries at low observation altitudes and low elevations, like in the case of the Königsstuhl at the border of the Baltic Sea or the Lake Merzbacher experiment, the time delay between direct and reflected signal is small and the recorded signal is a composite of both the direct and reflected signal, respectively. A new filter could be developed to suppress the direct signal and recover the reflected signal. The receiver tracking routine influences the recorded correlation data of the reflected signal at low elevations and small delays. At such circumstances the quad-phase component contains no or only a weak fraction of the reflected signal. A new method could be developed which generates the quad-phase data from the in-phase data. This study classifies a signal as a reflected signal in case the in-phase and quad-phase data vector describes a circular movement over time. In case of very small time delays between direct and reflected signal the in-phase and quad-phase data vector describes a non-circular movement over time. This indicates that the tracking routine of the receiver cannot separate between reflected and direct signal which could be illustrated during the Mercure hotel experiment. At Fahrenberg the visually observed lake water surface roughness was small in comparision to the measuring wavelength of the GPS L1 carrier. Several height profiles from both observed lakes Lake Walchen and Lake Kochel could be obtained with some centimeter accuracy. By applying a new developed method to minimize occuring cycle slips, continuous height time series could be extended to a duration of up to 15 min, covering a height profile of about 1700 m length. During very smooth surface conditions height accuracies below 2-centimeter could be observed at Lake Walchen. The Königsstuhl experiment demonstrates that below 4° elevation coherently reflected signals can be recorded even at water surface roughness conditions at which the observed wave heights exceed the GPS L1 carrier wavelength. Continuous data recordings with durations up to 25 min could be obtained. Single derived height profiles can represent sea surface heights at a length of more than 3000 m and up to distances between 6000 m and 8000 m to the receiver. The experiment demonstrates the capability of the OpenGPS receiver to observe up to 4 reflected GPS signals in parallel. Furthermore, the experiment illustrates an important error source of coherent phase altimetry. Especially at low elevation angles the measurements are heavily tackled by the influence of the local Earth's troposphere. This study already implemented a tropospheric correction model into the data processing. This correction model grounds on ECMWF model data and geometrical ray-tracing analysis in order to calculate the influence of the troposphere on the bending angle and optical path lengths of the direct and reflected signals. At Mount Fahren applied optical path corrections are in the range of 1-meter. The conducted experiments show that

especially at very low elevations – the signals have to travel a long path through the troposphere – the in-situ conditions cannot be adequately represented by the used tropospheric correction model. Especially below 4° elevation spurious height signatures within several decimeter range can migrate into the measurement. This study shows that the used tropospheric correction model is limited at grazing angles and that there is a strong demand to refined such a troposheric correction model. The carrier phase observations of the reflected signal allow to determine the change of the path difference between reflected and direct signal. Based on the known time-dependent geometry of the receiver, transmitter and specular reflection point, only a time serie of relative height changes can be obtained. In order to derive a height profil this study assumes a horizontal reflecting surface. A first a-priory height guess is adjusted until the resulting height profil has no overall slope. In case of reflecting water surfaces as in the case of Lake Walchen, Lake Kochel or the Baltic sea this assumption can be fullfilled quite well, if known slopes or curvatures are taken into account. This study models the geometry of the Earth's curvature by a best-fitting local sphere. The influence of inhomogeneous mass distribution on the water surface is corrected by applying a slope correction based on local or global geoid model data. At Mount Fahren such corrections range between 6 to 10 cm along a 1000 m long profile at a maximum and are of minor relevance. Slopes induced by, e.g., wind swell, are of more relevance and have to be taken into account, if known. Otherwise, the derived height profiles will have a height bias. At more complex situations the assumption of one horizontal reflector cannot be fullfilled and each derived height profile can be contaminated by a different height bias. The Merzbacher experiment illustrates this problem. At Lake Merzbacher nearly the complete lake surface is covered by floating ice floe and ice bergs. GPS reflections could be recorded not only from the water surface but also from ice. The experiment proves that ice reflections are strong enough to be detected but different and unknown sloped surfaces generate massive height biases to each single measurement. A careful manual selection of reasonable reflections made it possible to estimate the replenishment of the glacier lake level to a mean rise rate of 2 cm/h which agrees well with independent in-situ measurements of 4 cm/h. A glacier lake outbreak flood could be directly observed with the OpenGPS receiver and single measurements indicate a water level drop of 13.75 m during 3 days. By analyzing the measured reflection data after the glacier outbreak happened, a mean lake level decrease rate of -29cm/h or -7 m/day could be estimated. After the water completely drained the STD of the height profiles – used as an estimate of the surface roughness – increased and the power of the reflected signal significantly decreased.

The Merzbacher experiment illustrates for the first time the feasibility of GPS reflectometry to monitor hazardous glacier outburst flood events in remote high mountain areas [Helm et al., 2007b, Mayer et al., 2008]. Such monitoring scenario is a potential area for future applications, not only to minimize human casualties and structural damage, but to observe and understand the mechanisms and temporal evolution of the number and volume of such GLOF events which are an important indicator for global climatologic changes. For an operational ground-based water level observation system, such as planned as one component in the Central Asia Water (ZAWa) project, future work has to focus on the development of a robust processing scheme. Parallel observations have to be combined in order to minimize systematic errors. Tropospheric corrections from local radiooccultation observations have to be implemented in order to enhance the necessary tropospheric correction model. With the increasing number of available GNSS signals and GNSS capable receiver technology the number of possible reflectometry observables increase. Since 2006 activities are performed within the German Indonesian Tsunami Early Warning System (GITEWS) to establish a multi-frequency capable GNSS receiver for GNSS remote sensing applications from space [Helm et al., 2007a]. The open-loop tracking technique could be successfully implemented into the firmware of a commercial geodetic-grade 2-frequency receiver. At the Fahrenberg location ground-based experiments could be repeated. Based on the work of this study coherent carrier phase observations could be repeated for GPS L1 signals and observations could be extended to the new civil GPS L2C signals. The derived height profiles agree well with independend in-situ tide gauge measurements [Helm et al., 2008b]. In order to develop the necessary methodology for space-based GNSS reflectometry remote sensing, air-borne campaigns with the Zeppelin NT are planned above Lake Constance. Such air-borne experiments represent the necessary intermediate step for the transition from ground-based static observations to space-borne dynamic global GNSS-R remote sensing which is the longterm goal of this studies.

DOI: 10.2312/GFZ.b103-08104

Bibliography

D. Akos, A. Hansson, Per-Ludvig Normark, Christian Rosenlind, Adreas andStahlberg, and Fredrik Svensson. Real-time software radio architectures for GPS receivers. *GPS World*, pages 28–33, July 2001.

K. Anderson. Determination of water level and tides using interferometric observationsof GPS signals. *Journal of Atmospheric and Oceanic Technology*, 17:1118–1127, 2000.

J. Ashjaee. An analysis of y-code tracking techniques and associated technologies. *Geodetical Info Magazine*, 7(7):26–30, 1993.

J.-C. Auber, Al. Bibaut, and J.-M. Rigal. Characterization of multipath on land and sea at GPS frequencies. In *Proceedings of the 7th International Technical Meeting of the SatelliteDivision of the Institute of Navigation*, pages 1155–1171, Salt Lake City, UT; US, 20–23 September 1994.

P. Beckmann and A. Spizzichino. *The Scattering of electromagnetic waves from rough surfaces*, volume 4 of *International series of monographs on electromagnetic waves*. Pergamon Press, Oxford, 1963.

G. Beutler, G. W. Hein, W. G. Melbourne, and G. Seeber, editors. *GPS Trends in Precise Terrestial, Airborne, and Spaceborne Applications*. Springer-Verlag, New York, 1996.

G. Beyerle. Opengpsrec: An open source gps receiver. http://www.geocities.com/gbeyerle/software/download.html, July 2003.

G. Beyerle and K. Hocke. Observation and simulation of direct and reflected GPS signals in radiooccultation experiments. *Geophys. Res. Lett.*, 28(9):1895–1898, 2001.

G. Beyerle, K. Hocke, J. Wickert, T. Schmidt, and Ch. Reigber. GPS radio occultations with CHAMP: A radio holographic analysis of GPSsignal propagation in the troposphere and surface reflections. *J. Geophys. Res.*, 107(D24): doi:10.1029/2001JD001402, 2002.

I.N. Bronštein, K.A. Semendjajew, G. Musiol, and H. Mühlig, editors. *Taschenbuch der Mathematik*. Verlag Harri Deutsch, 1993.

M. Caparrini and M. Martin-Neira. Using reflected GNSS signals to estimate SWH over wide ocean areas. *ESTEC Working Paper*, 2003, 1998.

E. Cardellach, D. Behrend, G. Ruffini, and A. Rius. The use of GPS buoys in the determination of oceanic variables. *Earth Planets Space*, 52: 1113–1116, 2000.

E. Cardellach, G. Ruffini, D. Pino, A. Rius, and A.and Garrison J. L. Komjathy. Mediterranean ballon experiment: ocean wind speed sensing from the stratosphere,using GPS reflections. *Remote Sensing of Environment*, 88(3): doi:10.1016/S0034–4257(03)00176–7, 2003.

E. Cardellach, C. O. Ao, M. de la Torre, and G. A. Hajj. Carrier phase delay altimetry with GPS-reflection/occultation interferometryfrom low Earth orbiters. *Geophys. Res. Lett.*, 31(L10402): doi:10.1029/2004GL019775, 2004.

E. Cardellach Galí. *Sea Surface Determination using GNSS reflected signals*. PhD thesis, Universitat Politècnica de Catalunya, Barcelona, December 2001.

J.M. Dow, R.E. Neilan, and G. Gendt. The international GPS Service (IGS): Celebrating the 10th anniversary and looking to the next decade. *Adv. Space Res.*, 36(3): doi:10.1016/j.asr.2005.05.125, 2005.

R. D. Fontana, W. Cheung, and T. Stansell. The modernized L2 civil signal. *GPS World*, pages 28–34, September 2001.

C. Förste, R. Schmidt, R. Stubenvoll, F. Flechtner, U. Meyer, R. König, H. Neumayer, R. Biancale, J.-M. Lemoine, S. Bruinsma, S. Loyer, F. Barthelmes, and S. Esselborn. The GeoForschungsZentrum Potsdam / groupe de recherche de geodesie spatiale stellite-only and combined gravity field models: EIGEN-GL04S1 and EIGEN-GL04C. *Journal of Geodesy*, 82(6):331–346, June 2008. doi: 10.1007/s00190-007-0183-8.

L. L Fu and A. Cazenave, editors. *Satellite Altimetry and Earth Sciences*, volume 69 of *International Geophysical Series*. Academic Press, 2001.

GALILEO. The galilei project - GALILEO design consolidation. http://europa.eu.int/comm/dgs/energy_transport/galileo/doc/galilei_brochure.pdf, October 2003.

J. L. Garrison and S. J. Katzberg. The application of reflected GPS signals to ocean remote sensing. *Remote Sensing of Environment*, 73: 175–187, 2000.

J. L. Garrison, S. J. Katzberg, and M. I. Hill. Effect of sea roughness on bistatically scattered range coded signals fromthe global positioning system. *Geophys. Res. Lett.*, 25(13):2257–2260, 1998.

C. Gerlach. *Zur Höhensystemumstellung und Geoidberechnung in Bayern*, volume 571 of *Deutsche Geodätische Kommision*. C.H. Beck, München, reihe c edition, 2003.

O. Germain and G. Ruffini. A revisit to the GNSS-R code range precision. In *Proceedings of the GNSS-R'06 Workshop*. ESTEC, June 2006.

C. Gerthsen. *Gerthsen Physik*. Springer-Verlag, Berlin Heidelberg, 19 edition, 1997.

S. Gleason, S. Hodgart, Y. Sun, C. Gommenginger, S. Mackin, M. Adjrad, and M. Unwin. Detection and processing of bistatically reflected GPS signals from lowearth orbit for the purpose of ocean remote sensing. *IEEE Trans. Geosci. and Remote Sensing*, 43(6): doi10.1109/TGRS.2005.845643, June 2005.

K. Gold, A. Brown, and K. Stolk. Bistatic sensing and multipath mitigation with a 109-element GPS antennaarray and digital beam steering receiver. In *ION National Technical Meeting*, San Diego, CA, January 2005.

R. Gold. Optimal binary sequences for spread spectrum multiplexing. *IEEE Transactions on Information Theory*, pages 619–621, Oct. 1967.

GPS SPS. GPS SPS signal specification. Technical report, US Coast Guard Navigation Center, June 1995.

GPS SPS. GPS standard positioning service performance standard. Technical report, Assistant for GPS, Positioning and Navigation, 6000 Defense Pentagon, Washington, DC 20301-6000, October 2001.

G. Hajj and C. Zuffada. Theoretical description of a bistatic system for ocean altimetry using theGPS signal. *Radio Sci.*, 38(5): doi:10.1029/2002RS002787, 2003. 1089.

M. Harigae, I. Yamaguchi, T. Kasai, H. Igawa, H. Nakanishi, T. Murayama, Y. Iwanaka, and H. Suko. Abreast of the waves: Open-sea sensor to measure height and direction. *GPS World*, 16(5):16–26, May 2005.

A. Helm, A. Braun, S. Eickschen, and T. Schöne. Calibration of the shuttle radar topography mission X-SAR instrument usinga synthetic altimetry data model. *Ca. J. Remote Sensing*, 28(4):573–580, 2002.

A. Helm, G. Beyerle, S. Heise, T. Schmidt, and J. Wickert. *The Continuous Wavelet Transform, a valuable analysis tool to detect atmospherican ionospheric signatures in radiooccultation path delay data*, volume ISBN 3-540-22804-7, chapter Earth Observation with CHAMP, pages 591–596. Springer-Verlag, Berlin Heidelberg New York, 2004.

A. Helm, G. Beyerle, Ch. Reigber, and M. Rothacher. Remote monitoring of ocean heights by ground-based observations of reflectedgps signals: 2 case studies. In *GNSSR05 Workshop on Remote Sensing Using GNSS- Reflections*, pages SI–5, Guildford, UK, June 2005. University of Surrey.

A. Helm, G. Beyerle, Ch. Reigber, and M. Rothacher. Coastal altimetry at the baltic sea off-shore Rügen using L1 carrierphase-delay observations of reflected GPS signals at low elevation angles. In *GNSSR'06 workshop on GNSSR reflections*, Netherland, June 2006a. ESTEC.

A. Helm, U. Wetzel, W. Michajljow, G. Beyerle, Ch. Reigber, and M. Rothacher. Monitoring the 2005 dam failure event of Merzbacher glacier lake withground-based observations of reflected GPS signals. In *Geophysical Research Abstracts*, volume 8, pages SRef–ID: 1607–7962/gra/EGU06–A–02358, April 2006b.

A. Helm, U. Wetzel, W. Michajljow, G. Beyerle, Ch. Reigber, and M. Rothacher. Natural hazard monitoring with l1 carrier-phase-delay observations of reflectedGPS signals: The 2005 dam failure event of Merzbacher glacier lake. In *GNSSR'06 workshop on GNSSR reflections*, Netherlands, June 2006c. ESTEC.

A. Helm, O.Montenbruck, J. Ashjaee, S. Yudanov, G. Beyerle, R. Stosius, and M. Rothacher. Gors - a gnss occultation, reflectometry and scatterometry space receiver. In *20th International Technical Meeting of the Satellite Division of The Institute of Navigation - ION GNSS*, pages 2011–2021, Fort Worth, Texas, USA, 2007a.

A. Helm, U. Wetzel, W. Michajljow, G. Beyerle, Ch. Reigber, and M. Rothacher. *Vorträge Dreiländertagung SGPBF, DGPF und OVG : 27. wissenschaftlich-technische Jahrestagung der DGPF*, chapter Natural Hazard Monitoring with reflected GPS signals at Merzbacher Glacier Lake, pages 505–516. DGPF, 2007b.

A. Helm, G. Beyerle, and M. Nitschke. Detection of coherent reflections with gps bipath interferometry. *Canadian Journal of Remote Sensing, under review*, page http://arxiv.org/abs/physics/0407091, February 2008a.

A. Helm, R. Stosius, O.Montenbruck, S. Yudanov, G. Beyerle, and M. Rothacher. Ground-based water level observations at lake walchen with reflected GPS L1 C/A and L2C signals. In *General Assembly European Geosciences Union*, Vienna, Austria, 2008b.

B. Hofmann-Wellenhof, H. Lichtenegger, and J. Collins. *GPS Theory and Practice*. Springer, 5 edition, 2001.

U. Hugentobler, S. Schaer, and P. Fridez. *The Bernese GPS Software Version 4.2*. Astronomical Institute, University of Bern, February 2001.

U. Hugentobler, P. Dach, R.and Fridez, and M. Meindl. *Bernese GPS Software Version 5.0 draft*. Astronomical Institute, University of Bern, September 2005.

ICD-GPS-200. Navstar GPS space segment / navigation user interfaces. Technical Report IRN-200C-005R1, ARINC Inc., 2250 E. Imperial Highway, Suite 450, 2250 E. Imperial Highway, Suite 450,ElSegundo, CA 90245-3509, Jan 2003.

ICD-GPS-705. Navstar GPS space segment / user segment L5 interfaces. Technical Report ICD-GPS-705, rev. 2, ARINC Inc., 2250 E. Imperial Highway, Suite 450, 2250 E. Imperial Highway, Suite 450,ElSegundo, CA 90245-3509, Dec 2002.

J.D. Jackson. *Classical Elektrodynamics*. Wiley, New York, 3 edition, 1998.

N. Jakowski, Wehrenpfennig A., S. Heise, Ch. Reigber, H. Lühr, L. Grunwaldt, and T. K. Meehan. GPS radio occultation measurements of the ionosphere from CHAMP: Earlyresults. *Geophys. Res. Lett.*, 29:10.1029/2001GL014364, 2002.

Jülg, T. XXI-2 Gerät zur Messung der Korrelationsfunktion eines GPS-Signals. Technical report, ComNav Engineering, now ComNova GmbH, http://www.comnova.com, June 2002.

Z. Kang, P. Schwintzer, Ch. Reigber, and S.Y. Zhu. Precise orbit determination of low-earth satellites using SST data. *Advances in Space Research*, 19(11):pp. 1667–1670, 1997.

E. D. Kaplan. *Understanding GPS: principles and applications*, volume ISBN 0-89006-793-7 of *Mobile communications series*. Artech House, Inc., 685 Canton Street, Norwood, MA 02062, 1996.

C. Kelley and D. Baker. OpenSource GPS: A hardware/software platform for learning GPS: Parti, hardware. *GPS World*, pages 58–62, January 2006a.

C. Kelley and D. Baker. OpenSource GPS: A hardware/software platform for learning GPS: Partii, software. *GPS World*, pages 52–57, February 2006b.

C. Kelley, J. Barnes, and J. Cheng. OpenSource GPS: Open source software for learning about GPS. In *ION GPS 2002*, pages 2524–2533, Portland, USA, September 2002.

E. R. Kursinski, G. A. Hajj, J. T. Schofield, and K. R. Linfield, R. P.and Hardy. Observing Earth's atmosphere with radio occultation measurements usingthe Global Positioning System. *J. Geophys. Res.*, 102(D19):23,429–23,465, October 1997.

K. Larson, E. Small, E. Gutmann, A. Bilich, P. Axelrad, and J. Braun. Using GPS multipath to measure soil moisture fluctuations: initial results. *GPS Solutions*, 12:doi10.1007/s10291-007-0076-6, August 2007.

P.Y Le Traon and R. Morrow. *Ocean currents and mesoscale eddies*, volume 69 of *Int. Geophsics Series*, chapter 3, pages 171–210. Academic Press, 2001.

P.Y Le Traon, G. Dibarboure, G. Ruffini, and E. Cardellach. Mesoscale ocean altimetry requirements and impact of GPS-R measurementsfor ocean mesoscale circulation mapping. Extract from the paris-beta estec/esa study, EUROPEAN SPACE AGENCY, December 2002.

B.M. Ledvina, M.L. Psiaki, S.P. Powell, and P.M. Kintner. A 12-channel real-time GPS L1 software receiver. In *Proc. of the Institute of Navigation National Technical Meeting*, Anaheim, CA, January 22-24 2003.

B.M. Ledvina, M.L. Psiaki, D.J. Sheinfeld, S.P. Cerruti, A.P. andPowell, and P.M. Kintner. A real-time GPS civilian L1/L2 software receiver.

In *Proc. of the Institute of Navigation GNSS*, Long Beach, CA, September 21–24 2004.

F. Lehmann. Fresnel equations for reflection and transmission at boundaries betweentwo conductive media, with applications to georadar problems. In *Proceedings of the 6th International Conference on Ground Penetrating Radar(GPR96), Sep.30-Oct.3*, volume 96, pages 555–560, Sendai, Japan, 1996.

S. T. Lowe, J. L. LaBrecque, C. Zuffada, L. J. Romans, L. E. Young, and G. A. Hajj. First spaceborne observation of an earth-reflected GPS signal. *Radio Sci.*, 29(10): doi:10.1029/2000RS002539, 2002a.

S. T. Lowe, C. Zuffada, Y. Chao, P. Kroger, and J. L. Young, L. E.andLaBrecque. 5-cm-precision aircraft ocean altimetry using GPS reflections. *Geophys. Res. Lett.*, 29(10): doi:10.1029/2002GL014759, May 2002b.

G. MacGougan, P.L. Normark, and C. Ståhlberg. The software GNSS receiver. *GPS World*, 16(1): 48–55, January 1 2005.

D. Maliniak. The basics of FPGA design. *Electronic Design*, supplement:http://www.mentor.com/products/fpga_pld/techpubs/index.cfm, December 2003.

W. Mansfeld. *Satellitenortung und Navigation: Grundlagen und Anwendung globaler Satellitennavigationssysteme*. Vieweg, Wiesbaden, 2 edition, 2004.

M. Martín-Neira. A passive reflectometry and interferometry system (PARIS): Applicationto ocean altimetry. *ESA Journal*, 17:331–355, 1993.

M. Martín-Neira, M. Caparrini, J. Font-Rossello, S. Lannelongue, and C. Serra. The paris concept: An experimental demonstration of sea surface altimetryusing GPS reflected signals. *IEEE Trans. Geosci. and Remote Sensing*, 39:142–150, 2001.

M. Martín-Neira, P. Colmenarejo, G. Ruffini, and C. Serra. Altimetry precision of 1 cm over a pond using the wide-lane carrier phaseof gps reflected signals. *Ca. J. Remote Sensing*, 28(3): pp. 394–403, 2002.

M. Martin-Neira, C. Buck, S. Gleason, M. Unwin, M. Caparrini, Farrés E., O. Germain, G. Ruffini, and F. Soulat. Tsunami detection using the paris concept. In *GNSSR05 Workshop on Remote Sensing Using GNSS- Reflections*, pages TD–2, Guildford, UK, June 2005. University of Surrey.

D. Masters, V. Zavorotny, S. Katzberg, and W. Emery. GPS signal scattering from land for moisture content determination. *Proceedings of IEEE Int. Geoscience and Remote Sensing Symposium (IGARSS)*, July 24-28 2000.

D. Masters, P. Axelrad, and S. Katzberg. Initial results of land-reflected GPS bistatic radar measurements in SMEX02. *Remote Sensing of Environment*, 92: doi:10.1016/j.rse.2004.05.016, 2004.

C. Mayer, A. Lambrecht, W. Haag, and O. Eisen. The ice-flux into Merzbacher Lake, Inylchek Glacier, Kyrgyzstan. volume 8, pages SRef–ID: 1607–7962/gra/EGU06–A–08183, April 2006.

C. Mayer, A. Lambrecht, W. Hagg, A. Helm, and K. Scharrer. Post-drainage ice dam response at lake merzbacher, inylchek glacier, kyrgyzstan. *Geografiska Annaler, Series A: Physical Geography*, 90(1):87–96, 2008. doi: 10.1111/j.1468-0459.2008.00336.x.

M. A. Merrifield, Y. L. Firing, T. Aarup, W. Agricole, G. Brundrit, D. Chang-Seng, R. Farre, B. Kilonsky, L. Knight, W. andKong, C. Magori, P. Manurung, C. McCreery, S. Mitchell, W.and Pillay, F. Schindele, F. Shillington, E. M. S. Testut, L.andWijeratne, P. Cardwell, J. Jardin, F.-Y. Nakahara, S.andPorter, and N. Turetsky. Tide gauge observations of the indian Ocean tsunami, December 26, 2004. *GRL*, 32(L09603): doi:10.1029/2005GL022610, 2005.

O. Montenbruck and E. Gill. Ionospheric correction for GPS tracking of leo satellites. *J. Navig.*, 55(2):293–304, 2002.

J. C. Moore and S. Fujita. Dielectric properties of ice containing acid and salt impurity at microwaveand low frequencies. *J. Geophys. Res.*, 98(B6):9769–9780, June 1993.

NAVSTAR. Navstar GPS fact sheet. http://gps.losangeles.af.mil, September 15 2005.

NovAtel. *SUPERSTAR II*, November 2005. http://www.novatel.com/products/superstar.htm.

T. Pany, B. Eisfeller, G. Hein, S. W. Moon, and D. Sanroma. ipexSR: A PC based software GNSS receiver completely developed in Europe. In *Europeen Navigation Conference GNSS 2004*, Rotterdam, May 2004.

B.W. Parkinson and J.J. Spilker, editors. *Global Positioning System: Theory and Application*, volume 163 of *Progress in Astronautics and*

Aeronautics. American Institute of Aeronautics and Astronautics, 1996.

A. Pavelyev, A. Volkov, A. Zakharov, S. Krutikh, and A. Kucherjavenkov. Bistatic radar as a tool for Earth investigation using small satellites. *Acta Astronautica*, 39(9–12):721–730, 1996.

G. Picardi, R. Seu, S.G. Sorge, and Martin-Neira. Bistatic model of ocean scattering. *IEEE Trans. Antennas and Propagation*, 46(10):1531–1541, 1998.

W. H. Press, B. P. Flannery, S. A. Teukolsky, and W.T. Vetterling. Newton-Raphson Method Using Derivatives and Newton-Raphson Methods forNonlinear Systems of Equations. In *Numerical Recipes in FORTRAN: The Art of Scientific Computing*, 2nd, pages 355–362 and 372–375. Cambridge University Press, Cambridge, England, 1992.

W. H. Press, B. P. Flannery, S. A. Teukolsky, and W.T. Vetterling. Moments of a Distribution: Mean, Variance, Skewness. In *Numerical Recipes in C++: The Art of Scientific Computing*, 2nd, chapter 14, pages 619–620. Cambridge University Press, Cambridge, England, 2002.

Ch. Reigber, R. Schmidt, F. Flechtner, R. König, K.-H. Meyer, U.and Neumayer, P. Schwintzer, and S.Y. Zhu. An earth gravity field model complete to degree and order 150 from GRACE:EIGEN-GRACE02S. *J. of Geodynamics*, 39(1):1–10, 2005.

Ch. Reigber, P. Schwintzer, R. Stubenvoll, R. Schmidt, U. Flechtner, F.and Meyer, R. König, K.-H. Neumayer, Ch. Förste, F. Barthelmes, S.Y. Zhu, G. Balmino, R. Biancale, H. Lemoine, J.-M. andMeixner, and J.C. Raimondo. A high resolution global gravity field model combining CHAMP and GRACE-satellite mission and surface gravity data: EIGEN-CG01C. *GFZ STR*, 06/07, 2006. doi: 10.2312/GFZ.b103-06075.

R. Rew, G. Davis, S. Emmerson, and H. Davies. NetCDF User's Guide for C. Technical report, Unidata Program Center, Boulder, Colorado, June 1997.

A. Rius, J. M. Aparicio, E. Cardellach, and B. Martín-Neira, M.andChapron. Sea surface state measured using GPS reflected signals. *Geophys. Res. Lett.*, 29(23): doi:10.1029/2002GL015524, December 2002.

M. Rothacher and B. Zebhauser. Einführung in GPS. 3. SAPOS-Symposium 8, Rothacher M. and Zebhauser B., TU-München, IAPG, Mai 2000.

G. Ruffini, E. Cardellach, A. Rius, and J. M. Aparicio. Remote sensing of the ocean by bistatic radar observations: a review. IEEC report WP1000, REPORT # ESD-iom019-99, Barcelona, Spain, October 28 1999.

G. Ruffini, M. Caparrini, F. Soulat, E. Farres, B. Dunne, S.and Chapron, and C. Buck. Oceanpal experimental campaigns. In *GNSSR'06 workshop on GNSSR reflections*, 2006.

J. Sasstamoinen. Atmospheric correction for the troposphere and stratosphere in radio rangingof satellites. *Geophysical Monograph Series*, 15:247–251, 1972.

R. Schmidt, S. Petrovic, A. Güntner, F. Barthelmes, J. Wünsch, and J. Kusche. Periodic components of water storage changes from GRACE and global hydrological models. *Journal of Geophysical Research*, 113:B08419, 2008. doi: 10.1029/2007JB005363.

T. Schöne, A. Braun, and Reigber Ch. GPS offshore buoys and continuous GPS control of tide gauges. *Int. Hydrographic Rev.,*, 4(3):6–12, 2003.

C. K. Shum, P. L. Woodworth, O. B. Andersen, O. Egbert, G. D. andFrancis, C. King, S. M. Klosko, C. Le Provost, J. M. Li, X.and Molines, M. E. Parke, R. D. Ray, D. Schlax, M. G. andStammer, C. C. Tierney, P. Vincent, and C. I. Wunsch. Accuracy assessment of recent ocean tide models. *J. Geophys. Res.*, 102(C11): 25173–25194, 1997.

SiRF. SiRFstarIII™ GPS Single Chip. http://www.sirf.com, March 2005.

F. Soulat, M. Caparrini, O. Germain, P. Lopez-Dekker, and G. Taani, M.and Ruffini. Sea sate monitoring using coastal GNSS-R. *Geophys. Res. Lett.*, 31(L21303): doi:10.1029/2004GL0206680, 2004.

F. Soulat, O. Germain, G. Ruffini, E. Farres, I. Sephton, T.and Raper, and S. Kemble. STERNA: A feasibility study of PARIS tsunami detection. Technical Report ESA/ESTEC Contract 19016/05/NL/JA, Starlab SL, Barcelona, June 2005.

P.J.G. Teunissen and A. Kleusberg, editors. *GPS for Geodesy*. Springer, Berlin Heidelberg New York, 2 edition, 1998.

Ch. Torrence and G. P. Compo. A practical guide to wavelet analysis. *Bull. Amer. Meteor. Soc.*, 79:61–78, 1998.

O. Torres. Analysis of reflected GPS signals as a method for the determination ofsoil moisture. Master's thesis, The University of Texas, El Paso, Texas, May 2004.

R. Treuhaft, S. Lowe, C. Zuffada, and Y. Chao. 2-cm GPS altimetry over Crater Lake. *Geophys. Res. Lett.*, 22(23):4343–4346, December 2001.

J. B.-Y. Tsui. *Fundamentals of Global Positioning System Receivers: A Software Approach*, volume ISBN: 0-471-38154-3. John Wiley & Sons, Inc., 1 edition, May 2000.

F.T. Ulaby, R.K. Moore, and A.K. Fung. *Microwave remote sensing : active and passive*, volume II: Radar remote sensing and surface scattering and emission theory. Addison-Wesley Publ. Co., Reading, Mass, 1982.

Valenzuela. Theories for the interaction of electromagnetic and ocean waves – a review. *Boundary-Layer Meteorology*, 13:61–85, 1978.

D. von Grünigen. *Digitale Signalverarbeitung*. Fachbuchverlag Leipzig, Feb 2002.

A.G. Voronovich. On the theory of electromagnetic waves scattering from the sea surface atlow grazing angles. *Radio Science*, 31(6): 1519–1530, Nov-Dec 1994. 96RS02250.

S. H. Ward and G. W. Hohmann. *Electromagnetic theory for geophysical applications*, volume 1, pages 131–312. Soc. Expl. Geophys., 1988.

Wasserwirtschaftsamt Weilheim. Seenporträts. http://www.wwa-wm.bayern.de, 7 2004.

D.E. Wells. *Guide to GPS positioning*. Canadian GPS association, Fredericton,N.B., Canada, 1987.

P. Wessel and W. H. F. Smith. New, improved version of generic mapping tools released. *EOS trans.*, 79:579, 1998.

H.-U. Wetzel, A. Reigber, A. Richter, and W. Michajljow. Gletschermonitoring und Gletscherseebrüche am Inyltschik (ZentralerTienshan)- Interpretation mit optischen und Radarsatelliten. In *Tagungsband DGPF Wissenschaftlich-Technische Jahrestagung*, Rostock, September 2005.

J. Wickert, R. Galas, G. Beyerle, R. König, and Ch. Reigber. GPS ground station data for CHAMP radio occultation measurements. *Phys. Chem. Earth (A)*, 26(6-8):503–511, 2001.

W. H. Wooden. Navstar global positioning system. In *Proceedings of the first international symposion on precise positioningwiththe GPS*, volume 1, pages 23–32, Maryland, April 15-19 1985.

S. C. Wu, T. Meehan, and L. E. Young. The potential use of GPS signals as ocean altimetry observables. 1997 national technical meeting, Wu S.C. and Meehan T. and Young L.E., Santa Monica, California, January 1997.

T. Yunck. The promise of spaceborne GPS for Earth remote sensing. In *Proceedings of international Workshop on GPS Meteorology: GroundbasedandSpace-based applications*, pages 2–01–1/2–01–6, Tsukuba, Japan, January 2003.

ZARLINK. *GP2021 GPS 12 Channel Correlator*, DS4077-3.2 edition, April 2001. http://www.zarlink.com.

ZARLINK. *GP2010 GPS Receiver RF Front End*, DS4056-3.5 edition, February 2002a. http://www.zarlink.com.

ZARLINK. *GPS Receiver Hardware Design*, an4855 edition, October 1999.

ZARLINK. *GP4020 GPS Receiver Baseband Processor*, http://www.zarlink.com edition, June 2005.

ZARLINK. *GP4020 GPS Receiver Baseband Processor Design Manual*, dm5280 edition, January 2002b.

V. U. Zavorotny and A. G. Voronovich. Scattering of GPS signals from the ocean with wind remote sensing application. *IEEE Trans. Geoscience and Remote Sensing*, 38(2):951–964, 2000.

V.U. Zavorotny. Bistatic GPS signal scattering from an ocean surface: Theoretical modeling and wind speed retrieval from aircraft measurements. In *Workshop on meteorological and oceanographic applications of GNSS surfacereflections: from Modeling to user requirements*, NL, July 1999. KNMI.

A Acronyms

A/D	Analog-to-Digital Converter
AGC	Automatic Gain Control
AS	Anti-Spoofing
ASIC	Applications Specific Integrated Circuit
BPSK	Bi-Phase Shift Key
BLVA	Bayrisches Landesvermessungsamt
BMBF	Bundesministerium für Bildung und Forschung
BOC	Binary Offset Carrier
BSH	Bundesamt für Seeschifffahrt und Hydrographie
C/A-code	Coarse/Acquisition Code
CAIAG	Central Asian Institut of Applied Geosciences
CDMA	Code Division Multiple Access
CDM	Coherent Delay Mapping
CHAMP	CHAllenging Minisatellite Payload
COTS	Commercial Of The Shelf
CRPA	Controlled Radiation Pattern Antenna
CW	Continuous Wave
DCO	Digital Controlled Oscillator
DEM	Digital Elevation Model
DLL	Delay Lock Loop
DoD	Department of Defense
ECMWF	European Centre for Medium-Range Weather Forecasts
EGNOS	European Geostationary Navigation Overlay System
ENSO	El Niño Southern Oscillation
ENVISAT	ENVIronmental SATellite
ESA	European Space Agency
ESTEC	European Space Research and Technology Centre
FDMA	Frequency Division Multiple Access
FFT	Fast Fourier Transform
FLL	Frequency Lock Loop
FIFO	First In First Out
FPGA	Field Programmable Gate Array
FRPA	Fixed Radiation Pattern Antenna
GALILEO	European Satellite Navigation System
GCC	GNU Compiler Collection
GFZ	GeoForschungsZentrum Potsdam
GITEWS	German Indonesian Tsunami Early Warning System
GLONASS	GLObal'naya NAvigatsionnaya Sputnikova Sistema
GNSS	Global Navigation Satellite System
GNU	Recursive acronym for *GNU's Not UNIX*
GPS	Global Positioning System
GPST	GPS Time
GRACE	Gravity Recovery and Climate Experiment
HAGR	High-gain Advanced GPS Receiver
HOW	Hand Over Word
ICD	Interface Control Document
IF	Intermediate Frequency
IGS	International GNSS Service
Jason-1	Joint French/US altimeter mission
L1	GPS Carrier Frequency at 1575.42 MHz
L2	GPS Carrier Frequency at 1227.6 MHz
L2C	GPS new civil ranging Code superposed on L2
LEO	Low Earth Orbiter
LHCP	Left Hand Circular Polarization
LSB	Least Significant Bit
MAG	Magnitude
MBOC	Multiplexed Binary Offset Carrier
MEO	Medium Earth Orbit
MSB	Most Significant Bit
NAVSTAR	Navigation System with Time and Range
NCO	Numerically Controlled Oszillator
netCDF	Network Common Data Form
PARIS	PAssive Reflectometry and Interferometry System

DOI: 10.2312/GFZ.b103-08104

PCI	Peripheral Component Interconnect
PIC	Potsdam Institut für Klimaforschung
PLL	Phase Lock Loop
PPS	Precise Positioning Service
PRN	Pseudo Random Noise
P-code	Precise Code
PL	Pseudolite - Pseudo-satellite
RA	Radar Altimeter
RADAR	Radio Detection and Ranging
RF	Radio Frequency
RHCP	Right Hand Circular Polarization
RTAI	Real-Time Application Interface
RMS	Root-Mean-Square
SAC-C	Satelite de Aplicaciones Cientificas - C
SA	Selective Availability
SAW	Surface Acoustic Wave
SBAS	Space Based Augmentation System
SIGN	Sign
SV	Space Vehicle
SNR	Signal-to-Noise Ratio
SMA	Sub-Miniature-A
SPS	Standard Positioning Service
SSH	Sea Surface Height
SST	Spread Spectrum Techique
SSTL	Surrey Satellite Technology Limited
SRTM	Shuttle Radar Topography Mission
STD	Standard Deviation
SWH	Significant Wave Height
TCXO	Temperature Controlled Crystal Oscillator
TE	Transverse Electric
TEC	Total Electron Content
TIC	Time Interval Counter
TLE	Two Line Elements
TM	Transverse Magnetic
TOA	Time of Arrival
TOW	Time of Week
TTL	Transistor-Transistor-Logic Semiconductor technology for building discrete digital logic integrated circuits
UK-DMC	United Kingdom's Disaster Monitoring Constellation satellite
USO	Ultra Stable Oscillator
UTC	Universal Time Coordinated
W-code	Encrypting Code
WAAS	Wide Area Augmentation System
WGS-84	World Geodetic System 1984
Y-code	Encrypted Precise Code
ZAWa	Central Asia Water

DOI: 10.2312/GFZ.b103-08104

B Fresnel Equations: Reflection coefficients for non-conductive and conductive medium

Non-conductive medium: The coefficients describing reflection (and transmission) at a boundary layer between two media are simple functions of the relative contrast in permitivity of both media. The coefficients describe the ratio of the amplitudes of the incident and reflected (respectively transmitted) electric field vector. Any linearly polarized field vector can be transformed into a linear combination of a field vector parallel and perpendicular with respect to the incidence plane. Thus, only the parallel and perpendicular components are discussed. The reflection coefficient r is calculated for the perpendicular component of the electric field vector (TE-mode) according to

$$r_{\perp} = \frac{|\mathbf{E}_r|}{|\mathbf{E}_e|} = \frac{\mu_{r2} k_1 \cos\Theta_1 - \mu_{r1} k_2 \cos\Theta_2}{\mu_{r2} k_1 \cos\Theta_1 + \mu_{r1} k_2 \cos\Theta_2} \tag{B.1}$$

and using $|\mathbf{k}_e| = |\mathbf{k}_r| = k_1$ and $|\mathbf{k}_t| = k_2$ (see Fig. B.1). The parallel component (Transverse Magnetic (TM)-mode) results from

$$r_{\parallel} = \frac{|\mathbf{H}_r|}{|\mathbf{H}_e|} = \frac{\mu_{r1} k_2 \cos\Theta_1 - \mu_{r2} k_1 \cos\Theta_2}{\mu_{r1} k_2 \cos\Theta_1 + \mu_{r2} k_1 \cos\Theta_2}. \tag{B.2}$$

The derivation of the Fresnel equations for non-conductive media is fully described in Ward and Hohmann [1988]. Snellius's Law can be described by

$$\frac{k_2}{k_1} = \frac{\sin\Theta_1}{\sin\Theta_2}. \tag{B.3}$$

Conductive medium: In addition to the complex wave number $\tilde{k}$ the complex permitivity $\tilde{\varepsilon_r}$ has to be used, defined with

$$\tilde{\varepsilon_r} = \varepsilon_r + i\frac{\sigma}{\omega\varepsilon_0} \tag{B.4}$$

In case of conductive material, which is free of electric charges and currents (true in general for geological material), the same conditions dominate for the electric and magnetic field at the boundary layer as in the case of non-conductive media. Thus, the complex Fresnel equations and Snellius's

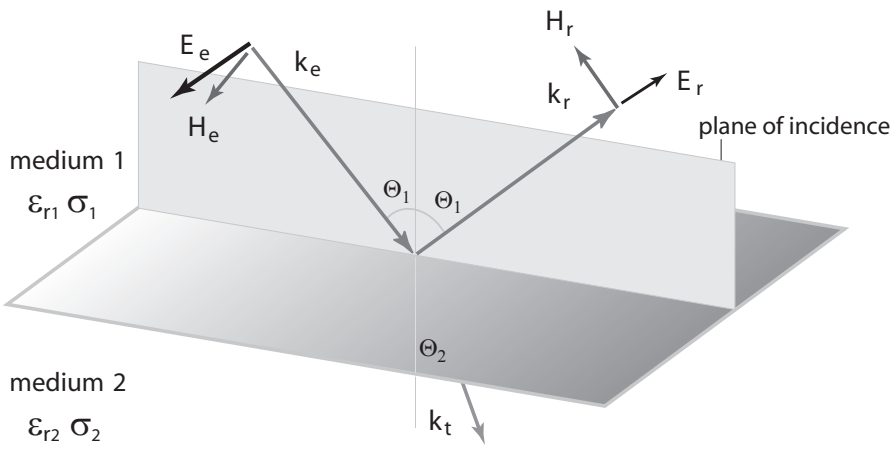

Fig. B.1: *Reflection and transmission at a boundary layer between medium 1 and medium 2. Incident and reflected field vectors for the electric and magnetic field* **E** *and* **H** *are shown for the Transverse Electric (TE)-mode.*

DOI: 10.2312/GFZ.b103-08104

Law can be described for complex angles by

$$\tilde{r}_{\perp} = \frac{\mu_{r2}\tilde{k}_1 \cos\Theta_1 - \mu_{r1}\tilde{k}_2 \cos\tilde{\Theta}_2}{\mu_{r2}\tilde{k}_1 \cos\Theta_1 + \mu_{r1}\tilde{k}_2 \cos\tilde{\Theta}_2}, \tag{B.5}$$

$$\tilde{r}_{\parallel} = \frac{\mu_{r1}\tilde{k}_2 \cos\Theta_1 - \mu_{r2}\tilde{k}_1 \cos\tilde{\Theta}_2}{\mu_{r1}\tilde{k}_2 \cos\Theta_1 + \mu_{r2}\tilde{k}_1 \cos\tilde{\Theta}_2}, \tag{B.6}$$

$$\frac{\tilde{k}_1}{\tilde{k}_2} = \frac{\sin\tilde{\Theta}_2}{\sin\Theta_1}. \tag{B.7}$$

We substitute $\tilde{k}_2$ and $\tilde{\Theta}_2$ with $\tilde{k}_2 \cos\tilde{\Theta}_2 = q + ip$ and calculate p and q from

$$p = \frac{k_2\alpha_2 - k_1\alpha_1 \sin^2\theta_1}{q}, \tag{B.8}$$

$$\begin{aligned} q = {} & \left\{ \frac{1}{2}[(k_2^2 - \alpha_2^2) - (k_1^2 - \alpha_1^2)\sin^2\theta_1] + \right. \\ & + \frac{1}{2}\Big\{ (k_2^2 + \alpha_2^2)^2 + \sin^4\theta_1 (k_1^2 + \alpha_1^2)^2 - \\ & \left. - 2\sin^2\theta_1 [(k_1^2 - \alpha_1^2)(k_2^2 - \alpha_2^2) + 4k_1\alpha_1 k_2\alpha_2] \Big\}^{\frac{1}{2}} \right\}^{\frac{1}{2}}. \end{aligned} \tag{B.9}$$

The reflection coefficients for perpendicular and parallel polarized electric fields can now be described by

$$\tilde{r}_{\perp} = \frac{\mu_{r2}k_1 \cos\Theta_1 - \mu_{r1}q}{\mu_{r2}k_1 \cos\Theta_1 + \mu_{r1}q} + i\frac{\mu_{r2}\alpha_1 \cos\theta_1 - \mu_{r1}p}{\mu_{r2}\alpha_1 \cos\theta_1 + \mu_{r1}p}, \tag{B.10}$$

$$\begin{aligned} \tilde{r}_{\parallel} = {} & \frac{\mu_1(k_2^2 - \alpha_2^2)\cos\Theta_1 - \mu_2(k_1 q - \alpha_1 p)}{\mu_{r1}(k_2^2 - \alpha_2^2)\cos\Theta_1 + \mu_{r2}(k_1 q - \alpha_1 p)} + \\ & + i\frac{2k_2\alpha_2\mu_{r1}\cos\Theta_1 - \mu_{r2}(\alpha_1 q + k_1 p)}{2k_2\alpha_2\mu_{r1}\cos\Theta_1 + \mu_{r2}(\alpha_1 q + k_1 p)}. \end{aligned} \tag{B.11}$$

The derivation of the Fresnel equations for conductive media is fully described in Lehmann [1996]. For most geologic material $\mu_r = 1$ can be applied. Hence, the Fresnel equations can further be simplified.

DOI: 10.2312/GFZ.b103-08104

C Experiments: Additional Data Plots

C.1 Mercure Hotel Experiment

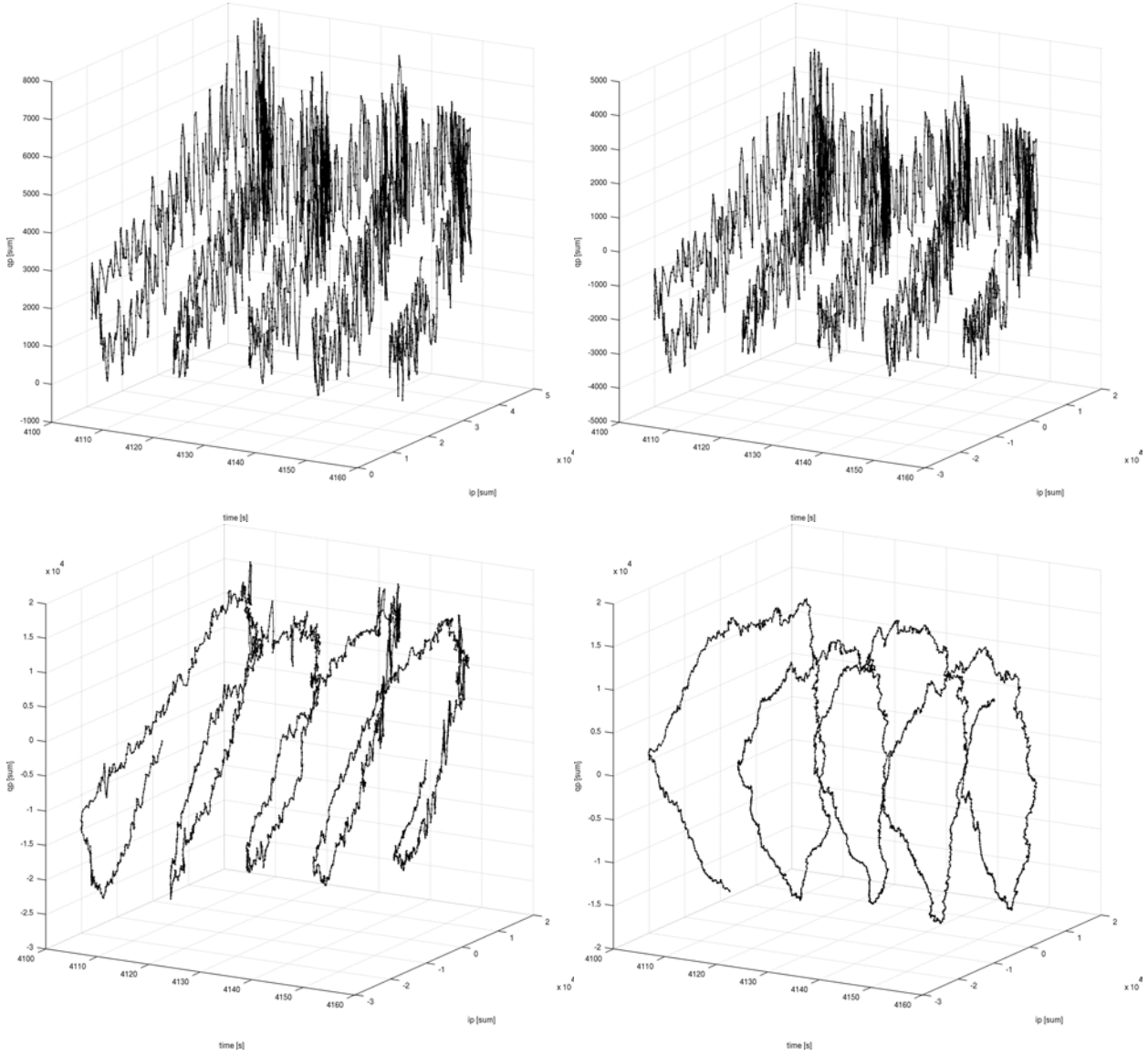

Fig. C.1: *Mercure experiment: Results of strategies 1-4 to process the measured in- and quad-phase correlation data (see Fig. 5.32-5.35 and Fig. 5.36). 3d plot of the cross plot of in- and quad-phase data over time.*

DOI: 10.2312/GFZ.b103-08104

C.2 Königsstuhl Experiment

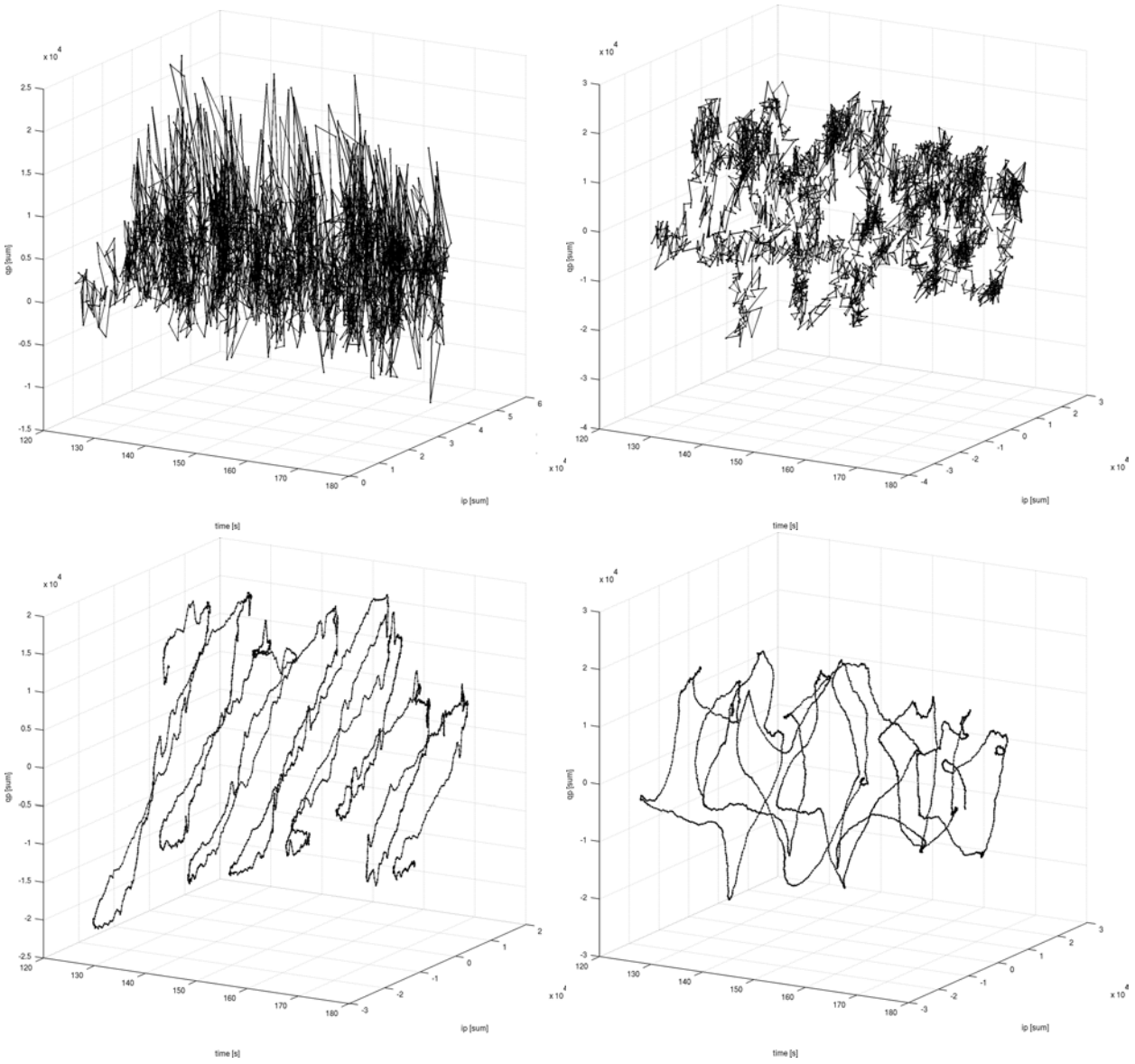

Fig. C.2: *Königsstuhl experiment: Different processing strategies (see Fig. 5.49 and 5.50 on page 102 and 102): Complex phasor, in-phase data (y-axis) plotted versus quad-phase data (z-axis) versus time (x-axis).*

DOI: 10.2312/GFZ.b103-08104

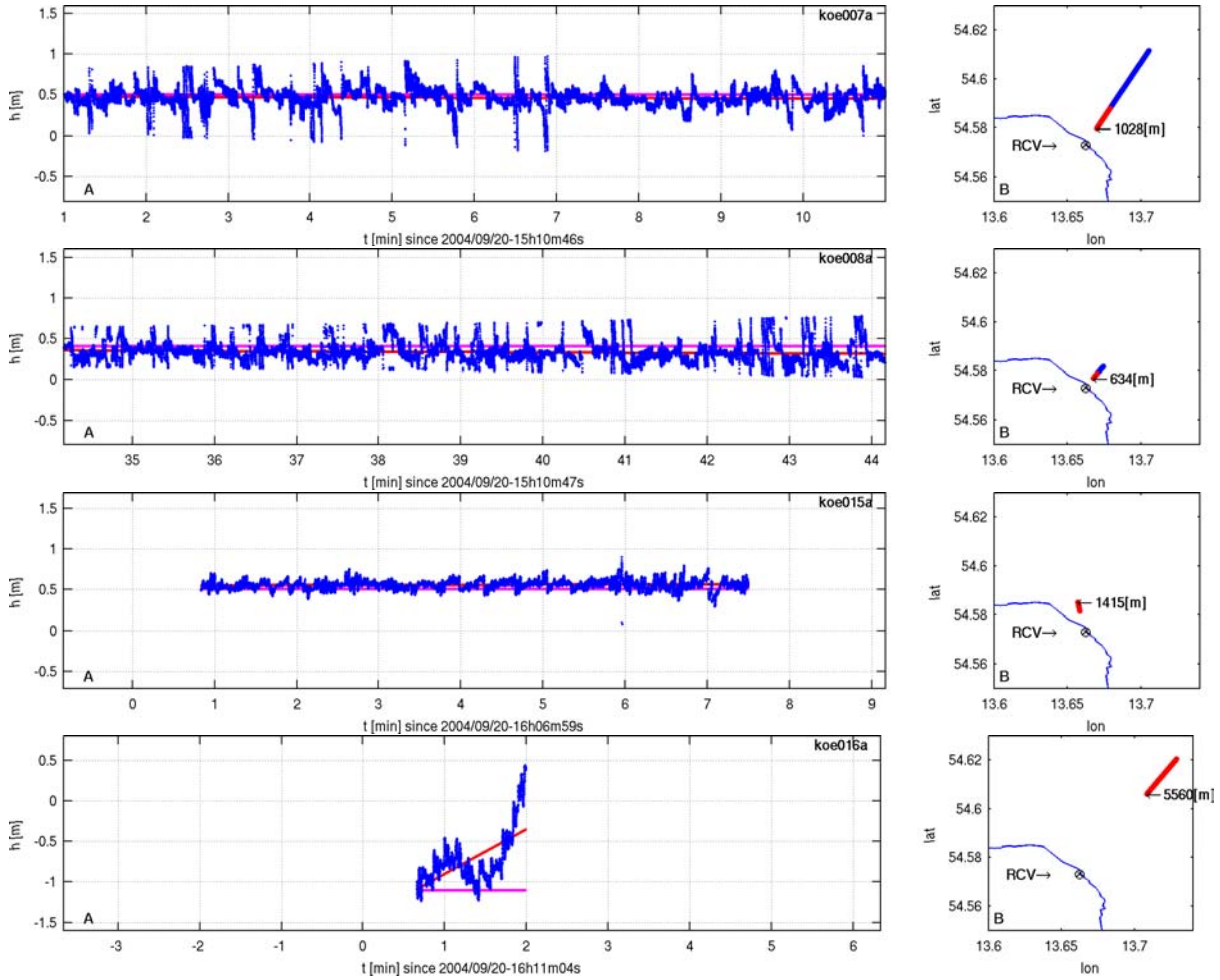

Fig. C.3: *Height time series (panel A) and the corresponding location of the specular reflection point (panel B) on September 20, 2004.*

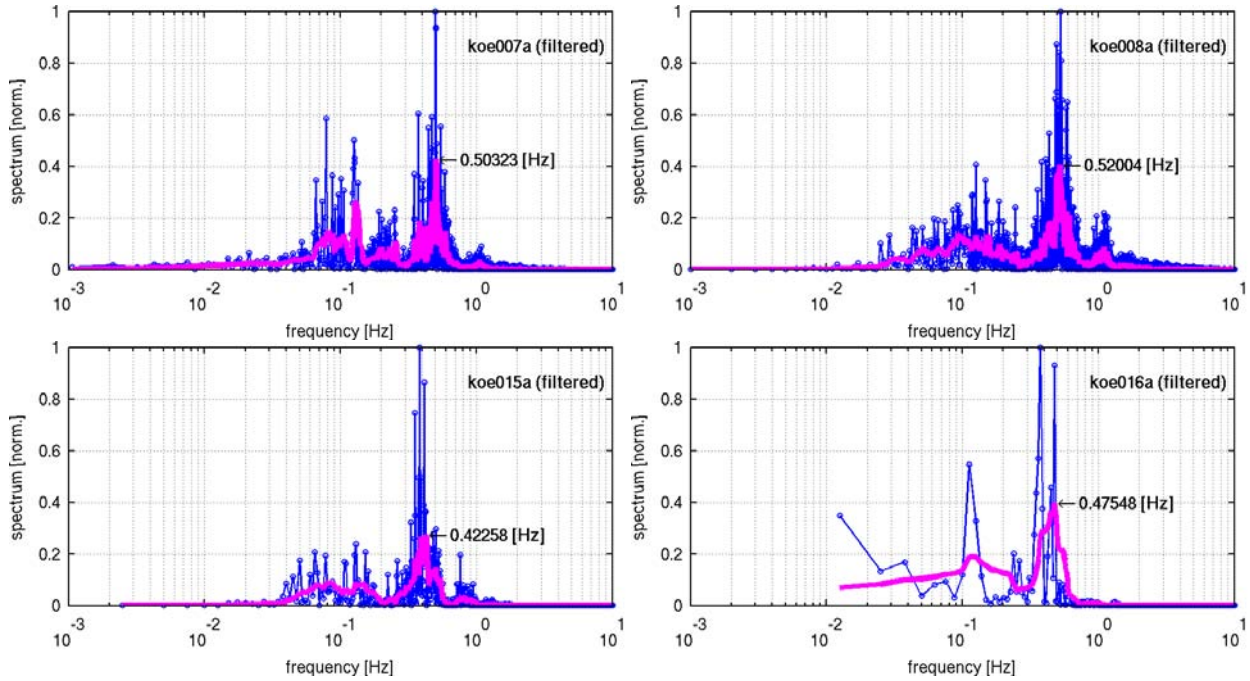

Fig. C.4: *Fourier spectra of the filtered height time series on September 21, 2004.*

DOI: 10.2312/GFZ.b103-08104

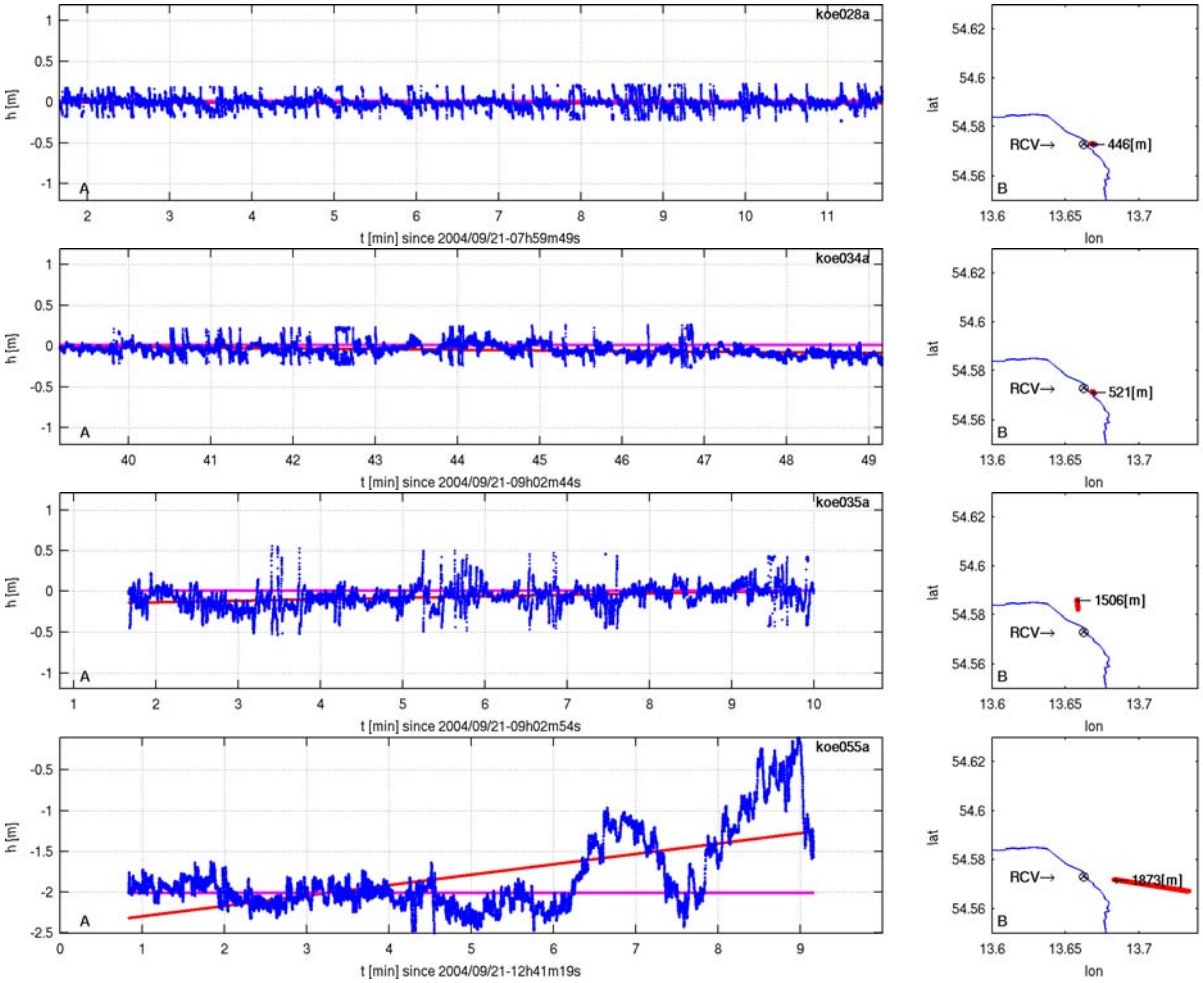

Fig. C.5: *Height time series (panel A) and the corresponding location of the specular reflection point (panel B) on September 21, 2004.*

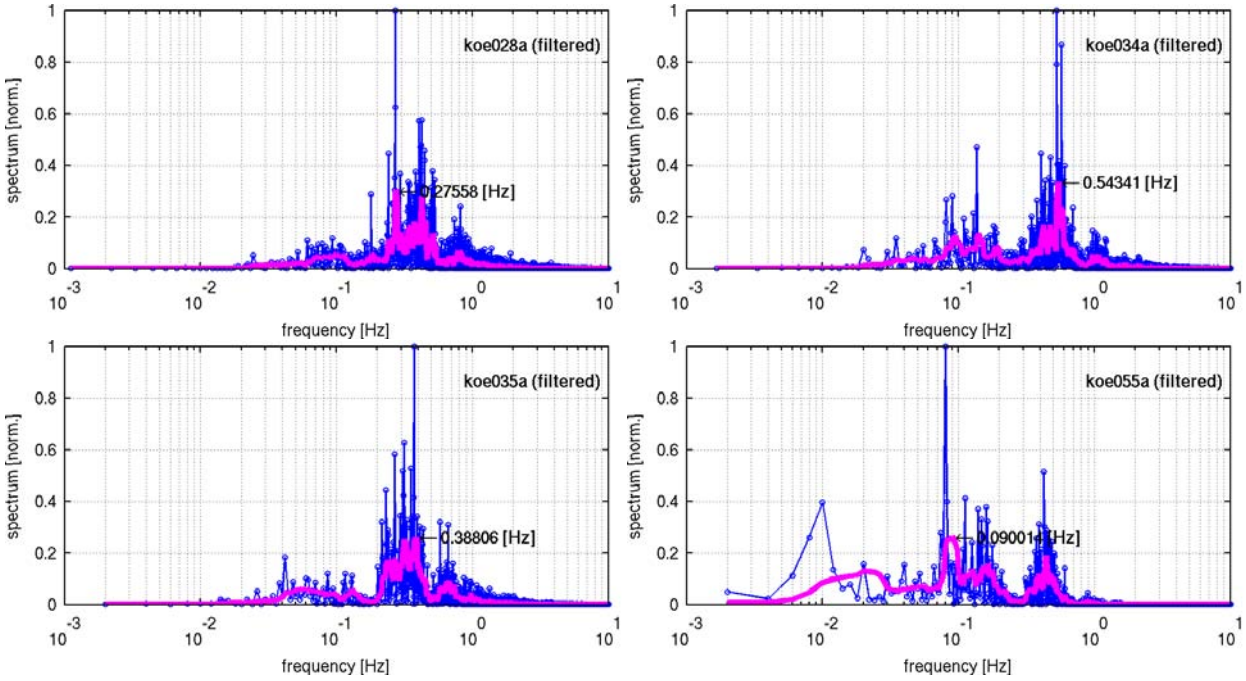

Fig. C.6: *Fourier spectra of the filtered height time series on September 21, 2004.*

DOI: 10.2312/GFZ.b103-08104

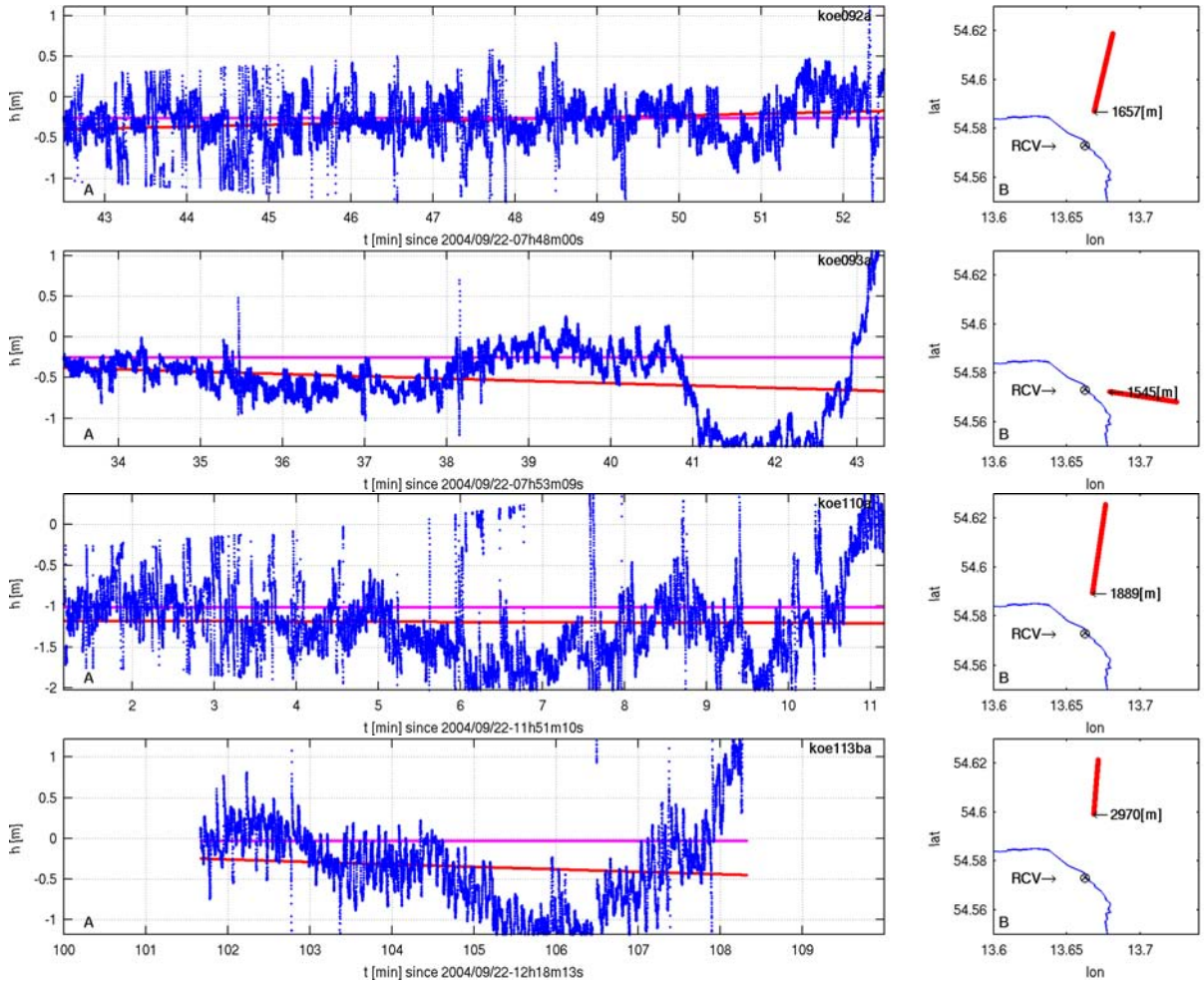

Fig. C.7: *Height time series (panel A) and the corresponding location of the specular reflection point (panel B) on September 22, 2004.*

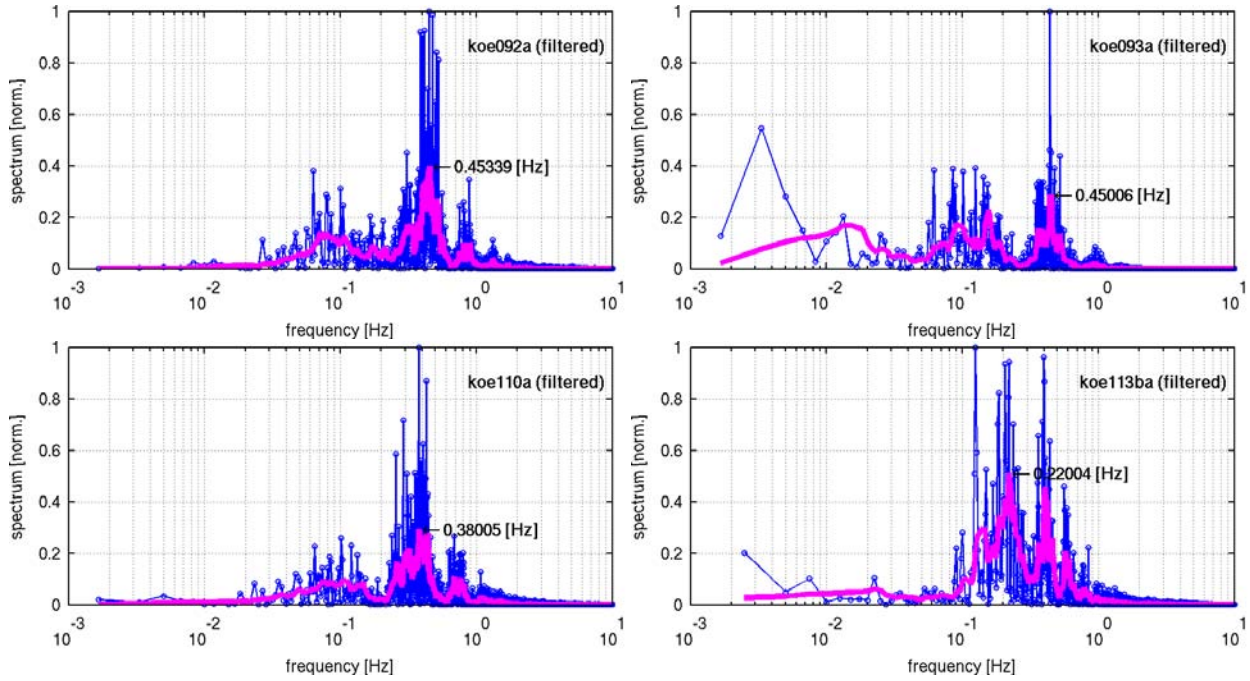

Fig. C.8: *Fourier spectra of the filtered height time series on September 22, 2004.*

DOI: 10.2312/GFZ.b103-08104

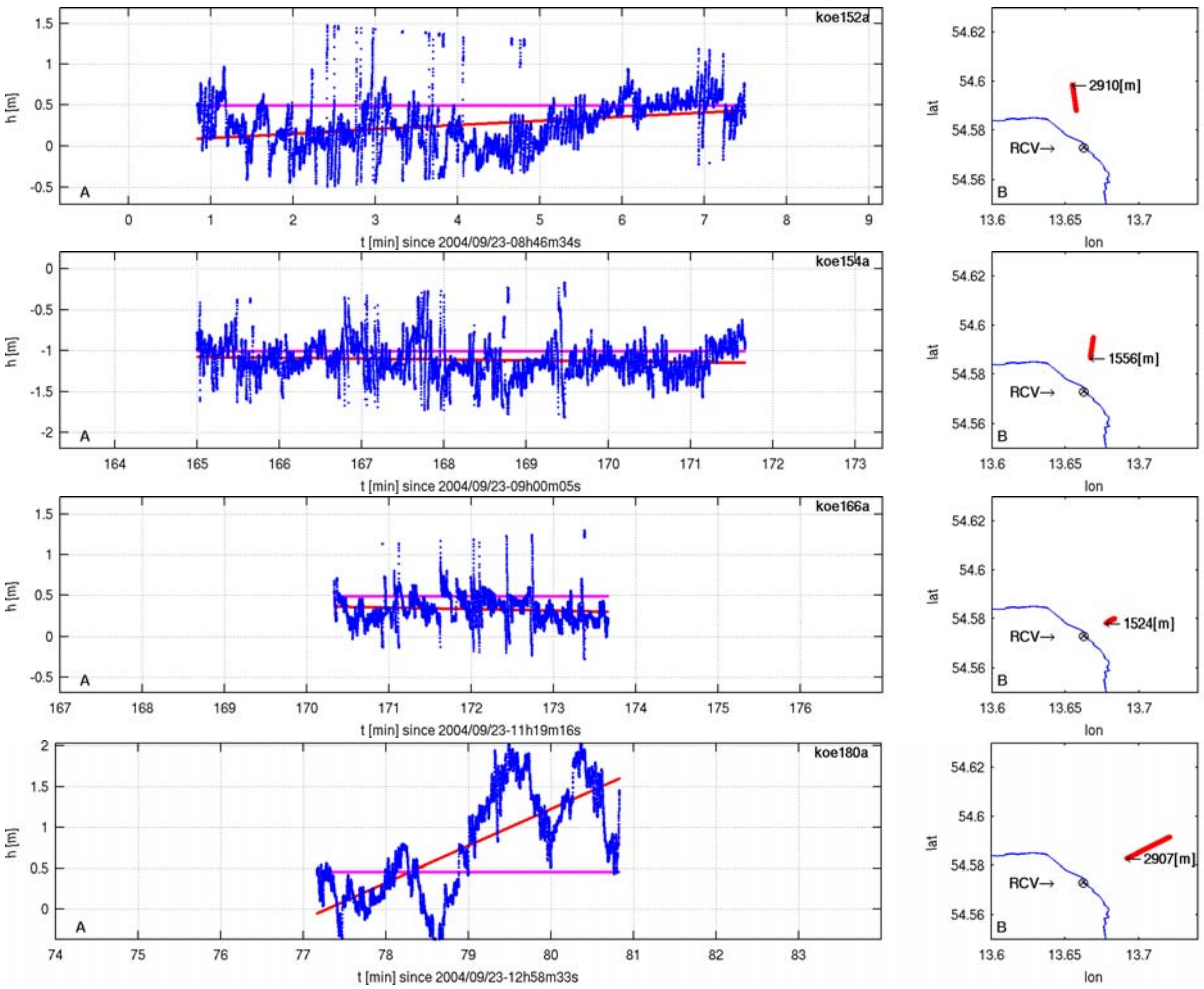

Fig. C.9: *Height time series (panel A) and the corresponding location of the specular reflection point (panel B) on September 23, 2004.*

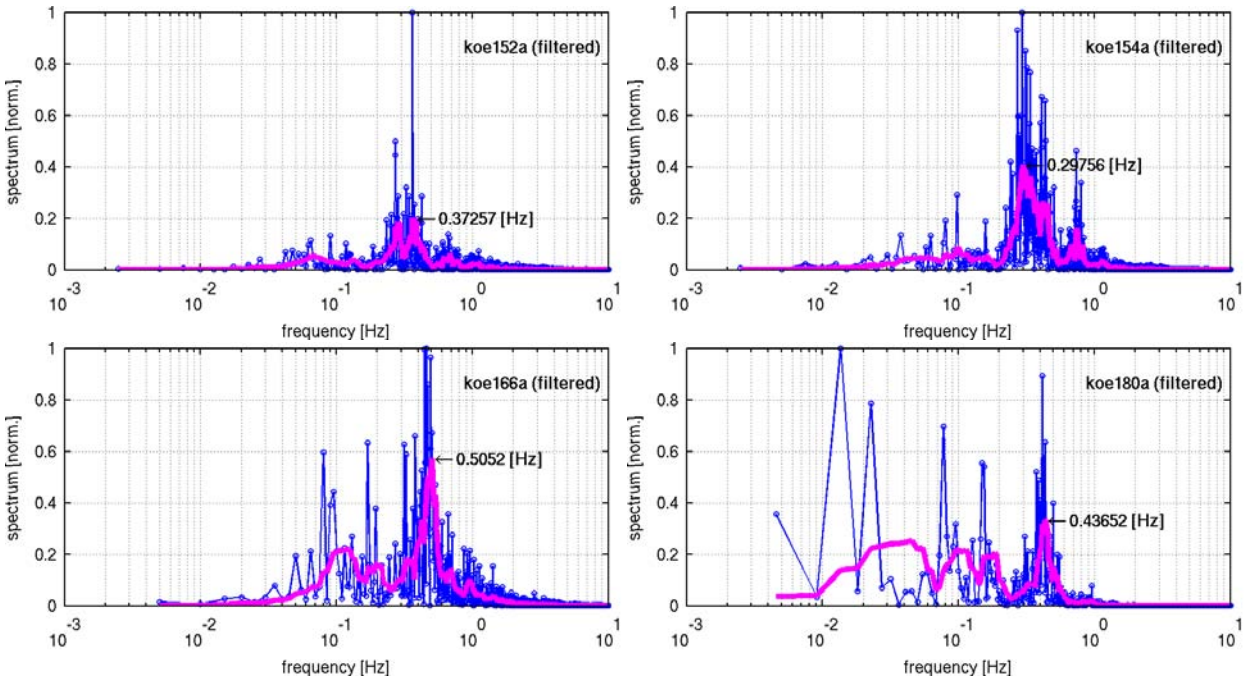

Fig. C.10: *Fourier spectra of the filtered height time series on September 23, 2004.*

DOI: 10.2312/GFZ.b103-08104

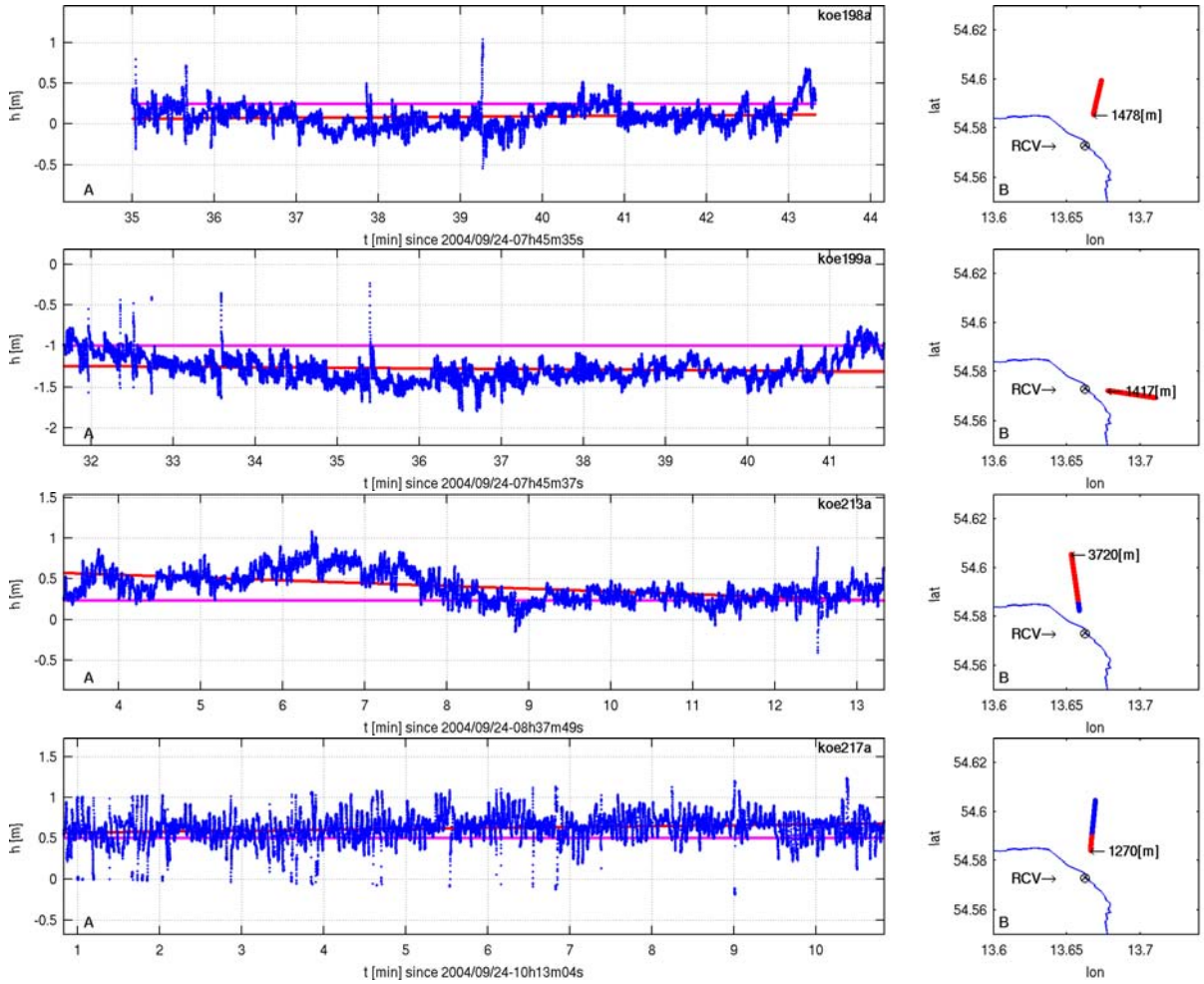

Fig. C.11: *Height time series (panel A) and the corresponding location of the specular reflection point (panel B) on September 24, 2004.*

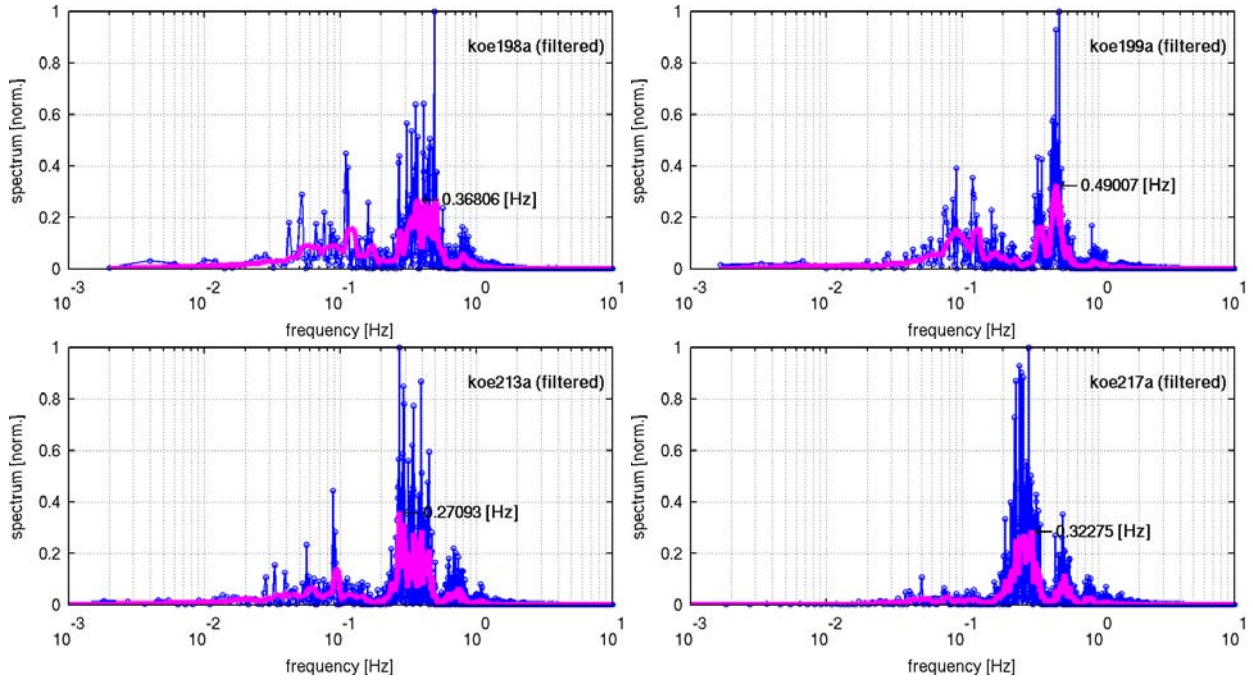

Fig. C.12: *Fourier spectra of the filtered height time series on September 24, 2004.*

DOI: 10.2312/GFZ.b103-08104

C.3 Inylshik Experiment

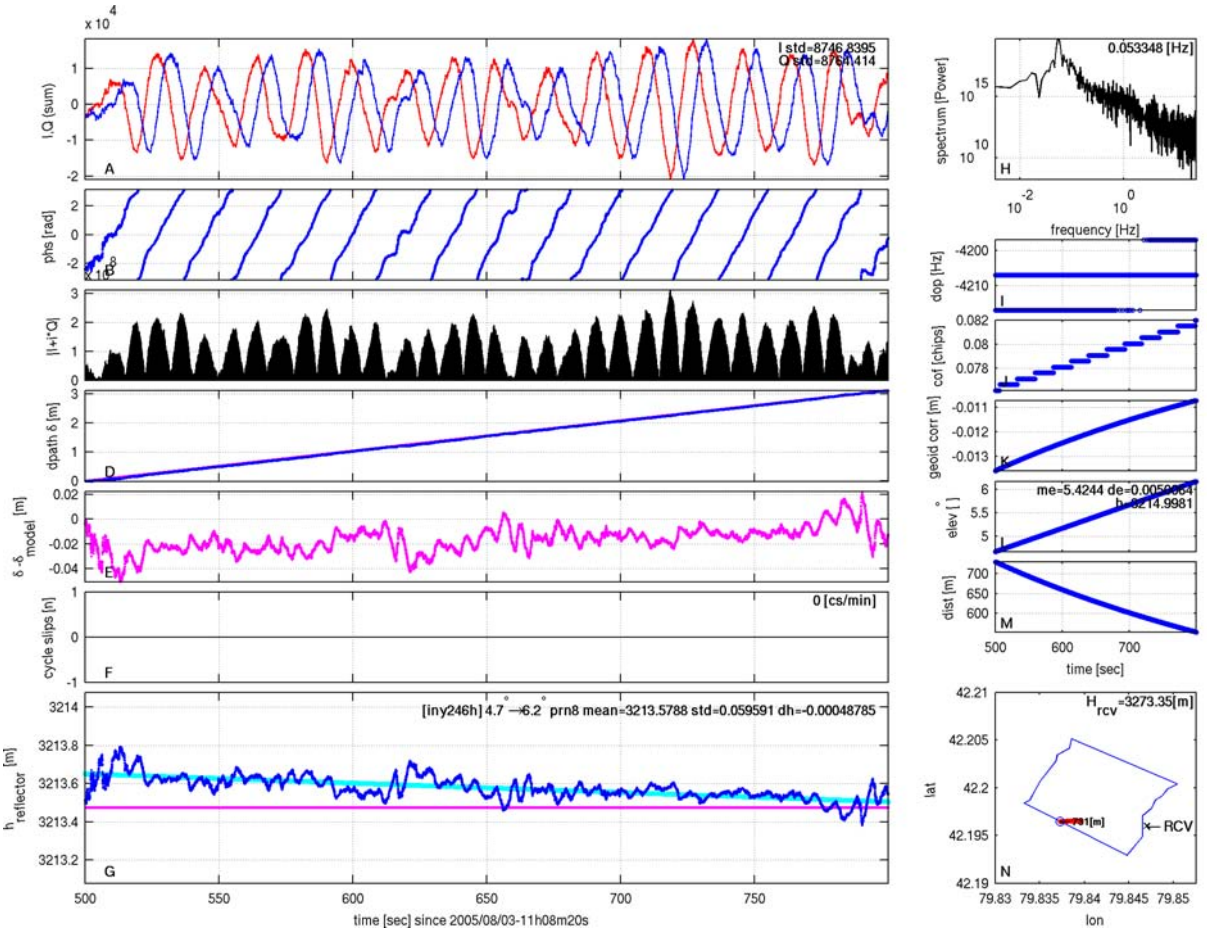

Fig. C.13: *Height profile of Merzbacher lake on August 3, 2005 starting at 11:08:20 GPST*

DOI: 10.2312/GFZ.b103-08104

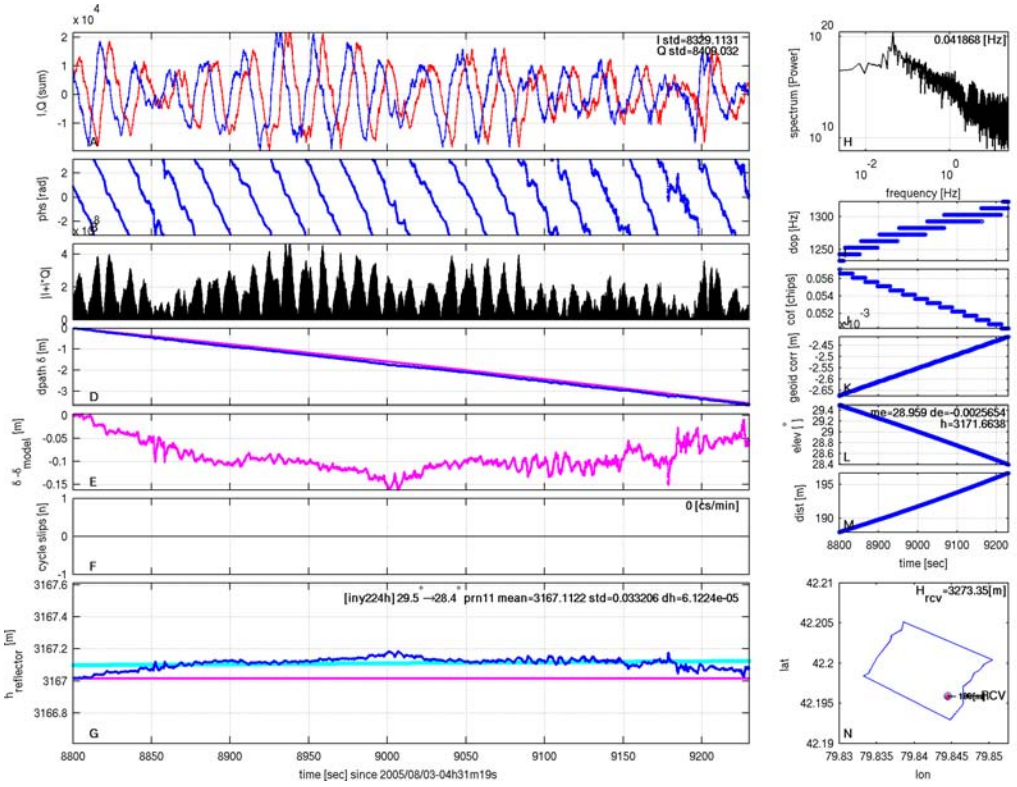

Fig. C.14: *Height profile of Merzbacher lake on August 3, 2005 starting at 04:31:19 GPST*

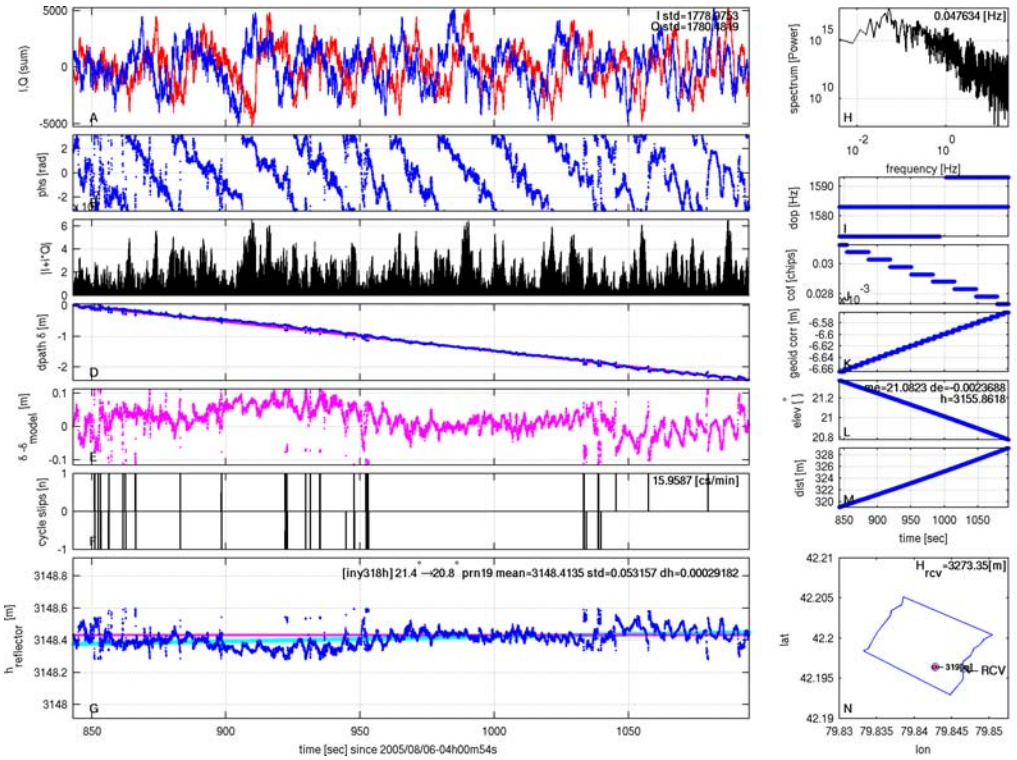

Fig. C.15: *Height profile of Merzbacher lake on August 6, 2005 starting at 04:00:54 GPST*

DOI: 10.2312/GFZ.b103-08104

DOI: 10.2312/GFZ.b103-08104

D OpenGPS Data Format

D.1 Version 1

The open2005 processing software uses the following information contained in the binary OpenGPS data. The OpenGPS version 1 data is divided into one headerblock (head) and a number of n consecutive datablocks (data) which are defined according to the following C++ data format:

```
headerblock head;
vector<datablock> data;// datablocks 1..n

headerblock {
  short int header_version;
  short int header_size;
  short int data_size;
  short int gps_week;
  int time_of_week;
  int tic_start;
  short int prn;
  short int dither_mode;
  short int cod_phs_ofs[12];
  short int car_phs_ofs[12];
  short int lead_ch;
  short int early_late;
};

datablock {
  short int ch;
  int tic_count;
  int ip;
  int id;
  int qp;
  int qd;
  short int car_cyc_l;
  short int car_cyc_h;
  short int car_dco_phs;
  short int cod_phs;
  short int cod_dco_phs;
}
```

The initialization time of the measurement is fixed by the GPS week (gps_week) and the time of week in seconds (time_of_week). Additionally, the tic counter at start is stored (tic_start). The observed PRN, the dither mode, the master channel and wether all channels are stet to early or late are stored in prn, dither_mode, lead_ch and early_late, respectively. The carrier and code phase offset at measurement start of all 12 channels are stored in the data vectors car_phs_ofs[12] and cod_phs_ofs[12]. Each datablock contains the correlator channel number ch and the tic counter value tic_count during the dump event. Attention, nominally 5 dump events occur until the tic counter is incremented every 100 msec. The in-phase and quad-phase correlation sums of the prompt and dither correlator arm are stored in ip,qp and id,qd, respectively. The actual carrier cycle is stored in car_cyc_l (low byte), car_cyc_h (high byte) and the fractional carrier cycles are stored in car_dco_phs. The code phase counter and the fractional code phase is stored in cod_phs and cod_dco_phs.

D.2 Version 2

The binary OpenGPS version 2 data is divided into one headerblock (head) and n consecutive pairs of equal datablocks which are assigned to the master (data_mc) and the appropriate slave channel (data_sc). The version 2 format is defined according to the following C++ data format:

```
  headerblock1 head1;
  vector<datablock> data_sc,data_mc;
  // 1..n datablocks slave/master pairs

   headerblock1{
       short int data_version;
       short int header_size;
       short int gps_week;
       int time_of_week;
   }

    datablock {
       short int ch;
       int tow;
       int tic_count;
       int ip;
       int id;
       int qp;
       int qd;
       int car_phs_res_fix;
       short int car_cyc_l;
       short int car_cyc_h;
       short int car_dco_phs;
       short int cod_phs;
       short int cod_dco_phs;
       short int cod_offset;
}
```

The following parameter values – valid at the dump event – are added to each datablock. The actual time of week seconds is stored in tow. The carrier and code phase offset are stored in car_phs_res_fix and cod_offset.

DOI: 10.2312/GFZ.b103-08104

E Open2005 Configuration File

```
#######################################
# configuration file for prg: open2005 #
#######################################
# $Id: open2005_info.cpp,v 1.5 2005/09/09 10:58:29 helm Exp $
PRG=open2005

# binary data file from open gps receiver
DATA_FILE=rfl-1273-230658-10.dat

# binary nav file from open gps receiver
NAV_FILE=out-1274-467423.dat

# if required, state broadcast ephemeris file (rinex 2)
# aquire from ftp cddisa.gsfc.nasa.gov
# dir /pub/gps/gpsdata/brdc/yyyy
EPHEMERIS_FILE=iCH-OG-3-PDO+BRC-GPS_2003_190_00.dat

# if required, state [ troposphere correction file or NONE ]
# lookup table gps-time,elevation,deflection of the PRN satellite
# applies tropo defl on elevation angle
# (calc file with MATLAB script gen_tropo_defl2.m)
TROPOSPHERE_FILE=defl-1226-298740-301200-11.dat

# apply additionally troposphere path correction[ 0=no|1=add|2=-mean|3=sub]
# to early and promt dpath variable
# (corr=diff ex.opt.path diff tropo defl h_rfl - h_rcv)
APPLY_TROPO_PATH_CORR=1

# if required, state [ geoid grd correction file | NONE ]
# geoid file has to be a gmt conform netCDF grd file
# with node registration and regional coverage
GEOID_GRD_FILE=geoid_fahr.grd

# if applicable, state tide model[ geoid grd correction file | NONE ]
# [ nao99b | NONE ]
# for nao99b: data dir(link) omap/*.nao must reside in caling directory
APPLY_TIDE_MODEL=nao99b

# data format version number
# [0|1]
# (0=12ch fahrenberg type)
# (1=1ch multi refl event koenigsstuhl type)
DATA_VERSION=1

# time offset correction [sec]
# due to wrong measurement start time
# extract time info from nav message
# (only needed for Version 0 data)
V0_TIME_OFFSET=0.0

# specify correlator channel
# (only needed for Version 0 data)
V0_MEASUREMENT_CHANNEL=1
# iq and qp outliers are interpolated outside limit
V0_MAX_DELTA_MEDIAN=5000

# ID mark of all output files
# depending on specified output, file extention
# will be appended automatically
OUTPUT_FILE_ID=test

# specify output quantity:
# head - header
# adat - all data
OUTPUT_QUANTITY=head

# specify output format:
# ascii (tab/space delimited ascii column data)
# matlab (ascii header file and matlab readable binary mat file)
# matlab (only implemented at sdat3)
# [ascii|matlab]
OUTPUT_QUANTITY=ascii

# if required, state user/receiver position
# ([deg] and [m/WGS-84])
USER_LAT=47.5
USER_LON=13.4
USER_HEIGHT=1700

# factor to detrend dpath-dpathm
# use as uncorrected height offset between model and data [m]
DPATH_DSLIP_HEIGHT=-4.5
# reflector height estimate (above ref. ellips [m])
# reference height and location
REFLECTOR_HEIGHT_GUESS=800.0
REFLECTOR_HEIGHT_GUESS_LAT=47.5
REFLECTOR_HEIGHT_GUESS_LON=13.4

# sometimes phase has to be inverted
# so that height guesses can detrend profil [0|1]
INVERT_PHASE=1

# if VAL>1 iterate height guess
# to find height time serie with
# minimal trend calculated
# from linear regression analyse
# (trend analyse only implemented for prompt channel!)
```

```
SEARCH_HEIGHT_ITERATIONS=100

# height iteration step size
# taken for search [m]
SEARCH_HEIGHT_STEPS=0.01

# limit output time series
# (but all data is processed/window filtered)
# start/stop values in sec since measurement start
# TIME_SEC_MIN < 0.0 == output all data
TIME_SEC_MIN=-1.0
TIME_SEC_MAX=-1.0

# substract running mean value from i/q data (only if LEN > 0)
# filter length in samples (==1/50 sec)
SUBSTRACT_MEAN_IQ_LENGTH=1500

# apply AGC of LEN to QUAD-PHASE data (only if LEN > 0)
# AGC FAC = (mean i)/(mean q) [samples]
# apply const gain to  QUAD-PHASE data (only if LEN <= 0)
# GAIN FAC = 1-1000 [%]
GAIN_AGC_Q_LENGTH=1500

# filter outliers in I/Q data (only if LEN > 0)
# filter length in samples
FILTER_OUTLIER_LENGTH=-1

# apply additional filter to IN-PHASE data
# [none|mean|median]
# filter length in samples
FILTER_I=mean
FILTER_I_LENGTH=20

# apply additional filter to QUAD-PHASE data
# [none|mean|median]
# filter length in samples
FILTER_Q=mean
FILTER_Q_LENGTH=20

# amplify QUAD-PHASE data (only if FAC > 0)
# data=FAC [%] x data
# do not use anymore, use GAIN_AGC_Q < 0
# no gain to Q, use GAIN_AGC_Q =-100
GAIN_Q_FACTOR=-200

# deslip jumps in deltapath data (only if FAC > 0.0)
# if jumps > abs(FAC * Lambda L1)
DESLIP_FACTOR=-1.0

# deslip jumps in deltapath data (only if FAC > 0.0)
# by comparing dpath with model dpath
# model based on reflector height estim. and geometry
# if jumps > abs(FAC * Lambda L1)
DESLIP_MODEL_FACTOR=0.5

# amplitude [m] of simple harmonic wave model
#(only applied if ampl. > 0.0)
MODEL_WAVE_AMPLITUDE=0.2
# frequency [Hz] of simple harmonic wave model
MODEL_WAVE_FREQUENCY=0.1

# assign a model to Q data
# based on shifted I data
# shift= x [samples]
# x=12.5/f_interf
# enter shift=0 for no q mod
Q_MOD_I_SHIFT=0

# estimate abs. height from max interference frequency
# and geometry (elev. and delev/dt)
# max f estimated from spectrum of a running time window
# length of window in samples (only if LEN < 0, best performance with LEN=2^n)
# [0|4096|8192|16384|32768|65536]
ABS_HEIGHT_WINDOW_LENGTH=4096

# comments start with # and are ignored
# empty lines are ignored
# order of parameters is ignored
#####################################
```

DOI: 10.2312/GFZ.b103-08104

F OpenGPS Circuit Layout

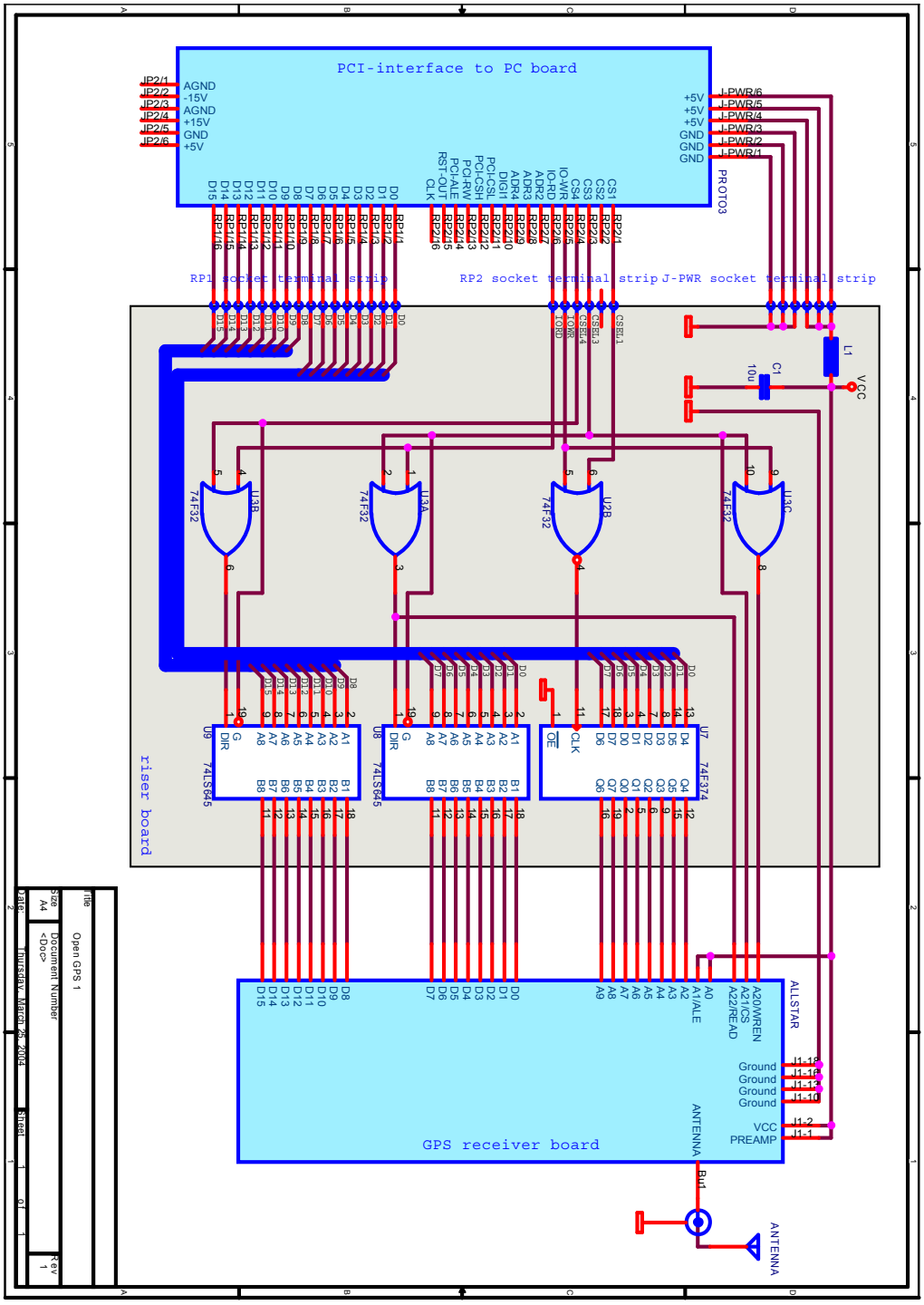

Fig. F.1: *OpenGPS receiver PCI-card board layout (P. Selke, pers. communication) with TTL logic interface riser board and Zarlink GPS receiver board attached.*

DOI: 10.2312/GFZ.b103-08104

STR08/10

Achim Helm, Ground-based GPS altimetry with the L1 OpenGPS receiver

ISSN 1610-0956

DOI: 10.2312/GFZ.b103-08104

Scientific Technical Report 08/10

Deutsches GeoForschungsZentrum GFZ